Order 2016LYSEI154

Ph.D. THESIS OF L'UNIVERSITE DE LYON

Performed at

INSA DE LYON

Doctoral formation
Mécanique, Énergétique, Génie Civil, Acoustique

Specialty:

MÉCANIQUE - GÉNIE MÉCANIQUE - GÉNIE CIVIL

Publicly defended on December 16th 2016 by:

Kwassi AMUZUGA

Mechanical Engineer

DAMAGE MECHANISM RELATED TO PLASTICITY AROUND HETEROGENEOUS INCLUSIONS UNDER ROLLING CONTACT LOADING IN HYBRID BEARINGS CERAMIC/STEEL

Before the jury:

Sylvie POMMIER	Prof.	ENS Cachan	Examiner
Farshid SADEGHI	Prof.	Purdue University	Rapporteur
Djimedo KONDO	Prof.	Paris 6 University	Rapporteur
Daniel NÉLIAS	Prof.	LaMCoS	Ph.D. Director
Sophie CAZOTTES	Lecturer	MATEIS	Supervisor
Guillermo MORALES	Research Director	SKF ERC	Examiner
Alexandre MONDELIN	Dr.	SKF Aerospace	Supervisor
Thibaut CHAISE	Lecturer	LaMCoS	Supervisor

Département FEDORA – INSA Lyon - Ecoles Doctorales – Quinquennal 2016-2020

SIGLE	ECOLE DOCTORALE	NOM ET COORDONNEES DU RESPONSABLE
CHIMIE	CHIMIE DE LYON http://www.edchimie-lyon.fr Sec : Renée EL MELHEM Bat Blaise Pascal 3e etage secretariat@edchimie-lyon.fr Insa : R. GOURDON	M. Stéphane DANIELE Institut de Recherches sur la Catalyse et l'Environnement de Lyon IRCELYON-UMR 5256 Équipe CDFA 2 avenue Albert Einstein 69626 Villeurbanne cedex directeur@edchimie-lyon.fr
E.E.A.	ELECTRONIQUE, ELECTROTECHNIQUE, AUTOMATIQUE http://edeea.ec-lyon.fr Sec : M.C. HAVGOUDOUKIAN Ecole-Doctorale.eea@ec-lyon.fr	M. Gérard SCORLETTI Ecole Centrale de Lyon 36 avenue Guy de Collongue 69134 ECULLY Tél : 04.72.18 60.97 Fax : 04 78 43 37 17 Gerard.scorletti@ec-lyon.fr
E2M2	EVOLUTION, ECOSYSTEME, MICROBIOLOGIE, MODELISATION http://e2m2.universite-lyon.fr Sec : Safia AIT CHALAL Bat Darwin - UCB Lyon 1 04.72.43.28.91 Insa : H. CHARLES Safia.ait-chalal@univ-lyon1.fr	Mme Gudrun BORNETTE CNRS UMR 5023 LEHNA Université Claude Bernard Lyon 1 Bât Forel 43 bd du 11 novembre 1918 69622 VILLEURBANNE Cédex Tél : 06.07.53.89.13 e2m2@ univ-lyon1.fr
EDISS	INTERDISCIPLINAIRE SCIENCES-SANTE http://www.ediss-lyon.fr Sec : Safia AIT CHALAL Hôpital Louis Pradel - Bron 04 72 68 49 09 Insa : M. LAGARDE Safia.ait-chalal@univ-lyon1.fr	Mme Emmanuelle CANET-SOULAS INSERM U1060, CarMeN lab, Univ. Lyon 1 Bâtiment IMBL 11 avenue Jean Capelle INSA de Lyon 696621 Villeurbanne Tél : 04.72.68.49.09 Fax :04 72 68 49 16 Emmanuelle.canet@univ-lyon1.fr
INFOMATHS	INFORMATIQUE ET MATHEMATIQUES http://infomaths.univ-lyon1.fr Sec :Renée EL MELHEM Bat Blaise Pascal 3e etage infomaths@univ-lyon1.fr	Mme Sylvie CALABRETTO LIRIS – INSA de Lyon Bat Blaise Pascal 7 avenue Jean Capelle 69622 VILLEURBANNE Cedex Tél : 04.72. 43. 80. 46 Fax 04 72 43 16 87 Sylvie.calabretto@insa-lyon.fr
Matériaux	MATERIAUX DE LYON http://ed34.universite-lyon.fr Sec : M. LABOUNE PM : 71.70 –Fax : 87.12 Bat. Saint Exupéry Ed.materiaux@insa-lyon.fr	M. Jean-Yves BUFFIERE INSA de Lyon MATEIS Bâtiment Saint Exupéry 7 avenue Jean Capelle 69621 VILLEURBANNE Cedex Tél : 04.72.43 71.70 Fax 04 72 43 85 28 Ed.materiaux@insa-lyon.fr
MEGA	MECANIQUE, ENERGETIQUE, GENIE CIVIL, ACOUSTIQUE http://mega.universite-lyon.fr Sec : M. LABOUNE PM : 71.70 –Fax : 87.12 Bat. Saint Exupéry mega@insa-lyon.fr	M. Philippe BOISSE INSA de Lyon Laboratoire LAMCOS Bâtiment Jacquard 25 bis avenue Jean Capelle 69621 VILLEURBANNE Cedex Tél : 04.72 .43.71.70 Fax : 04 72 43 72 37 Philippe.boisse@insa-lyon.fr
ScSo	ScSo* http://recherche.univ-lyon2.fr/scso/ Sec : Viviane POLSINELLI Brigitte DUBOIS Insa : J.Y. TOUSSAINT viviane.polsinelli@univ-lyon2.fr	Mme Isabelle VON BUELTZINGLOEWEN Université Lyon 2 86 rue Pasteur 69365 LYON Cedex 07 Tél : 04.78.77.23.86 Fax : 04.37.28.04.48

*ScSo : Histoire, Géographie, Aménagement, Urbanisme, Archéologie, Science politique, Sociologie, Anthropologie

He who possesses most must be most afraid of loss.
He who thinks little, errs much.
He who walks straight rarely falls.
It is easier to resist at the beginning than at the end.
Simplicity is the ultimate sophistication.

— Leonardo da Vinci [1]

ACKNOWLEDGEMENTS

ABSTRACT

The lifetime of contacting mechanical parts is strongly affected by the presence of heterogeneities in their materials, such as reinforcements (fibers, particles), precipitates, porosities, or cracks. Hard heterogeneities having complex forms can create local over-stress that initiating fatigue cracks near the contact surface. The presence of heterogeneities influences the physical and mechanical properties of the material at microscopic and macroscopic scales. A quantitative analysis of the over-stresses generated by heterogeneities is necessary to the comprehension of the damage mechanisms. The present study is applied to rolling bearings which are the critical elements of the aero-engine's mainshaft. The performance required for these bearings, led SKF Aerospace to introduce a new technology of hybrid bearing with ceramic rolling elements on high-strength steels having experienced a double surface treatment (carburizing followed by nitriding). The study aims to precisely determine the pressure field distribution on the effective contact area and to predict the profile and the evolution of the stress/strain fields at each loading cycle on a representative elementary volume that takes into account the gradient of hardness, the presence of carbides and the existence of an initial compressive stress from thermochemical origin.

A major part of this study is devoted to develop a heterogeneous elastic-plastic rolling contact solver, by semi-analytical methods ensuring an excellent saving of calculation time and resources. Thereafter, a homogenization algorithm was built to analyze the effective behavior of a heterogeneous elastic-plastic half-space subjected to an indentation loading. Finally, an experimental part is dedicated to the microstructure characterization of the studied steels with intent to determine their properties. A description of the carbides behavior inside the matrix during micro-tensile tests was carried out under SEM in-situ observation. In the scheme of all analyses conducted in the present work, it can be argued that, although the heterogeneities (such as carbides or nitrides) are responsible for the high resistance of the studied materials, some of them (those whose length exceeds tens of micrometer or those which form stringers in a particular direction) become, over fatigue cycles, the main sources of damage, from their local scale up to the macroscopic failure of the structure.

CONTENTS

LIST OF FIGURES

LIST OF TABLES

ACRONYMS

2D-FFT two-dimensional fast Fourier transform

3D-FFT three-dimensional fast Fourier transform

HEPC Heterogeneous Elastic-Plastic Contact

HEPRC Heterogeneous Elastic-Plastic Rolling Contact

LISTINGS

Greek letters

δx	Relative difference between the heterogeneity center position and the contact center position
ν_m, ν_I	Poisson's ratio of the matrix m and the inclusion I
ν_{ball}	Poisson's ratio of the ball
σ^y	Yield stress of the flat body (or the substrate matrix)
γ	Ratio of the heterogeneity's Young's modulus to the matrix's
β	Ratio of the heterogeneity's size and a
α	Ratio of the heterogeneity's center location in the depth and a
σ_{HP}	Hydrostatic pressure
ε^p_{max}	Accumulated plastic strain
θ	Stringer orientation relative to the rolling direction
τ	Effective accumulated plastic strain
τ_{max} or σ_{tresca}	Maximum shear stress
σ_{VM}	Von Mises equivalent stress

Letters

a	Contact radius for Hertzian homogeneous elastic contact problems
E_m,E_I	Young's modulus of the matrix m and the heterogeneity I
E_{ball}	Young's modulus of the ball
d	Roller diameter or Indenter diameter
P_0	Applied maximum Hertzian pressure
P_{max}	Contact maximum pressure
f	Surface friction coefficient
S_i	Heterogeneity's defined size in terms of semi-length comparable to the contact radius a
z_i	Heterogeneity's center location in the depth
B, C, n	Swift isotropic law parameters
D_x	Rolling distance
$D_i^{(P)}$	Pressure disturbance distance generated by the heterogeneity relative to the evolution in the homogeneous case
$D_i^{(\varepsilon)}$	Plastic strain disturbance distance generated by the heterogeneity relative to the evolution in the homogeneous case
$D_i^{(\tau)}$	Shear stress disturbance distance generated by the heterogeneity relative to the evolution in the homogeneous case
d_i	The interaction distance between each heterogeneity center in the stringer or cluster
N_i	The number of heterogeneities in the cluster
h	The gap between contact surfaces
S	Heterogeneity's defined size as semi-length in common with a the contact radius
z_i	Heterogeneity's center location in the depth
B_{VER}	Representative Elementary Volume (REV) boundary
N	Number of heterogeneities
D	Heterogeneities ranging and inter-centers distance
V_f	Heterogeneity content or Volume fraction: total heterogeneity volume over REV volume
D_{ensity}	Heterogeneity density: Heterogeneity size over the distribution inter-distance

Part I

CONTEXT AND BACKGROUND

The main objective of this thesis is to develop a fast and versatile tool for studying damage mechanisms related to plastic strain and residual stresses induced by rolling contact loading on heterogeneous elastic-plastic body. The present study interesting feature is the combination of analytical, numerical and experimental results in order to deal with the subject in issue. Semi-analytical model is created, in one hand to solve the rolling problem, and in the other hand to integrate the materials micromechanical behavior resulting from the heterogeneities population data, the presence of initial compressive stress and the gradient of plastic property. An accurate correlation between analysis from academic and industrial cases, is carefully devoted to ensure the applicability of this Ph.D. work. The results presented hereafter, have been sustained and commented by comparison with other works.

1 GENERAL INTRODUCTION

Thorough understanding of the consequence of every designing choice on the work-piece life in service is essential to meet the need of controlling every parameter of manufacturing procedures. This is a key point to no longer leave adjustment variable to empirical rules. Therefore the main motivation of the present work is to provide a fast and versatile tools that can be used from academic research to industrial applications for design analysis. This will aim to explore the aerospace materials from microscopic to mesoscopic, and towards macroscopic scales by the identification of damage mechanisms related to plasticity around heterogeneous inclusions under contact loading in aerospace bearings.

Contents

1.1 PROBLEMATIC AND MOTIVATIONS

A major objective of the engine manufacturers is to decrease weight, fuel consumption, pollution and noise of turbo-machines, while ensuring their performance, reliability and economic competitiveness. Thus, steady progress has been made on the performance of turbo shaft engines. Typically, Fig. 1.1 obtained from SAFRAN Helicopter Engines[a] communication journal, shows that, in 30 years, from **Artouste 2C** to **Arrius 2F** turbo engines, the fuel consumption decreased by -30%, while the engine power was increased up to $+30\%$.

[a] *the new label name of Turbomeca*

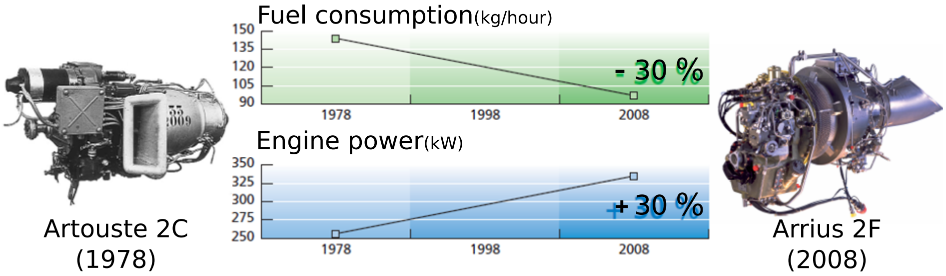

Figure 1.1: Overview of the consumption reduction of specific engines

Innovations realized in aircraft engines bearings framework constitute a major part of participation for achieving the aforementioned performance. Since bearings are excellent friction reducers, their enhancement enable a considerable decrease of energy expenditure thus an increase of the engine power. It is worth noting that bearings also play the greatest role in the load carrying as well as the moving machine parts positioning.

1.1.1 BEARINGS IN AIRCRAFT ENGINES

In the next few years the predicted rise of fuel prices will play an important role in aerospace industry. To decrease oil consumption and respect anti-pollution policy, the major subject became weight reducing with the constrain of performance conservation or enhancement. Advanced high-strength steels are in constant development for structural components and body parts. This demand also reaches specific elements such as bearings. The foremost output of this study is directly applied in aeronautical environment, especially on the new technology of hybrid (ceramic/steel) bearings under extreme conditions. The global knowledge of those components behavior is needed. It worth remembering that line shaft bearings are critical components of aeronautical engines. The reliability requirements, space constraints and weight inspired SKF[b] to advocate the use of hybrid bearings with ceramic rolling elements (Si_3N_4) and high yield strength steel rings keeping good mechanical properties up to high temperatures of about 250°C. The desired performance, including very long lifetime in the order of several tens of thousand hours that correspond to tens of billions of fatigue cycles and the consideration of rolling elements in droves with their speeds, led SKF to introduce new materials which are the M50 and M50NiL (with potential double thermochemical treatments). These steels undergo a double surface treatment: hardening[c] and nitriding. However, the fatigue resistance of these steels is not well known and poorly understood, especially for very large numbers of cycles. The behavior of the matrix in the vicinity of such carbides inclusions in droves for these types of steels, and the

[b] *SKF-Aerospace more precisely*

[c] *through-hardening for M50 because it has sufficient carbon amount and case-hardening for M50NiL with carbon intake*

strong gradient of properties in the vicinity of the surface, was not thoroughly studied, especially in contact loading involving ceramic rolling elements.

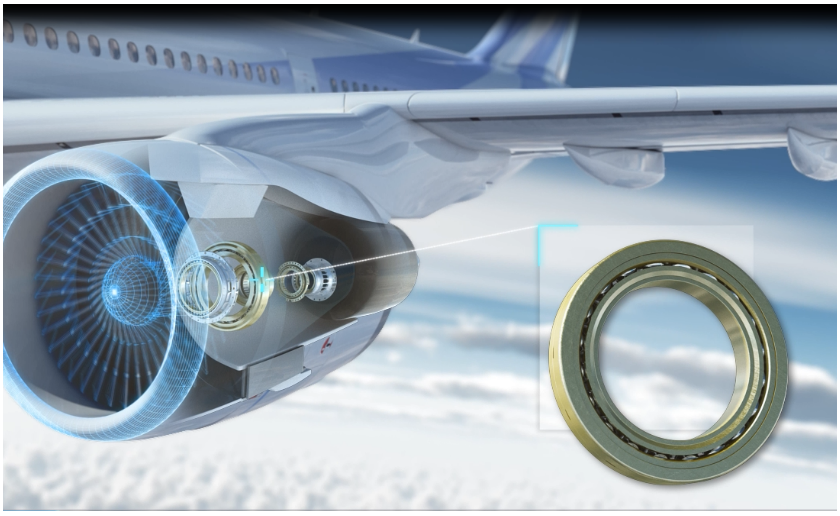

Figure 1.2: Bearings in aircraft engines

Fig. 1.2 presents the future position, on the engine mainshaft, of the hybrid[d] rolling bearing designed for aeronautical environment. The greatest claimed benefits for this new technology against all-steel bearings, consists in their:

[d] Si_3N_4 ceramic balls on M50NiL steel raceways

- High hardness
- Greater stiffness
- Lower density
- High fatigue resistance
- Greater corrosion resistance
- Lower thermal dilatation
- No chemical affinity with steel

However in front of these advantages stands two major issues:

- Global knowledge under extreme conditions
- Distinguish mechanisms that strengthen the bearing versus those that accent its damage risk.

The present study examined the principal factors relating plasticity around heterogeneity to damage mechanisms, when typical aerospace bearing experiencing high contact pressure over rolling cycles. It is recognized that rapid spall growth can lead to catastrophic bearing failure. Hence, understanding the spall growth phase and factors that may accelerate growth rates, is a key to achieving a reliable and robust bearing design. [2]

1.1.2 ROLLING FATIGUE MECHANISM

The Rolling Contact Fatigue (RCF) should be rigorously differentiated from the standard fatigue when mechanical parts are submitted to recurrent[e] loading over the time [3]. The RCF is a complex combination of the role of surface/subsurface defects (roughness/porosity, inclusion) and the tribological operating conditions [4]. It can be stated that:

[e] meaning a repetition that could be cyclic and/or periodic

- RCF is a multi-axial fatigue. The stress state is issued from non-conforming contact with respect to Hertzian theory assumptions.
- The phenomena related to RCF occurs in very localized volume. The involving contact areas are generally around a tenth of a millimeter.

- The stress field components evolve independently of each other by regarding the loading path on a fixed material point below the surface; even more in presence of plasticity and heterogeneity. As a consequence, the axes of the principal stresses are in constantly changing over cycles. Therefore it becomes complex to predict the plans most sensitive to fatigue by tracking maximum shear plans.
- The hydrostatic stress level is significantly high with a negative sign in reference to the applied compression. When, in certain locations, the hydrostatic stress gets a positive sign meaning pure tensile, a crack may be initiated and/or propagated.

The RCF could be distinguished and interpreted at two scales [5, 6]: (i) Pitting, micro-pitting or micro spalling, at the microscopic scale when the damage risk is attributed to the surface; (ii) flaking, spalling or macro-spalling, at the macroscopic scale when the damage risk is attributed to the subsurface.

1.1.2.1 Bearing races surface risk

Fig. 1.3 described the different stages of the RCF damage mechanism initiated from the surface and ending to a chunk of material removal called pitting. Surface defects are mostly caused by surface asperities left after the finishing process or created by debris denting [7, 8] or even more by wear. Then cracks are progressing towards the subsurface. The stress concentration at the crack front promotes its propagation by engaging slip-bands and plasticity [9] over cycles. The crack trajectory is governed by the range of shear stress acting on favorably oriented grains and depending the stiffness of each grain boundary [10]. The weakest grains could be cracked by cleavage or by cavitation. The intra-granular crack is due to a slipping of crystallographic planes or an alignment of dislocation cells, when the two opposite edges of the grain boundary are subjected to high shear stress. This microscopic rupture stress limit for the initiation of slip bands is very detailed as well by C. Zener's theoretical criterion [11]. Some thirty years later, K. Tanaka and T. Mura expose their slip-band crack theory in case of fatigue loading [12]. Thereafter, the network of inter and intra-granular cracks evolves in function of the statistical variation in the material microstructural characteristics [13]. At this stage, the crack evolution can be significantly delayed when the microstructure contains small grains with high disorientation. The micro-spalling or pitting occurred when some branches of the connected cracks emerged to the surface.

$\boxed{f}$ *even more when the contacting materials have a significant difference between their coefficient of heat transmission and/or their specific heat (in the present case of ceramic on steel contact)*

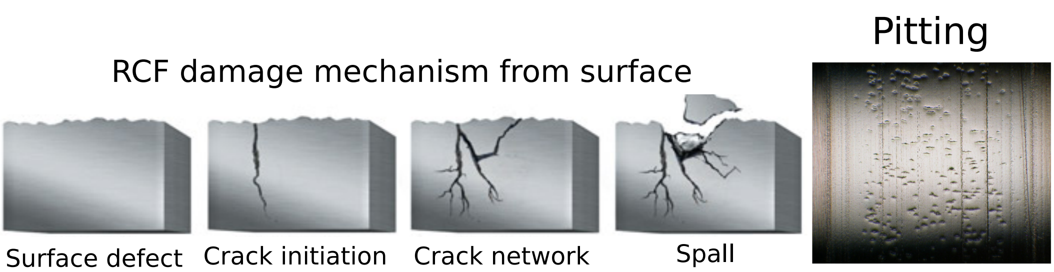

Figure 1.3: RCF damage mechanism initiated from surface [14] and ending to surface pitting [15]

Notwithstanding the pitting due to surface defects, abrasion and thermal fatigue can cause the emergence of cracks at the surface [16]. Since the thermal equilibrium is not spontaneously established (i) between the contacting surfaces^{f} and (ii) between each surface and its material core, then the cyclical differential of temperature that occurred over the load passage, will create thermal fatigue micro cracks. Indeed, in RCF situation a spot elevation of the temperature can reach or exceed very locally, the order of 910°C leading to austenitization[g] at grains scale. This is prone by a combination of various sources of thermal dissipation such as friction and plasticity. The phenomenon is emphasized in boundary lubrication regime if the contact stress has been increased accidentally. Moreover, if some microcracks existed at first, it is postulated that the friction at edges of microcracks can heat locally to temperatures between 750° and 1250°C [17, 18, 19]. Afterwards, a quenching occurred by the intense heat conduction into the material core or through the new arrival lubricant wave. This formed an extremely brittle martensite[h] at the surface. The martensite polycrystal will be snatched at the next rolling pass leading to micro-pitting.

g: *Transformation from alpha-iron called ferrite to gamma-iron called austenite*

h: *Unbalance phase that forms when steel is quenched*

1.1.2.2 Bearing races subsurface risk

Surface coating techniques are ones of the best alternatives to effectively prevent from surface risk [20]. However, depending on the coating deposition process, material and thickness, considerable near-surface heterogeneity constitute a favorable source of stress concentration. From the first crack initiations to spalling failure, the rolling bearing life is conditioned by multiple heterogeneity interactions [21, 22]. Fig. 1.4 presents the surface spalling as consequence of the growth of cracks that emanate from localized heterogeneity. It could be seen that the mechanism following a crack initiated in the subsurface is similar to that from surface defects as explained previously, with the exception that the crack network generated is conductive to a spalling instead of a micro-pitting according to size of the chunk of material removed. The surface spalling stage is succinctly described by Jin and Kang's [23].

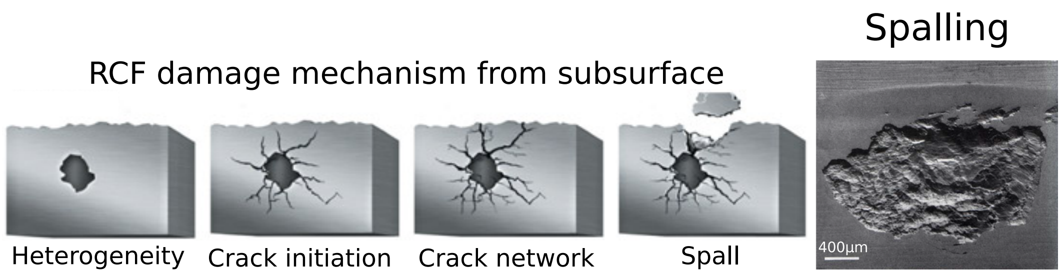

Figure 1.4: RCF damage mechanism initiated from subsurface [14] and ending to surface spalling [5, 6]

1.2 INDUSTRIAL AND ACADEMIC SOLUTIONS

The life-time of functional mechanical parts is strongly affected by the presence of inhomogeneity in the material, as reinforcements (fibers, particles), precipitates, porosities, or cracks. Soft and hard heterogeneity, whatever their shapes, act as stress concentrators that may lead to fatigue cracks. For contact problems this type of failure is classified as inclusion or porosity initiated contact fatigue [24, 25]. The presence of such heterogeneity greatly influences the physical and mechanical properties of the material both locally and globally [26]. A quantitative analysis of the over-stress created by heterogeneity is necessary to understand the damage mechanisms correctly. Heterogeneity can, also, alter the material behavior at the macroscopic scale and also the stress field in its vicinity. This is due to the incompatibility of deformation between the heterogeneity and the surrounding matrix. Eshelby [27, 28] studied the stress variations caused by a single ellipsoidal heterogeneity within an infinite solid. He proposed a method known as the Equivalent Inclusion Method (EIM) in which the heterogeneity is assimilated to an inclusion[a] containing incompatible strains and having the same material properties as those of the matrix. These incompatibility strains, also called eigenstrains, can be present in the form of inelastic strains in the heterogeneity such as plastic or thermal strains. N

[a] *in the sense of Mura [29]*

Strong stress gradients are encountered for contact problems. When the volume taken by the heterogeneity becomes large compared to the contact size, two numerical techniques can be employed. The first one uses the analytical developments of Moschovidis and Mura [30] expressing each elastic field in polynomial form. The second method is to discretize a heterogeneity of arbitrary shape into multiple elementary cuboids whose size corresponds to the mesh. Then, the eigenstrain within each cuboid is considered uniform. Usually, an initial inelastic deformation or an external load is considered as an input strain but few studies dealt with the combination of both eigenstrain sources. For contact problems, eigenstrain formulation corresponds to the sum of both sources [31]. This formulation will be used here to treat heterogeneity and plasticity as eigenstrains. In most cases, contact problems with the presence of heterogeneity beneath the surface are not explicitly solved and a semi-elliptical Hertzian contact pressure distribution is considered instead [32, 33]. In addition the contact pressure can be greatly affected by the presence of heterogeneity located in the vicinity of the surface [34, 35, 36]. Moreover, plasticity plays also a key role since it modifies the contact pressure distribution, often limiting the maximum contact pressure while increasing the contact area to keep the integral of the pressure (i.e. the applied load) constant. The resolution of the contact problem when the material is elastic-plastic [37, 38, 39] or when it contains heterogeneity [36, 40] is treated by updating the contact geometry by adding the contribution of eigenstrains to surface displacements [41].

Several bearing manufacturers concluded that the determination of the bearing fatigue life based on criteria from an elastic analysis is not accurately predictive. It has been demonstrated that, as soon as the Von Mises stress exceeds the yield strength of the material, the contact pressure distribution and contact area start to deviate from the Hertzian (elastic) solution. One also has to keep in mind the fact that, if the material is often assumed (macroscopically) homogeneous and isotropic, a look at a smaller scale reveals that the micro-structure contains oriented grains and inhomogeneity also called heterogeneous inclusions. The Weibull distribution of the fatigue life is often attributed to the stochastic distribution of defects within the material. The concept of endurance limit has been introduced so far [25, 42] based on a purely elastic analysis considering the worst types of inhomogeneity and their locations below the surface, however, assuming that the contact pressure distribution is Hertzian i.e. not perturbed by the presence of inhomogeneity.

Contact mechanics is based on unilateral inequalities concerning the gap (positive or nil) and the pressure (positive or nil) between contacting surfaces, whatever the body geometry, material internal structure and loading conditions are [43]. Even if these unilateral inequalities are found to be a key point common to any existing methods of contact problems resolution, the physical phenomena that occur at/in the vicinity of contacting half-spaces, result in inexhaustible industrial and scientific frameworks. Therefore, solutions are nowadays developed at the interface of applied mathematics, mechanics, numerical analysis, computer science, surface physics, subsurface chemistry and experimental methods.

1.3 OUTLINE

The general problem consists to study the rolling contact between a ceramic ball and a heterogeneous elastic-plastic body containing multiple carbide inclusions of arbitrary shapes, positions and sizes. The elastic-plastic behavior is taken into account by the gradient of properties evolving as a function of the depth. The present work combines numerical and experimental studies. The simulation part concerns the development of a semi-analytical model to investigate the effect of multiple carbides, their mutual influence and the coupled interaction with their surroundings plastic zone when the medium is subjected to contact load. Experimental part is devoted to determine material properties and related damage mechanisms. Note that in reality both studies are conducted in parallel during this research. By doing so, experimental results are used to supply the numerical model when at its turn provides the requisite evidence for supporting the analysis and the explanation of facts observed during the experimental tests.

1.3.1 NUMERICAL STUDY

A heterogeneous elastic-plastic contact (HEPC) solver is developed. First, an indentation model is created to examine carefully, on the one hand, the contribution of heterogeneity concentration stress by taking into account its interaction with the surrounding plastic zone, and in the other hand the contribution of the residual stress due to plastic strain by taking into account its interaction with the inclusion. Parametric study is conducted by varying the heterogeneity shape, position and size. The essential aspects studied are listed below.

- The contact pressure distribution and the contact area size
- Eigen-stress field generated by the heterogeneity
- Residual stress field generated by the plasticity
- Total subsurface stress field
- Accumulated plastic strain distribution

Secondly, the HEPC solver is extended to the resolution of rolling contact problem by moving the applied load. The HEPC is solved at each time-step, in quasi-static sense. Motion velocity effect is not considered. However inertial forces due to accelerations could be directly taken into account in the balance of applied forces. Note that the contact solver enables an application of normal and tangential loads (forces or displacements). During loading cycles, a heterogeneity acts as stress intensifier and becomes the site of subsurface crack initiation and propagation. Therefore, Dang Van crack initiation criterion is involved in relationship with the shear and the hydrostatic stresses, in other to seek the potential risky zones for crack departure around the heterogeneity

Finally the HEPC solver is coupled with the Levenberg-Marquardt minimization algorithm to identify the overall non-linear inelastic behavior of a heterogeneous elastic plastic body under indentation. The effective elastic modulus and effective yield stress are obtained by fitting the load-displacement curves of the heterogeneous body with that of the homogenized body. Special care is devoted to build an objective and consistent representative elementary volume (REV) ensuring an accurate estimation of the heterogeneity content and density. The role of heterogeneity size, location and material properties, along with the hardening properties of the indented body are investigated.

1.3.2 EXPERIMENTAL STUDY

Micromechanical and microstructural characterizations are conducted to investigate material properties and their consequence on the behavior under an applied stress field. Scanning electron microscope (SEM) and Energy Dispersive X-ray (EDX) are the main means used to characterize the matrix (M50, M50-Nil), the carbides and the nitrites. Indentation tests allowed to obtain the material plastic behavior related to hardness according to the depth. Also, micro indentation tests lead to determine the carbides elastic modulus. Moreover, micro-tensile tests are performed in purpose to propose a mechanism of carbides damaging. The results obtained from the experimental tests have enabled a means of obtaining key components:

- Microstructure features: carbides and nitrides size, shape, distribution and volume fraction
- Comparison of M50 and M50-Nil media
- Data to build representative elementary volumes
- Local behavior of the matrix plastic strain around damaged and undamaged carbide

1.3.3 SYNTHETIC STUDY

Synthetic analysis is directly included in both experimental and numerical studies when correlation is needed. Observations and material properties resulting from experimental tests are used as input of semi-analytical rolling contact model for numerical simulations. The knowledge developed herein by summarizing experimental and numerical studies consists in:

- The determination of the evolution of stress/strain fields in M50 and M50-Nil bearing material before damage occurrence.
- The prediction of the behavior of a cracked carbide stringer in relation with the ductile matrix
- The consequence of heat-treatment on the microstructure (gradient of properties, initial residual stress) and on the fatigue life (Dang Van damage criteria)
- A proper analysis of surface tribological behavior and accurate prediction of surface and subsurface damage in rolling contact problems conducted on heterogeneous elastic-plastic materials

2

THEORETICAL BACKGROUND

The recent progress in the development of semi-analytical methods makes it now possible to model three dimensional heterogeneous elastic-plastic contact (HEPC) problems. A first attempt was made by Kabo and Ekberg [32] to model the over-stress due to a cylindrical inclusion in an elastic-plastic rolling contact situation using a two-dimensional finite element analysis. The same type of analysis was recently revisited by Pandkar et al. [44]. The purpose of the present chapter is to present the foundation of a three-dimensional elastic-plastic contact model in the presence of a single or several interacting inhomogeneities.

Contents

2.1 INTRODUCTION

Two methods are employed to solve the contact problem when at least one of the bodies in contact contains heterogeneities. The first one uses a method of decomposition of the semi-infinite space into subspaces, requiring a numerical solution [45]. This method was initially introduced and validated by Jacq [37] and reiterated by Chaise [39] and Fulleringer [41] and will be used to describe the plastic phenomenon. A second direct method [46, 47], initially proposed by Mindlin and Cheng [48], which allows to analytically determine the solution of the elastic field caused by eigenstrain in an elastic semi-infinite body. Because of the difficulty to treat the interactions between heterogeneities, most research works focus on the interactions between two or three maximum heterogeneities. Moschovidis and Mura [30] have specifically studied the influence of two ellipsoidal heterogeneities without interpenetration by approximating the expression of equivalent eigenstrains with Taylor's series. This approach was heavily explored and adapted to different cases of restrictive applications [31, 49]. These solutions become very heavy when hundreds or thousands of heterogeneities have to be treated numerically. It is worth developing a numerical method based on conjugate gradient algorithms to solve a linear system of equations induced by these multiples of thousands heterogeneities in order to minimize convergence iterations.

2.2 FORMULATION OF HETEROGENEOUS ELASTIC-PLASTIC CONTACT PROBLEM

The Heterogeneous Elastic-Plastic Contact (HEPC) problem is considered in this study as a contact involving an elastic indenter normally loaded onto an elastic-plastic matrix containing one or several heterogeneities. For demonstration purposes the analysis and the discussion are limited here to one elastic-plastic body only. However the model can be easily applied to the problem when two heterogeneous elastic-plastic bodies in contact are involved. For the same reason of simplicity the heterogeneous inclusions are assumed to behave elastically with perfect bonding between them and the matrix (i.e. continuity of displacements).

2.2.1 ELASTIC CONTACT

The resolution of the contact problem between two bodies B_1 and B_2 (Fig. 2.1), consists of finding the solution fulfilling a set of equations describing the physics of the problem as following:

THE LOAD BALANCE EQUATION. The equality between the applied load W and the integral of the contact pressure $p(x,y)$ on the contact area Γ_c must be satisfied.

$$W = \int_{\Gamma_c} p(x,y)\,d\Gamma \tag{2.1}$$

THE SURFACE SEPARATION EQUATION. The contact gap h is equal to the summation of the initial distance between the contacting surfaces $h_i(x,y)$, the rigid body displacement δ and the normal component of the body displacements $u_3^{B1+B2}(x,y)$. The subscript $_3$ corresponds to the direction normal to the surface[a] .

[a] $(1,2,3)$ *used are consistent to the Cartesian coordinate system* (x,y,z)

$$h(x,y) = h_i(x,y) + \delta + u_3^{B1+B2}(x,y) \tag{2.2}$$

THE CONTACT CONDITION EQUATION. The non-interpenetration of contacting bodies holds the distance $h(x,y)$ positive or nil.

$$\begin{array}{ll} \text{When } h(x,y) = 0 \text{ then } p(x,y) > 0 & \Leftrightarrow \text{ contact} \\ \text{When } h(x,y) > 0 \text{ then } p(x,y) = 0 & \Leftrightarrow \text{ separation} \end{array} \qquad (2.3)$$

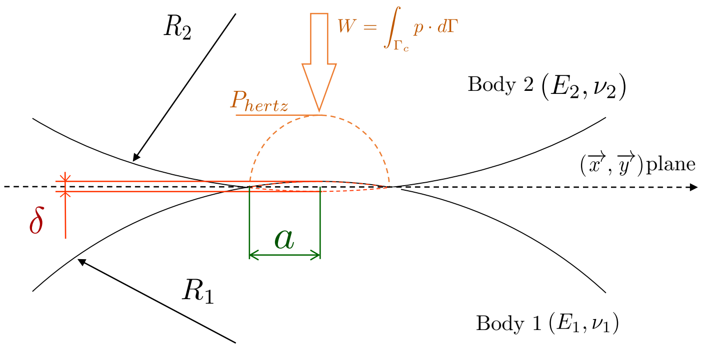

Figure 2.1: Description of the elastic contact variables

Polonsky and Keer [50] proposed a semi analytical algorithm based on the Conjugate Gradient Method (CGM) and Fast Fourier Transform (FFT) to solve the set of Eq. 2.1-2.2-2.3. Fig. 2.2

Since then the algorithm has been continuously improved for elastic contact problems, in particular by Liu et al. [46] and Gallego et al. [51] for frictionless and for frictional contact, respectively. One of the key elements is the use of zero padding and wrap-around order to avoid signal aliasing from the FFT treatment. This FFT algorithm remains numerically efficient as far as a linear relation exists between the contact pressure at any surface point A_i and the surface displacement at another point A_j.

Under homogeneous isotropic and elastic assumptions, similarity and equilibrium considerations dictated that the surface displacement has to vary inversely with the distance from any point force applied on the half-space free surface.

It should be specified that the tangential components of u^{B1+B2} are not considered here since the problem is assumed frictionless. The effect of plasticity on the contact problem consists of superposing an additional term to the gap h in eq. (2.2), due to distributed plastic strain (eigenstrain) within the plastic domain.

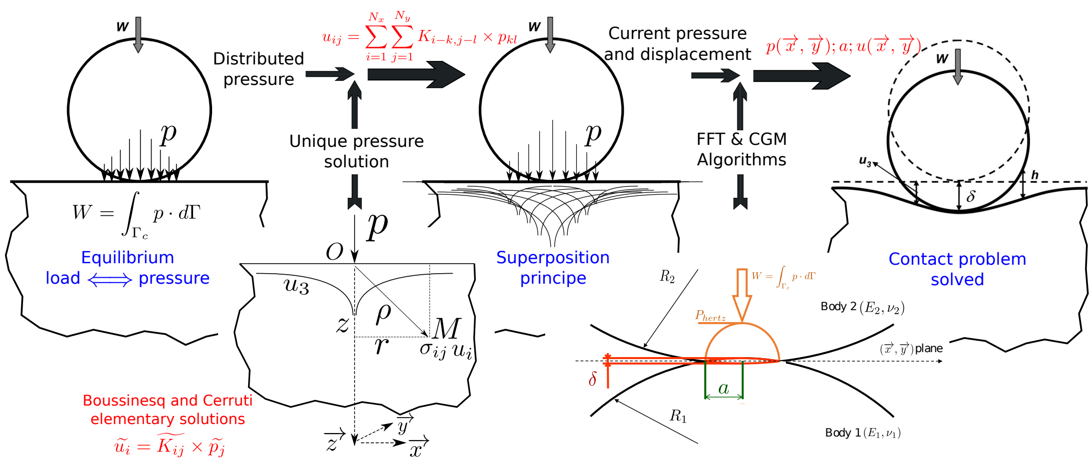

Figure 2.2: Resolution of the elastic contact problem

2.2.2 INTEGRATION SUBSURFACE PROBLEM IN THE CONTACT RESOLUTION

Knowing that the contact solution does not depend only on the contact load but also on the contacting body subsurface responses, two kinds of misfit displacements u^{res} and u^* are introduced into the contact solver as heterogeneous elastic-plastic contact parameters. Note that misfit displacement also depends on the contact loading and their determination is discussed in the next section. Thus, the heterogeneous elastic-plastic contact could be treated such as elastic contact problem by considering the updated geometry. This geometry is obtained by summing the elastic displacement to that induced by plasticity and the presence of inhomogeneities. Only h is changed into h^{mod} in the separation eq. (2.2) as:

$$h_{mod}(x, y) = h(x, y) + u^{res}(x, y) + u^*(x, y) \tag{2.4}$$

Where h is the gap between contacting surfaces. The surface displacement u^{res} is related to plasticity while u^* comes from the presence of inhomogeneities. Note that these two effects are dependent on each other and so must be solved together numerically.

2.2.3 COUPLING THE EFFECT OF PLASTICITY AND INHOMOGENEITIES

The HEPC problem can be split into a contact problem and a subsurface one. Since the bulk contains both heterogeneous inclusions and plastic strains, the subsurface problem can be treated as a heterogeneous elastic part and an elastic-plastic one coupled each other by making them interact as presented in Fig. 2.3. The heterogeneous elastic contact is first solved in order to get the stress state of the material before checking if plastic flow occurs. When the total stress around a heterogeneous inclusion reaches the yield condition, the plastic part is solved. Plasticity and inhomogeneity create additional surface displacements that are the added to the initial surface geometry, and the contact problem is then solved again with the updated geometry. The process is repeated until convergence.

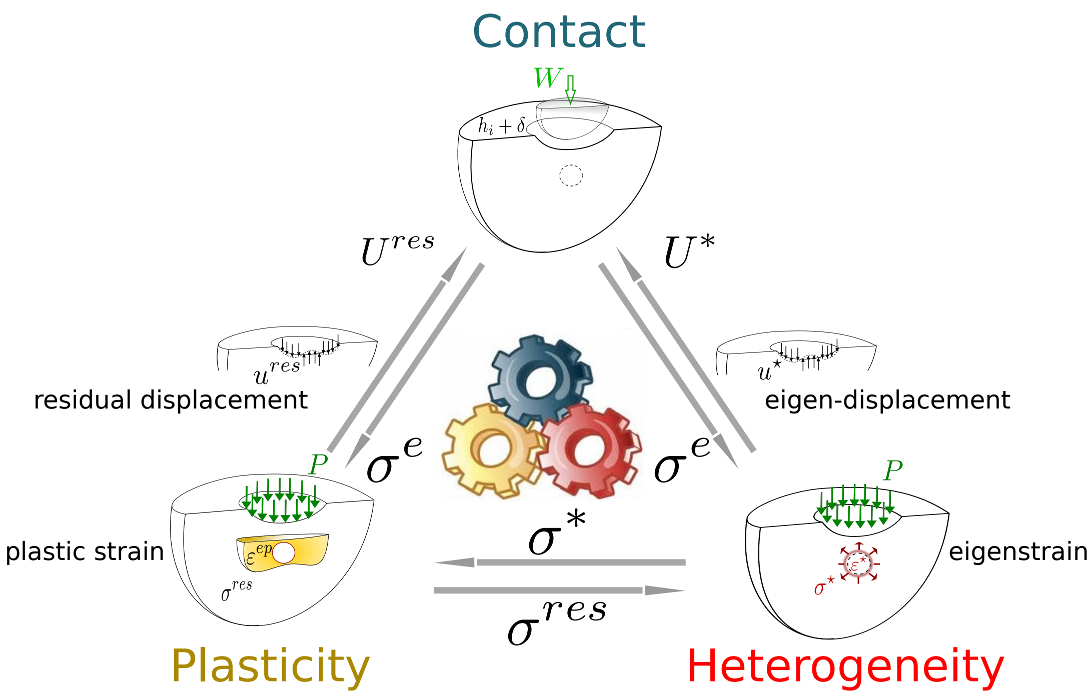

Figure 2.3: Subsurface contribution for solving the HEPC problem

The theoretical background part is fully detailed in the following section but could be in a nutshell commented here as:

Theoretical background of the heterogeneity contribution
Eshelby s equivalent inclusion method is used to take into account the presence of a single or multiple inhomogeneities within one of the bodies in contact from the determination of the eigenstrain to the calculation of the subsurface eigenstresses and surface misfit displacement.

Theoretical background of the plasticity contribution
The plasticity is taken into account by the determination of the plastic strain using Newton-Raphson algorithm. Then the residual stress and residual surface displacement are calculated using the influence coefficient from Maxwell and Betti's reciprocal theorem [52].

Numerical background to solve heterogeneity and plasticity contribution separately
To solve heterogeneity and plasticity respective problems, 3D-FFT and 2D-FFT are employed to accelerate the calculation. Wrap around order and zero-padding techniques are used in order to remove the induced periodicity error (See [53]). A decomposition technique is used to determine to solutions of heterogeneity and plasticity problems for semi-infinite bodies.

The HEPC problem consists into a weak coupling of three problems: the contact, plastic and heterogeneous problems. All three problems are solved sequentially by considering the two other problems constant. The iterations between all three problems are pursued until all are converged.

- The contact problem accounts for the plastic and heterogeneous contributions in the gap computation Eq.(2.2) through the residual u^{res} and heterogeneous displacements u^*

- The plastic problem takes as input the total stress $\underline{\sigma}^{tot}$ into the body that is the sum of the stresses due to the contact pressure (and potential shears) $\underline{\sigma}^{c}$, over-stress due to the heterogeneity $\underline{\sigma}^{*}$ and residual stresses due to the pre-existing plastic strains $\underline{\sigma}^{res}$ as:

$$\underline{\sigma}^{tot} = \underline{\sigma}^{c} + \underline{\sigma}^{*} + \underline{\sigma}^{res}$$

  Convergence is reached when the yield function is negative or equal to zero at every point.
- The heterogeneous problem similarly takes as input the total stress at each point of the body. Note that the heterogeneity is here purely elastic and presents no plastic behavior. Yet, plastic flow could be computed, potentially with a hardening law different than that of the matrix, for the heterogeneity also and the heterogeneous problem would then simply need to add the plastic strain to the eigenstrain of the heterogeneity for the stress computation.

2.3 CONTRIBUTION OF PLASTICITY

2.3.1 PLASTIC STRAIN

The elastic-plastic behavior is described by the occurrence of irreversible deformation inside the material (starting from the threshold value of the yield strength). For metallic materials and alloys, the plastic deformation appears as the slippage of atomic plans moving ones over the others. This phenomenon can be amplified by the presence of material defects or the accumulation of dislocations. The theory of plasticity is based on the fundamental concept of yield function defining the state of the material and the limit at which it becomes plastic:

$$\begin{aligned} f &= f_0(\underline{\sigma}^{tot} - \underline{\chi}(\bar{\varepsilon}^p)) - K(\bar{\varepsilon}^p) \\ f &< 0 \Leftrightarrow \text{Elastic deformation} \\ f &= 0 \Leftrightarrow \text{Plastic flow} \end{aligned} \tag{2.5}$$

Where $\underline{\sigma}^{tot}$ is the total stress field and $\bar{\varepsilon}^p$ the effective accumulated plastic strain defined by $\bar{\varepsilon}^p = \sqrt{\frac{2}{3}\varepsilon^p_{ij}\varepsilon^p_{ij}}$, $\underline{\chi}$ described the kinematic part of the hardening and K described the isotropic one. Tensors are distinguished from scalars by the underline symbol.

The plastic strain assessment makes use of:

THE VON MISES CRITERION f_0 – The Von Mises equivalent stress is considered here, $f_0 = f_{VM}$. It is often referred as J_2 plasticity.

$$f_{VM}(\underline{\sigma}^{tot} - \underline{\chi}) = \sqrt{3} \times J_2(\underline{\sigma}^{tot} - \underline{\chi}) = \left(\frac{3}{2}\left(\underline{\sigma}^{tot} - \underline{\chi}\right) : \left(\underline{\sigma}^{tot} - \underline{\chi}\right)\right)^{1/2} \tag{2.6}$$

THE HARDENING LAW describes the stress-strain relationship once plastic flow occurs. It is also called the flow rule. The kinematic hardening law $\underline{\chi}$ is used when the difference between the traction and compression yield strengths remains constant during the plastic flow. This is expressed by the translation of the yield function center. Equation 2.7 presents an example of a linear kinematic hardening law. Conversely, the isotropic hardening law K represents the growth of the yield function. Note that the combination of kinematic and isotropic hardening laws is possible. This is often used to better fit the real material behavior. A material elastic-perfectly plastic is a particular case when plastic flow occurs without hardening, then $\underline{\chi}$ and K are nil. The application of the current model to the behavior of bearing steels, for which the isotropic hardening dominates, justifies the choice of a Swift law [37]:

$$
\begin{aligned}
&\underline{\chi} = \underline{\chi}_1 + \underline{\chi}_2\,,\ d\underline{\chi}_1 = \tfrac{2}{3}C_1 d\underline{\varepsilon}^p\,,\ d\underline{\chi}_2 = \tfrac{2}{3}C_2 d\underline{\varepsilon}^p - \gamma_2\underline{\chi}_2 d\lambda && \text{Armstrong-Frederick law}\\
&K(\overline{\varepsilon}^p) = B(C + \overline{\varepsilon}^p)^n && \text{Swift law}
\end{aligned}
\tag{2.7}
$$

Where $d\lambda$ is the plastic multiplier and $\underline{\varepsilon}^p$ the plastic strain tensor. Note that Armstrong-Frederick law uses two hardening variables $\underline{\chi}_1$ and $\underline{\chi}_2$ that are both tensors representing the center of the yield surface in the stress domain. The use of two variables allows to represent a wide range of non-linear hardening behaviors, though empirically. The first variable $\underline{\chi}_1$ evolves linearly with the plastic strain while $\underline{\chi}_2$ allows to introduce a saturation term with the parameter γ_2. Note here that this law is purely phenomenological but was chosen as it allows to describe a material easily whose hardening curve under pure tension is equivalent to an isotropic hardening material described by a Swift law.

THE CONSISTENCY CONDITION must be satisfied as:

$$
df = 0 \ \Rightarrow\ \frac{\partial f}{\partial \sigma_{ij}^{tot}} d\sigma_{ij}^{tot} + \frac{\partial f}{\partial \overline{\varepsilon}^p} d\overline{\varepsilon}^p = 0 \tag{2.8}
$$

THE NORMALITY RULE ensures that the direction of the plastic strain increment is normal to the yield surface. This constitutes the main rule to determine the final plastic strain by summing up its increments.

$$
d\varepsilon_{ij}^p = \frac{\partial f}{\partial \sigma_{ij}} d\lambda = n_{ij} d\lambda \tag{2.9}
$$

where $\underline{\sigma} = \underline{\sigma}^{tot} - \underline{\chi}(\overline{\varepsilon}^p)$.

Finally, based on those previous equations, a three-dimensional implicit return mapping algorithm, as described by Simo and Taylor [54] and implemented by Chaise et al. [55], is used to compute the plastic strain induced by the total stress field.

2.3.2 RESIDUAL DISPLACEMENTS AND STRESSES

The Maxwell and Betti's reciprocal theorem is employed to compute the set of influence coefficients involved in the calculation. Let's consider two different states $(S) = (u, \varepsilon, \sigma, \varepsilon^0)$ and $(S') = (u', \varepsilon', \sigma')$ of an elastic body of volume Ω and boundary Γ.

(S) represent a state with existing initial strain ε^0 and $(S^{'})$ is an elastic state at some indeterminate time. Maxwell and Betti establish from $\sigma_{ij} \cdot \varepsilon^{'}_{ij}$ the following equation:

$$-\int_{\Gamma} u^{'}_i \cdot \sigma_{ij} \cdot n_j \cdot d\Gamma + \int_{\Omega} f_i \cdot u^{'}_i \cdot d\Omega = -\int_{\Gamma} u_i \cdot \sigma^{'}_{ij} \cdot n_j \cdot d\Gamma + \int_{\Omega} f^{'}_i \cdot u_i \cdot d\Omega - \int_{\Omega} \varepsilon^0_{ij} \cdot \sigma^{'}_{ij} \cdot d\Omega \tag{2.10}$$

Where volume forces $f^{'}_i$ and f_i are those used in the equilibrium equation $\sigma_{ij,j} + f_i = 0$ for each state. n_j is the unit normal inward-oriented vector. From Eq. (2.10), after having substituted the initial strain ε^0 by plastic strain ε^p, and taking into account the incompressibility of the plastic strain tensor, the following relation can be derived:

$$tr(\varepsilon^p) = 0 \;\Rightarrow\; \varepsilon^p_{ij} \cdot \sigma^{'}_{ij} = 2\mu\varepsilon^p_{ij} \cdot \varepsilon^{'}_{ij}$$

It yields:

$$-\int_{\Gamma} u^{'}_i \cdot \sigma_{ij} \cdot n_j \cdot d\Gamma + \int_{\Omega} f_i \cdot u^{'}_i \cdot d\Omega = -\int_{\Gamma} u_i \cdot \sigma^{'}_{ij} \cdot n_j \cdot d\Gamma + \int_{\Omega} f^{'}_i \cdot u_i \cdot d\Omega - 2\mu \int_{\Omega^{(p)}} \varepsilon^p_{ij} \cdot \varepsilon^{'}_{ij} \cdot d\Omega \tag{2.11}$$

Where μ is the material shear modulus and $\Omega^{(p)}$ is the plastic domain.
The contact pressure p and $p^{'}$ are introduced by $\sigma_{ij} \cdot n_j = -p_i$ and $\sigma^{'}_{ij} \cdot n_j = -p^{'}_i$ on Γ_c, and Eq. (2.11) becomes:

$$\int_{\Gamma_c} u^{'}_i \cdot p_i \cdot d\Gamma + \int_{\Omega} f_i \cdot u^{'}_i \cdot d\Omega = \int_{\Gamma} u_i \cdot p^{'}_i \cdot d\Gamma + \int_{\Omega} f^{'}_i \cdot u_i \cdot d\Omega - 2\mu \int_{\Omega^{(p)}} \varepsilon^p_{ij} \cdot \varepsilon^{'}_{ij} \cdot d\Omega \tag{2.12}$$

Equation (2.12) is sufficient to determine the influence coefficient necessary to compute the residual displacements and residual stresses due to the plastic strains. Note that each term of this equation contains the variable from both state (S) and $(S^{'})$ all at once. Now, with the intent to keep out the surface displacement field of (S), considering $(S)^{'}$ as a state corresponding to an applied unit normal force at point A on Γ_c, the pressure equals to $p^{'}(M) = \delta(M - A)$ at any point M. The volume forces are set to $f^{'}_i = 0$ and $f_i = 0$. Eq.(2.12) leads to:

$$\int_{\Gamma} u_i \cdot p^{'}_i \cdot d\Gamma = u_z(A) = \int_{\Gamma_c} u^{'}_i \cdot p_i \cdot d\Gamma + 2\mu \int_{\Omega^{(p)}} \varepsilon^p_{ij} \cdot \varepsilon^{'}_{ij} \cdot d\Omega \tag{2.13}$$

One can conclude that, when the contact pressure p_i vanishes, the residual displacement on the contact area becomes:

$$u^r_z(A) = 2\mu \int_{\Omega} \varepsilon^p_{ij} \cdot \varepsilon^{'}_{ij} \cdot d\Omega^{(p)} \tag{2.14}$$

If the plastic zone $\Omega^{(p)}$ is meshed with N_p cuboid $\Omega_n^{(p)}$ each containing constant plastic strain, Eq. (2.14) can be expressed as:

$$u_z^r(A) = 2\mu \sum_{n=1}^{N_p} \varepsilon_{ij}^p(n) \cdot \int_{\Omega_n^{(p)}} \varepsilon_{zij}^{'} \cdot d\Omega = \sum_{n=1}^{N_p} \varepsilon_{ij}^p(n) \cdot D_{ij}^r(n) \tag{2.15}$$

where D_{ij}^r is the influence coefficient relating the plastic strain to residual displacement, see Appendix A.4. The residual stress is obtained by a similar method. In this case, state $(S)^{'}$ corresponds to an applied unit normal force at point B in the volume Ω. The volume force $f_i^{'} = \delta(M - B)$ at any point M and the other one remains $f_i = 0$. The pressure is considered to be $p^{'}(M) = 0$. Eq.(2.12) gives:

$$u_k^r(B) = \int_{\Gamma_c} u_{ki}^{'} \cdot p_i \cdot d\Gamma + 2\mu \int_{\Omega^{(p)}} \varepsilon_{ij}^p \cdot \varepsilon_{kij}^{'} \cdot d\Omega \tag{2.16}$$

Then, when the contact pressure p_i vanishes, one can get the residual displacement in the volume Ω as follows:

$$u_k^r(B) = 2\mu \int_{\Omega^{(p)}} \varepsilon_{ij}^p \cdot \varepsilon_{kij}^{'} \cdot d\Omega \tag{2.17}$$

The residual stresses are related to the residual displacements by the Hooke's law in the form of:

$$\sigma_{ij}^r(B) = C_{ijkl} \left(\frac{1}{2} \left(u_{k,l}^r(B) + u_{l,k}^r(B) \right) \right) \tag{2.18}$$

2.4 CONTRIBUTION OF HETEROGENEOUS INCLUSIONS

As for plasticity, the presence of inhomogeneity modifies the contact problem by adding a supplementary term to the surface displacement, called here surface eigen-displacements, see Fig. 2.3. Note that the displacements due to plasticity are called residual displacements.

2.4.1 SWITCH BETWEEN A HETEREGENEOUS INCLUSION AND A HOMOGENEOUS ONE

Eshelby defined a heterogeneity as a subdomain $\Omega^{(i)}$ having the same elastic properties as the surrounding matrix (infinite-space) $\Omega^{(m)}$ but containing misfit strains called eigenstrains. One can imagine eigenstrain as the strain free from the stress generated by any external force or surface constraint. However, Mura [56] claimed that eigenstresses are produced by the incompatibility of eigenstrain as a self-equilibrated stress field. Indeed, for a heterogeneous body, the notion of eigenstrain comes out when an external load is applied. Then, the deformation between the heterogeneity and the surrounding matrix is incompatible and generates stresses. Thus, eigenstrain may be considered as elastic in poroelasticity [57] and thermoelasticity [58] problems, or inelastic when the studied body presents initial strains due to phenomena such as phase transformation or material precipitations. Given this background, a heterogeneity can be seen as a domain with elastic constants different from those of the matrix. Therefore a transformation, as schematically illustrated in Fig. 2.4, is needed. This process consists to consider a heterogeneity located within a loaded matrix which, in fine, is equivalent to the problem with a homogeneous inclusion plus an eigenstrain that creates an eigenstress within the matrix in reaction to the external load.

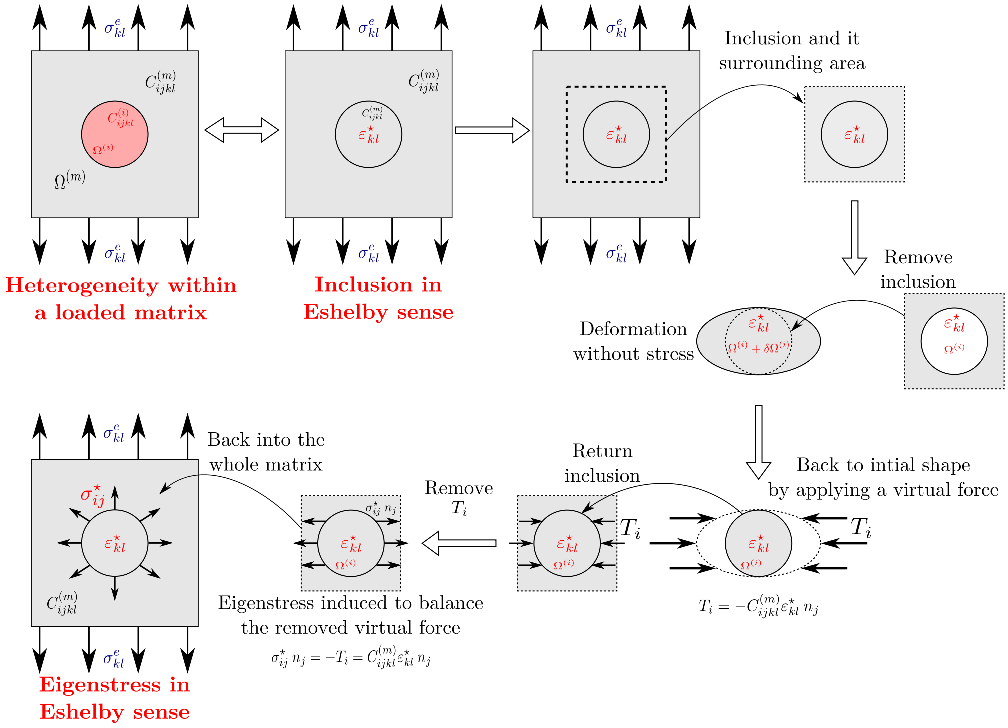

Figure 2.4: Single heterogeneity transformation into inclusion in the sense of Eshelby and subsequent eigenstress

2.4.2 HETEROGENEITY UNDER EXTERNAL APPLIED LOADING

In the framework of Eshelby [27] the main difficulty is to determine the tensor that links the eigenstrain ε^*_{ij} to the compatibility strain ε_{ij}, with S known as the stress tensor:

$$\varepsilon_{ij} = S_{ijkl} \times \varepsilon^*_{kl} \tag{2.19}$$

The general form of this tensor is not simple because it involves harmonic and biharmonic potentials which are elliptic integrals (see Appendix A.1). Eshelby proposed an analytical solution for some particular heterogeneity shapes: ellipsoids and spheres. Moschovidis and Mura [30] determined ε_{ij} and σ_{ij} inside and outside a single heterogeneity domain $\Omega^{(i)}$ and allowed to treat arbitrary shape as a cluster of multiple subdomains $\Omega^{(i)}_1, \cdots, \Omega^{(i)}_k, \cdots, \Omega^{(i)}_n$. The sum of the contributions of each k subdomain permits to get the compatibility strain ε_{ij} at any point $M(x, y, z)$ as:

$$\varepsilon_{ij}(x, y, z) = \sum_{k=1}^{n} \varepsilon^k_{ij}(x, y, z) \tag{2.20}$$

Note that this expression holds under the assumption of small strains, only.

Eshelby's Equivalent Inclusion Method (EIM)

In the case of linear isotropic elasticity, when a matrix[a] $\Omega^{(M)}$ of stiffness $C^{(M)}_{ijkl}$ is subjected to uniform strain[b] $\varepsilon^{(c)}_{kl}$, the over (elastic) stress $\sigma^{(c)}_{ij}$ is expressed by the Hooke's law as:

$$\sigma^{(c)}_{ij} = C^{(M)}_{ijkl} \cdot \varepsilon^{(c)}_{kl} \tag{2.21}$$

A single heterogeneity[c] $\Omega^{(I)}$ of stiffness $C^{(I)}_{ijkl}$ embedded into $\Omega^{(M)}$ generates mismatch strains ε_{ij} due to the difference of the elastic properties between the heterogeneity and the matrix. The overstress is expressed as:

$$\begin{aligned} \sigma^{(c)}_{ij} &= C^{(I)}_{ijkl}\left(\varepsilon^{(c)}_{kl} + \varepsilon_{kl}\right) \quad \text{in } \Omega^{(I)} \\ \sigma^{(c)}_{ij} &= C^{(M)}_{ijkl}\left(\varepsilon^{(c)}_{kl} + \varepsilon_{kl}\right) \quad \text{in } \Omega^{(M)} \end{aligned} \tag{2.22}$$

Applying Eshelby's transformation, the heterogeneous inclusion $\Omega^{(I)}$ is mathematically equivalent to an inclusion with the same elastic properties as the matrix $C^{(M)}_{ijkl}$ plus an additional strain (eigenstrain) ε^*_{ij}:

$$\sigma_{ij} = C^{(I)}_{ijkl}\left(\varepsilon^{(c)}_{kl} + \varepsilon_{ij}\right) = C^{(M)}_{ijkl}\left(\varepsilon^{(c)}_{kl} + \varepsilon_{kl} - \varepsilon^*_{kl}\right) \quad \text{in } \Omega^{(I)} \tag{2.23}$$

Including Eq. (2.19) into Eq.(2.23) leads to:

$$\left(\left(C^{(I)}_{ijkl} - C^{(M)}_{ijkl}\right) S_{klmn} + C^{(M)}_{ijmn}\right) \varepsilon^*_{mn} = -\left(C^{(I)}_{ijkl} - C^{(M)}_{ijkl}\right) \varepsilon^{(c)}_{kl} \tag{2.24}$$

Note that an additional eigenstrain ϵ^{*res}_{ij} caused by plasticity can be added in the same way. Therefore Eq. (2.24) becomes:

$$\left(\left(C^{(I)}_{ijkl} - C^{(M)}_{ijkl}\right) S_{klmn} + C^{(M)}_{ijmn}\right) \left(\varepsilon^*_{mn} + \epsilon^{*res}_{mn}\right) = -\left(C^{(I)}_{ijkl} - C^{(M)}_{ijkl}\right) \varepsilon^{(c)}_{kl} \tag{2.25}$$

From Eq. (2.24), the eigenstrain ϵ^* inside the heterogeneity is related to the contact applied strain $\varepsilon^{(c)}$ by a linear expression. Finally, one can deal with the heterogeneity part of the whole heterogeneous elastic plastic contact problem by determining the eigenstresses and the surface eigen-displacement generated by the eigenstrains.

Determination of eigenstress and surface eigen-displacement

A solution for eigenstresses induced by an eigenstrain included in an isotropic infinite space has been described. This solution is adapted for a half-space with a free surface. The superposition principle is applied to three sub-problems which, by summation, is equivalent to the general problem presented in Fig. 2.5.

- (1) is the solution of the inclusion included in a full space.
- (2) is the solution of the mirror image of the inclusion when the symmetrical plan is the boundary surface of the half space. Note that $\varepsilon^{*(mirror)}_{iz} = -\varepsilon^*_{iz}$.
- (3) is the solution of the normal traction induced at the surface of the half-space due to both inclusions.

[a] the upper-script $^{(M)}$ refers to the matrix

[b] the upper-script $^{(c)}$ refers to fields coming from the contact

[c] The upper-script $^{(I)}$ refers to the inclusion

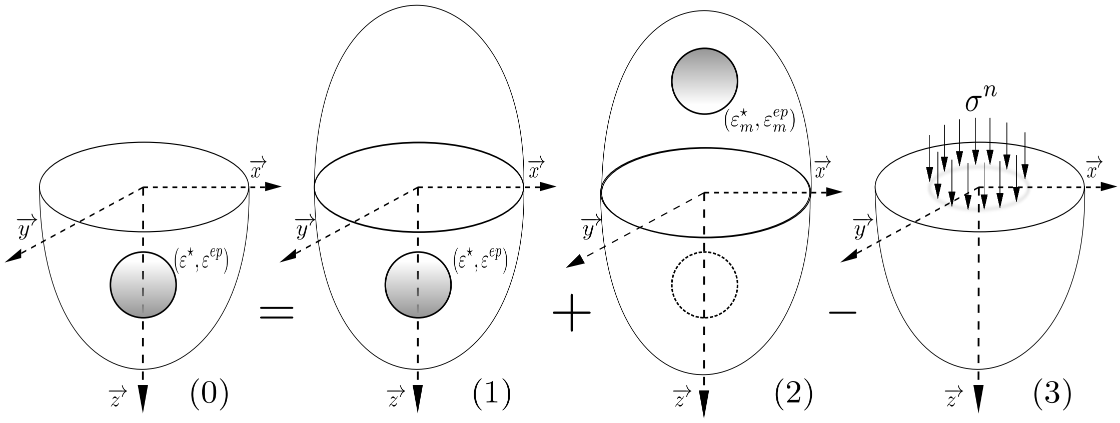

Figure 2.5: EIM decomposition method for a half-space

It should be noted that the same decomposition method is used the compute the residual stresses created by plastic strains located beneath a three-dimensional half space. One can get directly from this method the normal surface displacement induced by plasticity or the presence of inhomogeneity as the solution of the sub-problem (3). In the presence of multiple heterogeneities or a discretized heterogeneity, the eigenstress solution is obtained from the summation of the contribution of each eigenstrain. Note that in this case the stresses generated by the plastic strains or eigenstrains at any point influence the others, then an iterative resolution process must be implemented. The computational domain is meshed into $N_x \times N_y \times N_z$ cuboids and the eigenstress at point (x, y, z) is related to the eigenstrain at point (x', y', z') by:

$$
\begin{aligned}
\sigma_{ij}^{*}(x,y,z) \;=\; & \sum_{z=0}^{N_z-1}\sum_{y=0}^{N_y-1}\sum_{x=0}^{N_x-1} B_{ijkl}\left(x-x',y-y',z-z'\right)\varepsilon_{kl}^{*}\left(x',y',z'\right) \\
& + \sum_{z=0}^{N_z-1}\sum_{y=0}^{N_y-1}\sum_{x=0}^{N_x-1} B_{ijkl}\left(x-x',y-y',z+z'\right)\varepsilon_{kl}^{*(s)}\left(x',y',-z'\right) \\
& - \sum_{y=0}^{N_y-1}\sum_{x=0}^{N_x-1} M_{ij}\left(x-x',y-y',z\right)\sigma^{*n}\left(x',y',0\right)
\end{aligned}
\tag{2.26}
$$

where B_{ijkl} and M_{ij} represent the influence coefficients for a unit eigenstrain, see Appendix A.2. The normal traction $\sigma^{*n}(x, y, 0)$ at a surface point $(x, y, 0)$ is:

$$
\begin{aligned}
\sigma^{*n}(x,y,0) \;=\; & -\sum_{z=0}^{N_z-1}\sum_{y=0}^{N_y-1}\sum_{x=0}^{N_x-1} B_{33kl}\left(x-x',y-y',z-z'\right)\varepsilon_{kl}^{*}\left(x',y',z'\right) \\
& - \sum_{z=0}^{N_z-1}\sum_{y=0}^{N_y-1}\sum_{x=0}^{N_x-1} B_{33kl}\left(x-x',y-y',z+z'\right)\varepsilon_{kl}^{*(s)}\left(x',y',-z'\right)
\end{aligned}
\tag{2.27}
$$

Finally, the eigen-displacement at point (x, y) of the surface is obtained by:

$$u_3^*(x,y) = \sum_{y=0}^{N_y-1}\sum_{x=0}^{N_x-1} K^n\left(x-x^{'}, y-y^{'}\right)\sigma^{*n}\left(x^{'}, y^{'}\right) \tag{2.28}$$

where K^n represent the influence coefficients relating the pressure to the surface displacement, see Appendix A.3.

Part II

NUMERICAL MODELING

The semi analytical method offers the possibility to create contact and rolling contact models in three dimensions, while maintaining an excellent computational performance. Mostly, as long as non conforming contact and small strain hypotheses are fulfilled, the models could be applied to solve indentation and rolling contact problems. The contact solutions (pressure and area) are compared against those obtained by Finite Element Method (FEM), for validation. Some interesting results about the plasticity around the heterogeneity are discussed. The local distribution of the stress field is analyzed in the case of rolling contact. It was found out that, the heterogeneity raised the local plastic strain at its vicinity. Due to the presence of plastic strain and residual stress, the heterogeneity remains constantly under stress even if the external load is removed. The total residual stress is then a combination of the residual stress due to plasticity and the residual eigen-stress from the heterogeneity.

3 HETEROGENEOUS ELASTIC PLASTIC CONTACT PROBLEM

The recent developments of the semi-analytical methods have led to numerous improvements in their capabilities. They allow now to perform fast and robust simulations of contact between semi infinite bodies with either plastic or visco-elastic behavior [55, 59], with anisotropic elasticity [60, 61, 62] or when containing heterogeneities [63]. The latter can be considered as inclusions without restriction about their nature or property. Thus, the model found its direct applications in, respectively, hetero-elasticity, poroelasticity [64], thermoelasticity [65], visco-elasticity [66] and elastic-plasticity when the inclusions get the nature of, respectively, material precipitations (carbides), voids (or defects), phase transformations of thermal origin and plastic strain (initial or not). The influence of the size, depth, shape – cubic or spherical– and inclusion alignment on the residual stresses and elastic-plastic strains after a purely normal loading and unloading is presented and discussed in detail.

Contents

3.1 INTRODUCTION

The application of the Eshelby's EIM to three-dimensional contact problems involves two difficulties. The first one is the presence of a free surface (half-space) instead of an infinite space. The second one is the strain gradient in the vicinity of the contact, which means a non-uniform eigenstrain within the heterogeneity instead of a uniform one when the applied strain field (at infinite) is uniform. In the literature most documented studies focus on heterogeneities having simple and regular geometries (ellipsoid [27], cuboidal [67], cylindrical [68]) in an infinite elastic and isotropic matrix. Very few studies consider heterogeneities having arbitrary two-dimensional shapes [69] and even less for three-dimensional shapes within a semi-infinite body. Mura and co-authors [70, 71] and Chiu [72] provided integral solutions for ellipsoidal or cuboidal heterogeneity in a semi-infinite isotropic elastic body. The first analytical solution for cuboidal heterogeneities containing hydrostatic eigenstrains ($\varepsilon_{kk} = 0$) in a 3D contact problem was derived by Jacq et al. in 2002 [37] and applied to elastic-plastic materials. Note that for a large heterogeneity or for a complex shape it is always possible to discretize it into small cuboids. Although the discretization of an arbitrary three-dimensional shape with cubes requires a finer mesh than with tetrahedral elements [71, 73], the use of the latter shape is not numerically efficient since the analytical solutions are not known yet for such geometries.

3.2 ALGORITHM OF HETEROGENEOUS ELASTIC-PLASTIC CONTACT PROBLEM

The HEPC-problem algorithm is presented in Fig. 3.1. At first, the initial state is defined by the geometries of the two bodies in contact and their material properties. Note that only one body is considered heterogeneous elastic-plastic in this study. This body can include initial strains and stresses and have an initial hardening state. Then the loading path is defined by a prescribed contact force or rigid body displacement. From that input, the elastic contact is computed using a conjugate gradient method (CGM) and the contact pressure distribution and elastic stresses are derived. The latter is added to residual stresses forming the total stress used as input to perform eigenstrain, eigenstress and eigen-displacement calculation based on the Equivalent Inclusion Method (EIM). This loop, called heterogeneous elastic contact, is repeated until convergence is reached on the eigen-displacement. A new total stress is calculated taking into account the additional stress generated by heterogeneities. Then, the plastic strain increment is solved using the return-mapping algorithm. From plastic strain computed at each point of the body, a new residual stress state and an update of surface residual displacements are obtained using the superposition method described in Fig. 2.5 involving the 3D-FFT method as in [74]. The convergence of the problem is checked with the residual displacement. Note that in Fig. 3.1 δu_f is the final output displacement getting from the calculation core. It is used to validate the convergence of the contact problem as: $\frac{|\delta u_f - \delta u_i|}{|\delta u_i|} < \xi$. Where δu_i is the initial or previous displacement and ξ the convergence test tolerance.

η_1 and η_2 must be chosen in $]0;1[$ as relaxation coefficients for the current displacement used to update the surface geometry. If convergence of surface eigen-displacement and plastic strains are reached, the load is incremented. Otherwise, the geometry is updated for a new iteration of the heterogeneous elastic-plastic loop until convergence is reached. A computational code has been developed based on the described algorithm and is validated in the following section.

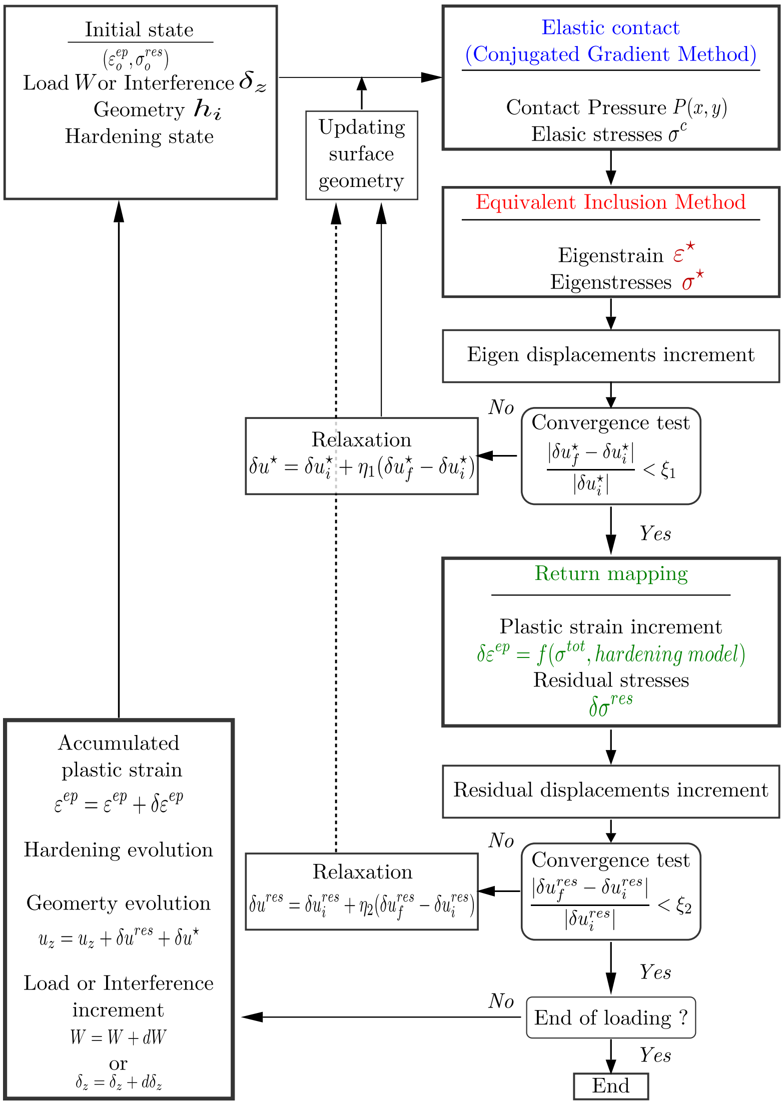

Figure 3.1: Algorithm of Heterogeneous Elastic-Plastic Contact Problem

3.3 MODEL VALIDATION

For validation purpose, a comparison with the solution from a Finite Element Method (FEM) is first performed. The maximum contact pressure and the yield strength are chosen so that a relatively high level of plasticity is reached. The maximum contact pressure is set to $4GPa$ for the elastic homogeneous solution. Figure 3.2 presents schematically the dry contact between a spherical indenter ($d^{ball} = 2.78mm$) and a HEP body. A single spherical heterogeneity of radius $0.2 \times a$ is located at depth $0.3 \times a$ below the surface, where a is the Hertzian contact radius. The elastic modulus ratio between the matrix and the heterogeneity is defined as γ and set to the value of 3 or $\frac{1}{4}$. When $\gamma > 1$, the heterogeneity is stiffer than the matrix and when $0 < \gamma < 1$, the heterogeneity is softer than the matrix. The Poisson's ratio ν is set to 0.3 for the heterogeneity. A Swift hardening law is chosen for the matrix of the HEP body (Eq. 2.7 where

$B = 640MPa, C = 4$, and $n = 0.0095$) which gives an elastic limit $\sigma^y = 730MPa$. Table. 3.1 recaps the values of parameters used for the validation.

Table 3.1: Values of parameters used for the validation

Parameter	Value
Indenter radius	$R = 2.78$
Indenter elastic properties	$E = 310GPa$; $\nu = 0.3$
Matrix elastic properties	$E = 205GPa$; $\nu = 0.3$
Matrix plastic properties	Swift law $\sigma^y = B(C+\varepsilon)^n$: $B = 640MPa, C = 4, n = 0.0095 \Rightarrow \sigma^y = 730MPa$
Heterogeneity elastic properties	$\gamma = (3 \text{ or } \frac{1}{4})$; $\nu = 0.3$
Heterogeneity size (radius)	$\beta = 0.2$
Heterogeneity location (depth)	$\alpha = 0.3$

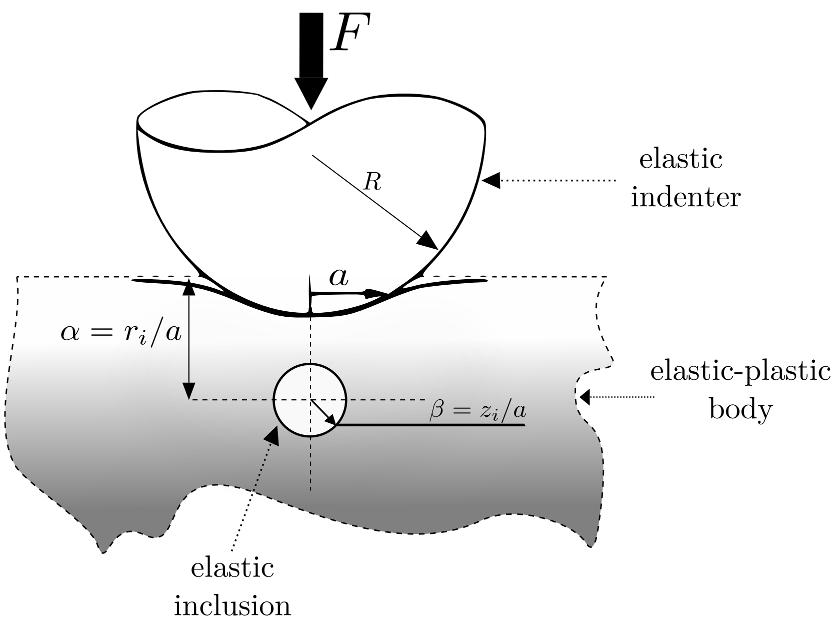

Figure 3.2: Heterogeneous Elastic-Plastic Contact Problem

In order to ensure consistency with the Hertz contact theory, a homogeneous elastic contact is performed with both methods (FEM and SAM). For the finite element model, the aim is to validate the geometry, mesh grid, type of elements and the axisymmetric boundary conditions. Note that a finer mesh is needed for the HEPC problem in order to better represent the eigenstrain inside the heterogeneity and the eigenstresses outside. Details of the mesh are presented in Fig. 3.3 and in Table. 3.1. Note that the size of the linear axisymmetric triangular elements inside and in the vicinity of the heterogeneity is $0.025 \times a$ for the FE model. Simulations using the semi analytical method (SAM), have been performed with 57×57 elements in the x and y directions and 93 elements in the z direction. This corresponds to an element size of $0.05a$ compared to $0.025a$ for the FEM model. The semi analytical model mesh is limited to the potential plastic zone defined as $1.5a \times 1.5a \times 2a$. The mesh needs to be extended over a wider domain for the FEM model to fulfill the infinite body assumption. Therefore each element has size $20\mu m \times 20\mu m \times 10\mu m$. Note that a finer element size is used in the z direction, being the direction of the higher stress gradient. The semi analytical model computations last in average six hours on a laptop when the FEM takes about five to eight days on a workstation.

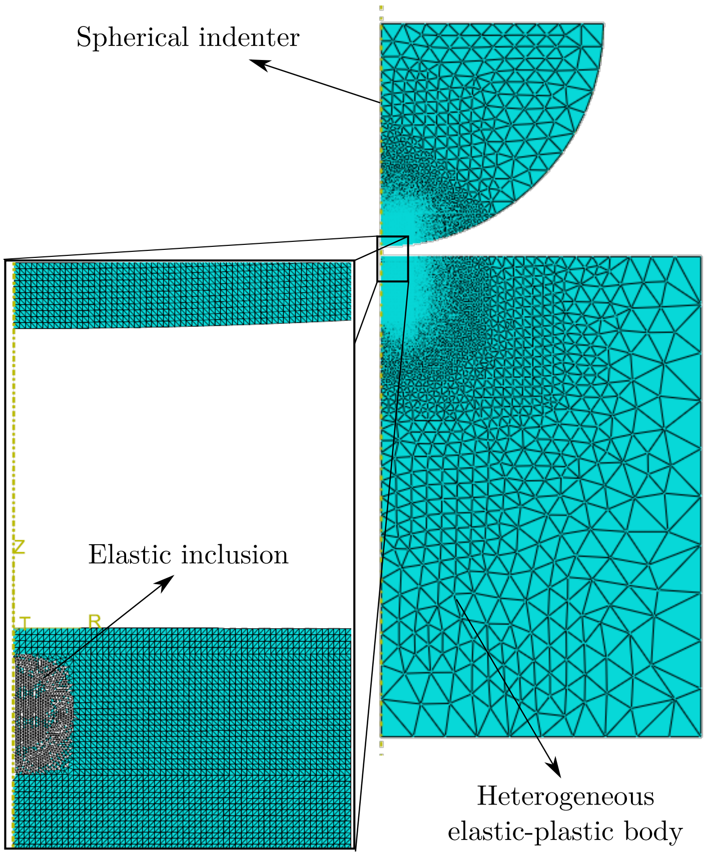

Figure 3.3: Finite element model used for the validation

Table 3.2: Details on the type and number of elements of the FE model

Part	Geometry [mm]	Element type	Number
Indenter	$R = 2.78$	3-node linear axisymmetric triangle (CAX3)	207,763
Matrix	$L_x = 4$; $L_z = 6$	3-node linear axisymmetric triangle (CAX3)	136,522
Heterogeneity	$r = 0.2 \times a$	3-node linear axisymmetric triangle (CAX3)	1,686

As expected the contact pressure distribution with Semi Analytical Method (SAM) matches perfectly the one with the FEM, see Fig. 3.4(a) for homogeneous elastic and homogeneous elastic-plastic assumptions. The contact pressure, in the HEPC case, is plotted in Fig. 3.4(b) validating the semi analytical results by the FE model. Both pressure profiles appear very close even if a minor difference (less than 2%) is observed near the center of the contact for the softer heterogeneity. This relative difference can likely be attributed to the way the spherical heterogeneity is meshed with cuboids in the SAM. For stiffer heterogeneity the agreement is very good.

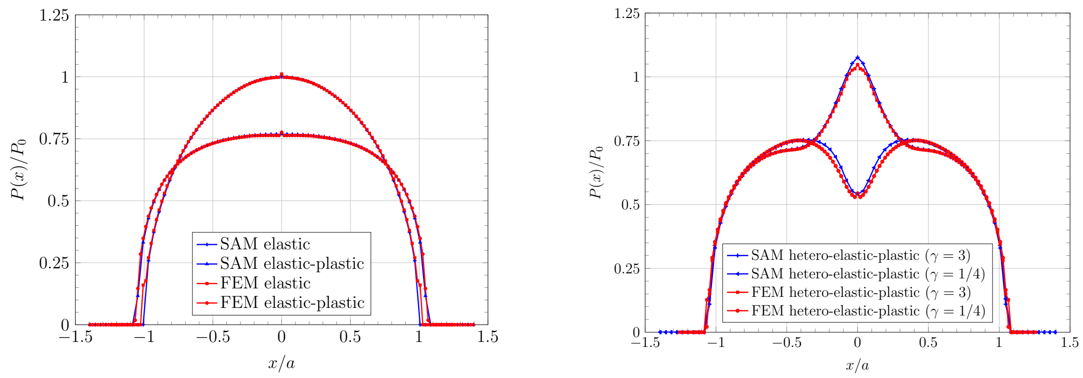

(a) (b)

Figure 3.4: Comparison of the contact pressure profiles by SAM and FEM: (a) homogeneous half-space; (b) half-space containing one single spherical heterogeneous inclusion

3.4 NUMERICAL RESULTS

This section aims to investigate the effects of the elastic properties (stiffer or softer), shape (sphere or cube) and location (depth) of the heterogeneity on the elastic-plastic response of the matrix (plastic strain and residual stress). The presence of a cluster of inhomogeneity is also treated. Lastly, the influence of the matrix hardening properties is also studied, by diminishing its yield strength, as to simulate overload. For fatigue resistance of bearing steels, these parameters are very important when the bearing life has to be improved. For instance, the gradient of carbide volume fractions in case-hardened steels (M50NiL) due to the thermo-chemical surface treatment induces a beneficial effect on the material resistance as long as it introduces residual compressive stresses up to the Hertzian depth. Such type of analysis would be useful to optimize the surface treatment parameters for a given application (mostly the contact size and the contact pressure). This constitutes the engineering interest of this study. The plastic strain will be kept moderate here in order to be close to what is encountered in most industrial applications, with a maximum equivalent plastic strain lower than 2%.

3.4.1 INFLUENCE OF PLASTIC BEHAVIOR AND HETEROGENEITIES ON THE CONTACT PRESSURE DISTRIBUTION

It is well known since Hertz that the maximum pressure within an elastic contact increases linearly with the equivalent Young's modulus E_{eq} at the power $2/3$, whereas the contact radius decreases with E_{eq} at the power $-1/3$. In this study a spherical indenter is considered as a homogeneous elastic material with $E = 310GPa$ and $\nu = 0.3$ corresponding to silicon nitride (Si_3N_4) ceramic material. The elastic-plastic properties of the matrix are those already mentioned in Table 3.1 excepted the Young's modulus which is now and in what follows $E = 210GPa$. Data regarding the heterogeneity is given in Table 3.3.

Table 3.3: Heterogeneity data

Heterogeneity data	Value
Shape	cube
Elastic properties	$\gamma = (2 \text{ or } \frac{1}{3})\ ;\ \nu = 0.3$
Size (semi-length)	$\beta = 0.2$
Location (depth)	$\alpha = 0.3$

It can be seen in Fig. 3.5 that, for homogeneous half-space, the accumulation of plasticity beneath the surface tends to flatten the contact pressure distribution while increasing the contact area. The presence of a heterogeneity stiffer than the matrix increases locally the contact pressure (see Fig. 3.5(a)) whereas a softer one decreases it, see Fig. 3.5(b). One can also observe that the pressure peak is considerably reduced by the plastic flow for the heterogeneous elastic-plastic case compared to the heterogeneous elastic one when the heterogeneity is harder than the matrix. Similarly, the pressure reduction is less in the heterogeneous elastic-plastic case when the heterogeneity is softer than the matrix. In Fig. 3.5, the actual contact radius a^{*p} for Hetero-Elastic-Plastic case is $1.17a$. Where a is the contact radius for a homogeneous elastic contact (Hertzian solution). The Hetero-Elastic radius a^* is close to the elastic one a. Similarly the Hetero-Elastic-Plastic one a^{*p} is very close to the Elastic-Plastic contact radius a^p. Also note the contact pressure discontinuity due to the shape of the heterogeneity which is here a cube. It is also found by plotting together the contact pressure when the heterogeneity is either a cube or a sphere (Fig. 3.6), that the maximum pressure is almost the same. Actually, the two cases presented in Fig. 3.5 and Fig. 3.6 are quite different. In Fig. 3.5, the applied load is significantly higher than the load leading to plastic flow ($\sigma_0/\sigma_0^y = 4.7$ where $\sigma_0 = 0.62P_0$) therefore the homogeneous elastic-plastic case highly differs from the elastic one. For the heterogeneous elastic case, strong peaks of pressure are observed since there is no plastic flow to regularize those stresses. Meanwhile, in Fig. 3.6, the applied pressure is lower than the limit load ($\sigma_0/\sigma_0^y = 0.9$) such that without heterogeneity no plastic flow occurs. Only the overstress due to the presence of a heterogeneity leads to a plastic flow. Note that in this figure, no elastic heterogeneous case is presented. Furthermore, the depths of heterogeneities are different for both cases and therefore those can't be directly compared. The very strong influence of plasticity and heterogeneity on the pressure emphasizes the need for the development of such techniques.

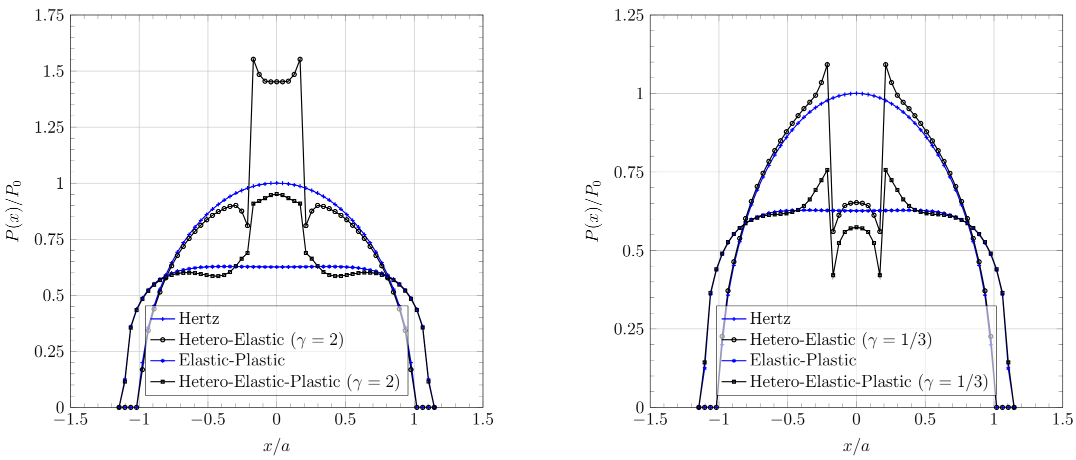

(a) (b)

Figure 3.5: Contact pressure profiles between a spherical indenter and HEP body: (a) Heterogeneity stiffer than the matrix; (b) Heterogeneity softer than the matrix

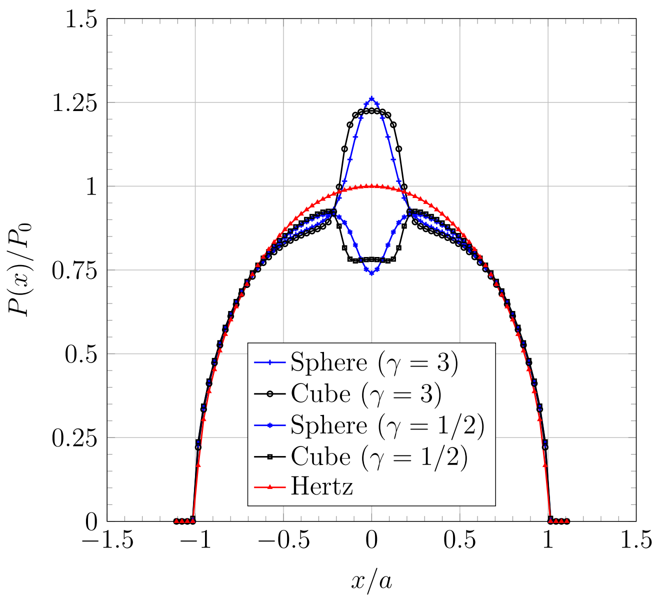

Figure 3.6: Comparison of the contact pressure profiles for cuboidal and spherical heterogeneities

3.4.2 ACCUMULATION OF PLASTIC STRAIN LOCALLY AROUND THE HETEROGENEITY

The accumulation of plasticity around the heterogeneity is investigated here. Figure 3.7 shows the plastic strain distribution around a stiff heterogeneity ($\gamma = 3$) located at different depths as given in Table 3.4. The presence of the heterogeneity disturbs the plastic strain distribution, creating a local plastic strain concentration by a factor 2.5 compared to the homogeneous situation (Fig. 3.7(a)).

Table 3.4: Location (depth) of the heterogeneity beneath the surface

Heterogeneity in Fig. 3.7	Depth: $z_i = \alpha \times a$
(b)	$\alpha = 0.25$
(c)	$\alpha = 0.40$
(d)	$\alpha = 0.48$

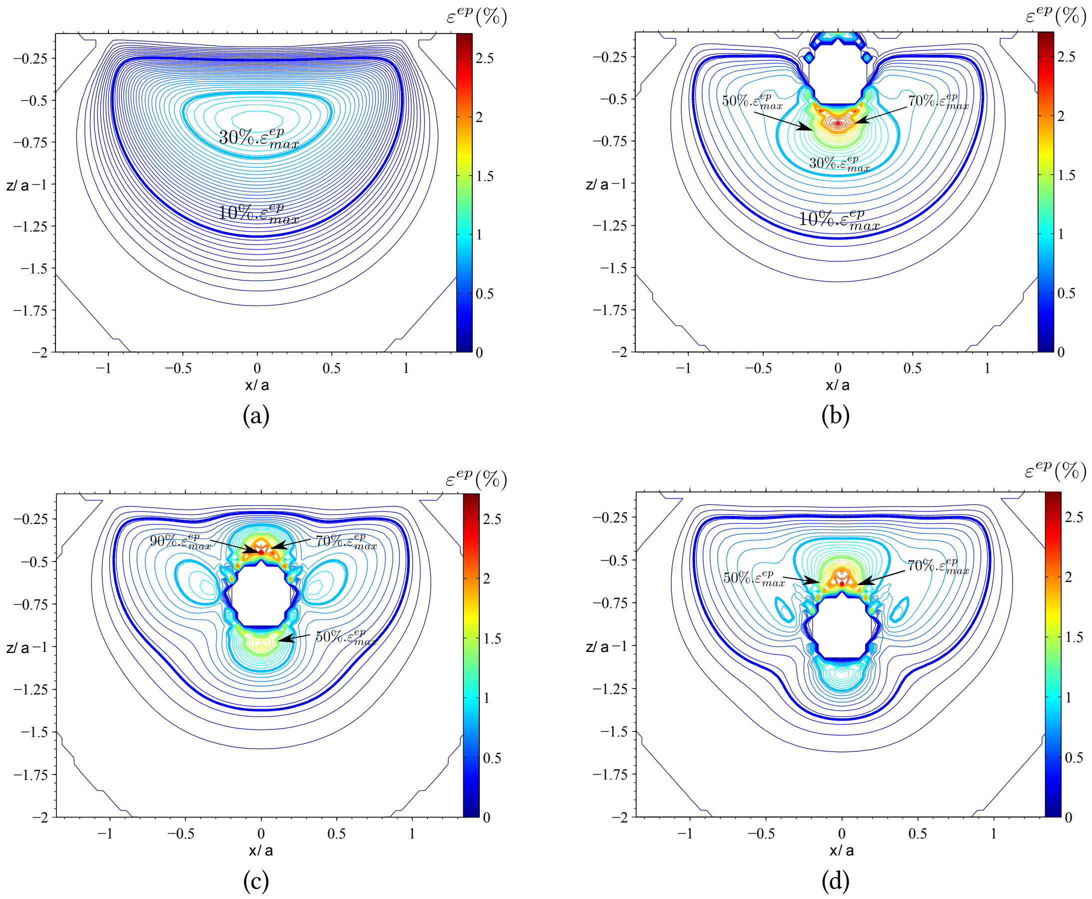

Figure 3.7: Plastic strain distribution around a single stiff ($\gamma = 3$) and spherical heterogeneity: (a) Elastic-plastic matrix without heterogeneity; heterogeneity centered at (b) $z_i = 0.35 \times a$; (c) $z_i = 0.7 \times a$; (d) $z_i = 0.9 \times a$. The heterogeneities have the same size of $0.2a$

Figure 3.8 and Table 3.5 show that the plastic strain distribution around an heterogeneity is also dependent on its nature. When the heterogeneity is stiffer than the matrix the plasticity grows up from the south pole. This explains the plastic strain concentration below the heterogeneity in this case (Fig. 3.8(b)). In contrast, the concentration is located on the equator of the heterogeneity when it is softer than the matrix (see Fig. 3.8(a) for a cavity).

Table 3.5: Data used for soft and stiff heterogeneities in Fig. 3.8

heterogeneity in Fig. 3.8	Parameter
(a)	Spherical shape; Size $\beta = 0.2$; Depth $\alpha = 0.3$; Elastic modulus ratio $\gamma = 0$
(b)	Spherical shape; Size $\beta = 0.2$; Depth $\alpha = 0.3$; Elastic modulus ratio $\gamma = 3$

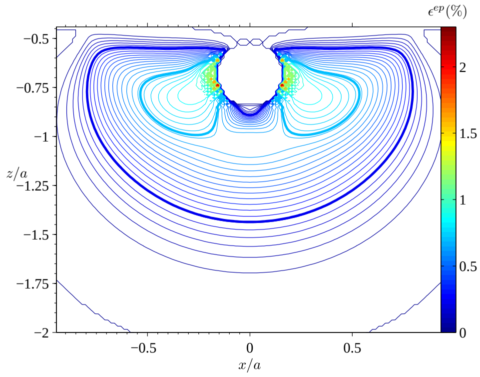

(a)

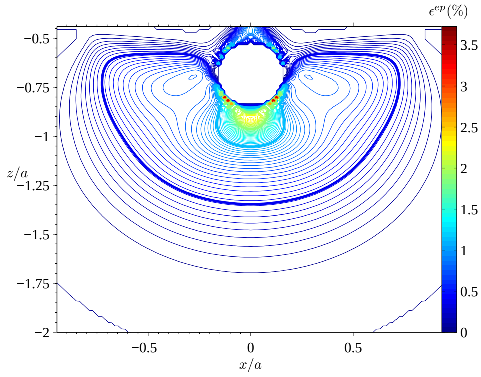

(b)

Figure 3.8: Plastic strain according to heterogeneity nature: (a) Heterogeneity softer than the matrix; (b) Heterogeneity harder than the matrix

It might be needed to quantify the plastic strain around a heterogeneity located out of the Hertzian zone. This situation is similar to that of a heterogeneity located out of the Hertzian zone along the rolling direction in the case of rolling contact. As plotted in Fig. 3.9, the plastic strain level is related to the heterogeneity size. These figures compare the plastic strain for a centered heterogeneity to a decentered one when the distance d between their centers is kept constant ($d = a$). The outer heterogeneity radius ranges from $\beta = 0.05 \times a$ to $\beta = 0.4 \times a$. Table 3.6 recaps the heterogeneity data used for this computation.

Table 3.6: Data used for heterogeneity located out of the Hertzian zone in Fig. 3.9

heterogeneity in Fig. 3.9	Parameter
(b)	Size $\beta = 0.05$; Depth $\alpha = 0.48$; Elastic modulus ratio $\gamma = 3$
(c)	Size $\beta = 0.2$; Depth $\alpha = 0.48$; Elastic modulus ratio $\gamma = 3$
(d)	Size $\beta = 0.3$; Depth $\alpha = 0.48$; Elastic modulus ratio $\gamma = 3$
(e)	Size $\beta = 0.4$; Depth $\alpha = 0.48$; Elastic modulus ratio $\gamma = 3$
Centered heterogeneity	Size $\beta = 0.05$; Depth $\alpha = 0.48$; Elastic modulus ratio $\gamma = 3$

It is found that there is no plasticity accumulation around the outer heterogeneity when $\beta = 0.05 \times a$ (see Fig. 3.9(a)), and an increase of up to 30% of the maximum plastic strain for the largest size. However the highest value always corresponds to the one found around the smallest centered heterogeneity. Note also that the plastic volume increases when the outer heterogeneity get larger.

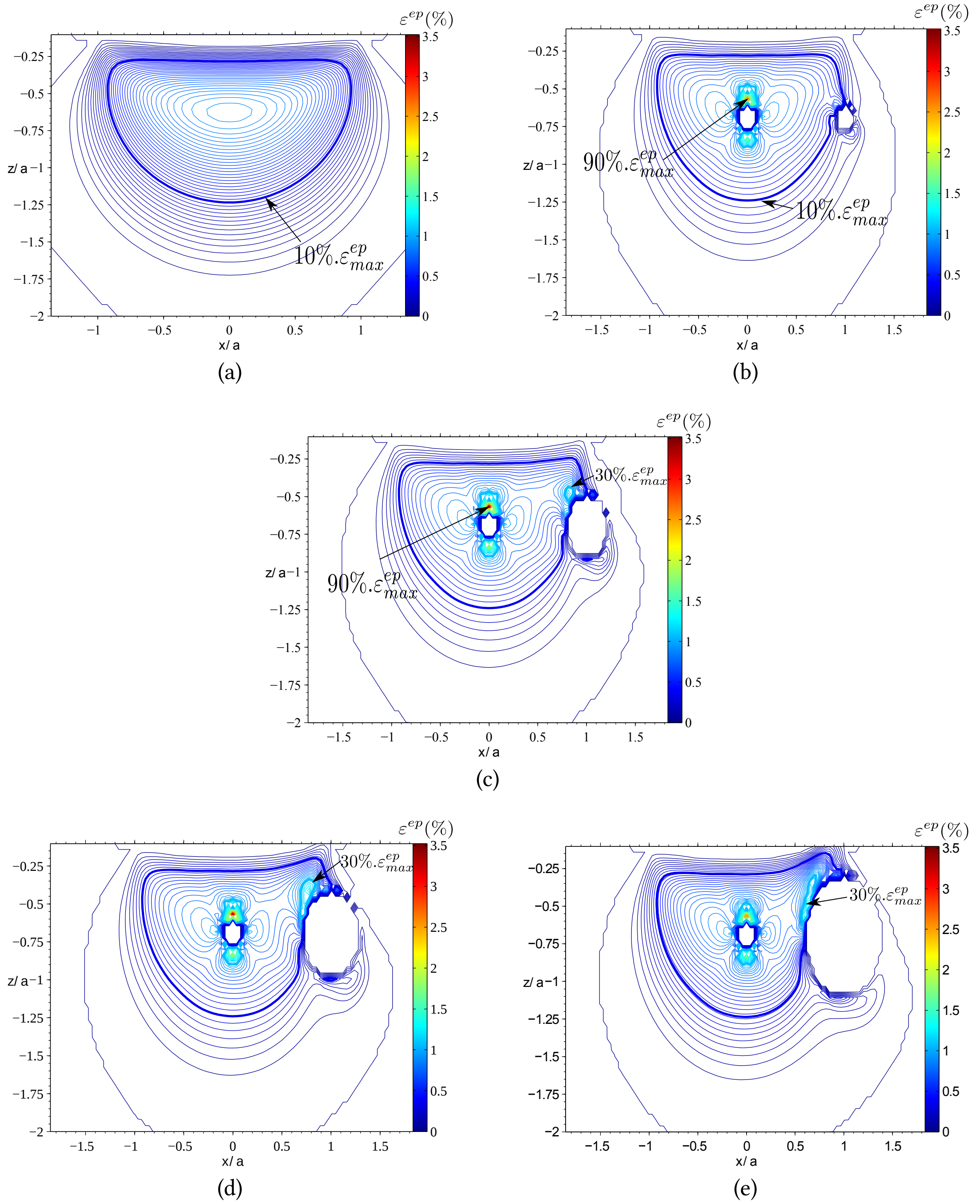

Figure 3.9: Local plastic strain concentration produced around two spherical heterogeneous inclusions, the first one of small size located in the center of the contact and at the Hertzian depth, the second one being an outer heterogeneity of varying size and located at the Hertzian depth at the border of the contact ($r = a$): Elastic-plastic matrix without heterogeneity (a); with an outer heterogeneity of radius $r_i = 0.05 \times a$ (b); $r_i = 0.2 \times a$ (c) ; $r_i = 0.3 \times a$ (d); and $r_i = 0.4 \times a$ (e)

The effect of a cluster of heterogeneities is now investigated. It was found [75] that most commonly hardened materials contain large heterogeneities which are often oriented in bands forming stringers. This orientation is generated by the rolling/forging operations performed between the casting and the heat treatment. Therefore, it is quite interesting to look at the effect of the cluster orientation. A set of simulations has been performed for a half-space containing a stringer of three stiff heterogeneities

$(\gamma = 3\ ,\ \beta = 0.1)$ located in the plane $(y = 0)$. The orientation of the stringer is represented by the angle θ ranging from 0 to $\dfrac{\pi}{2}$. The distance between the heterogeneity centers is $d_i = 0.4 \times a$. Figure 3.10 shows that the maximum plastic strain accumulation is obtained for a vertical stringer i.e. for $\theta = \dfrac{\pi}{2}$. One can also observe that 50% of this value is reached for a horizontal stringer compared to only 10% without heterogeneity (Fig. 3.10(a)). What can also be shown is that, for inclusions softer than the matrix, the most critical orientation is the horizontal one or the direction parallel to the contact surface.

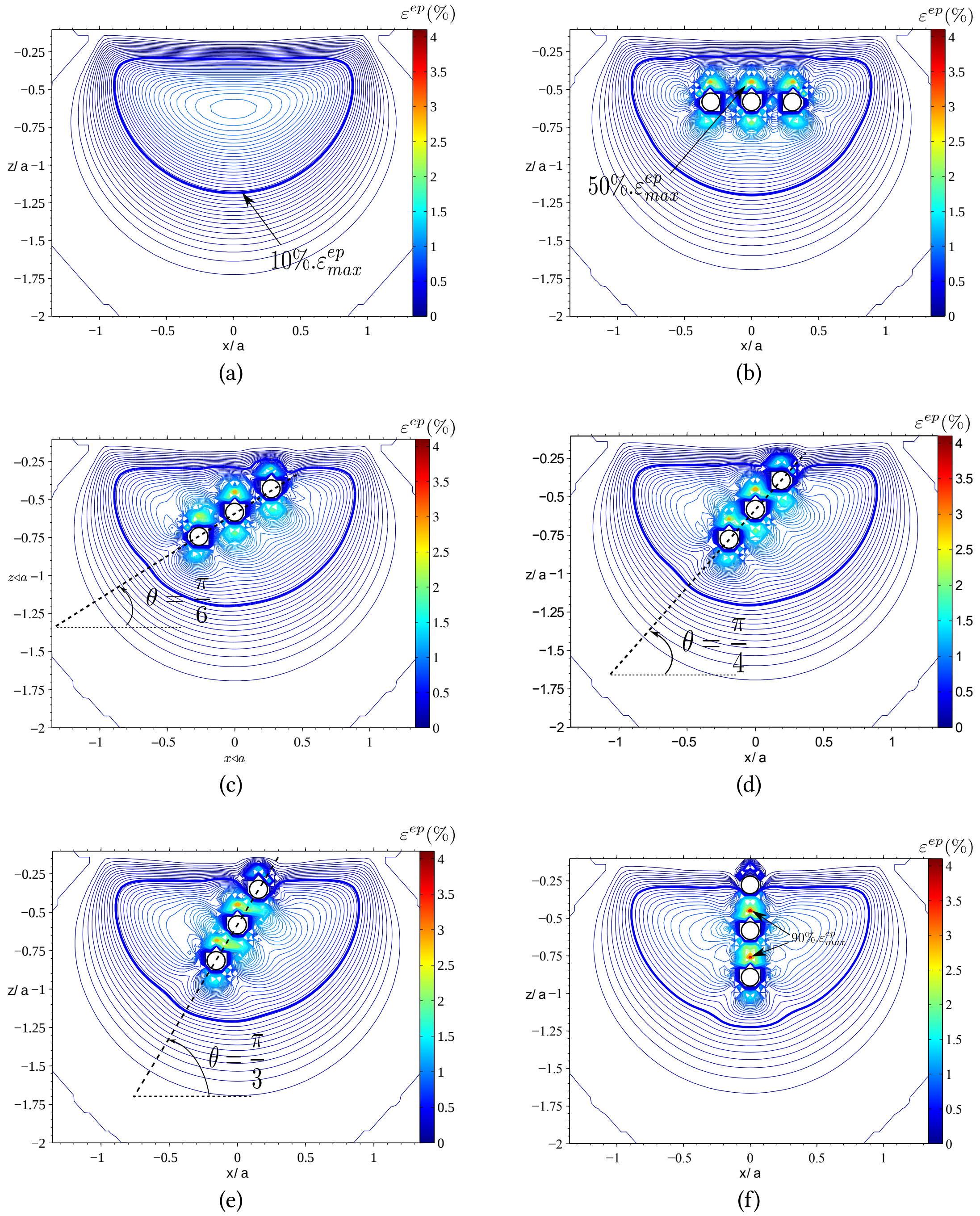

Figure 3.10: Plastic strain according to the heterogeneity stringer orientation:(a) Elastic-plastic matrix without heterogeneity; (b) Horizontal orientation; (c) Tilted stringer of orientation $\theta = \dfrac{\pi}{6}$; (d) Tilted stringer of orientation $\theta = \dfrac{\pi}{4}$; (e) Tilted stringer of orientation $\theta = \dfrac{\pi}{3}$; (f) Vertical orientation

3.4.3 RESIDUAL STRESS CONCENTRATION IN THE VICINITY OF AN ISOLATED HETEROGENEITY

The total residual stresses in a heterogeneous elastic-plastic body are a combination of residual stresses due to plasticity and eigenstresses due to the presence of heterogeneities. The material and geometrical data used for the heterogeneity are listed in Table 3.7. Fig. 3.11(a) shows the contact pressure distribution and related subsurface

plastic strains for both homogeneous and heterogeneous elastic-plastic bodies. Note that the maximum plastic strain for the homogeneous body is 2% (Fig. 3.11(b)) about, whereas it reaches nearly 4% (Fig. 3.11(c)) with the heterogeneous inclusion.
The contribution of residual stresses (due to plasticity) and eigen-stresses (due to the heterogeneity) to the total stress is plotted in Fig. 3.12. The contribution of the contact pressure only is plotted in Fig. 3.12(a), the eigenstress due to the presence of the heterogeneity in Fig. 3.12(b), the residual stress due to plasticity in Fig. 3.12(c), and the total stress in Fig. 3.12(d). It should be outlined that the maximum residual stress can reach up to 0.4 times the maximum Hertzian pressure P_0 (Fig. 3.12(c)) whereas it is limited to about $0.2 \times P_0$ in the absence of heterogeneity (Fig. 3.12(a)). As a consequence the total residual stress, summation of both contributions and which is observed directly above and below the heterogeneity (Fig. 3.12(d)) may reach up to 70% of the maximum Hertzian pressure. Similar plots are shown in Fig. 3.13 for the hydrostatic pressure. Negative zones indicate compressive residual stress. Unlike the case of a homogeneous elastic-plastic body, the presence of the heterogeneity localizes the residual compressive stress between the inclusion and the surface with significant residual compressive stress at the corners of the heterogeneity.

Table 3.7: Heterogeneity data for residual stresses computation

Heterogeneity data	Value
Shape	cube
Elastic properties	$\gamma = 3\ ;\ \mu = 0.3$
Size (semi-length)	$\beta = 0.2$
Location (depth)	$\alpha = 0.3$

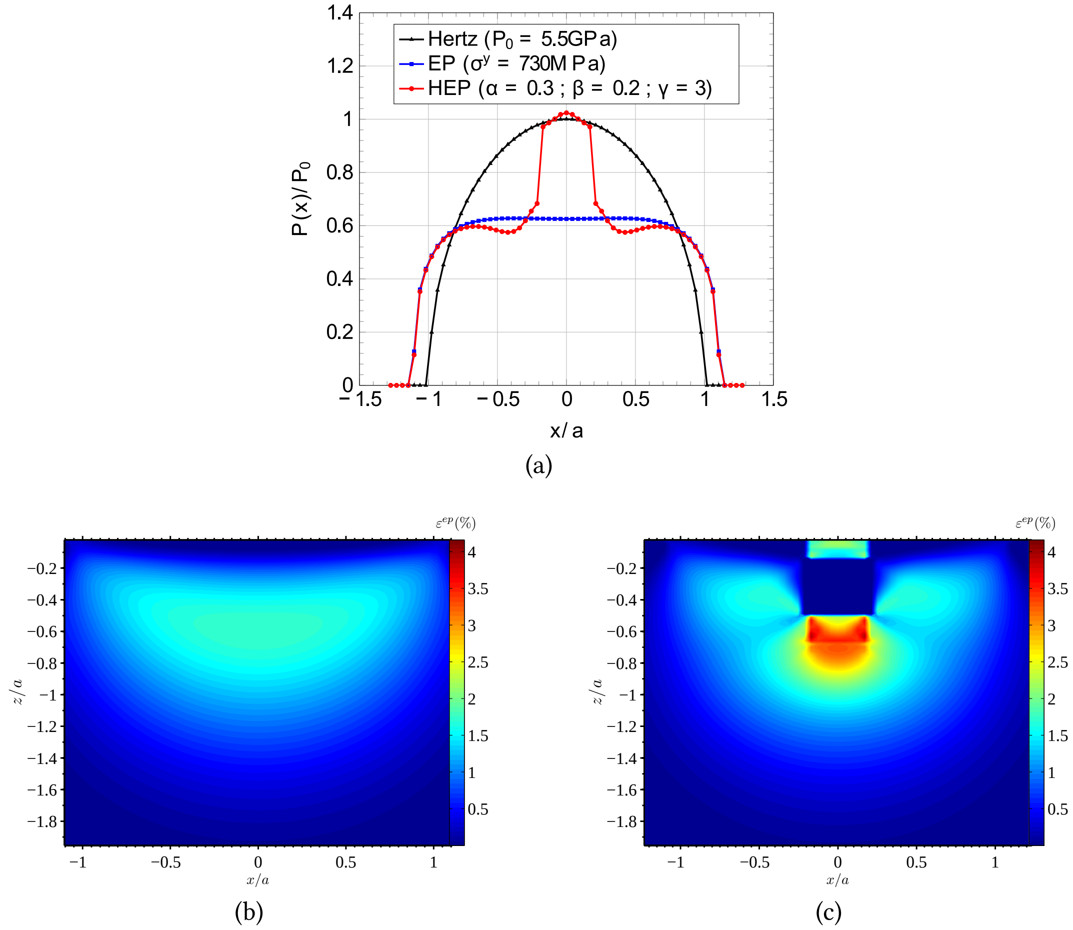

Figure 3.11: Contact pressure profiles and related plastic strain fields: (a) Pressure distribution; (b) Plastic strain within the homogeneous body; (c) Plastic strain within the heterogeneous body

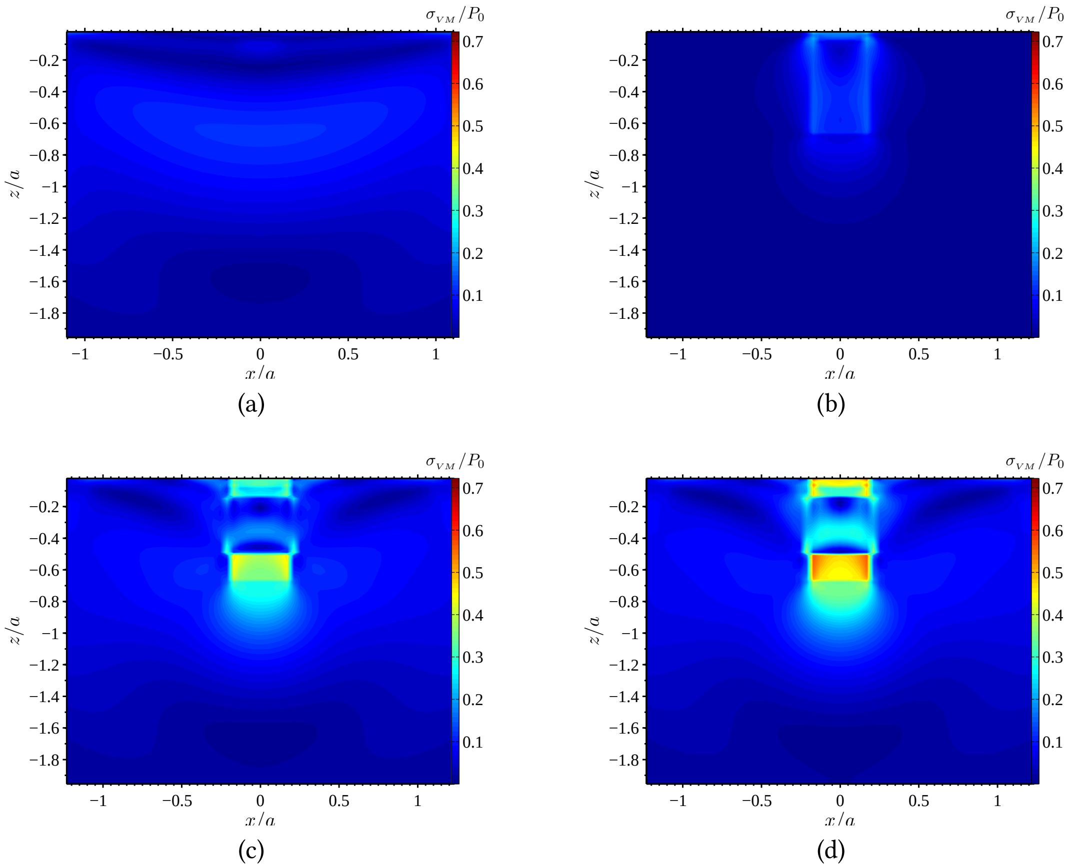

Figure 3.12: Decomposition of the total residual stress (Von Mises) observed after unloading: (a) Residual stress due to plasticity only without heterogeneity within the EP matrix; (b) Eigen-residual stress due to the presence of the heterogeneity and residual stresses resulting from the surrounding plasticity; (c) Residual stress due to plasticity only in the presence of the heterogeneity; (d) Total balanced residual stress

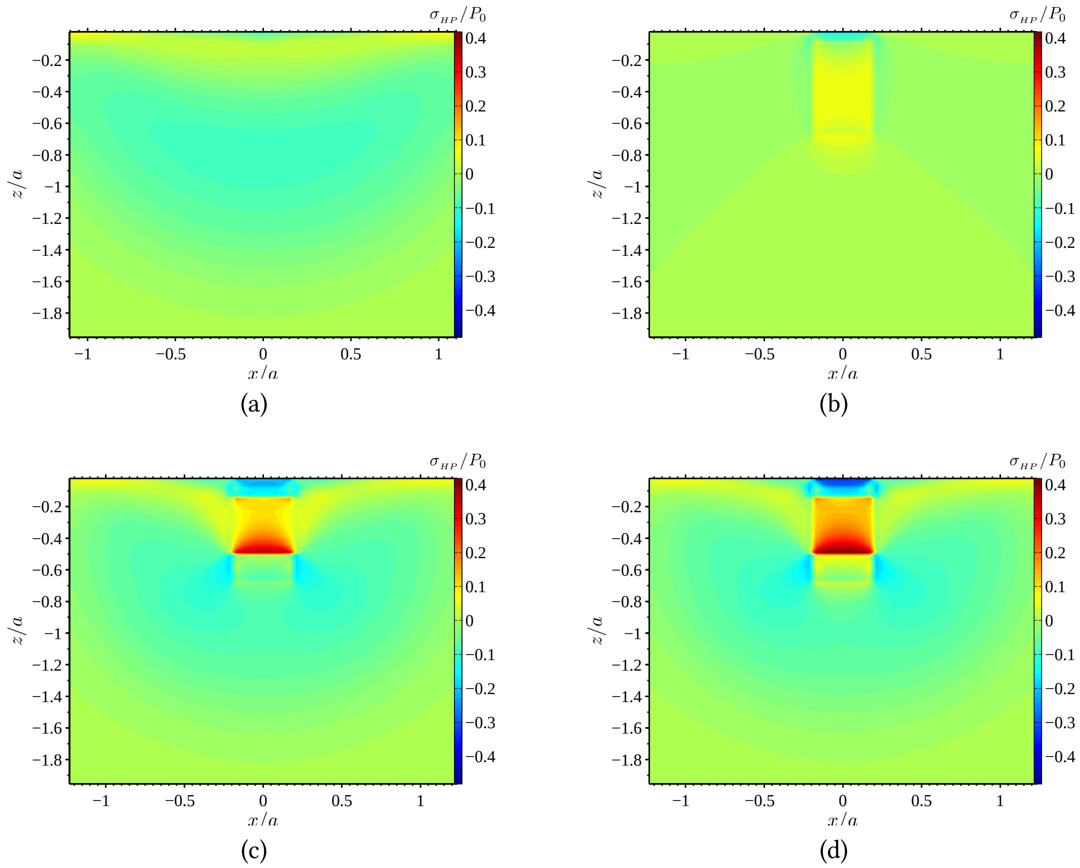

Figure 3.13: Decomposition of the total residual stress (Hydrostatic Pressure) observed after unloading: (a) Residual stress due to plasticity only without heterogeneity within the EP matrix; (b) Eigen-residual stress due to the presence of the heterogeneity and residual stresses resulting from the surrounding plasticity; (c) Residual stress due to plasticity only in the presence of the heterogeneity; (d) Total balanced residual stress

3.4.4 ANALYSIS OF PRINCIPAL STRESSES AND DIRECTIONS

In order to investigate and explain the damage mechanisms related to residual stresses near an isolated heterogeneous inclusion, the principal residual stresses and their directions are studied. From Fig. 3.14 one can forecast the crack initiation site and growth direction nearby a cuboidal heterogeneity within an elastic-plastic matrix subjected to a contact load.

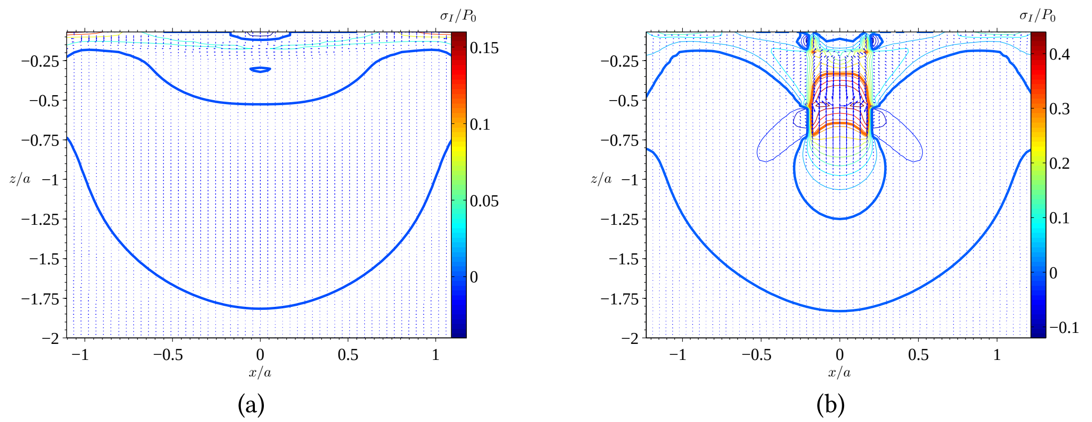

Figure 3.14: Principal stress I and principal direction I: (a) Elastic-plastic matrix; (b) Heterogeneous elastic-plastic body

For a cubic heterogeneity, that can be assimilated to a carbide in bearing steel, the highest values of the principal stress are located at the bottom of the heterogeneity and at its upper corners. Crack initiation can then be expected to occur at these locations. The orientation of the first principal stress σ_I is shown in Fig. 3.14(b) and zoomed in Fig. 3.15, bringing insights to the most probable direction in which cracks may propagate after initiation (in a plane perpendicular to the first principal direction). Note that $\sigma_I^{max} = 0.45 \times P_0$, when the homogeneous elastic-plastic case shows $\sigma_I^{max} = 0.15 \times P_0$ in Fig. 3.14(a).

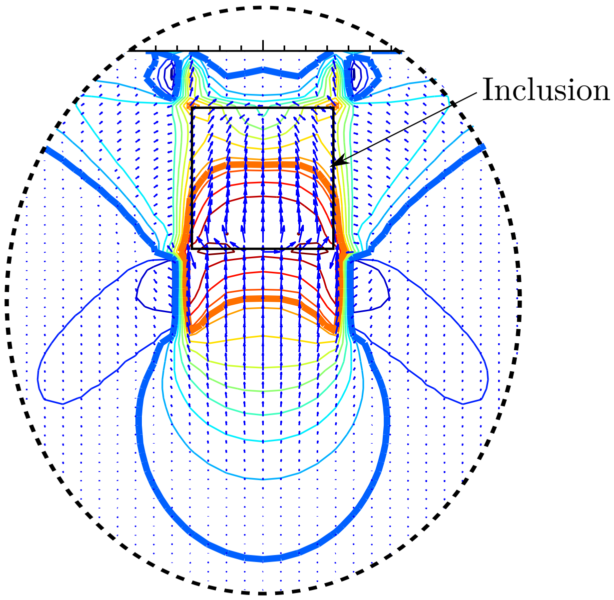

Figure 3.15: Zoom on the highest principal stress location and orientation: Prediction of crack initiation direction that should be perpendicular the principal stress direction for the mode I

3.5 PARAMETRIC STUDY

A parametric study is conducted for a heterogeneous elastic-plastic contact problem investigating the influence of the heterogeneity material, size and location, on the contact pressure distribution and subsurface plastic strain. The values of the parameters used here are recalled in Table 3.8 for one single heterogeneity of cubic shape.

Table 3.8: Data for parametric study, with α, β and γ being the dimensionless depth, semi-length and Young modulus ratio, respectively

Contact	Heterogeneity	Plasticity
$P_0 = 4\mathrm{GPa}$; $5\mathrm{GPa}$	$\alpha =$ 0.25 ; 0.3 ; 0.4 ; 0.48 ; 0.6	Swift Law
$(E, \nu)_{indenter} =$ $(310\mathrm{GPa}, 0.3)$	$\beta = 0.05$; 0.1 ; 0.2 ; 0.3	$(B, C, n) =$ $(640\mathrm{MPa}, 4, 0.095)$
$(E, \nu)_{HEPC-body} =$ $(205\mathrm{GPa}, 0.3)$	$\gamma =$ 0 ; $1/7$; $1/3$; 2 ; 3 ; 4	$\sigma^y = 730\mathrm{MPa}$

3.5.1 CONTACT PRESSURE

Figure 3.16 shows the influence of the depth $\alpha = z_i/a$ (Fig. 3.16(a)), semi-length $\beta = r_i/a$ (Fig. 3.16(b)) and elastic modulus $\gamma = E_i/E_m$ (Fig. 3.16(c)) of the cuboidal heterogeneity on the contact pressure distribution. As expected for a stiff heterogeneity, the closest the heterogeneity is to the surface, the highest the peak of pressure is. For a stiff heterogeneity ($\gamma = 3$) having a relatively small size ($\beta = 0.2$) with its center at depth $\alpha = 0.25$, the peak pressure reaches 1.15 times the Hertzian one, which is approximately twice that observed for a homogeneous EP body (Fig. 3.16(a)). The most critical size for a stiff heterogeneous inclusion located a depth $\alpha = 0.3$ (Fig. 3.16(b)), corresponds to $\beta = 0.3$, i.e. when it becomes tangent to the surface for which the maximum pressure is found at the edge of the heterogeneity. This is of particular importance for carbides that are sometimes observed at the surface of the raceway in rolling bearings, that may be detached after a few rolling cycles. Finally, it can be observed (Fig. 3.16(c)) that hard heterogeneities increase locally the pressure while soft ones logically reduce it.

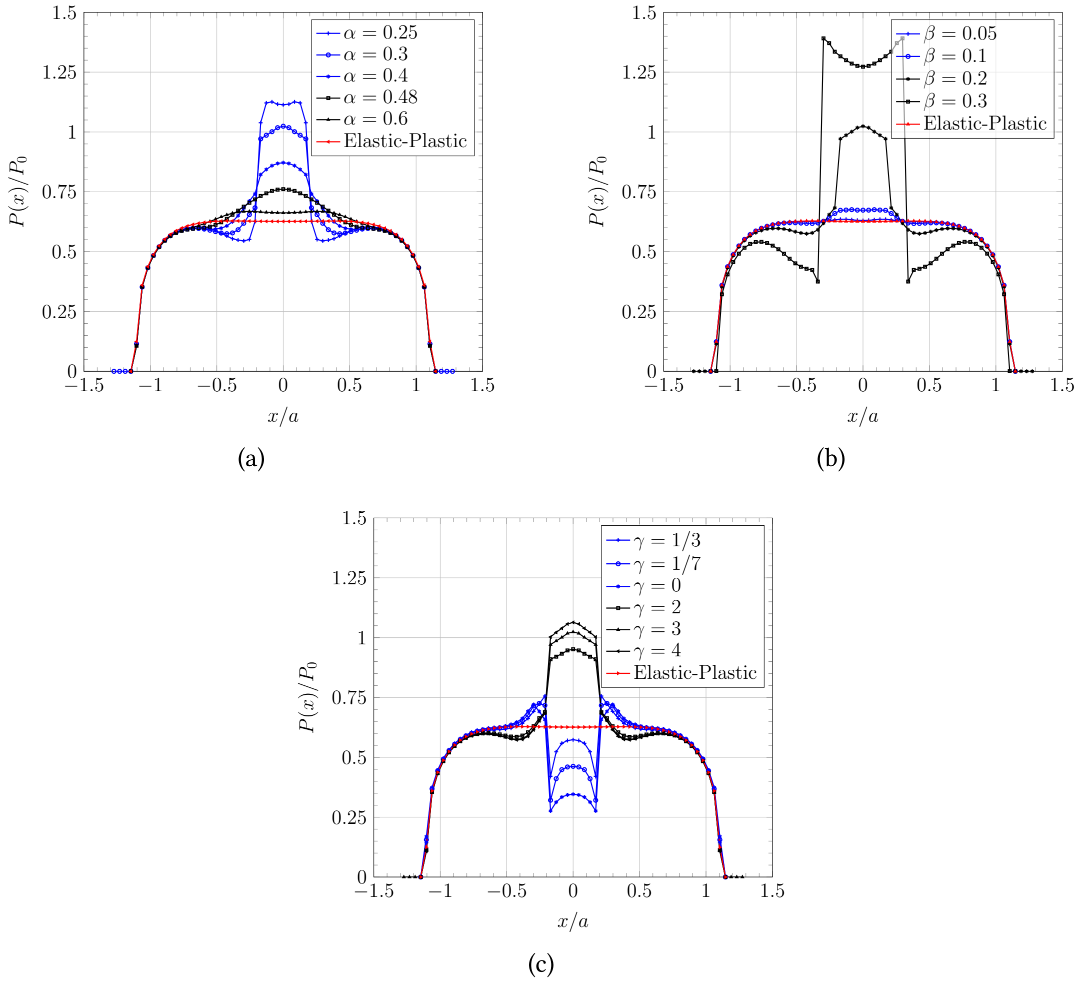

Figure 3.16: Effect of a cubic heterogeneity on the contact pressure distribution, according to (a) its depth (for $\beta = 0.2$, $\gamma = 3$); (b) its size (for $\alpha = 0.3$, $\gamma = 3$); and (c) elastic modulus (for $\alpha = 0.3$, $\beta = 0.2$)

3.5.2 EQUIVALENT PLASTIC STRAIN

The equivalent plastic strain profile along depth from the contact center $(x, y) = (0, 0)$ is plotted in Fig. 3.17, for various values of depth $\alpha = z_i/a$ – Fig. 3.17(a), size $\beta = r_i/a$ – Fig. 3.17(b) and elastic modulus $\gamma = E_i/E_m$ – Fig. 3.17(c). The shape of the heterogeneity remains a cube, and the reference parameters are those of Fig. 3.16, i.e. $\alpha = 0.3$, $\beta = 0.2$, and $\gamma = 3$. In all sub-figures the plastic strain obtained for a homogeneous elastic plastic body with the same loading is plotted for reference. Note that here again the heterogeneity remains elastic for simplicity. It can be observed that, for a stiff heterogeneity, the maximum is always found above the top face or below its bottom face, whatever are its depth and its size. This is consistent with the results presented earlier in Fig. 3.8 for a spherical heterogeneity, for which the maximum was found at the south or north pole for a stiff inclusion and at its equator for a soft one. Note also that for a stiff heterogeneity the maximum plastic strain is found between the contact surface and its top face when its center is below the Hertzian depth, see Fig. 3.17(a). As the heterogeneity moves closer to the surface, the maximum of the plastic strain switches to a depth below the bottom face. Finally, closer to the surface is the heterogeneous inclusion, higher is the maximum plastic strain at a point that also moves toward the contact surface. It can also be observed in Fig. 3.17(b) that it exists a critical size (here $\beta = 0.1$ when $\alpha = 0.3$ and $\gamma = 3$) for which the plastic strain is maximum ($\varepsilon^p = 5\%$) compared to 3.5% and 3% only for $\beta = 0.2$ and 0.05, respectively. At last, it can be seen in Fig. 3.17(c) that the presence of a soft heterogeneity acts as a damper or a screen reducing the plastic strain level while a stiff one increases it, with peaks of plastic strain significantly higher, up to the double (for $\gamma = 4$) of the one observed in the homogeneous case.

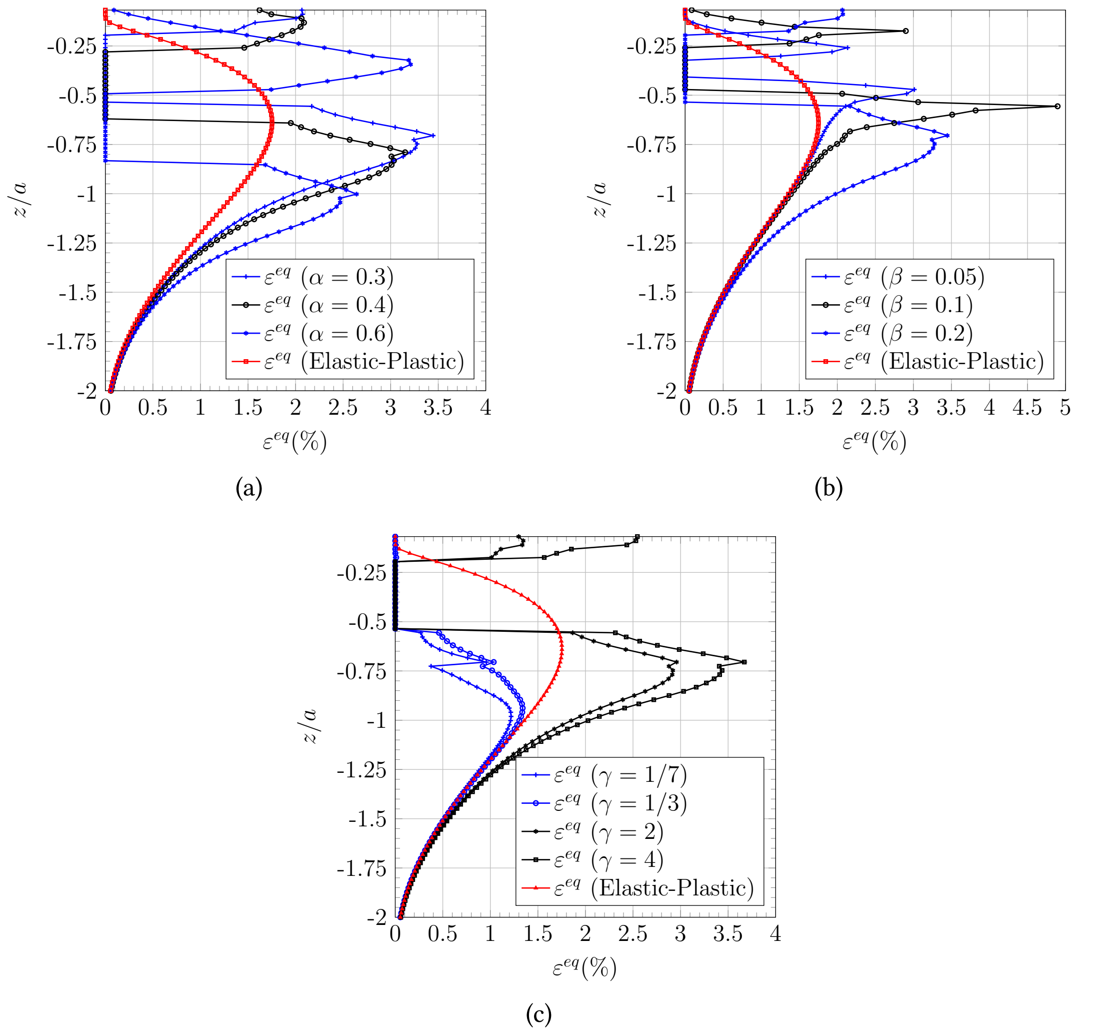

Figure 3.17: Effect of a cubic heterogeneity on the equivalent plastic strain profile versus depth, according to (a) its depth (for $\beta = 0.2, \gamma = 3$); (b) its size (for $\alpha = 0.3, \gamma = 3$); and (c) elastic modulus (for $\alpha = 0.3$, $\beta = 0.2$)

3.5.3 STUDY OF THE OVERALL PLASTIC STRAIN

For evaluating the subsurface global behavior, an overall plastic strain is defined as:

$$\tau = \frac{1}{V_p} \int_{\Omega_c} \varepsilon^{ep}(x, y, z) d\Omega_c \tag{3.1}$$

Where V_p is the volume of the total plastic domain Ω_c and τ the effective accumulated plastic strain.
The overall plastic strain is plotted in Fig.3.18 and Fig.3.19 for various heterogeneity parameters and as a function of the applied load. Results show that for various hetero-

geneity depths (Fig.3.18(a)) and elastic modulus (Fig.3.18(a)) the presence of a heterogeneity mainly redistributes the plastic strain but barely changes it. This is not true for low load values, i.e for the first step of plasticity when the presence of the heterogeneity causes a change in stress distribution and then cause either advanced or delayed plasticity. Once the plastic flow is rather general in the zone surrounding the heterogeneity (at about 0.6 times the maximum load for this specific case, like in Fig. 3.11(a)), the influence of the heterogeneity on the overall plastic strain, and consequently dissipated energy, is negligible. A few more specific cases are studied. Fig.3.19(a) shows that the previous conclusion is not valid for heterogeneities tangent to the surface. The case ($\beta = 0.1$ and $\alpha = 0.1$) is that of a small (compared to the maximum contact radius) hard heterogeneity, typically a carbide, tangent to the surface. Its presence causes early apparition of plastic flow but its influence becomes negligible for increased load, i.e. when the plastic and contact zones become considerably large relatively to the heterogeneity size. A similar, but deeper heterogeneity ($\beta = 0.1$ and $\alpha = 0.3$) does not present a similar effect. A large, hard heterogeneity tangent to the surface ($\beta = 0.3$ and $\alpha = 0.3$), causes for all load values an increase in the plastic flow. Critical sizes and depth, both being interdependent, of heterogeneities can use the proposed method be identified.

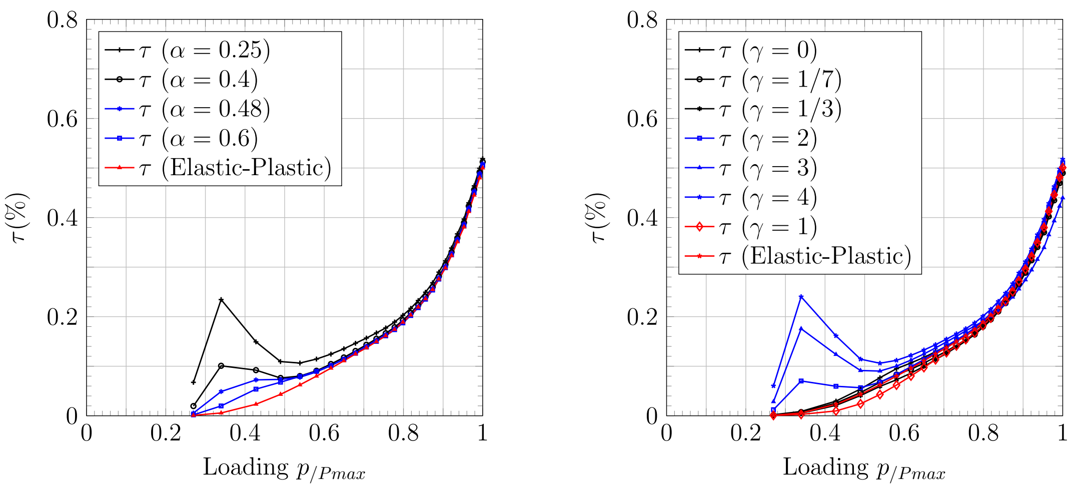

(a) (b)

Figure 3.18: Independence of the overall plastic strain on heterogeneity's parameters: (a) location; (b) elastic modulus

For hard heterogeneities ($\gamma = 3$), some simulations are performed to investigate on particular values of heterogeneity's parameters α and β which strongly affect the overall plastic strain. Fig.3.19(c) presents the overall plastic strain when the heterogeneity is tangent to the surface (See that $\alpha = \beta$). One can notice that, in these studied cases, the overall plastic strain increases when the couple $(\alpha\ ,\ \beta)$ increases. For small values of $(\alpha\ ,\ \beta) < (0.1\ ,\ 0.1)$, the overall plastic strain reach the homogeneous elastic-plastic one, when $\dfrac{P}{P_{max}} > 0.6$. Note that in this studied cases, when $(\alpha\ ,\ \beta) > (0.1\ ,\ 0.1)$ tangential heterogeneities are causing non-negligible overall plastic flow compared to that of the homogeneous elastic-plastic bulk, even for low contact pressures. Fig.3.19(b) shows that for the same location $\alpha = 0.4$ the overall plastic strain of $\beta = 0.3$ is more important than $\beta = 0.1$ one. This result emphasis that the critical parameter is the heterogeneity's size when it is completely embedded beneath the surface $\alpha > \beta$. Note that one can also conclude that, if $\alpha > 0.4$ and $\beta < 0.1$ the overall plastic strain matches with the homogeneous elastic-plastic one. For the same size $\beta = 0.1$ the overall plastic strain of $\alpha = 0.1$ (tangential heterogeneity) is higher than the embedded heterogeneity $\alpha = 0.4$ one, at $\dfrac{P}{P_{max}} < 0.6$. But their behaviors match once the pressure exceeded the threshold of $0.6 \times P_{max}$. In contrast, for the same size $\beta = 0.3$ the overall plastic strain of tangential heterogeneity $\alpha = 0.3$ is lower than the embedded heterogeneity $\alpha = 0.4$ one, at $\dfrac{P}{P_{max}} < 0.6$. And their behaviors change once the pressure $0.6 \times P_{max}$ was exceeded. The tangential heterogeneity becomes more critical. One can summary that $\beta > 0.3$ is the worth encountered case for embedded heterogeneity or tangential heterogeneity independently of the other heterogeneity's parameters.

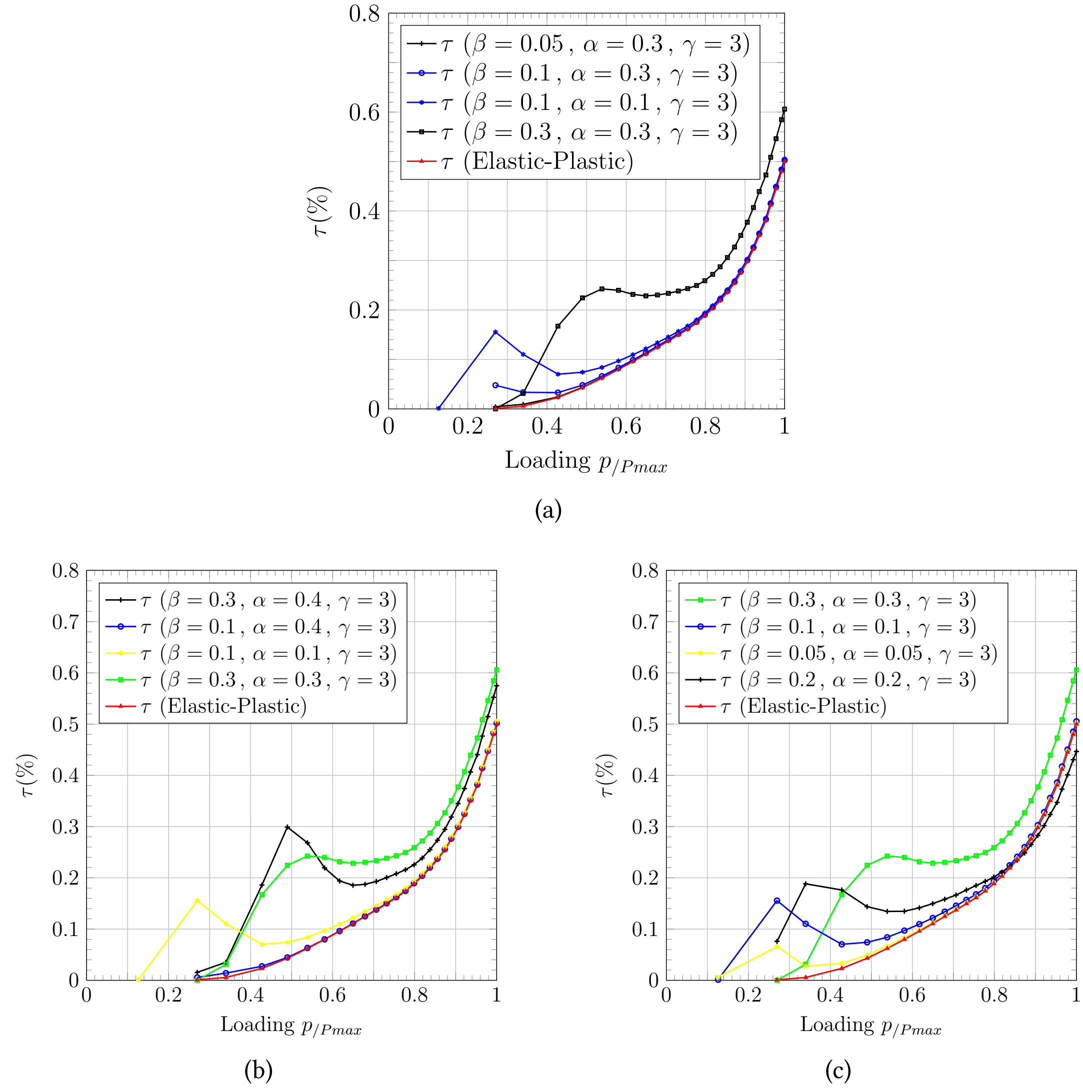

Figure 3.19: Dependence of the overall plastic strain on some particulars set of heterogeneity's parameters: (a) size; (b) size and location; (c) size and tangential position

3.6 PARTIAL CONCLUSION

This study presents a three-dimensional model of heterogeneous elastic-plastic contact (HEPC) using a semi-analytical method. The model is versatile and able to cover any kind of heterogeneity size, shape, distribution and location. Interaction between close inhomogeneities is also considered in the numerical algorithm. The following major conclusions have been reached:

- The proposed method permits to couple the contact problem (the algorithm is almost identical to the one for the homogeneous elastic contact problem), the presence of heterogeneous inclusions (based on the Eshelby's EIM) and plasticity. All is solved simultaneously in the framework of semi-analytical methods. The algorithm is very robust and converges at relatively high plastic strain. For instance, plastic strain of 20% can be very easily reached.
- It is shown that the residual stress and the plastic strain state after loading arise from a complex combination of the effects of plasticity and eigenstresses due to the presence of inclusions.
- It exists for each configuration (size, location, shape and material properties of an isolated inclusion, one of these parameters being a variable) a critical value for which the plastic strain is the highest. Critical locations of heterogeneities, depending on their size and the loading conditions can therefore be determined.
- For inclusions stiffer than the matrix the maximum plastic strain is found at the top and bottom face of the heterogeneity (north and south pole for a spherical one) whereas it is found on the lateral sides of it (equator for a spherical one) for a soft one.
- The presence of soft inhomogeneities tend to minors the level of plasticity: they act as a damper.
- In presence of a stringer or cluster of interacting inclusions (i.e. close enough so that they interact), the most detrimental orientation of the inclusions can be determined. For stiff and iso-spaced inclusions the most critical orientation is the vertical one (i.e. normal to the contact surface).

4 HETEROGENEOUS ELASTIC PLASTIC ROLLING CONTACT

The objective of this chapter is to characterize the critical effects generated by the presence of heterogeneous inclusions in roller rings that may generate peaks of stress and potential plastic flow. The role of the size, depth and material properties of the inclusion, along with the hardening properties of the body will be studied. Special care will be devoted to the stabilization of the pressure load when several rolling cycles are considered. For that the coupling between the plastic behavior of the material and the inclusion must be correctly accounted for. The semi analytical methods have proven their efficiency to solve contact problems even when the contacting bodies are heterogeneous and behave plastically. The method used here is fully coupled: the mutual influence between inclusions, plasticity and with the contact is considered. Potential applications involve practical prediction of the criticality of inclusions and engineering best practices for bearing ring manufacturing.

Contents

4.1 INTRODUCTION

The pioneering works of D. Tabor, Eldredge [76] and Crook [77] in the middle of 50s about the mechanism of rolling friction revealed that the rolling resistance was not only due to interfacial slip since full lubrication regime is ensured, but also owed to the permanent displacement of the material ahead the ball related to the plastic deformation generated underneath. This new point of view led to the emergence of several investigations to integrate plasticity phenomena in rolling contact failure studies. Afterwards, considerable experimental studies and observations [78, 79] brought out that non-metallic inclusions are the main source of subsurface damage mechanism initiation and propagation driving to the so-called white structure flaking (WSF). Hence, both surface failure (from circumferential and axial cracks located at contact path shoulder) and subsurface failure (from material imperfection as defects and heterogeneous inclusions) became welcomed research topics. Existing studies demonstrated that the genesis of subsurface damage mechanisms around inclusions is representative of the degradation of material crystallographic structure from martensite to ferrite [80] manifested by the well-known butterfly wings which debonding regions are the site of microcracks. Some suggested [81, 79] microstructural alteration which yields a decaying of the butterfly wingspan regions into microcavities. Strong evidences, provided by miscellaneous serial sectioning of test specimens and ex-service bearing rings, elucidate statistically that the network connection of butterfly wingspan in presence of multiple inclusions forms small white etching cracks that after a while propagate to the surface [82].

However, the detection of the very first crack instant and location needs in-situ control technology and it seems to be complex because of the compact design of mechanical systems and working conditions as lubrication and temperature. Even if helpful approaches such as vibration sensor techniques are used as alternative to a proper planning of substantial maintenance work, the detection threshold is a function of several parameters such as the overall cost of the equipment and the physical limitations (like signal interference when there is a need to lower detection threshold). Therefore modest developments were made over the last two decades to establish an adequate connection between the fatigue failure and the material properties when the contacting elements (gears, rail-wheel and aerospace bearing) are getting nowadays complex responses due to requirements specification. Material property adjustment to improve rolling elements tribological behavior, has been analyzed numerically in [83]. Several numerical models[84, 85, 86] offer the alternative to provide the fatigue life prediction base theoretical and experimental background. Some of them can take to account the effect of initial compressive stress as well as the effect of the tensile hoop stresses induced during the mounting on the shaft with heavy fits and the additional centrifugal stress in high shaft speed conditions [85]. But it has been claimed that the development of nascent residual stress during cyclic stress conditions due to plasticity must be considered. Then semi-empirical descriptions have been proposed in [87]. The residual stress scatter can also be incorporated in the RFC life model, [88]. In addition, RCF crack initiation life models have been proposed in [89] with good accuracy estimation. Recently, Ghosh [90] simulates subsurface cracks initiation and propagation due to surface fatigue during rolling contact, employing linear elastic fracture mechanics. But in the present study, the rolling contact resolution consists of moving the contact problem solved at each time-step, under quasi-static consideration, along a given direction.

Furthermore, models based on Finite Element Method (FEM) have been commonly used in rolling contact analysis treating crack propagation [91, 92], fatigue failure [93, 3], spalling [10], adhesion and slip effects [94]. Yet, solving three dimensional rolling contact problem involving heterogeneity or plasticity with FEM is proven by Wang and coworkers in [95], to be resources and time consuming, compared to Semi Analytical Method (SAM) especially when a fine mesh is required to effectively capture fields in interesting zones. A three-dimensional elastic plastic rolling contact modeling by FEM is too computational resources demanding and even more if several cycles must be performed when analyzing shakedown [96] or ratcheting [97] phenomena. Generally, the contact pressure distribution is calculated separately for instance by using Carter's contact theory as in [98], before solving the subsurface problem by FEM.

The efficiency and rapidity of SAM owe to the use of Conjugated Gradient Method (CGM) [50] and Fast Fourier Transform FFT [53] techniques. Further enhancement take into account the effect of non-linear behavior as plasticity [37], thermal-elastic-plasticity [99], dynamic [55], visco-elasticity [100] along with the presence of heterogeneous inclusion from different origins [66, 41, 101, 102], fretting stick-slip [51, 40] and lubricated plasto-elastohydrodinamic [103]. A numerical resolution of heterogeneous elastic plastic contact problem has been proposed in [104] by fully coupling contact, plasticity and heterogeneity interactions in the same flowchart. This algorithm is the core of the rolling contact model reported in this study. Guler [105] constructs a mathematical model of the rolling problem by using a singular integral equation approach. But in the present work, the rolling contact resolution consists of moving the contact problem solved at each time-step, under quasi-static consideration, along a given direction.

The principal objective is to provide a comprehensive analysis based on the solutions in terms of contact stress and subsurface stress-strain considering plasticity and heterogeneity effect on the rolling contact. Conceding that the main failure mode of mechanical components undergoing repeated rolling contact appropriates to surface spalling, frictional contact has been achieved in purpose to examine the excessive plastic strain endured by the material in presence of heterogeneity. Also the model yielded good results when including the presence of initial compressive stress and/or gradient of plastic behavior. Although the entire results obtained here stand for numerical aspect, it has practical merit for replicating and confirming advanced analysis performed by expert firms dealing with rolling contact problem in engineering systems from design to manufacturing in reference to successful experiments works evaluating fatigue life concerning aircraft engine mainshaft bearing [86]. Bearing industry engaging for high performance, perfected materials as AISI 52100 steel which have very high strength. Also in order to raise its fracture-toughness, the AISI 52100 steel has been substantially enhanced to the M50 steel by metallurgical purity, then M50 NiL appears as an improved processed variant of M50 with high low-nickel carbon. The latter materials owe their strengthening to the presence of carbides and nitrides together with intermetallic particles. Over loading cycles, the carbides and nitrides act as stress intensifier and become the site of subsurface crack initiation and propagation. In other to seek the potential risky zones for crack departure around heterogeneity, Dang Van crack initiation criterion [106] is used in relationship with the shear and hydrostatic stress. This method allows to distinguish the initiation life from the total life among a variety of empirical criteria as Goodman rules based on the mean and alternative stress. Similar to Sines criterion [107], Dang Van criterion offered a simply explanation for understanding high cycle multiaxial fatigue life when the employed material must withstand a located stress concentration. Dang Van criterion has been used by Ekberg [108] to treat railway wheels rolling contact involving heavy load up to 240kN. But the study assumed the material to be homogeneous and the plasticity effect are not accounted despite the fact that it might be reasonably present in view of the load magnitude. Further, Hofmann *et al.* [109] include plastic shakedown effect and heterogeneity by considering a distribution of polycrystalline grains. However the analysis was limited to two dimensions by means of calculation power.

In the following sections, let's abbreviate Elastic by E, Elastic-Plastic by EP, Homogeneous Ho and Heterogeneous by He. These abbreviations are used as superscript or subscript. Other abbreviations are used such as HEPC standing for heterogeneous elastic plastic contact and HEP-RC for heterogeneous elastic plastic rolling contact.

4.2 ROLLING CONTACT ANALYSIS

Based on previous work of Amuzuga et *al.* [104] presenting the solver of heterogeneous elastic plastic contact (HEPC) problem and its validation, the model is extended to a rolling contact problem. The theoretical background and the flowchart are briefly described here.

4.2.1 DESCRIPTION OF THE HETEROGENEOUS ELASTIC-PLASTIC ROLLING CONTACT MODEL

Now, a rolling contact is conducted on a heterogeneous elastic-plastic (HEP) bulk by and an elastic spherical roller. The bulk could be considered as the AISI 52100 or M50 - M50NiL steels containing stiff heterogeneous inclusions as carbides and the roller stands for Silicon Nitride material (Si_3N_4). The Heterogeneous Elastic-Plastic Rolling Contact (HEP-RC) simulation is described in Fig.4.1 and the parameter settings are indicated in Table. 4.1. The heterogeneity is elastic and centered below the surface in the plane $\mathcal{P}(y = 0)$. Numerical results are presented in dimensionless form. The surface/subsurface stresses and distance are normalized by the homogeneous Hertz maximum pressure P_0 and radius a, respectively. The accumulative plastic strain ε^p is expressed in percentage, and ε^p_{max} refers to its maximum value within the whole body. The relative distances between the heterogeneity center position x_i along the rolling motion direction and the contact center position x_c is noted $\delta x = x_i - x_c$. Hence δx is negative when the load is arriving backward on the heterogeneity, positive when the load passed over the heterogeneity and is going forward.

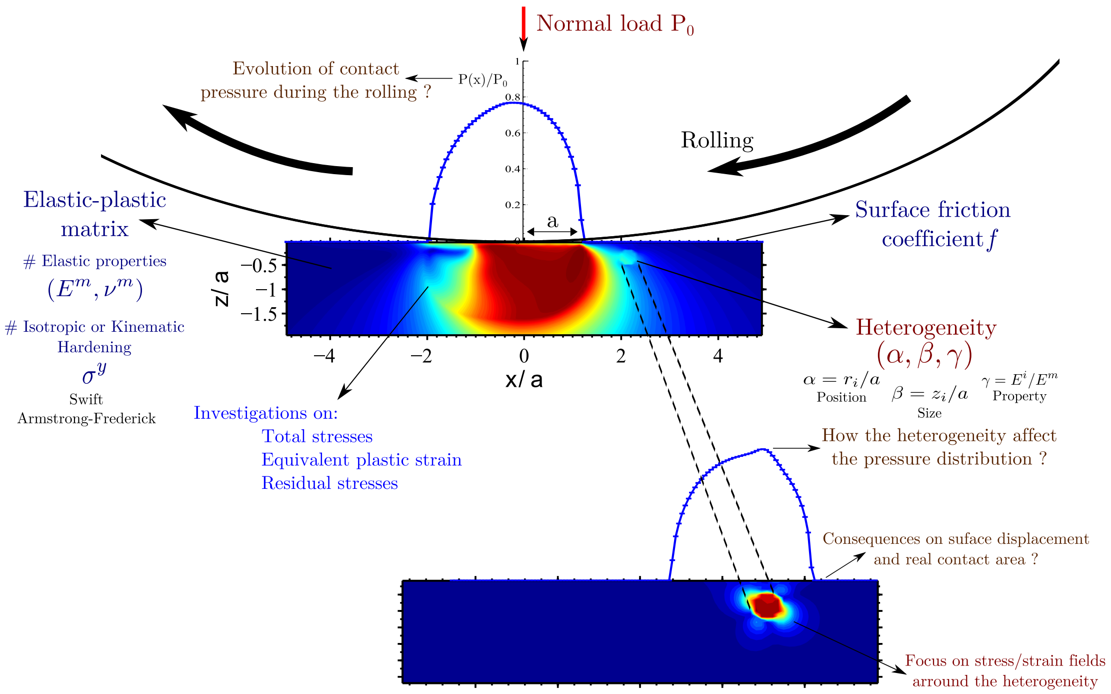

Figure 4.1: The Heterogeneous Elastic-Plastic Rolling Contact simulations setting

Table 4.1: Values of HEPRC simulations parameters

Parameter	Value
Indenter diameter	$d = 5.56mm$
Applied maximum Hertzian pressure	$P_0 = 2.0GPa$
Roller elastic properties	$E_{ball} = 310GPa$ (Silicon Nitride) ; $\nu_{ball} = 0.3$
Surface friction coefficient	$f = 0$; 0.05 ; 0.1 ; 0.15 ; 0.2 and 0.25
Matrix elastic properties	$E_m = 210GPa$ (M50NiL) ; $\nu_m = 0.3$
Matrix plastic properties	$\sigma^y = B(C + \varepsilon^p)^n$ where $B = 240MPa, C = 4$, and $n = 0.095$
Heterogeneity elastic properties	$E_I = 490GPa$ (Vanadium carbide) ; $\nu_I = 0.3$
Heterogeneity size	$S_i = \beta \times a$ where $\beta = 0.05$; 0.1 ; 0.2 ; 0.4 with a the contact radius
Heterogeneity location	$z_i = \alpha \times a$ where $\alpha = 0.3$; 0.5 ; 0.8 and $a = 63.48\mu m$
Rolling distance	D_x, from $x = -2a = -120\mu m$ to $x = 2a = 120\mu m$

The maximum values reached by different fields during the rolling motion evolution are analyzed. These maxima are not located at the same point during the entire cycle. One can also notice that, when the bulk is elastic-plastic, the plotted fields profiles present a non-symmetrical aspect. As these profiles are obtained from the first rolling cycle, the non-symmetrical aspect is a physical phenomena known as the contact surfaces permanent groove creation. It was first observed by G. Hamilton [110] when performing rolling tests on copper rolling. The microscopic images reveal a forward movement or distortions in some case, of the surface layer of copper disc on grain level. Further photoelastic imagery on aluminum glass disc has shown tilted fringe pattern of the stress distribution even if normal loading is applied. This allows to explain the phenomena as the material rolling resistance in the motion opposite direction when plastic flow occurred above the yield point. Indeed, in other to overcome this resistance, the center of the pressure (where its magnitude is high) is thrown ahead of the contact geometrical center. Note that the test conditions and specimens arrangement ensure that the tilted stress distribution is not due to the shear traction induced by the surface friction coefficient f according to Coulomb's friction law. This is confirmed here since $f = 0$ but the tilted stress distribution held as shown by Fig.4.3(c). It is necessary to specify that the groove phenomena cannot be captured if the rolling motion is modeled by moving a constant given distribution of pressure as seen in many studies. The contact problem needs to be solved at each rolling step. Whatever, the groove phenomenon is not crucial for statements established here since only the comparisons of field orders of magnitude are mainly analyzed throughout present study. In addition, when the bulk is homogeneous elastic-plastic, the steady state is reached for all the considered fields (pressure Fig.4.2, stress Fig.4.3 and strain Fig.4.6) after a rolling distance of $D_x = 3a$. For calculation resources minimization purpose, the heterogeneity center is placed at $\delta x = 2a$ from the rolling starting point. Thus, the steady state is not reached before the load is approaching the heterogeneity. But the error committed, by this reduction of the computational zone is less than 1% which is admissible with regard to the advantage in terms of the numerical code speed performance.

4.2.2 CONTACT PRESSURE EVOLUTION DURING THE ROLLING

The comparison between the contact pressure maximum during a rolling cycle is presented in Fig.4.2 when the flat body is assumed homogeneous/heterogeneous and elastic/elastic-plastic. It could be seen that when the flat body is homogeneous elastic, the pressure maximum is equal to the Hertzian one during the rolling. By adding a heterogeneity (defined by $S_i = 0.1a$, $z_i = 0.3a$ and $E_I = 490GPa \Rightarrow \gamma = 2.33$), the pressure maximum started increasing when the contact x_c is coming closer to the heterogeneity x_i in the motion direction. The increase begins at $\delta x = x_i - x_c = -0.5a$ and reaches the peak at $\delta x = 0$ where the *over-pressure* is $P^{He}_{max} - P^{Ho}_{max} = 0.08P_0$. Afterwards, the *overpressure* decreased and vanished at $\delta x = 0.5a$. Note that, in the presence of heterogeneity and when the flat is elastic, the maximum contact pressure is disturbed over a distance of $D_i^{(P)} = a$. But, when plasticity occurred, the disturbance distance is more enlarged $D_i^{(P)} = 1.8a$ and the *over-pressure* is higher $P^{He}_{max} - P^{Ho}_{max} = 0.16P_0$. In this regarded case, the disturbance distance and the *overpressure* are practically doubled when the flat body is elastic-plastic.

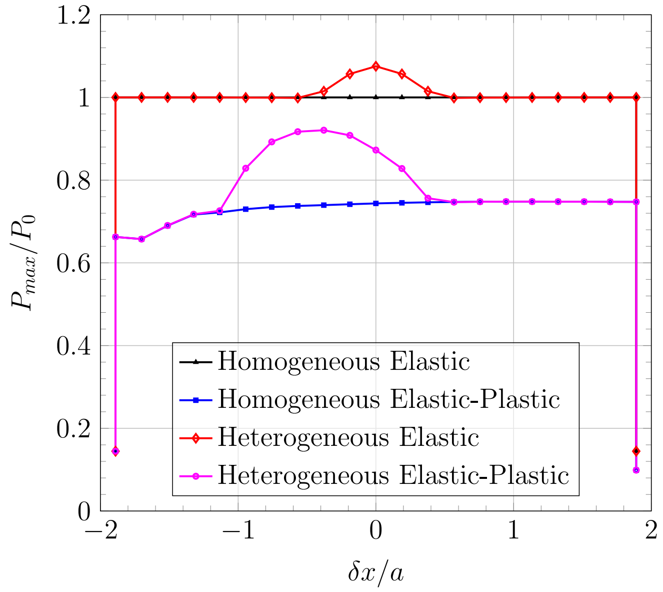

Heterogeneity parameters	value
Size	$S_i = 0.1a$
Location	$z_i = 0.3a$
Elastic modulus	$E_I = 490GPa$

Figure 4.2: Contact pressure evolution during the rolling

4.2.3 SUBSURFACE MAXIMUM SHEAR STRESS DURING THE ROLLING

Similarly to the evolution of the contact pressure, it could be seen in Fig.4.3 that, when the bulk is elastic, the subsurface total stress [a] in the presence of the heterogeneity leads to a stress field disturbance spread over a distance of $D_i^{(\tau)} = 2.2a$ with an *over-stress* about $\tau_{max}^{He} - \tau_{max}^{Ho} = 0.18P_0$. More critical, it turns out that, when the bulk is elastic-plastic the disturbance spread over $D_i^{(\tau)} = 3.4a$ with an *over-stress* of $0.22P_0$. The maximum shear stress $0.4P_0$ exceeded the maximum Hertzian $\tau_{max}^{Hertz} = 0.31P_0$ which is often used by product staff to design the applied load.

[a] *the maximum shear stress is used here as Tresca stress* $\tau_{max} = \sigma_{Tresca} = \frac{1}{2}Max(\sigma_I - \sigma_J)_{I,J=1,2,3}$

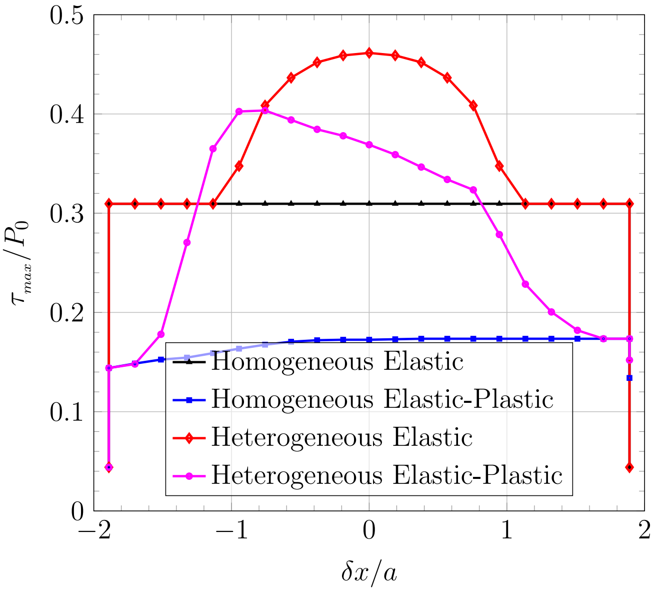

Heterogeneity parameters	value
Size	$S_i = 0.1a$
Location	$z_i = 0.3a$
Elastic modulus	$E_I = 490GPa$

Figure 4.3: Subsurface maximum shear stresses during the rolling

4.2.4 MAXIMUM SHEAR STRESS DISTRIBUTION DURING THE ROLLING

Now the heterogeneity is centered at the depth of the maximum shear stress peak. The maximum shear stress contours in the subsurface is presented in Fig.4.2, 4.3 , 4.4, 4.5. The sub-figures (a) and (b) show the stress distribution at the rolling motion starting where $\delta x = -2a$. Following this logic, the sub-figures (c) and (d) correspond to the moment when the rolling contact center is aligned with the heterogeneity center along the vertical axis z implying that $\delta x = 0$. The sub-figures (e) and (f) stand for the unloading at the end of the motion, where $\delta x = 2a$. It should be clarified that the sub-figures (a), (c) and (e) represent the view in the plane $\mathcal{P}(y = 0)$ when the sub-figures (b), (d) and (f) represent the view in the plane $\mathcal{P}(x = 0)$. The main reference (O, x, y, z) is defined by its origin O located at the contact surface intersection with the vertical axis z passing through the heterogeneity center. This means that the planes $\mathcal{P}(y = 0)$ and $\mathcal{P}(x = 0)$ are centered on the heterogeneity and they intersect on the vertical axis z.

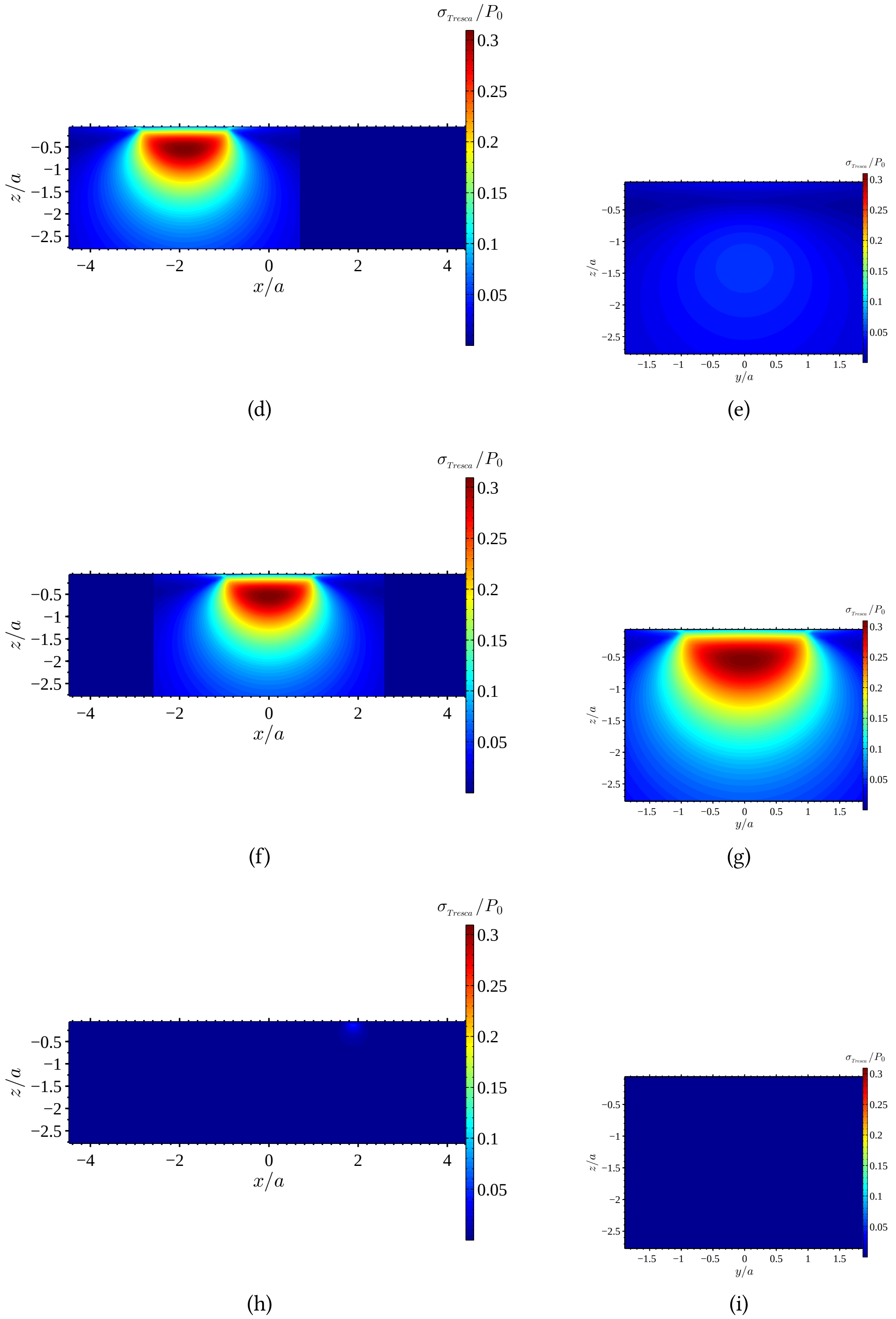

Figure 4.2: Evolution of the maximum shear stresses at particular rolling motion steps when the body is homogeneous elastic: Step I $\dashrightarrow$ Contact loaded at $\overrightarrow{\delta_x} = -2a$, (a) rolling viewed in the plane $\mathcal{P}(y = 0)$, (b) rolling viewed in the transverse plane $\mathcal{P}(x = 0)$ centered on the heterogeneity; Step II $\dashrightarrow$ Rolling up to $\delta x = 0$, (c) rolling viewed in the plane $\mathcal{P}(y = 0)$, (d) rolling viewed in the transverse plane $\mathcal{P}(x = 0)$ centered on the heterogeneity; Step III $\dashrightarrow$ Contact unloaded at $\delta x = 2a$, (e) rolling viewed in the plane $\mathcal{P}(y = 0)$, (f) rolling viewed in the transverse plane $\mathcal{P}(x = 0)$ centered on the heterogeneity

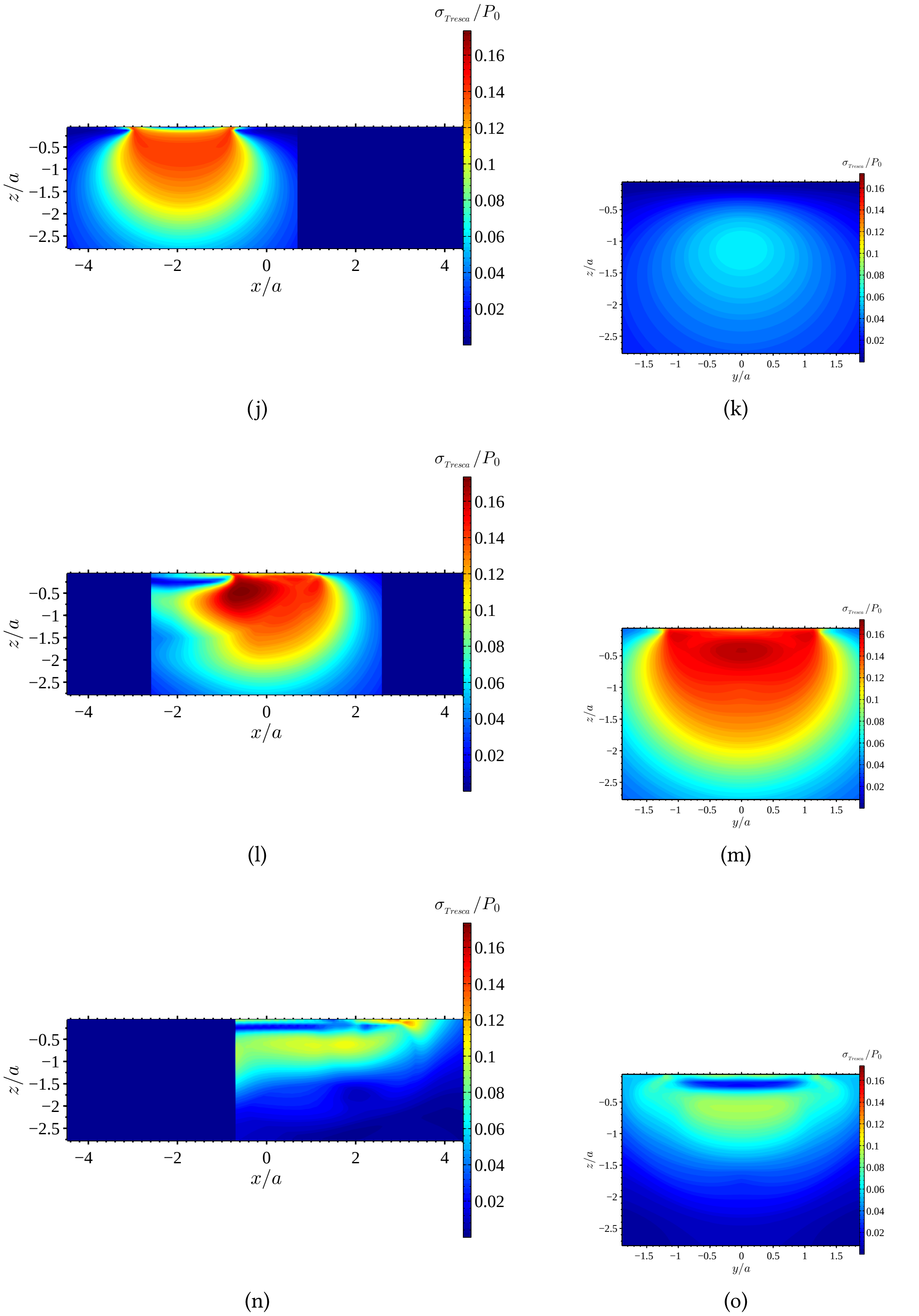

Figure 4.3: Evolution of the maximum shear stresses at particular rolling motion steps when the body is homogeneous elastic-plastic: Step I $\dashrightarrow$ Contact loaded at $\delta x = -2a$, (a) rolling viewed in the plane $\mathcal{P}(y = 0)$, (b) rolling viewed in the transverse plane $\mathcal{P}(x = 0)$ centered on the heterogeneity; Step II $\dashrightarrow$ Rolling up to $\delta x = 0$, (c) rolling viewed in the plane $\mathcal{P}(y = 0)$, (d) rolling viewed in the transverse plane $\mathcal{P}(x = 0)$ centered on the heterogeneity; Step III $\dashrightarrow$ Contact unloaded at $\delta x = 2a$, (e) rolling viewed in the plane $\mathcal{P}(y = 0)$, (f) rolling viewed in the transverse plane $\mathcal{P}(x = 0)$ centered on the heterogeneity

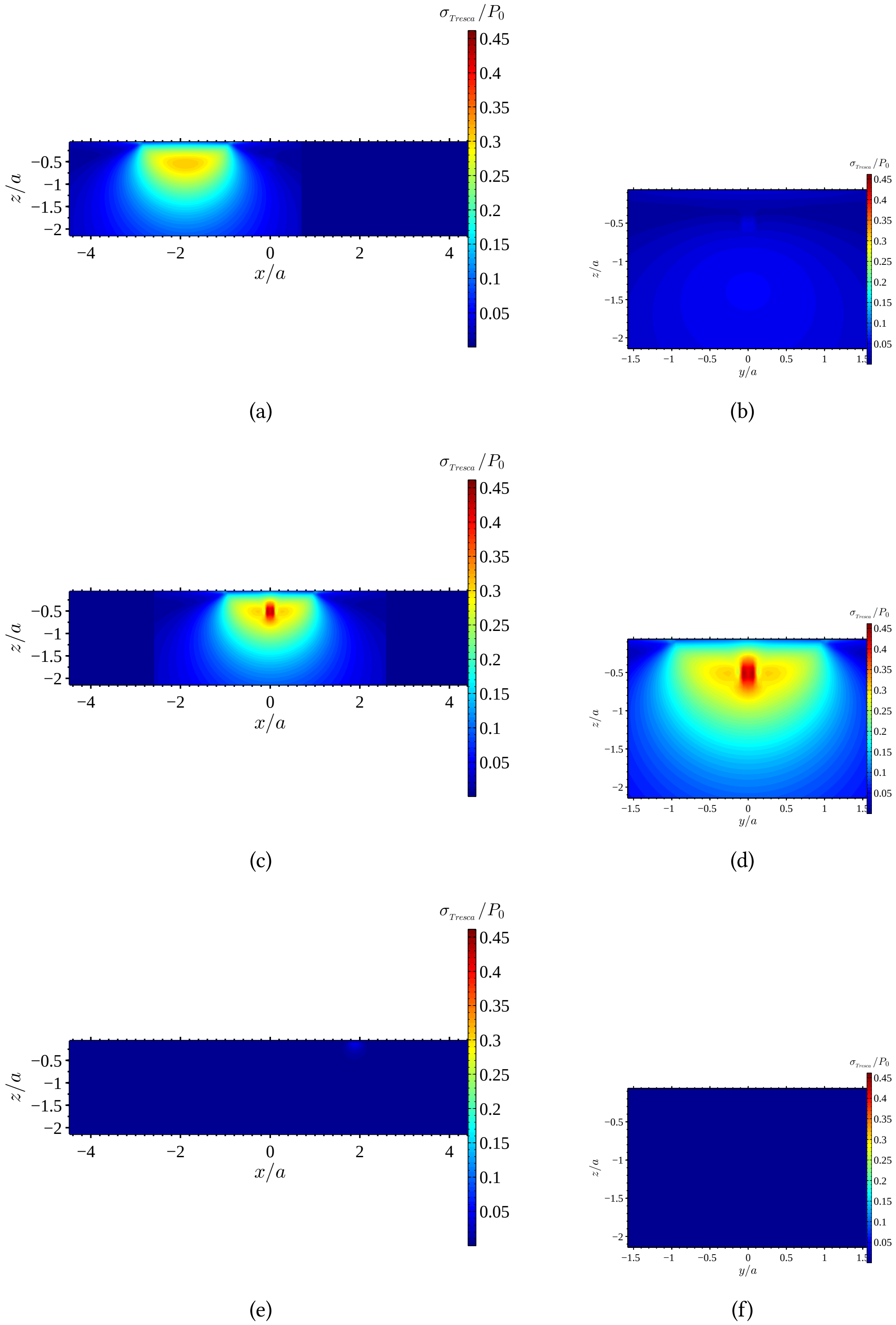

Figure 4.4: Evolution of the maximum shear stresses at particular rolling motion steps when the body is heterogeneous elastic: Step I ⇢ Contact loaded at $\delta x = -2a$, (a) rolling viewed in the plane $\mathcal{P}(y = 0)$, (b) rolling viewed in the transverse plane $\mathcal{P}(x = 0)$ centered on the heterogeneity; Step II ⇢ Rolling up to $\delta x = 0$, (c) rolling viewed in the plane $\mathcal{P}(y = 0)$, (d) rolling viewed in the transverse plane $\mathcal{P}(x = 0)$ centered on the heterogeneity; Step III ⇢ Contact unloaded at $\delta x = 2a$, (e) rolling viewed in the plane $\mathcal{P}(y = 0)$, (f) rolling viewed in the transverse plane $\mathcal{P}(x = 0)$ centered on the heterogeneity

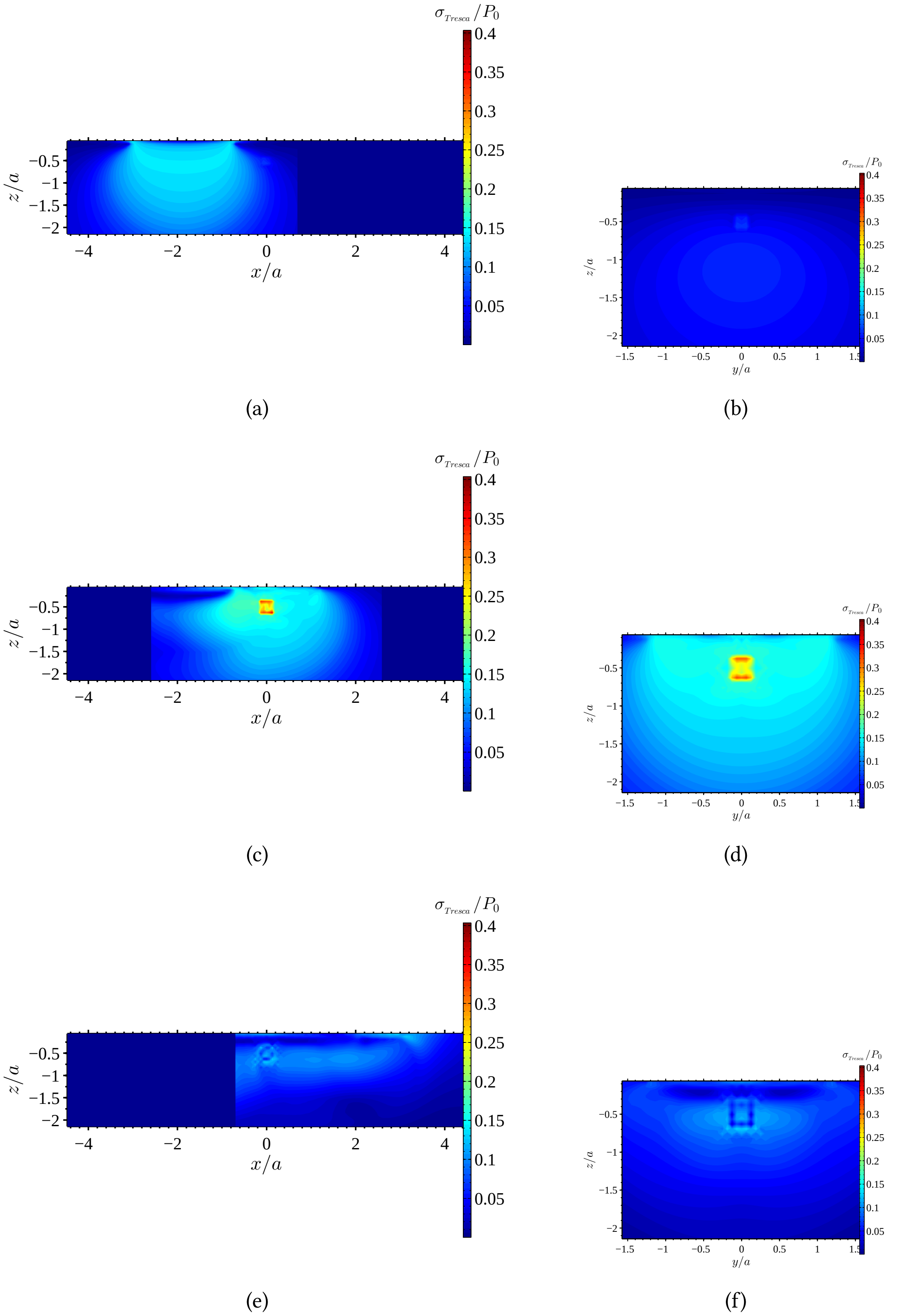

Figure 4.5: Evolution of the maximum shear stresses at particular rolling motion steps when the body is heterogeneous elastic-plastic: Step I $\dashrightarrow$ Contact loaded at $\delta x = -2a$, (a) rolling viewed in the plane $\mathcal{P}(y = 0)$, (b) rolling viewed in the transverse plane $\mathcal{P}(x = 0)$ centered on the heterogeneity; Step II $\dashrightarrow$ Rolling up to $\delta x = 0$, (c) rolling viewed in the plane $\mathcal{P}(y = 0)$, (d) rolling viewed in the transverse plane $\mathcal{P}(x = 0)$ centered on the heterogeneity; Step III $\dashrightarrow$ Contact unloaded at $\delta x = 2a$, (e) rolling viewed in the plane $\mathcal{P}(y = 0)$, (f) rolling viewed in the transverse plane $\mathcal{P}(x = 0)$ centered on the heterogeneity

For homogeneous elastic (HoE) body, Fig.4.2 shows a Hertzian distribution of the maximum shear stress moving with rolling load. This distribution is symmetrical with respect to the local contact vertical axis z_c as it can be observed in Fig.4.2 (a,c,d). The symmetrical distribution can also be noted for the heterogeneous elastic (HeE) body shown by Fig.4.4(a,c,d). But it turns out that in HeE case, the maximum shear stress level is raised up in the heterogeneity environment. The peak value is $\tau_{max} = 0.45P_0$ versus $0.31P_0$ noted in the HoE case. One can also point out that when the contact is applied at $\delta x = -2a$, in both HoE and HeE cases the shear stress field reaching the section plane $\mathcal{P}(x = 0)$ (where the heterogeneity is centered) is relatively very low (less than $0.1P_0$) as shown by Fig.4.2(b) and Fig.4.4(b). Also, because of the elastic behavior, the stress field vanishes after the unloading at the rolling motion end where $\delta x = 2a$ as illustrated by Fig.4.2 (e,f) and Fig.4.4(e,f). In contrast, if the substrate matrix is elastic-plastic one can observe the residual stress field distribution after the unloading in Fig.4.3(e,f) and Fig.4.5(e,f). When the body is heterogeneous elastic-plastic (HeEP), the maximum shear stress value is considerably high at the vicinity of the heterogeneity compared to the rest of the subsurface. Also, in this case the maximum shear stress is slightly high comparing against the homogeneous elastic-plastic (HoEP) case, regarding identical regions. As indication, the peak of τ_{max} is worth $0.15P_0$ in the HeEP case versus $0.1P_0$ in the HoEP case. Furthermore, Fig.4.2 versus Fig.4.3 and Fig.4.4 versus Fig.4.5 confirm that the stress field is more widely distributed within an elastic-plastic matrix than the elastic one. But the τ_{max} level is less within an elastic-plastic matrix than the elastic one. For guidance, the peak values are $\tau_{max}^{(HoE)} = 0.31P_0$ versus $\tau_{max}^{(HoEP)} = 0.16P_0$ and $\tau_{max}^{(HeE)} = 0.45P_0$ versus $\tau_{max}^{(HeEP)} = 0.4$. The presence of heterogeneity brings closer the elastic and elastic plastic cases maximum shear stress peaks. But a factor of three appears when one looks at their peaks difference as $(\tau_{max}^{(HoE)} - \tau_{max}^{(HoEP)} = 0.15P_0) = 3 \times (\tau_{max}^{(HeE)} - \tau_{max}^{(HeEP)} = 0.05P_0)$ indicating that the plastic strain ease three times the heterogeneity's reaction on the shear stress maximum magnitude. It should be pointed out from Fig.4.3(c) and Fig.4.5(c) that when the substrate matrix is elastic-plastic the symmetrical distribution around the local contact vertical axis z_c during the rolling is lost. This asymmetry is caused by permanent groove creation owing to the surface permanent deformation as well as subsurface plastic strain occurrences. From Fig.4.3(e,f) and Fig.4.5(e,f), the residual stress field distribution reveals a free shear stress area of $0.2a$ thickness, $2a$ width and $D_x + 2a$ length [b] confined between a stressed surface layer of $0.1a$ thickness and the stressed subsurface. It must be emphasized that the free shear stress area is completely surrounded by the residual stress zone.

[b] *D_x is the total rolling distance. This is not completely identified in Fig.4.3(e) and Fig.4.5(e) because they considered current computational zone has $5a$ length. The current computational zone is, at each time step moved, in consistency with to the rolling motion*

4.2.5 SUBSURFACE EQUIVALENT PLASTIC STRAIN DURING THE ROLLING

The evolution of the maximum equivalent plastic strain in the homogeneous matrix and heterogeneous is compared in Fig.4.6 during the rolling contact. It could be noticed that the presence of heterogeneity leads to plastic strain increasing starting from $\delta x = -0.4a$. The heterogeneity semi-length is $S_i = 0.1a$ [c] . The plastic strain continues to increase until it holds a steady magnitude from $\delta x = a$ to the motion end. The difference of the plastic strain peaks obtained between the homogeneous and heterogeneous matrix is called here the *over-plasticity* and is $\varepsilon_{max}^{p\,(He)} - \varepsilon_{max}^{p\,(Ho)} = 0.5\%$ knowing that the heterogeneity is 2.33 times stiffer than the substrate matrix.

[c] *see more detail about the heterogeneity in the table attached to Fig.4.6*

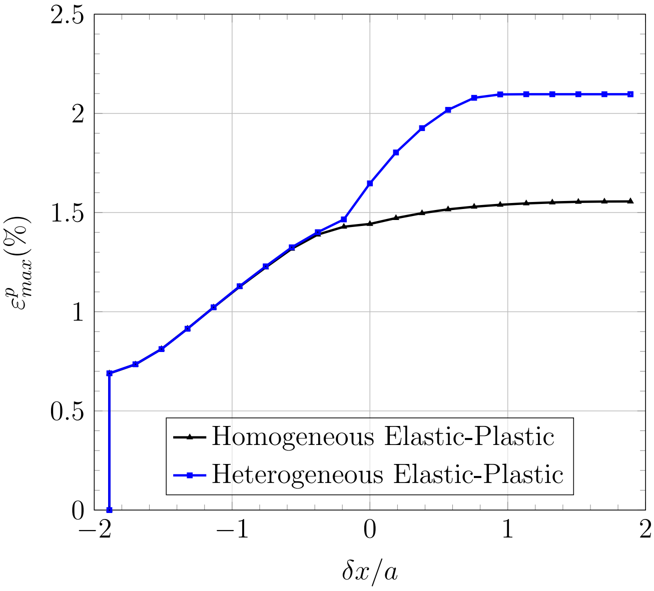

Heterogeneity parameters	value
Size	$S_i = 0.1a$
Location	$z_i = 0.3a$
Elastic modulus	$E_I = 490GPa$

Figure 4.6: Subsurface equivalent plastic strain during the rolling

4.3 PARAMETRIC STUDY

Owing to the given number of parameters involved in the Heterogeneous Elastic Plastic Rolling Contact (HEP-RC) analysis, sub-problems were treated distinctly. The regarded parameters have been studied independently and then in a combined way. One focus on parameters related to the heterogeneity's nature, size, location, cluster, stringer orientation and mutual influence.

4.3.1 INFLUENCE OF HETEROGENEITY PARAMETERS

Let's consider a heterogeneity having cuboidal shape with a semi-length S_i, centered at the depth z_i beneath the surface and having an elastic modulus E_I.

4.3.1.1 Heterogeneity location effect

Suppose that the heterogeneity described above is, for instance, a Vanadium carbide 2.33 times harder than the substrate matrix ($E_I = 490GPa$ and $E_m = 210GPa$). Let's vary its center location $z_i = \alpha a$ to examine the consequence on the surface pressure and the subsurface stress-strain fields during the rolling contact. Four depths $\alpha = 0.3$, 0.5 , 0.8 and 1.5 are chosen hereafter in purpose to relate the interpretations issued from these simulations to some typical position noticed in practice. Thereby, $\alpha = 0.3$ stands for a carbide close to the surface, $\alpha = 0.5$ for carbide centered at the Hertzian depth, $\alpha = 0.8$ corresponds to a carbide located far from the surface but belongs to a region influenced by the rolling stress and finally $\alpha = 1.5$ simulating a carbide located far from the Hertzian depth and relativity less influenced by the rolling stress.

Contact pressure evolution according to heterogeneity location

Fig.4.7 reveals that the heterogeneity location which steps up the contact *overpressure* value corresponds to $\alpha = 0.3$. A small value of the *over-pressure* is found when the carbide is located at the Hertzian depth $\alpha = 0.5$. Then, for carbides located from $\alpha = 0.8$ their maximum contact pressure profiles coincide with the homogeneous one, regardless if the substrate matrix is elastic or elastic-plastic. Let's recall that the good knowledge of the contact pressure field is essential to design the tolerable efforts of the rolling elements contacting surfaces.

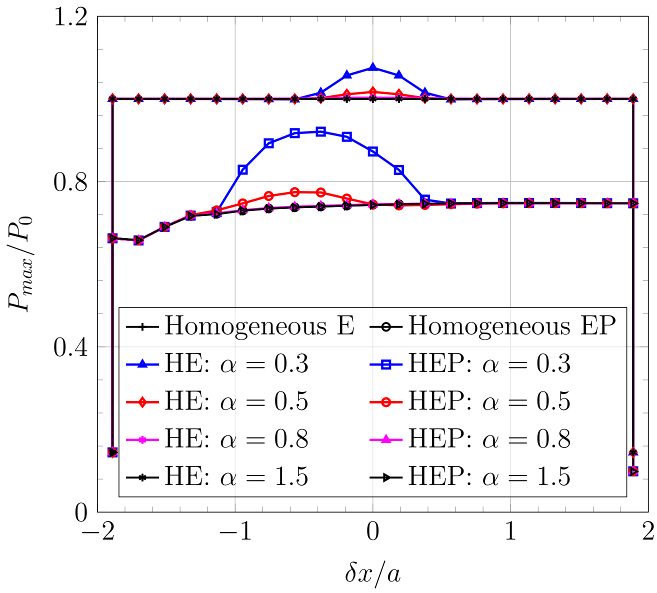

Heterogeneity parameters	value
Size	$S_i = 0.1a$
Elastic modulus	$E_I = 490GPa$

Figure 4.7: Contact pressure evolution according to heterogeneity location

Maximum shear stress evolution according to heterogeneity location

It has been observed experimentally that the location of the maximum shear stress is identical to the maximum predicted damage location. To this end, the maximum shear stress evolution is presented in Fig.4.8 for different values of α. It brings out that the carbide centered on the Hertzian depth $\alpha = 0.5$ produced the highest *overstress*, regardless if the substrate matrix is elastic or elastic-plastic. Let's specify that the depth $\alpha = 0.3$ and 0.8 induced a sharper *overstress* in the elastic case than the elastic-plastic one. When the substrate matrix is elastic, from $\alpha = 1.5$ the carbide generates a quasi-nil *overstress* and the maximum shear stress evolution is almost the same as that of the homogeneous case, see Fig.4.8(a). But when the substrate matrix is elastic-plastic, the *overstress* generated is about $\tau_{max}^{(HeEP)} - \tau_{max}^{(HoEP)} = 0.04P_0$. The carbide effect must not be neglected since its presence disturbs the stress field along a certain distance $D_i^{(\tau)}$ [a], see Fig.4.8(b). This is because the residual stress generated during the rolling contributes to increase the subsurface total stressed zone. Hence the carbide located deep down at $\alpha = 1.5$ becomes subjected to the total stress field even if that location was a *stress-free* zone in the homogeneous case. It could be noticed that the final residual stress is slightly higher when the carbide is close to the surface ($\alpha = 0.3$) than the other locations. The residual stress value obtained for $\alpha = 0.5$ and for $\alpha = 0.8$ are almost matched.

[a] $D_i^{(\tau)}$ *Shear stress disturbance distance created by the inhomogeneity relative to the evolution in the homogeneous case*

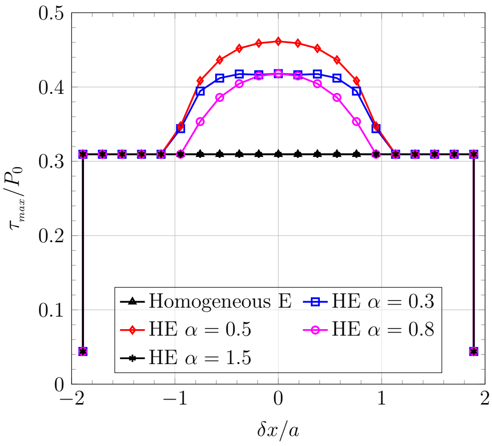

(a)

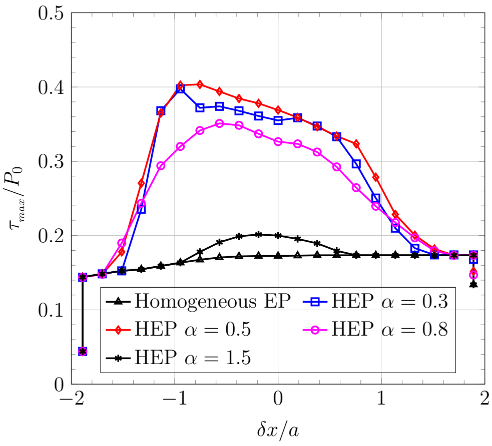

(b)

Figure 4.8: Maximum shear stress evolution according to heterogeneity location: (a) Elastic; (b) Elastic-plastic

Equivalent plastic strain evolution according to heterogeneity location

Looking to the maximum plastic strain plotted in Fig.4.9 during the loading, one could establish that the values reached at the steady state decrease when the carbide is getting located deeper and deeper. It holds that from $\alpha = 1.5$ the presence of the carbide did not affect the plastic strain evolution and its trend is similar to that of the homogeneous body. Table 4.2 lists the *over-plasticity* according to z_i and one can underwrite that ε^p_{max} is not linearly dependent to the carbide location.

Table 4.2: Maximum plastic strain peaks during rolling

Carbide location $z_i = \alpha a$	Maximum plastic strain peaks $Max\left(\varepsilon^p_{max}\right)$
$z_i = 0.3a$	2.3
$z_i = 0.5a$	2.1
$z_i = 0.8a$	1.75
$z_i = 1.5a$	1.55

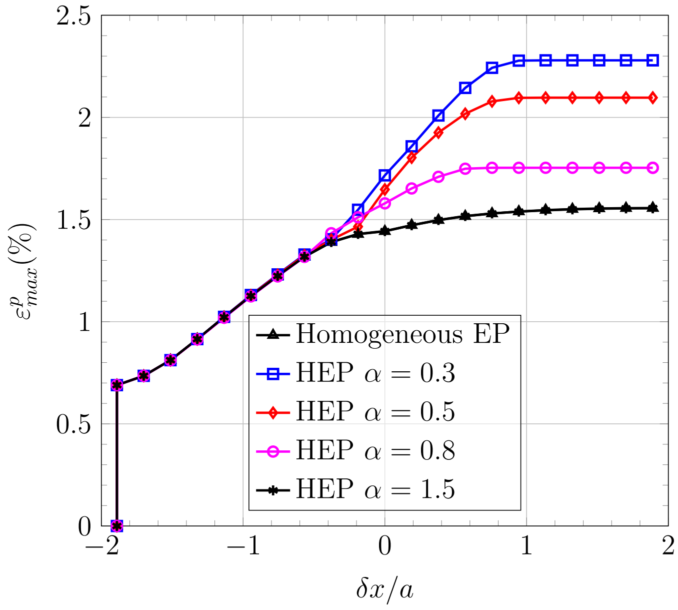

Figure 4.9: Equivalent plastic strain evolution according to heterogeneity location

4.3.1.2 Heterogeneity size effect

One is interested in the effect of Vanadium carbide size $S_i = \beta a$ on the contact pressure, subsurface stress and strain fields under the rolling load. Hereabout, four sizes are considered as $\beta = 0.05$, 0.1 , 0.2 and 0.4. The size $S_i = 0.05a$ replicates the very small inter-granular carbide precipitates found in typical nitrided M50 microstructure and the size $S_i = 0.1a$ approximates the average carbide size mostly found. It is worth reminding that the Hertzian contact radius $a = 60\mu m$ is kept the same all over the study. Larger sizes $S_i = 0.2a$ and $0.4a$ are used to simulate a heap of condensed carbides. All those carbides are centered at the Hertzian depth $z_i = 0.5a$.

Contact pressure evolution according to heterogeneity size

First of all, Fig.4.10 indicates that the carbide size strongly influences the maximum of the contact pressure during the rolling. The size effect is more noticeable than the position effect in accordance with Fig.4.10 against Fig.4.7. For an elastic-plastic matrix the contact pressure can achieve the Hertzian pressure peak P_0 when the carbide size is $z_i = 0.2a$. If the body is homogeneous, the contact pressure reaches $P_{max} = 0.72P_0$. More critical, when $z_i = 0.4a$ the pressure peak noted in the elastic-plastic case is greater than the one in the elastic case. In terms of meaningful value, a heap of condensed carbides with a size of $z_i = 0.4a$ located at $z_i = 0.5a$ can almost double the contact pressure maximum, since the body behaves plastically. One can add that the pressure disturbance distance created by the carbide is spread over $D_i^{(P)} = 2.4a$ which corresponds to three times the carbide length. In general, the *over-pressure* increase whereas the carbide size grows up regardless if the substrate matrix is elastic or elastic-plastic. But in particular, when the carbide size is $\beta = 0.1$ the *over-pressure* generated staring to be quite small, then from size less than $\beta = 0.05$ the maximum pressure is almost confounded with the homogeneous case.

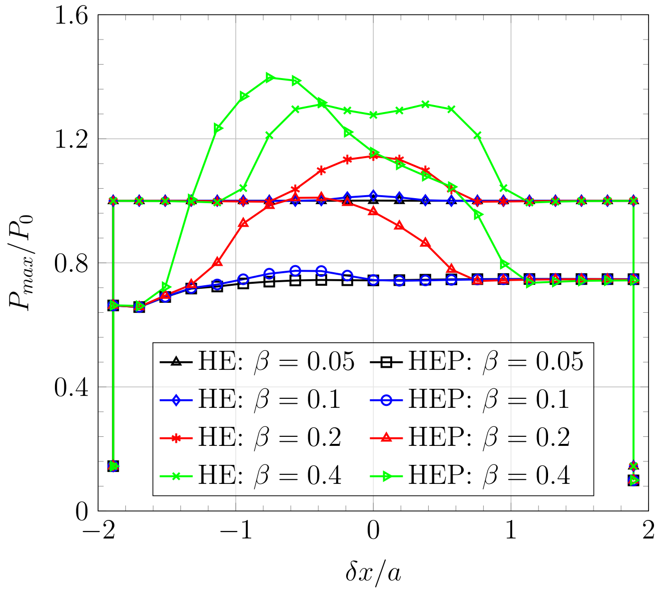

Heterogeneity parameters	value
Location	$z_i = 0.5a$
Elastic modulus	$E_I = 490GPa$

Figure 4.10: Contact pressure evolution according to heterogeneity size

Maximum shear stress evolution according to heterogeneity size

From Fig.4.11 one can note that, the maximum shear stress is arising when the carbide size is increasing, regardless if the substrate matrix is elastic or elastic-plastic. Unlike the pressure fields, the stress is widely affected by even the smallest carbide sizes considered here. Hence, Fig.4.11(b) shows that the peak reached by the maximum shear stress owing to $\beta = 0.05$ sized carbide is more than twice the value reached in the homogeneous case, when the matrix is elastic plastic. The worst case encountered here is when $\beta = 0.4$ where the peak of the maximum shear stress is trice the homogeneous one. Then, the residual stress after the loading is $\tau_{max} = 0.32P_0$. This maximum value of the residual shear stress remaining after the unloading becomes even greater than maximum shear stress with which the bulk might be designed using homogeneous elastic theory. The present result justifies claims advocating that high residual stress could be responsible for the lost cohesion between the carbide and the substrate matrix even when the body is no more subjected to the rolling load.

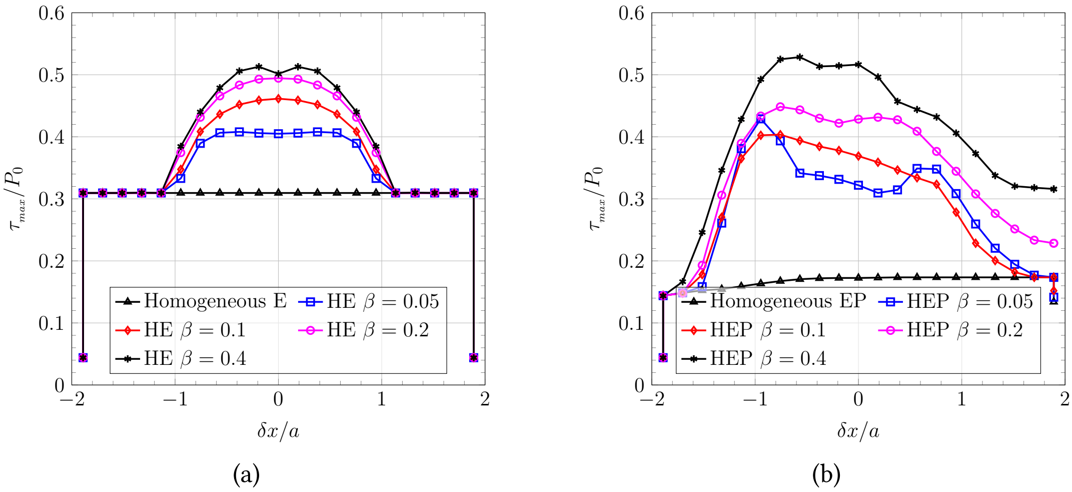

Figure 4.11: Maximum shear stress evolution according to heterogeneity size: (a) Elastic; (b) Elastic-plastic

Equivalent plastic strain evolution according to heterogeneity size

Fig.4.12 reveals that the maximum plastic strain increase with the size until $\beta = 0.2$. Then when $\beta = 0.4$ there is an abnormality in the maximum plastic strain trend in concordance with the one observed for other sizes. The maximum plastic strain peak reached for $\beta = 0.4$ is less than the one noted for the other sizes when the rolling contact is moving from $\delta x = -a$ to $\delta x = 0$. Also the steady value reached when $\beta = 0.4$ is smaller than when $\beta = 0.1$ and $\beta = 0.2$. One can tempt to relate this observation to the fact that when a certain amount of deformation energy is subjected to the heterogeneous elastic plastic body via the contact, one part is absorbed by the heterogeneity and the substrate matrix, another part is dissipated in a form of plastic strain. The heterogeneity reaction leads to a redistribution of the absorbed energy according to its property, location and shape. Inside the matrix's region where the energy was redistributed, local concentration of *overstress* appears as a function of heterogeneity size. Then according to how the *over-stress* is focused, the stress state could be favorable to generate additional plastic flow or be balanced by the residual stress released by the existing plasticity. But it is sure that residual stress benefit effect is bounded according to the stress state as well as the heterogeneity reaction relative to its size. It should be kept that for all cases the steady is reached from $\delta x = a$. Also when the rolling contact center is behind $\delta x = -a$, the maximum plastic strain evolution is indistinct to the homogeneous case regardless the carbide size.

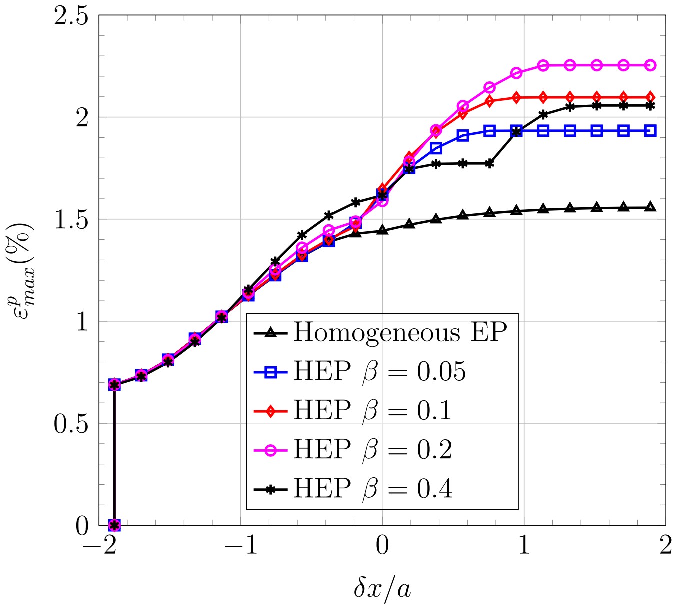

Figure 4.12: Equivalent plastic strain evolution according to heterogeneity size

4.3.1.3 Elastic properties effect

The heterogeneity properties effect on the rolling contact behavior, has an important role in the comprehension of the damage mechanisms related to the interactions between plasticity and heterogeneity. Different heterogeneity natures are modeled by varying the elastic properties. A porosity is considered as a material with nil Young's modulus, an incompressible heterogeneity is set by a Poisson ratio of 0.5 and a stiff heterogeneity or carbide is modeled by the ratio γ of its Young's modulus and the substrate matrix one.

Maximum shear stress evolution according to heterogeneity material property

The maximum shear stress evolution is presented in Fig.4.13. The heterogeneity size is set to $S_i = 0.1a$. In order to distinguish the material responses, when the heterogeneity is close to the surface from when it is centered in the Hertzian depth, two locations $z_i = 0.3$ and $z_i = 0.5$ are considered, respectively. If the heterogeneity is taken as a porosity, Fig.4.13(a) shows that when the substrate matrix is elastic, the maximum shear stress reached a peak of $\tau_{max} = 0.48P_0$ for $z_i = 0.3$ and a slightly lower value of $\tau_{max} = 0.47P_0$ for $z_i = 0.5$. But when the substrate matrix is elastic-plastic, the maximum shear stress magnitudes as well as the difference between each case's magnitudes, become significant. This is confirmed in Fig.4.13 (b), where the maximum shear stress reached a peak of $\tau_{max} = 0.72P_0$ for $z_i = 0.3$ and $\tau_{max} = 1.16P_0$ for $z_i = 0.5$. These values also correspond to the residual stress after the unloading. Let's recall that the results of these simulations are intended to provide an accurate stress-strain data to support optimal design when dealing with functional materials having heterogeneous microstructures. The aim is to reduce the needs of safety coefficients or life reduction factors often put in front of fatigue resistance formulas in order to adjusted predictions on test results. This provides a more realistic endurance limit since it is accepted that the phenomena incarnated by those reduction factors may interact then cause aliasing issues during tests attempting to record the proper value of each factor. Considering the incompressible heterogeneity case, it could be noticed that when the substrate matrix is elastic-plastic, the maximum shear stress evolution is close to the porosity case one, until the moving contact reached $\delta x = 0.4a$, regardless the heterogeneity position. But from the steady stress state to the unloading, the maximum shear stress peak is less than the porosity case one. One can identify that $\tau_{max} = 0.58P_0$ for $z_i = 0.3$ and $\tau_{max} = 0.96P_0$ for $z_i = 0.5$. Regarding the maximum shear stress, for the same setting (position, shape, size), the porosity and the incompressible heterogeneity are more critical than the stiff heterogeneity [b] .

[b] *the stiff heterogeneity corresponds here to a Vanadium carbide which $\gamma = 2.33$ times harder than the substrate matrix*

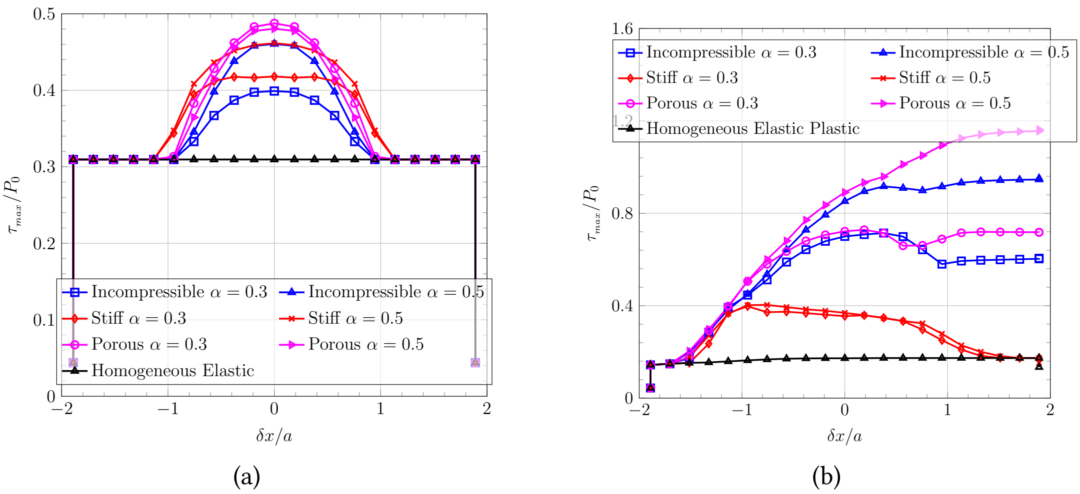

Figure 4.13: Maximum shear stress evolution according to heterogeneity material property: (a) Elastic; (b) Elastic-plastic

Equivalent plastic strain evolution according to heterogeneity material property

The maximum equivalent plastic strain presented in Fig.4.14 confirms that, for the same configuration (position, shape, size), the porosity and the incompressible heterogeneity produced more *over-plasticity* than the stiff heterogeneity. The highest plastic strain is generated when the heterogeneity is incompressible and located close to surface ($z_i = 0.3a$). This observation can be explained by the fact that this incompressible heterogeneity had the lowest *overstress* in the elastic case presented in Fig.4.13(a). The contrast installed is that, knowing the *overstress* produced in the elastic case, one might be tempted to predict that incompressible heterogeneity would have less plastic strain in the elastic-plastic case. Whence this type of reasoning, often encountered, could be sometimes misleading. Knowledge of the stress behavior in an elastic framework is not fully sufficient to make predictions about the behavior of plastic strain in a similar elastic-plastic framework. Furthermore it should be kept that when the rolling contact center is behind $\delta x = -a$, the maximum plastic strain evolution is consistent with the homogeneous case regardless the heterogeneity material property.

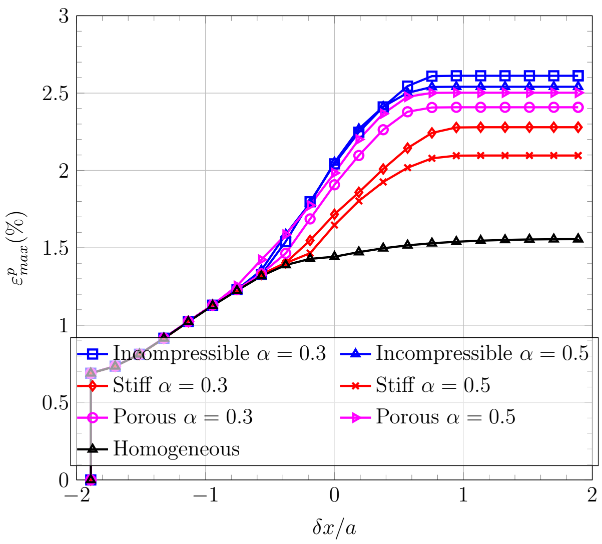

Heterogeneity parameters	Value
Size	$S_i = 0.1a$
Location	$z_i = 0.3a$ and $z_i = 0.5a$
Incompressible	$E_I = 2.2GPa$; $\nu_I = 0.5$
Stiff	$E_I = 490GPa$; $\nu_I = 0.3$
Porous	$E_I = 0GPa$; $\nu_I = 0.3$

Figure 4.14: Equivalent plastic strain evolution according to heterogeneity material property

Fatigue analysis by Dang Van crack initiation criterion

One is interested in the local behavior around the heterogeneity. Fig.4.16 and Fig.4.17 present the diagram of maximum shear stress evolution versus the hydrostatic pressure on some particulars fixed points around the heterogeneity during the rolling motion. Two lines are plotted in Figures, the horizontal line corresponds to $\tau_{max} = 0.31P_0$ standing for the Hertzian maximum shear stress and the vertical line corresponds to $\sigma_{HP} = 0$ separating the compression state by negative values on his left to the tension state by positive values on his right.

This part consists to give a key point to perform a coarse fatigue analysis of damage likelihood according to heterogeneity material property. Dang Van criterion is used to investigate on the critical point where crack may firstly initiate and grow in accordance relationship with the stress state in the heterogeneity environment. It is well known that once crack has initiated, the expected number of cycles to failure could be no longer held. The criterion recalled in Eq.(4.1) is an inequality related to the mesoscopic shear stress and hydrostatic stress at all instants t of the cycle, so that damaging loads can be precisely characterized.

$$\underset{i}{MAX}\{\tau_{max}(t) + a_{DV}.\sigma_{HP}(t)\} \leqslant b_{DV} \tag{4.1}$$

Where $\tau_{max}(t)$ and $\sigma_{HP}(t)$ are the time-dependent values of mesoscopic shear stress and hydrostatic pressure, respectively. Note that a is a positive dimensionless constant incarnating the effect of the hydrostatic pressure determined by $a_{DV} = 3(b_{DV} - 0.5b_{\infty})/b_{\infty}$, where b_{∞} stands for the bending fatigue test endurance limit. Then $b_{DV} = t_{\infty}$ represents the endurance limit t_{∞} of the employed material in pure shear under torsion fatigue test. Hills and coworkers [111] demonstrated how a_{DV} and b_{DV} could also be related to the yield stress σ_Y and the ultimate tensile stress σ_{UTS} as:

$$a_{DV} = \frac{2\sigma_0}{2(\sigma_* - \sigma_0)} \; ; b_{DV} = \frac{\sigma_* \dot{\sigma}_0}{2(\sigma_* - \sigma_0)}; \text{ where } \sigma_* = \sigma_Y \text{ or } \sigma_{UTS} \tag{4.2}$$

Having noticed that the parameters required for Dang Van's line representation are strongly dependent on the material and cannot be chosen arbitrarily. In other to support interpretations stated here, the Dang van's line was taken from Nelias and Antaluca [112] study when they evaluate the contact risk zone in rolling on dented surface. This representation stands for AISI 52100 steel having a similar elastic-plastic behavior as the material modeled here, where $a_{DV} = 0.299$ and $b_{DV} = 0.32P_0$. The Dang Van's line is plotted in Fig.4.16 and Fig.4.17 as the fatigue threshold during the HEP-RC and it splits the $\tau_{max} \leftrightarrow \sigma_{HP}$ stresses space across load paths. The region below the line $(\tau_{max}(t) + a_{DV}.\sigma_{HP}(t) = b_{DV})$ constitutes the safe area where crack is not expected. Conversely, the region above that line is considered as the failure risk area. Now the risk of fatigue can be evaluated for each heterogeneity edge points at all rolling instants.

The observed points are localized in the local referential centered on the heterogeneity illustrated by Fig.4.16(e) and Fig.4.17(c). These latter sub-figures are surrounded by sub-figures presenting the results associated with the observed points located between their centers and the heterogeneity center. For instance, the sub-figure Fig .4.16(a) is associated to the observed point $M(-1, 0, 1)$ and the sub-figure Fig.4.16(f) is associated to the observed point $M(1, 0, 0)$. The consistency between sub-figures and theirs associated targeted points, which are observed at each time step of the motion, is fully detailed in Fig.4.16 and Fig.4.17 captions.

In the first place, it could be noticed in Fig.4.16 and Fig.4.17 that the homogeneous elastic-plastic (HoEP) body is in a compression state and the maximum shear stress is less than $\tau_{max} = 0.31P_0$ regardless the targeted point during the rolling motion. The body behavior is the same if the targeted points are observed at the depths $z_i = 0.3a$ and $z_i = 0.5a$. The residual stress remains in compression state after the unloading. Now in the presence of stiff heterogeneity (Vanadium carbide), all the targeted points located at the heterogeneity bottom undergo a residual tensile stress, Fig.4.16(g,h,i) and Fig.4.17(d,e). But the residual stress levels in these places are relatively low. The maximum shear stresses are coming close to $\tau_{max} = 0.08P_0$ and the hydrostatic pressures almost reached $\sigma_{HP} = 0.16P_0$. Yet in the same locations, if the heterogeneity is incompressible, the residual stress, still being in tensile state and it reveals a significant high levels exceeding $\tau_{max} = 0.31P_0$. Knowing that tensile state tends to open the cracks during rolling, this becomes a main issue for bearing product developers when some defaults are unavoidable inside the materials due to the manufacturing process. Regarding the targeted point $M(1, 1, 1)$, Fig.4.17(b) shows that porosity located at the Hertzian depth generates an elevated maximum shear stress peak beyond three times the Hertzian stress. Also the hydrostatic pressure is found in tensile state and is worth $\sigma_{HP} = 0.4P_0$. Dang Van criterion indicates a likely damage at that location as well as at the targeted point $M(-1, 1, 1)$.

Having found that incompressible heterogeneity and porosity attest severity than the carbide, it is worthwhile now to define a critical instant which represents the moment of loading step or even the number of cycles, when the $(\tau_{max}(t), \sigma_{HP}(t))$ stress tra-

jectory crossed the fatigue threshold. Hence it appears that in all regarded cases the points around the porosity passed the critical instant before the incompressible heterogeneity.
In addition, it should be specified that the body with carbide presents higher stress levels compared to the homogeneous body. Then an underestimation of the role of the heterogeneity nature may turn out to be risky for the material. As guidance, one can argue that rolling bearing lifetimes could be improved when materials are designed according to parameters a_{DV} and b_{DV} which directly influence the resistance to likely damage related to the presence of heterogeneity. The frontier of the critical instant could be lifted by increasing the slope a_{DV}. Also it is possible to shift upward the fatigue threshold by augmenting b_{DV}. However, being aware that the aforementioned recommendation is not a trivial task in practice for designers to act on these parameters, another existing solution consists to lower the $(\tau_{max}, \sigma_{HP})$ stress levels. Forthcoming section will demonstrate how a certain quantity of initial compressive stress along with the yield stress could be beneficial for the fatigue life.
For example, let's put the analysis wording here in conceivable situation. During rolling cycles, the tensile stress generated at a carbide interface could be conducive to a loss of cohesion with the substrate matrix. This appearing void could be simulated in principle as a porosity. Yet, the porosity leads to a more critical stress level. Finally, the material would end up with starting cracks. In addition, assuming that, when the porosity is close to the surface, it can be infiltrated by the lubricant by the bias of grain boundaries defects or microcrack connected to the surface, then the filled void could be seen as an incompressible heterogeneity. The latter situation, even unlikely, would speed up the damage than the last one because the shear stress and hydrostatic pressure levels should become higher, according to the results discussed above and supported by Fig.4.16 and Fig.4.17. It should be noted that, in the literature, only few investigations discussed about porosity infiltrated by lubricant. One can cite the works of Bold [113], Fletcher [114] and Bogdanski [115] which encountered the oil entrapment via inclined crack in the elastohydrodynamic lubrication contact problem. The fluid is drained by the dynamic pressure during the flow as illustrated by Fig .4.15. An incompressible heterogeneity close to the surface is an alternative to model this configuration.

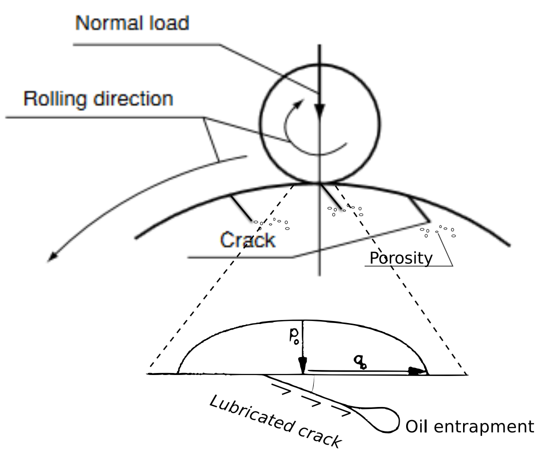

Figure 4.15: Oil entrapment in lubricated crack

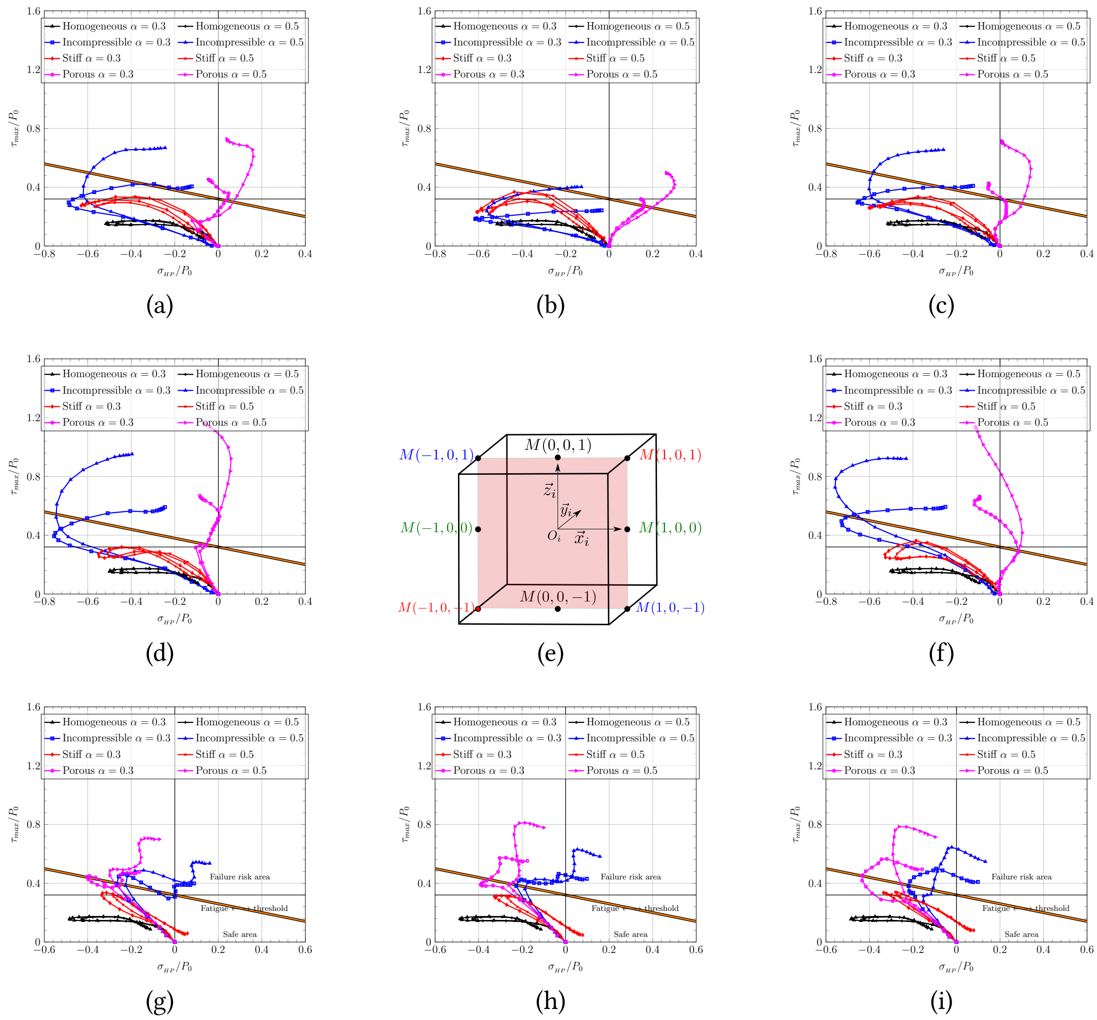

Figure 4.16: Maximum shear stress versus hydrostatic pressure evolution according to heterogeneity material property: (a) heterogeneity edges point $M(-1,0,1)$; (b) heterogeneity edge point $M(0,0,1)$; (c) heterogeneity edge point $M(1,0,1)$; (d) heterogeneity edge point $M(-1,0,0)$; (e) heterogeneity referential and edge points locations; (f) heterogeneity edge point $M(1,0,0)$; (g) heterogeneity edge point $M(-1,0,-1)$; (h) heterogeneity edge point $M(0,0,-1)$; (i) heterogeneity edge point $M(1,0,-1)$

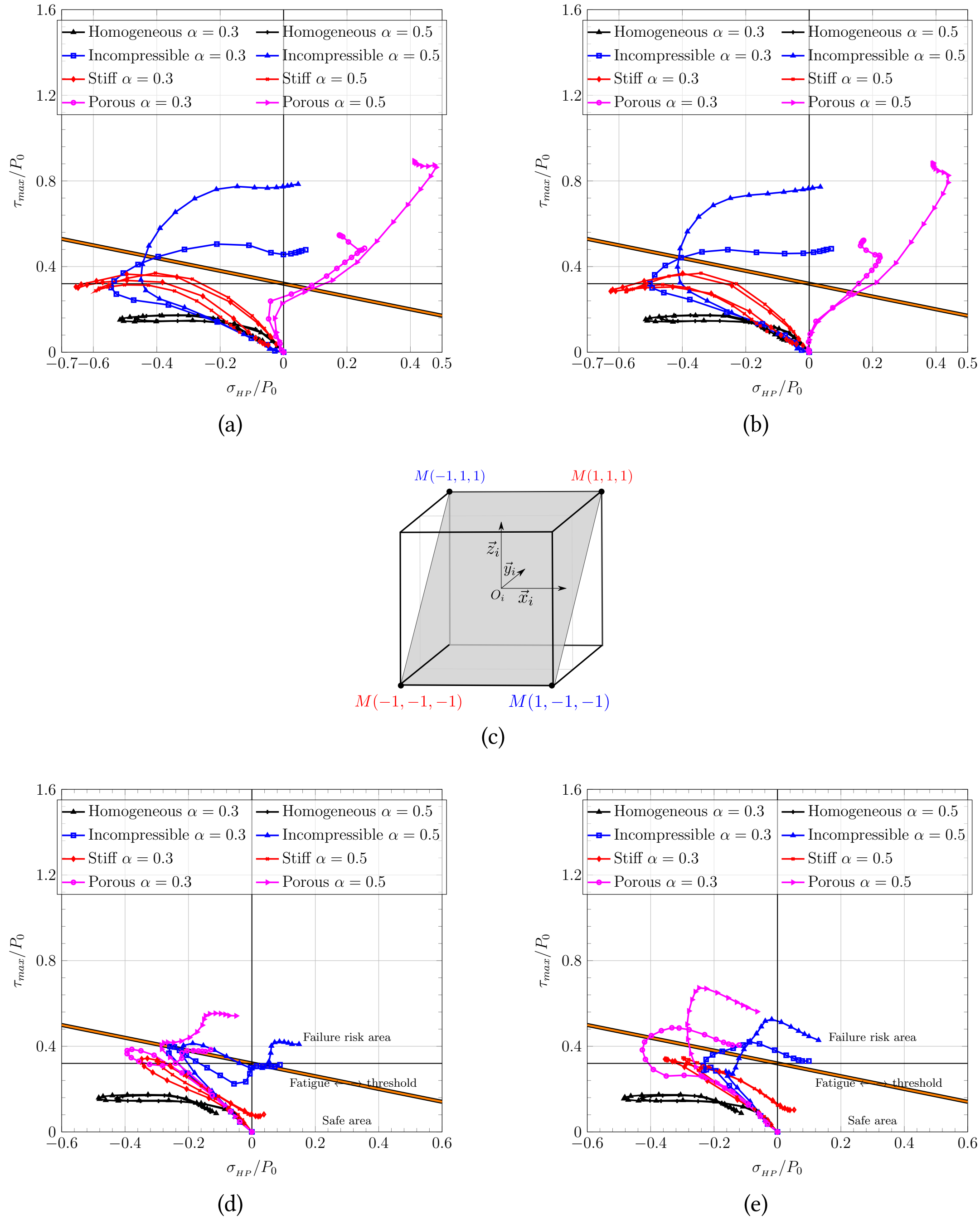

Figure 4.17: Maximum shear stress versus hydrostatic pressure evolution according to heterogeneity material property:(a) heterogeneity edges point $M(-1,1,1)$; (b) heterogeneity edge point $M(1,1,1)$; (c) heterogeneity referential and edge points locations; (d) heterogeneity edge point $M(-1,-1,-1)$; (e) heterogeneity edge point $M(1,-1,-1)$

Eigenstress generated by a porosity and a carbide

The eigenstress in Eshelby's sense generated by a porosity and a carbide are compared under the same rolling conditions to confirm the porosity critical nature in front of the carbide one. Fig.4.18 presents the eigenstress as the additional elastic stress in reaction to the eigenstrain undergone by the heterogeneity subjected to external load. Three heterogeneity locations are considered as $z_i = 0.3a$, $0.5a$ and $0.8a$. The subfigures Fig.4.18(a,b,c,d) correspond to different sizes $S_i = 0.05a$, $0.1a$, $0.2a$ and $0.4a$, respectively. Note that the substrate matrix is elastic. A general view shows that the eigenstress generated by a porosity had a higher magnitude than the carbide one whatever their chosen sizes and locations. It can be seen in particular that, even the smallest sized porosity in Fig.4.18(a), regardless its location in depth, produces more eigenstress than any larger sized carbide in Fig.4.18(b,c,d), located at any depth except when the carbide appears at the surface as the one labeled by $z_i = 0.3a$(C) in Fig.4.18(b) legend. The eigenstress associated to a porosity of size $S_i = 0.4a$ at the depth $z_i = 0.3a$ was not fully shown in Fig.4.18(d) because it corresponds to an emerging porosity. In practice, this configuration simulates a perforated surface under a rolling. This causes a convergence issue in the computation since the rolling pitch is $0.02a$ which is much less than that surface misfit hole length. But no issue occurred for the carbide located at the same place and having the same size, because the carbide implies a presence of matter in contrast to the porosity which represents a void. One can discern from Fig.4.18(c,d) that the eigenstress induced by a carbide sized $S_i = 0.4a$ appearing in the surface with $z_i = 0.3a$, is almost equivalent to the on induced by a porosity half-sized $S_i = 0.2a$ located far from the surface with $z_i = 0.8a$.

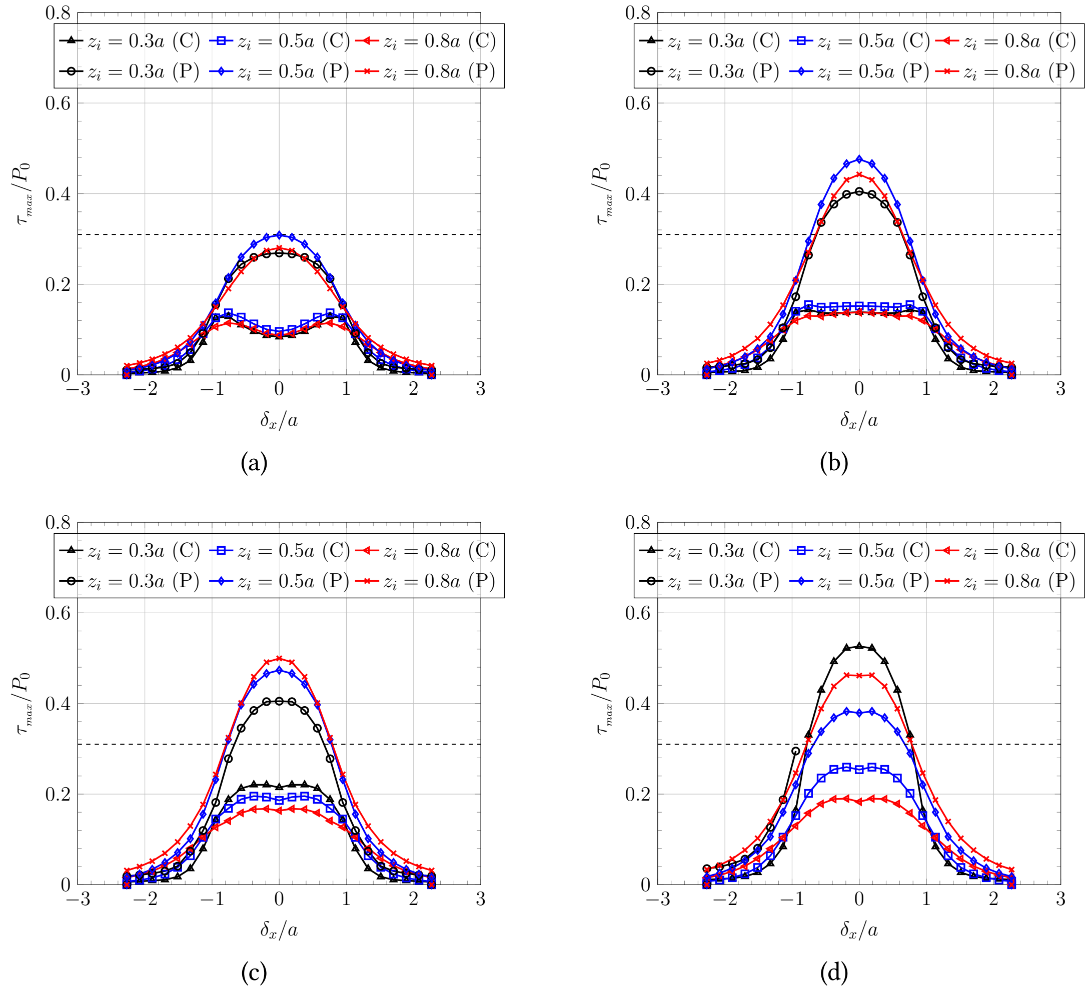

Parameter	value
Heterogeneity size	from $S_i = 0.05a$ to $S_i = 0.4a$
Heterogeneity location	from $z_i = 0.3a$ to $z_i = 0.8a$
Carbide Heterogeneity material property	$E_I = 490GPa$ and $\nu_I = 0.3$
Porosity Heterogeneity material property	$E_I = 0GPa$ and $\nu_I = 0$

Figure 4.18: The additional overstress criticality of porosity versus carbide according to the location and size : (a) size $S_i = 5a/100$; (b) size $S_i = a/10$; (c) size $S_i = 2a/10$; (d) size $S_i = 4a/10$

4.3.2 EFFECT OF DISTRIBUTED HETEROGENEITY MUTUAL INFLUENCE

Having studied a single heterogeneity, now, one is interested in gathered heterogeneities. Let's recall that in bearing materials as M50, the carbide stringers preferentially orientation is managed by the mechanical processing (forging, rolling). Also the carbides cluster characteristics can evolve depending on the thermo-chemical treatment (case hardening, quenching, nitriding) instructions. Thus knowledge of the consequences associated with each variety of stringers and cluster allows to master the choice of parameters that control the processes to improve and tailor the materials according to its future functions and resistance expected in service.

Stringer distribution

Three heterogeneities are arranged along an axis passing through their centers. They are set by a variable angle θ relative to the rolling direction. Each heterogeneity which composing the stringer sizes $S_i = 0.1a$. The heterogeneity close to the surface is centered at $z_i = 0.3a$. The distance d_i between each heterogeneity center allows to control their mutual influence. When $d_i = 2S_i$ then heterogeneities touch each other but if $d_i = 3S_i$ then they interact through the substrate matrix that is settled between them. One considered four particular orientations mainly observed in the studied materials. When the value of θ is $0°$ and $90°$ then the cluster is parallel and perpendicular to the rolling direction,respectively. The orientations $\theta = 45°$ and $\theta = -45°$ approximate the most current stringers formed during intra-granular migration of segregated carbides and nitrides during heat treatment.

First of all, based on Fig.4.19, one can argue that during the Heterogeneous Elastic Plastic Rolling Contact (HEP-RC), the maximum pressure, shear stress and plastic strain are dependent on the stringer orientation θ and the interaction distance d_i. The magnitude of the maximum contact pressure depends not only on the individual heterogeneity close to the surface. Fig.4.19(a) claims that each heterogeneity composing the stringer contributes to the change in pressure evolution according to its positioning via θ and d_i. It is observed in Fig.4.19(b) that horizontal stringer ($\theta = 0°$) generated the most severe plastic strain. In this case the maximum plastic strain value is more lifted when the heterogeneities touched each other ($d_i = 2S_i$). In contrast, when the orientations are $\theta = 90°$ and $\theta = -45°$, the separated heterogeneities produced higher plastic strain than those which are touching each other. More, when $\theta = 45°$, the maximum plastic strains reached are almost identical once the steady state has been established, regardless the gap between heterogeneities. Whatever the considered stringer, the plastic strain always gets its steady value from $\delta x = a$.

To review, in some cases, the presence or not of the substrate matrix between the heterogeneities can generate more or less or even the same level of plastic strain. It could be recalled, from our previous work [104] that the zone where the plastic strain is maximal depends on the heterogeneity nature. When the heterogeneity is softer than the substrate matrix, then the stress concentration yielded at certain portions of its border. Conversely, if the heterogeneity is stiffer then stress concentration is reached maximum at its center and also in some regions of the matrix closed to the heterogeneity according to the applied stress gradient direction. Hence the combination of these regions in interaction with the position of the stringer's heterogeneities, could be the reason of the plastic strain level variability. To define the stringer harmfulness in terms of *over-stress*, one can see from Fig.4.19(c) that the maximum shear stress peak is produced by the stringer oriented by $\theta = -45°$. Therewith, when the heterogeneities are separated by the substrate matrix ($d_i = 3S_i$), the residual stress reaches the greatest amplitude compared to all cases observed.

Fig.4.22 shows the distribution of the maximum shear stress around the stringer when the rolling load center is vertically coincided with that of the stringer. The concordance between sub-figures and the stringers orientations is detailed in the figure's caption. When the stringer is parallel to the rolling direction ($\theta = 0°$), the zone where the stress is maximum, spreads below the stringer. This zone is continuous if heterogeneities are in contact ($d_i = 2S_i$) but it is crenelated otherwise ($d_i = 3S_i$). However, whatever the interaction distance d_i, if the stringer is vertical ($\theta = 90°$) then the shear stress is concentrated along heterogeneities central axis. Hence, in the case where there is a substrate matrix between heterogeneities, it undergoes a very high shear stress. Recalling that the substrate matrix is less rigid than the considered heterogeneities, the material area between heterogeneities is exposed to more damage risk than the rest when the stringer is vertical. When the stringer is oriented at $\theta = -45°$, the high stress zones are located in the stringer diagonal plane which is passing by each heterogeneity center, whatever d_i. Then, in that plane, the maximum shear stress value has been seen concentrated at heterogeneities borders when they are separated, Fig.4.22(h). But, when $\theta = 45°$, the high stress zones are located at each heterogeneity's top and bottom faces.

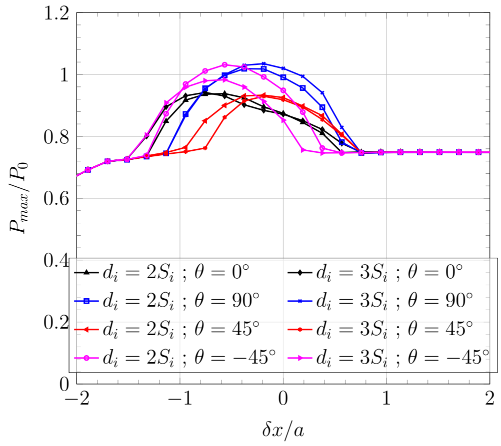

(a)

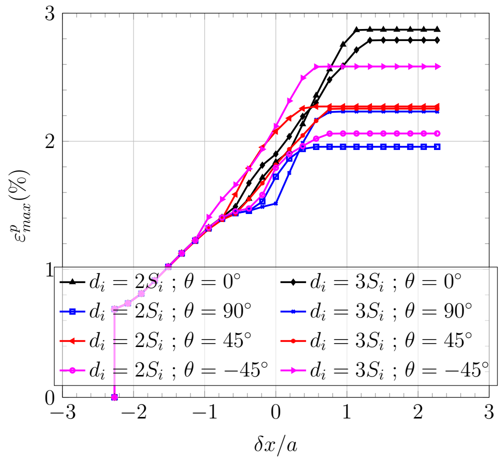

(b)

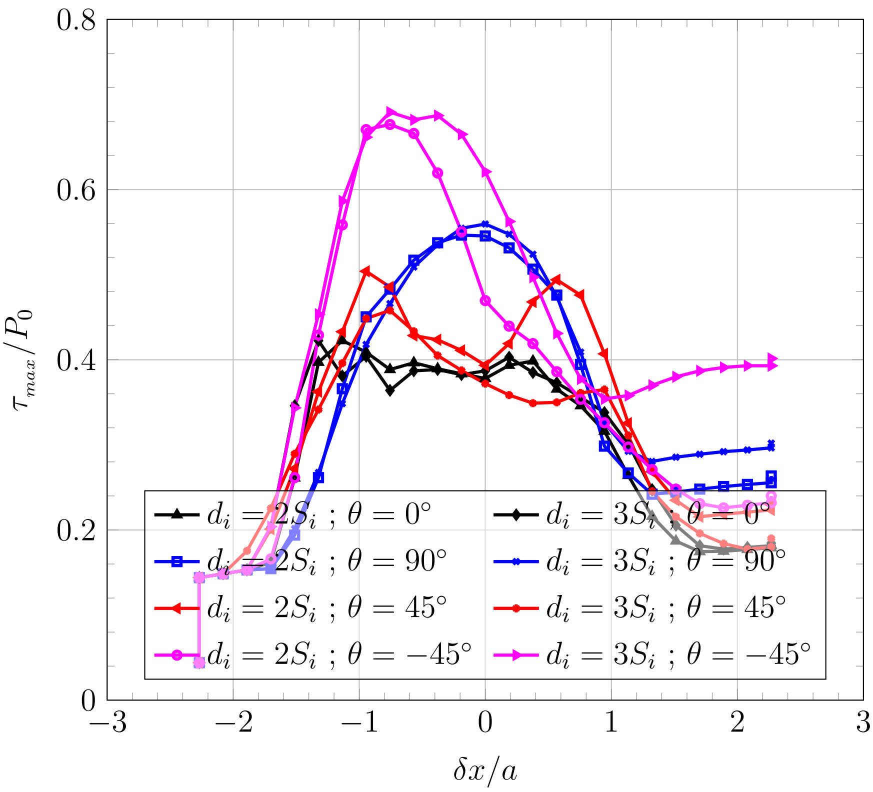

(c)

Parameter	value
Central Heterogeneity location	$z_i = 0.3a$
Heterogeneity size	$S_i = 0.1a$
Heterogeneity elastic modulus	$E_I = 490GPa$
Heterogeneities density	$N_i = 3$
Heterogeneities distribution	d_i driving the mutual influence
Heterogeneities orientation	θ driving the stringer orientation

Figure 4.19: Fields evolution according heterogeneity stringer orientation and mutual influence: (a) Contact pressure; (b) Equivalent plastic strain; (c) Maximum shear stress

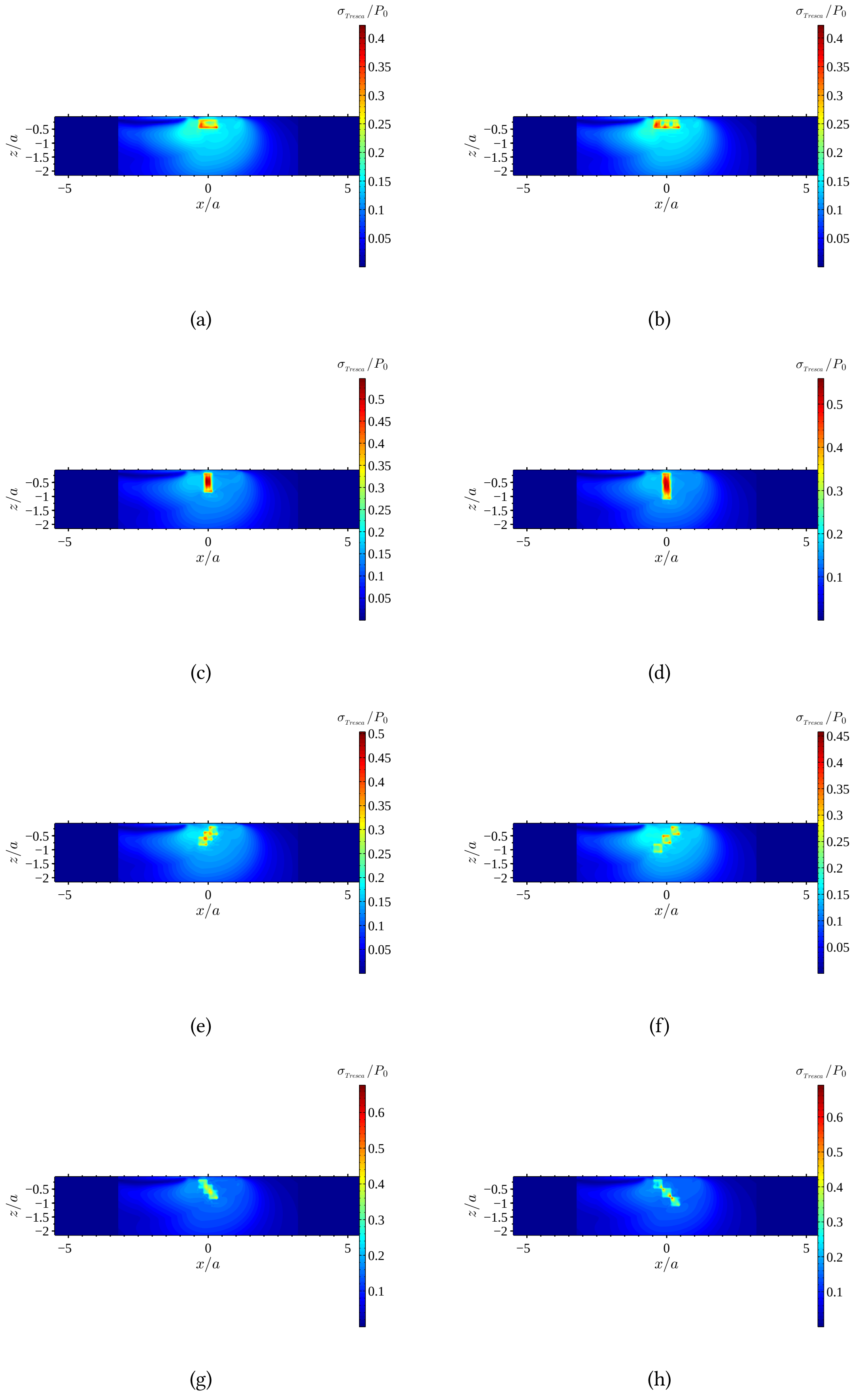

Figure 4.20: Maximum shear stress evolution according heterogeneity stringer orientation and mutual influence: (a) $d_i = 2S_i$ and $\theta = 0°$; (b) $d_i = 3S_i$ and $\theta = 0°$; (c) $d_i = 2S_i$ and $\theta = 90°$; (d) $d_i = 3S_i$ and $\theta = 90°$; (e) $d_i = 2S_i$ and $\theta = 45°$; (f) $d_i = 3S_i$ and $\theta = 45°$; (g) $d_i = 2S_i$ and $\theta = -45°$; (h) $d_i = 3S_i$ and $\theta = -45°$

Cluster distribution

A cluster of N_i number of heterogeneities is studied here. Within a considered cluster, each heterogeneity has a constant size S_i and separated by d_i meaning once again the smallest inter-center distance. A regular arrangement was established relative to the three Cartesian directions to shape the cluster as a cube and to keep it outer size constant regardless of N_i. Then the combination of N_i, S_i and d_i is used to set the cluster apparent volume fraction and density. Three clusters have been simulated. The first one has $N_i = 3 \times 3 \times 3$ with $S_i = 0.1a$, when the second has much more number of heterogeneities $N_i = 7 \times 7 \times 7$ with smaller size $S_i = 0.05a$. In this way, the two clusters have the same volume fraction but not the same density. Every heterogeneity, from each of the two clusters, feels a similar mutual influence since the separating gap is held according to their respective size as $d_i = 3S_i$. The last cluster has only one heterogeneity meaning 100% of the volume fraction. Recalling that all clusters have the same outer size, they are also centered at the same depth of $0.6a$ beneath the surface. During the HEP-RC, Fig.4.21 compares the evolution of the maximum of contact pressure, shear stress and plastic strain. One can see at first that these fields maximum are disturbed by the heterogeneities presence, over the same distance whatever the regarded cluster. This implies that the distance over which the fields disturbances are scattered does not depend on the heterogeneity number N_i or their individual size S_i, but maybe only on the cluster's apparent outer size. Except their magnitudes, also the trend of fields are not depended on N_i and S_i. However Fig.4.21(a) shows that the maximum pressure highest level is found when the cluster is formed by a single heterogeneity and this is the highest level possible since that cluster has 100% of the volume fraction. But for the same volume fraction, the maximum pressure lowest level is attributed to the denser cluster which means the one having the larger amount of heterogeneities with consequently the smaller sizes. One can argue that the maximum pressure upper bound is driven by the volume fraction and the lower bound is controlled by the density. Conversely to the pressure field, Fig.4.21(b,c) noticed that the cluster formed by a single heterogeneity produced a lower level of maximum plastic strain and maximum shear stress than the two others which are formed by distributed heterogeneities. Even if the single heterogeneity has the largest volume fraction, the mutual influence between heterogeneities composing the two other clusters, is capable of increasing their stress and strain levels. Furthermore, for the same volume fraction and similar mutual influence, the highest plastic strain and maximum shear stress was found when the cluster is less denser. Above all, it should be mentioned that the residual maximum shear stresses, after the unloading, have nearly identical levels regardless of the given cluster.

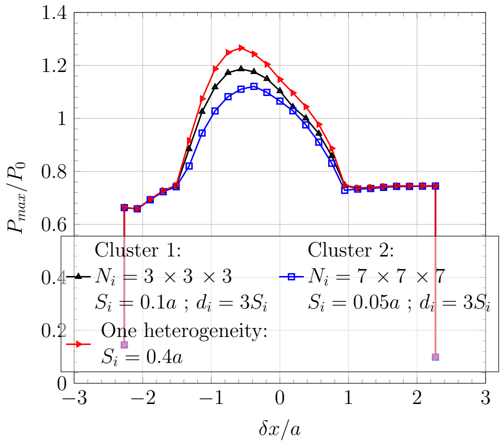

(a)

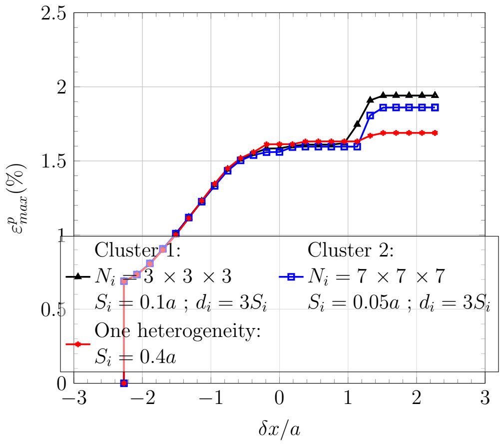

(b)

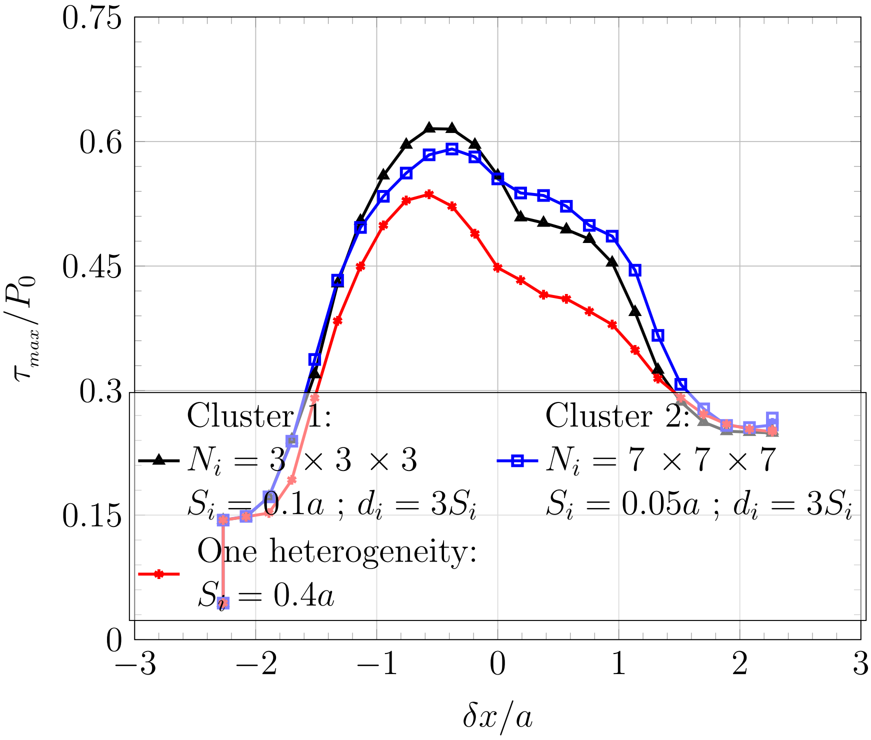

(c)

Parameter	value
Heterogeneities location	$z_i = 0.3a$ first row
Heterogeneity elastic modulus	$E_I = 490GPa$
Heterogeneity size	S_i driving the cluster density
Heterogeneities density	N_i driving the cluster density
Heterogeneities distribution	d_i driving the mutual influence

Figure 4.21: Fields evolution according heterogeneity cluster density and mutual influence: (a) Contact pressure; (b) Equivalent plastic strain; (c) Maximum shear stress

The maximum shear stress distributions have been represented in Fig.4.22 at two moments during the rolling. The first, when the load arrives at the cluster's vertical central axis position $\delta x = 0$, and the second when the load was removed at $\delta x = 2a$. It is found out that when the load is passing on the clusters, the zones where the maximum shear stress has higher values are distributed in the same way whatever the cluster regarded. But the stress concentrations are more discretized when the density increases, in Fig.4.22(a,c,e). The same phenomenon is observed on the residual stress distributions, after the unloading, in Fig.4.22(b,d,f).

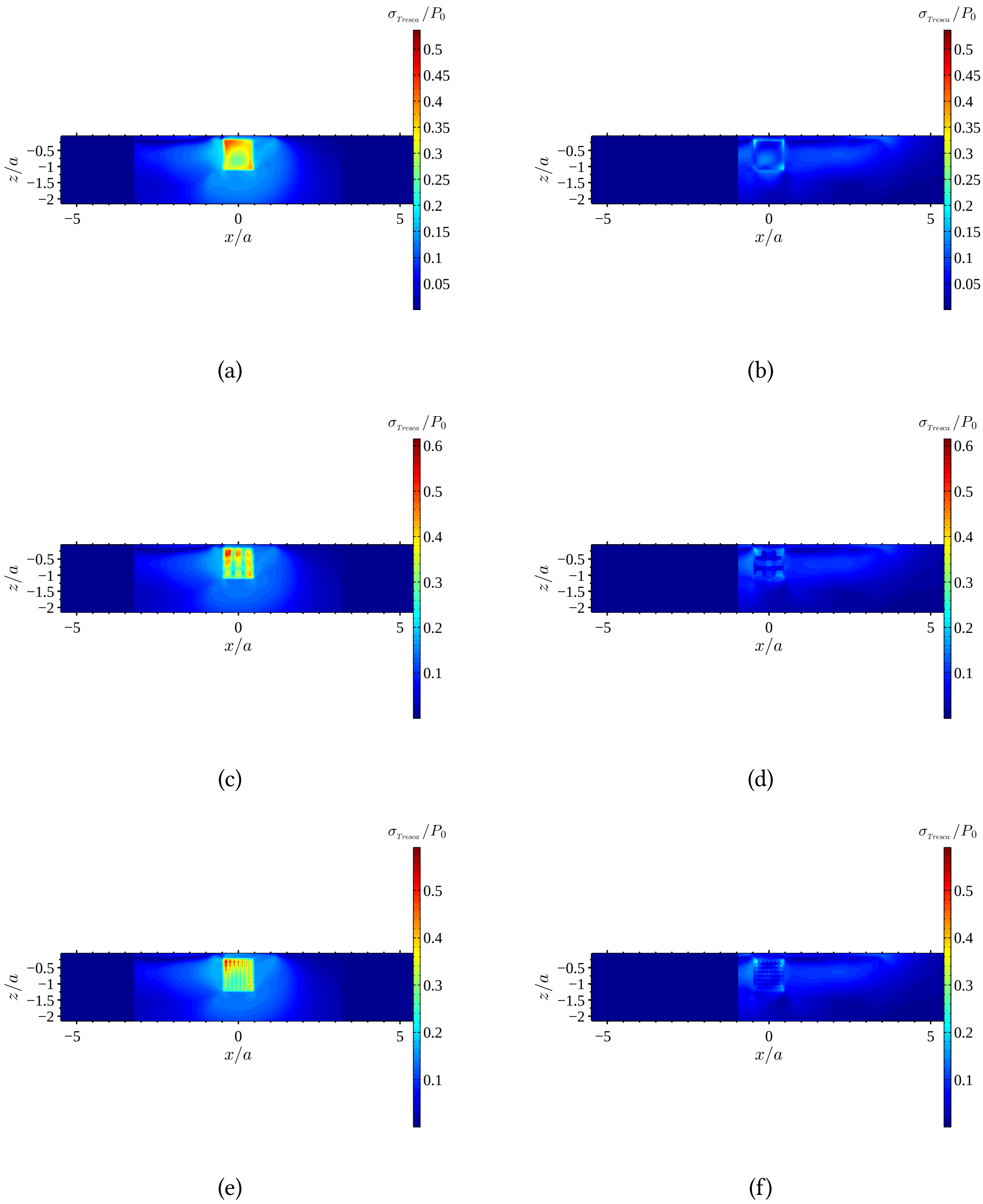

Figure 4.22: Maximum shear stress evolution according heterogeneity cluster density and mutual influence: One heterogeneity $S_i = 0.4a$ $\dashrightarrow$ (a) Rolling contact loaded at $\delta x = 0$; (b) Contact unloaded at $\delta x = 2a$; Cluster 1 $N_i = 3\vec{x} \times 3\vec{y} \times 3\vec{z}$ and $S_i = 0.1a$; $d_i = 3S_i$ $\dashrightarrow$ (c) Rolling contact loaded at $\delta x = 0$; (d) Contact unloaded at $\delta x = 2a$; Cluster 2 $N_i = 7\vec{x} \times 7\vec{y} \times 7\vec{z}$ and $S_i = 0.05a$; $d_i = 3S_i$ $\dashrightarrow$ (e) Rolling contact loaded at $\delta x = 0$; Contact unloaded at $\delta x = 2a$

4.4 ADVANCED APPLICATIONS OF THE HEP-RC

This part is dedicated to evaluate to effect of the parameters describing the surface friction coefficient and the material hardening properties on the HEP-RC. Also an analysis of multi-cyclical rolling is conducted when plasticity ratcheting regime primed.

4.4.1 INFLUENCE OF HARDENING PROPERTIES

In general, owing to thermo-mechanical and thermo-chemical treatments, some variety of rolling contact elements result in Plastically Graded Materials (PGM). These treatments are at the origin of heterogeneities precipitated with a diffusion starting from the outer surface to the core of the material. This diffusion results in a gradient of elastic plastic properties incarnated by the yield stress gradient. The permanent deformation, due to the thermo-chemical processes, induces initial residual stress that are often in a state of compression within the surface layer. Assuming that the permanent deformation is planar, steady and continuous, then the initial stress components $\sigma_{xx}^{init} = \sigma_{yy}^{init}$ which act parallel to the surface, are considered as non-nil and they vary along the depth. In service, the aforementioned components since they are negative, they will accommodate the applied stress tensile components in x and y directions. The input initial stress and the input yield stress are plotted in Fig 4.23(a) as a function of the depth. It could be found in the literature [116] how the parameters related the material treatments control the initial stress and the yield stress profiles and magnitude. Hereafter, the initial stress is set to $-0.16P_0$ at the surface, and its norm decreases within a thinner layer of $0.1a$, then it is maintained about a value of $-0.13P_0$ on the layer from $z_i = 0.5a$ to $z_i = 1.5a$. The yield stress was increased to 30% at the surface relatively to the given value in the material core unreached by the treatment. The yield stress varies almost linearly from the surface up to a depth of $z_i = 2a$ which is the lowest depth of the computational zone used in the simulations. Note that, the initial stress and yield stress trends are consistent with data obtained from really treated materials, but the sources cannot be divulged. Likewise, the profile magnitudes were modified in supporting of the confidentiality. However some publications give the initial stress [86] and yield stress [117] evolution according to the employed materials and the treatments.

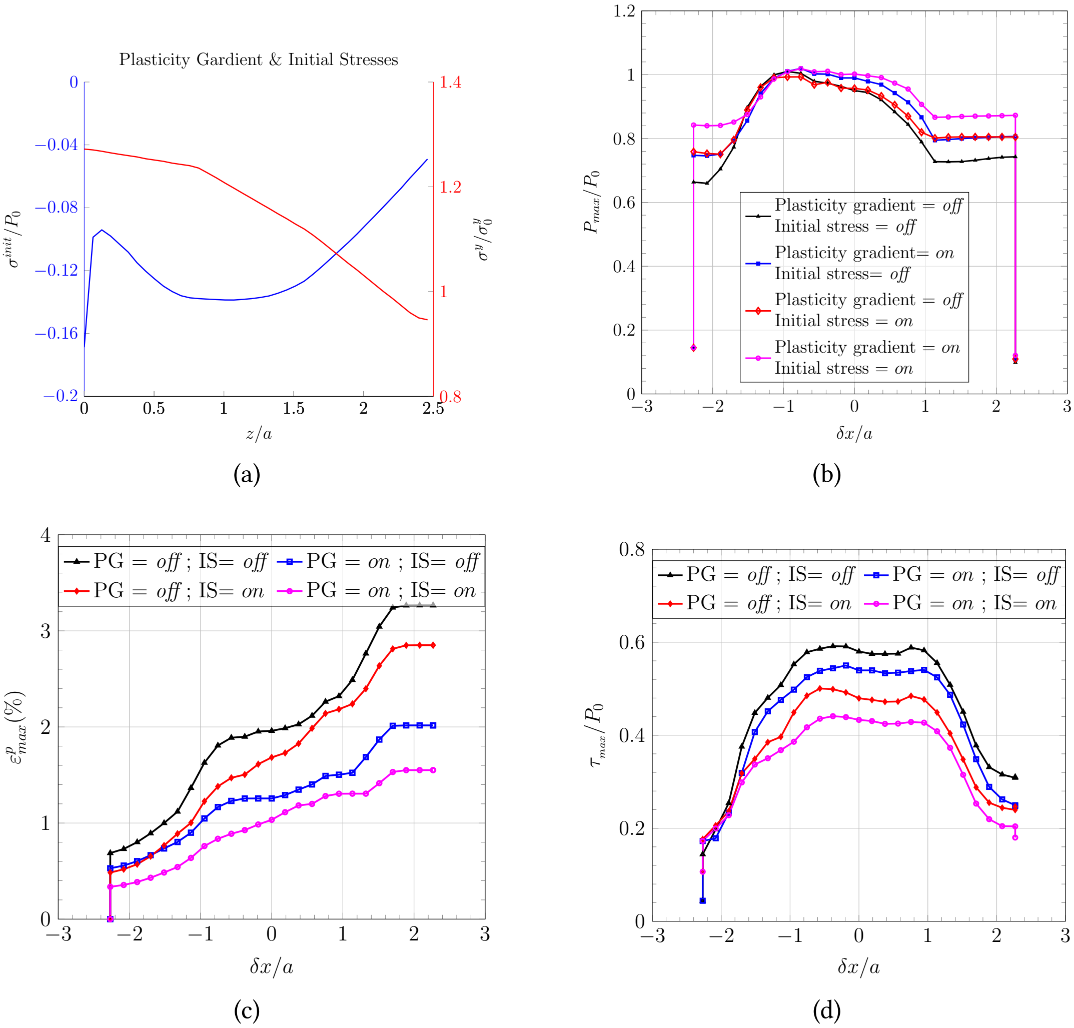

Parameter	value
Heterogeneities location	$z_i = 0.3a$ first row
Heterogeny size	$S_i = 0.1a$
Heterogeneity elastic modulus	$E_I = 490GPa$
Heterogeneities distribution	$d_i = 3S_i$
Heterogeneities density	$N_i = 5\vec{x} \times 5\vec{y} \times 3\vec{z}$
Plasticity gradient	$PG = yes$; no driving yield stress
Initial stress	$IS = yes$; no driving compressive stress

Figure 4.23: Fields evolution according to hardening properties: (a) The input initial stress and yield stress; (b) Contact pressure; (c) Equivalent plastic strain; (d) Maximum shear stress

To simulate the effect of the hardening properties, which means the presence of Initial Stress (IS) and Plasticity Gradient (PG), a cluster of $5\,x \times 5\,y \times 3\,z$ heterogeneities is created and embedded in an elastic plastic medium. The properties associated with the heterogeneous microstructure are listed in the table attached to Fig.4.23. Four configurations are compared against each other. The first, $(PG = \mathit{off}\ ;\ IS = \mathit{off})$, represents the material without any plasticity gradient and initial stress as the untreated material. The second, $(PG = on\ ;\ IS = \mathit{off})$, corresponds to a situation where the plastically graded material (PGM) loses its initial compression stress. The so-called relaxation effect occurs when the subsurface accumulated plastic strain releases the certain sufficient quantity of residual tensile stress over loading cycles. This phenomenon is explained in Le et al. (2013) [118] where authors are studying the effect of intergranular cementite arrays in nitrided steels on gear rolling contact fatigue. The third case, $(PG = \textit{offf} \; ; \; IS = on)$, envisages the presence of initial stress in the layer of large thickness without any plasticity gradient. This could be a result of a isotopic distribution of heterogeneities precipitates giving a uniform overall elastic-plastic property without any gradient, followed by a permanent deformation left by the heat produced during the surface finishing processes. The last case, $(PG = on \; ; \; IS = on)$, concerns an ordinary PGM having both initial stress and plasticity gradient.

It could be seen in Fig.4.30(b) that the peak reached by the maximum pressure is quite identical for all considered materials, at $\delta x = -a$, but the magnitude decrease from that point to a steady level which is established from $\delta x = a$. The highest steady level is obtained when $(PG = on \; ; \; IS = on)$ and the lowest when $(PG = \textit{off} \; ; \; IS = \textit{off})$. More interesting, the intermediate configurations $(PG = \textit{off} \; ; \; IS = on)$ and $(PG = on \; ; \; IS = \textit{off})$ have almost an equal steady maximum pressure level. It appears that the input yield stress profile could, vice versa, compensates the effect of the input initial stress on the pressure, when one of them is off. However, this effect did not hold for the plastic strain. One can see in Fig.4.30(c), that $(PG = \textit{off} \; ; \; IS = on)$ generates more plastic strain, at the steady state, than $(PG = on \; ; \; IS = \textit{off})$. This confirmed in this framework that the simply way to diminish the plastic strain level remains to increase the yield stress instead of introducing initial compressive stress. But the efficient way to keep the plastic strain lower is to input both plasticity gradient and initial stress. It should be pointed out that the case $(PG = \textit{off} \; ; \; IS = \textit{off})$ remains detrimental since the plastic strain produced is almost the double of the case $(PG = on \; ; \; IS = on)$. It could also be noticed in Fig.4.30(d) that, $(PG = \textit{off} \; ; \; IS = \textit{off})$ has the most upped level of maximum shear stress and $(PG = on \; ; \; IS = on)$ still is the preventive configuration since it has the lowest maximum shear stress level. The intermediate case behaviors offer the insight that to purposely soften the maximum shear stress, it is better to insert an initial stress instead of increasing the yield stress. This is why $(PG = on \; ; \; IS = \textit{off})$ presents higher maximum shear stress than $(PG = \textit{off} \; ; \; IS = on)$. However, one can observe that both intermediate cases end up with the same level of residual stress after the rolling. This implies that the initial stress and the yield stress have compensatory effect on the residual stress. The minimum residual stress level is observed when the plasticity gradient and initial stress are present in the material and the highest level stands for the opposite case.

Considering the benefit presence of a plasticity gradient and an initial stress, according to the effect on the stress/strain field, some furthers simulations are made to investigate how that could ease the stress state (τ_{max} vs σ_{HP}) induced by a porosity. Let's remind that it has been proven in the previous section that porosity is more harmful than the given stiff heterogeneity in this study. Hereafter, the porosity is placed at the depth $z_i = 0.3a$ then at $z_i = 0.5a$ and it sized $S_i = 0.1a$. The maximum shear stress versus the hydrostatic pressure evolution path around the porosity edges is compared to the body in absence of plasticity gradient (PG) and initial stress (IS), against the body having both PG & IS, in Fig.4.29 and Fig.4.30.

It should be noticed at first that the maximum shear stress has been significantly reduced at the porosity edges by introducing PG & IS, whatever the porosity's location.

This minimizes the damage risk. Hence, when the porosity is centered at the Hertzian depth,in Fig.4.29(d,f), the maximum shear stress τ_{max} drops from $1.2P_0$ to about its quarter $0.3P_0$ at the porosity's front edge $M(-1,0,0)$ and behind edge $M(1,0,0)$. It is worth specifying that the tensile or compression states could change and evolve in the presence of PG & IS compared to the untreated material at the same location as for $M(-1,1,1)$ in Fig.4.29(d). There, the residual hydrostatic pressure becomes more important and has been in tensile state when PG & IS are present. But the residual hydrostatic pressure and the shear stress are reduced in other places like $M(-1,1,1)$ and $M(1,1,1)$ as shown in Fig.4.30(a,b). In general, according to Dang Van threshold plotted in the analyzed charts, the endurance limit has been enhanced by the introduction of initial compressive stress and the increasing of the yield stress via the plasticity gradient, as expected. This is in qualitative agreement with results of earlier studies of Harris [119] at the beginning the 90s.

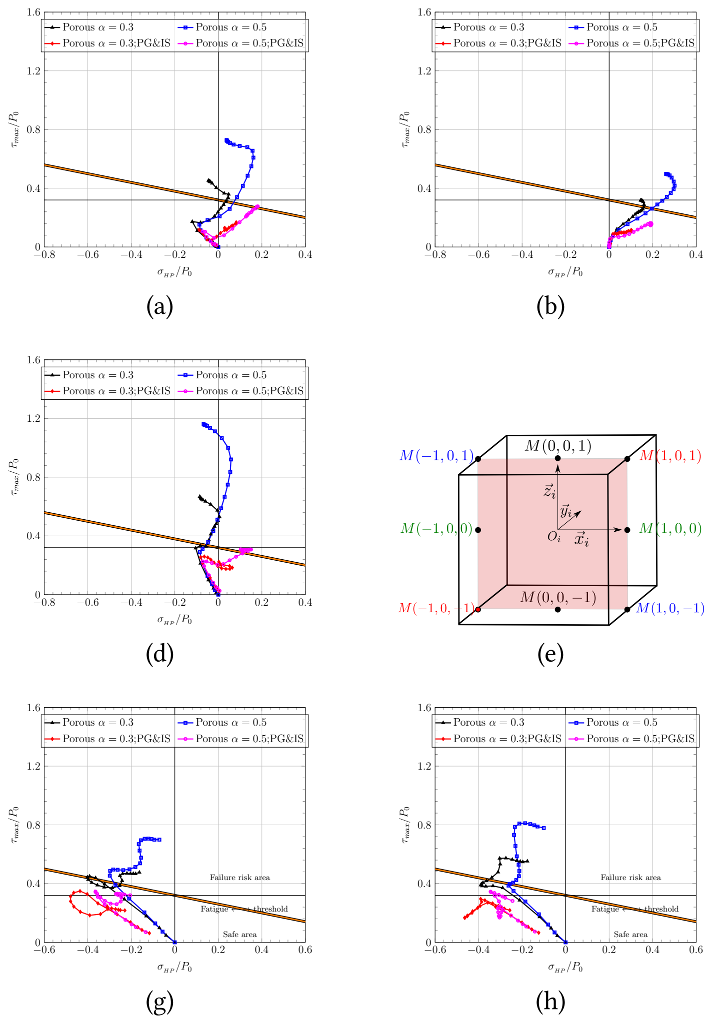

Figure 4.24: Initial stress effect on plastically graded material fatigue life according to Dang Van criterion: (a) heterogeneity edges point $M(-1,0,1)$; (b) heterogeneity edge point $M(0,0,1)$; (c) heterogeneity edge point $M(1,0,1)$; (d) heterogeneity edge point $M(-1,0,0)$; (e) heterogeneity referential and edge points locations; (f) heterogeneity edge point $M(1,0,0)$; (g) heterogeneity edge point $M(-1,0,-1)$; (h) heterogeneity edge point $M(0,0,-1)$; (i) heterogeneity edge point $M(1,0,-1)$

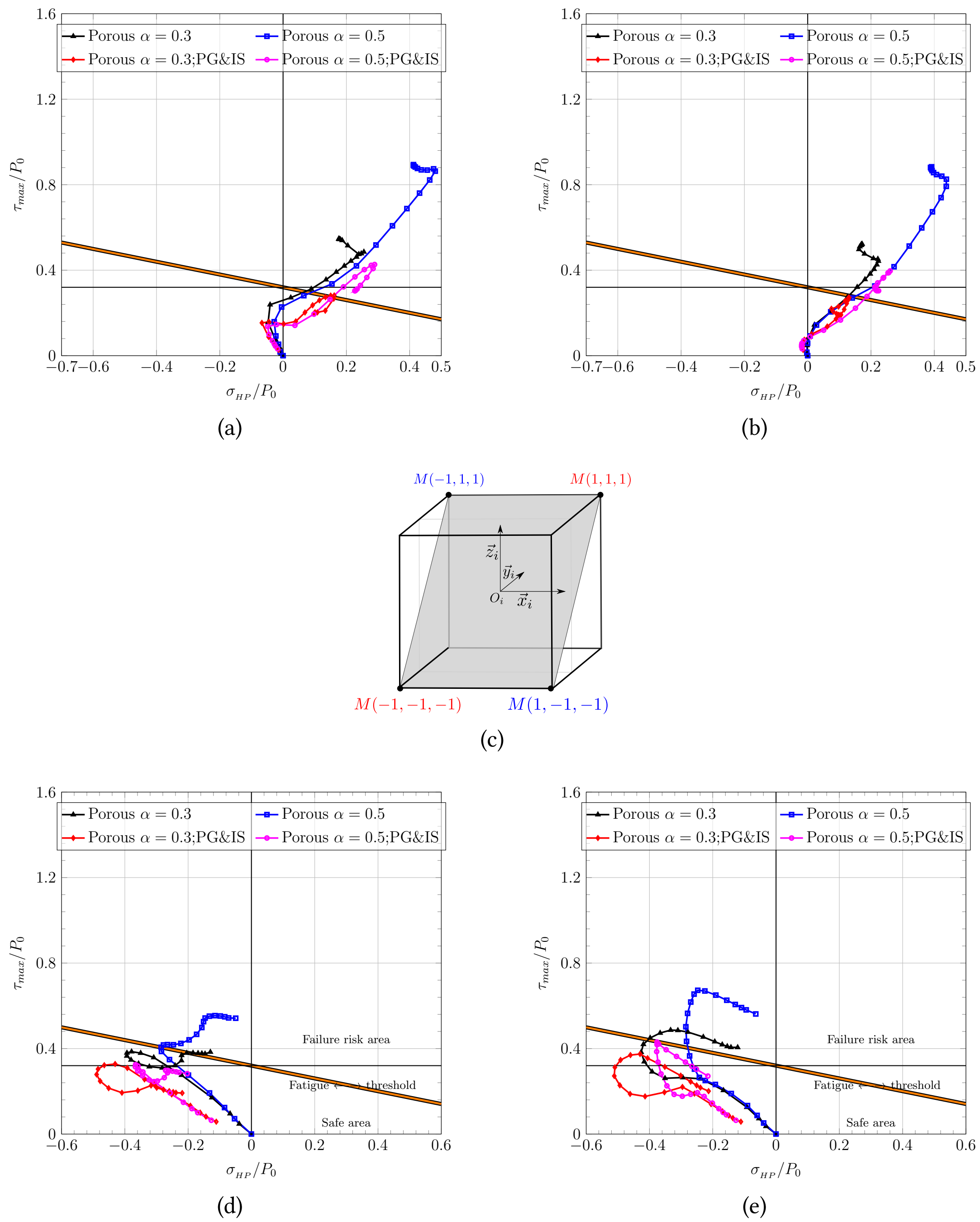

Figure 4.25: Initial stress effect on plastically graded material fatigue life according to Dang Van criterion: (a) heterogeneity edges point $M(-1,1,1)$; (b) heterogeneity edge point $M(1,1,1)$; (c) heterogeneity referential and edges points location; (d) heterogeneity edge point $M(-1,-1,-1)$; (e) heterogeneity edge point $M(1,-1,-1)$

4.4.2 CYCLICAL ROLLING AND RATCHETING ANALYSIS

Now multi-cycles rolling contact is implemented in the sake of the ratcheting regime which starts right after the shakedown limit known as the limit loading state from which the elastic regime is lost turning the optimal residual stress to a non-protective stress then undergoing the material to an incremental failure. The analytical shakedown limit had been given by Johnson and Jefferis [120, 121] and proven by Hills *et al.* [122, 123] to be $P_0/\tau_0^y = 4.68$, where p_0 is the maximum applied Hertzian pressure and τ_0^y the shear yield strength. Note that, the shear yield strength could be related to the tensile yield strength σ_0^y for steel material $\tau_0^y = c\ \sigma_0^y$, where the coefficient c could be 0.577 by Von Mises criterion, 0.5 by Tresca criterion , 0.6 recommended by Shigley [124], or 0.58 considering experimental results from tests made on many aeronautics steels. It has been proven that shakedown limit not only depends on load level but also on the material plastic hardening law. He *et al.* [103] shows when studying the plasto-elastohydrodynamic lubrication behaviors in rolling contact that under a working condition that exceeding ratcheting threshold ($p_0/\tau_0^y = 5.84$), a linear-isotropic-kinematic plastic law can end up with a shakedown. Hereafter, the shakedown limit is largely exceeded ($p_0/\tau_0^y = 12.65$ using Von Mises criterion) in purpose to stay in the ratcheting regime even if isotropic hardening is assumed.

Turning now to the HEP-RC problem, Fig.4.27(c) attests an accumulative plastic flow which sustains that the shakedown limit is exceeded and ratcheting regime occurred. Indeed the combination of the residual and the current contact stress cannot prevent from the yield even if the loading is the same over the cycles. The result plotted in Fig.4.26(a) shows that there is no increase of the contact pressure from the 3rd cycle. From Fig.4.27(a) one can see that the plastic strain increment per cycle brings out that the ratcheting rate is not constant. Non-asymptotic trend is observed advocating that the plastic strain increasing will not cease until the critical point of fracture. The evolution of the maximum plastic strain over cycles is fitted from the 2nd cycle to capture the contact conforming groove. The curve fitting, very precise (see Appendix. B.1), leads to a prefect power law as $\varepsilon^p_{max} = c_0 + (c_1 + c_2 \times N_{cycles})^n$, where the constant values are $c_0 = 0.16$, $c_1 = 13.5$, $c_2 = 5$ and $n = 0.11$. Considering the identified curve equation, one can estimate the number of cycles for the ratcheting to reach material critical point. This critical point has been taken from Klecka's [75] compression test on M50 Through hardened material containing 20% of uniformly distributed carbides inclusions up to $800\mu m$ under the surface. The fracture occurs when deformation is found around 0.05. Therefore the number of cycle up to the failure of the homogeneous media is estimated to $N^{critical}_{homogeneous} = 336429\ cycles$. In the same time when the media is heterogeneous the simulation is accordingly stopped at $\varepsilon^p_{max} = 0.05$ corresponding to $N^{critical}_{heterogeneous} = 10\ cycles$. One can conclude that, in ratcheting regime, the heterogeneous media lifetime becomes more critical and the failure is sped up compared to the homogeneous media. Therefore preventing the media from ratcheting regime could save a lot of fatigue cycles when it contains heterogeneites.

Further analysis presented in Fig.4.27(b) shows that in the homogeneous case the maximum pressure decreases slowly during cycles when the maximum shear stress and residual shear stress get stabilized from 5th cycle. But in the presence of heterogeneity, the maximum pressure and residual shear stress increasing when the maximum shear stress trend decreases until the 8th cycle after where a sharp increase happened. This sharp increase leads to the fracture critical point aforementioned. In this moment, the maximum shear stress peak and the maximum residual shear stress peak are the same at the 10th cycle. One can explain this by considering the evolution of the maximum shear stress over rolling cycles plotted on Fig.4.26(f). Very high maximum shear stress is produced during the 10th cycle and the residual shear stress peak is greater than the one produced during the loading. Then an elevation of the plastic strain occurred at the unloading as observed from Fig.4.26(d). In the meantime, Fig.4.28 reveals that the accumulated plastic strain comes up to the contact surface with the attributed critical value of almost 0.05. This could suggest a source of damage.

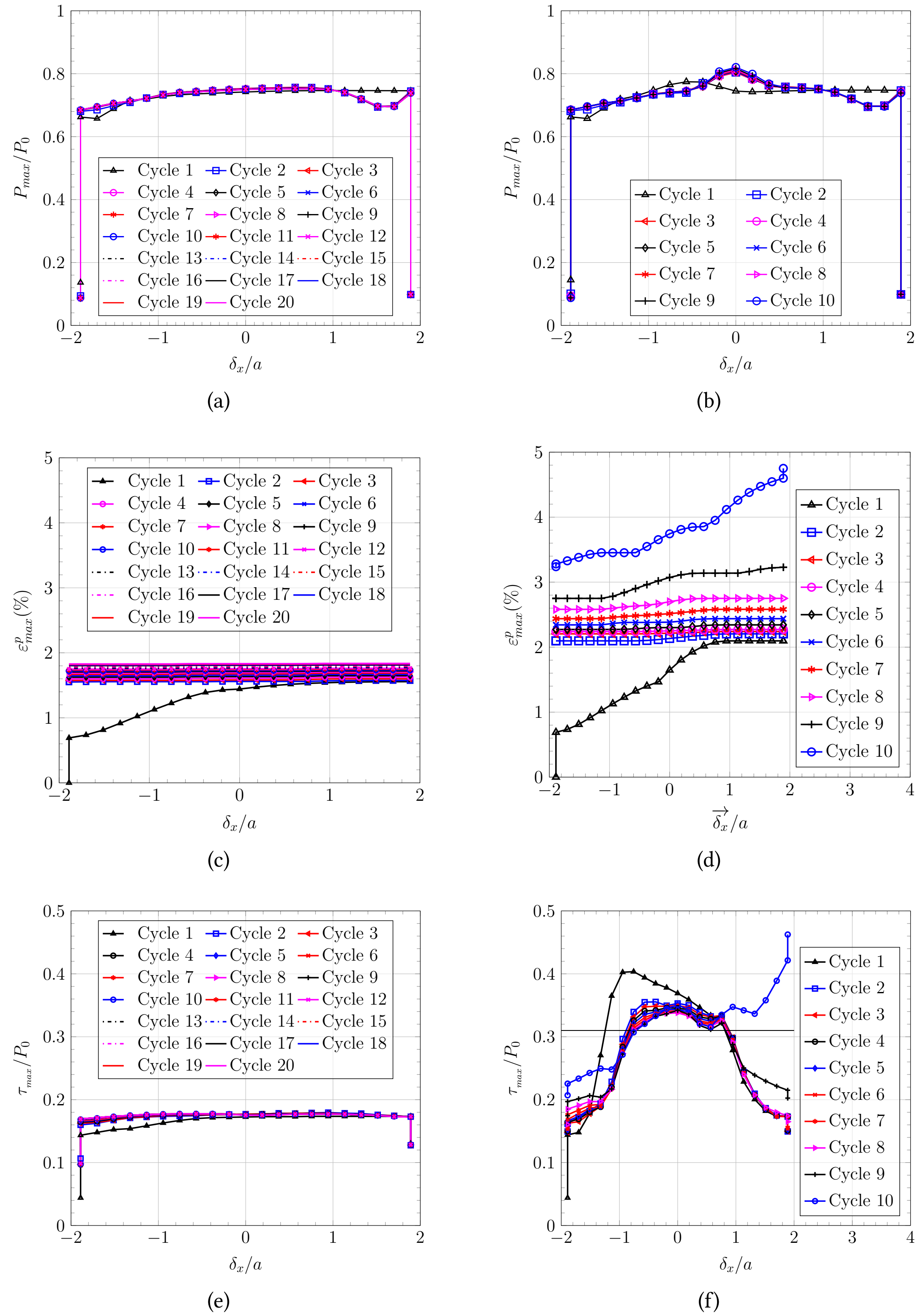

Parameter	value
Heterogeneity size	$S_i = 0.1a$
Heterogeneity location	$z_i = 0.5a$
Heterogeneity elastic modulus	$E_I = 490GPa$

Figure 4.26: Fields evolution during several rolling cycles: Contact pressure (a) Homogeneous; (b) Heterogeneous; Equivalent plastic strain (c) Homogeneous; (d) Heterogeneous; Maximum shear stress (e) Homogeneous; (f) Heterogeneous

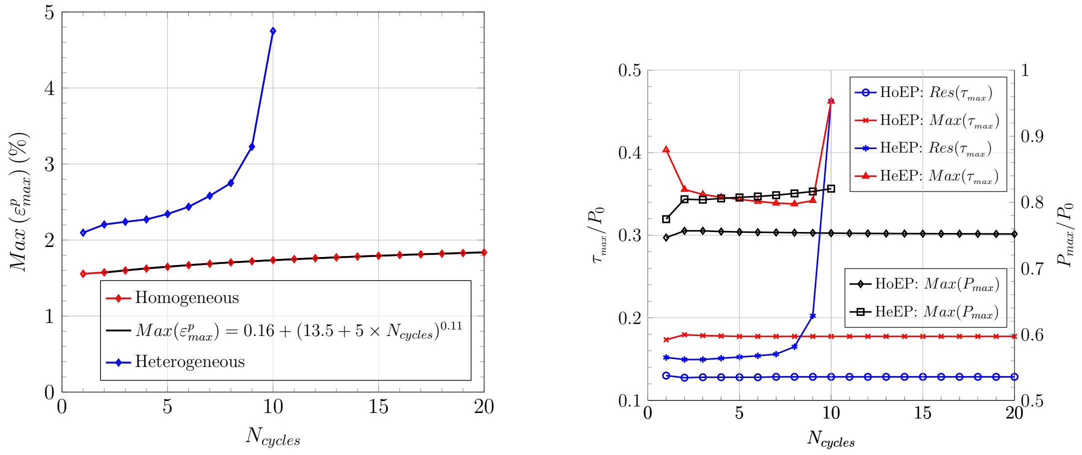

(a) (b)

Figure 4.27: Fields evolution according to the number of rolling cycles: (a) Peaks of the equivalent plastic strain maxima; (b) Peaks of residual maximum shear stress and peaks of maximum contact pressure

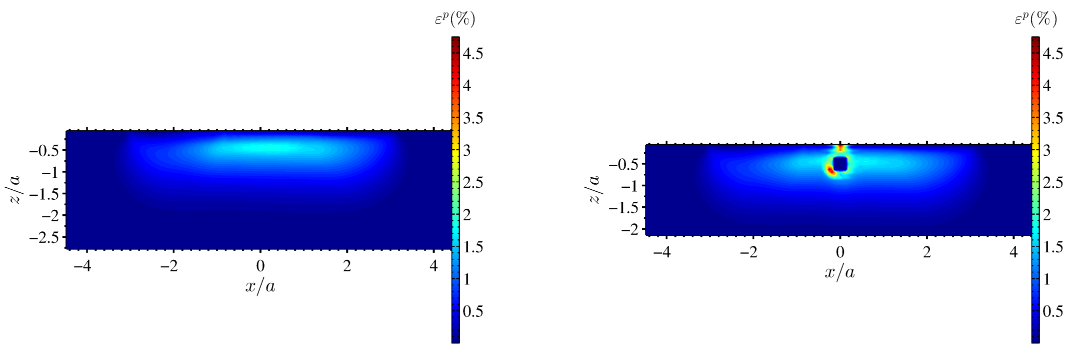

(a) (b)

Figure 4.28: Plastic strain evolution in the plane $\mathcal{P}(y = 0)$ during rolling cycles: (a) Homogeneous material at 20th cycle; (c) Heterogeneous material at 10th cycle

Moreover, the evolution of the maximum shear stress versus the hydrostatic pressure around the heterogeneity is described in Fig.4.29 and Fig.4.30, for 10 HEP-RC cycles. The heterogeneity is as always a Vanadium carbide ($\gamma = 2.33$) centered at the Hertzian depth $z_i = 0.5a$ and sized $S_i = 0.1a$. One can observe a closed-loop of the response for all cycles except for first cycle which presents a remarkable shifting whatever the regarded points. This deviation reflects an exaggeration of the shear stress during the first cycle which is explained by the creation of surface permanent groove. Hence, from the second cycle, the maximum shear stress and the hydrostatic pressure amplitudes are generally preserved at all the considered points. Note that at the first cycle stresses $(\tau_{max}; \sigma_{HP})$ begins from $(0; 0)$ but the following cycles start with a non-nil value due to the residual stress stored over cycles. The alternation between tensile and compression states, at the carbide bottom points as $M(-1, 0, -1)$ and $M(1, -1, -1)$, establishes a fatigue cyclic behavior favorable to damage. Also the residual stress is constantly in tensile state at these points. Finally, the Dang Van criterion demonstrated that $\tau_{max} \leftrightarrow \sigma_{HP}$ stresses path never cross the fatigue threshold around the heterogeneity implying accordingly infinite life until the critical point of fracture is nevertheless reached when the plastic strain comes up to the surface, Fig.4.28. This confirms that accumulative plastic strain trend and its history must be well accounted in failure prediction especially when ratcheting regime primed in mesoscopic scale. Therefore, even if in the presented case the heterogeneity not serve as nucleation points for crack, its action as the plasticity riser contributes to large plastic strain gradients between subsurface layers exhibiting plastic shearing and distortion as shown in Fig.4.28(b). This very significant plastically deformed narrow vertically straight band of material becomes a site of backward and forward flow occurrence with respect to the motion direction in case of alternative rolling as described by Johnson [125] and Welsh [126]. Consequently, stiff heterogeneity like Vanadium carbide acts indirectly as precursors of decohesion in the subsurface as well as wear by delamination in the surface subjected to repeated rolling and sliding cycles.

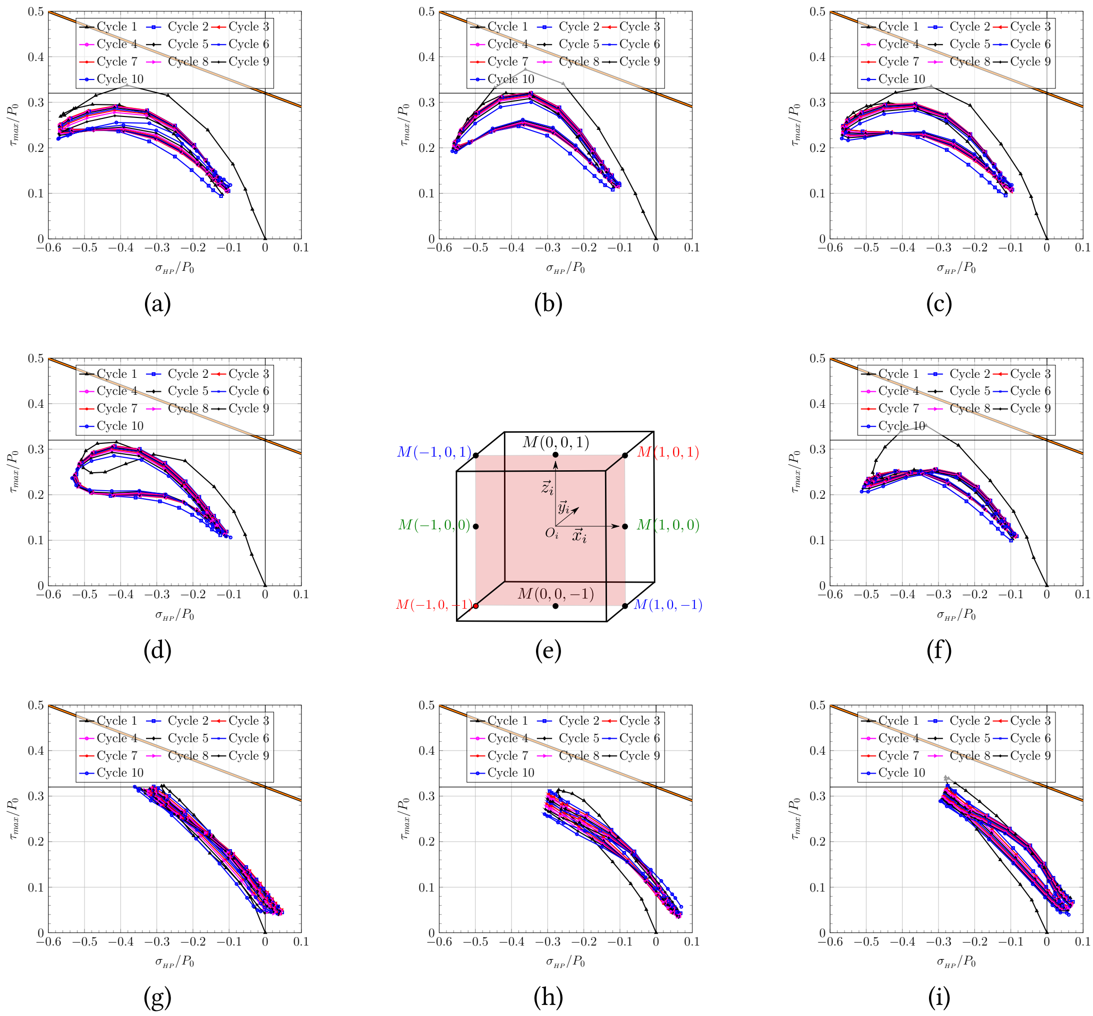

Figure 4.29: Maximum shear stress versus hydrostatic pressure evolution according to rolling cycles: (a) heterogeneity edges point $M(-1,0,1)$; (b) heterogeneity edge point $M(0,0,1)$; (c) heterogeneity edge point $M(1,0,1)$; (d) heterogeneity edge point $M(-1,0,0)$; (e) heterogeneity referential and edge points locations; (f) heterogeneity edge point $M(1,0,0)$; (g) heterogeneity edge point $M(-1,0,-1)$; (h) heterogeneity edge point $M(0,0,-1)$; (i) heterogeneity edge point $M(1,0,-1)$

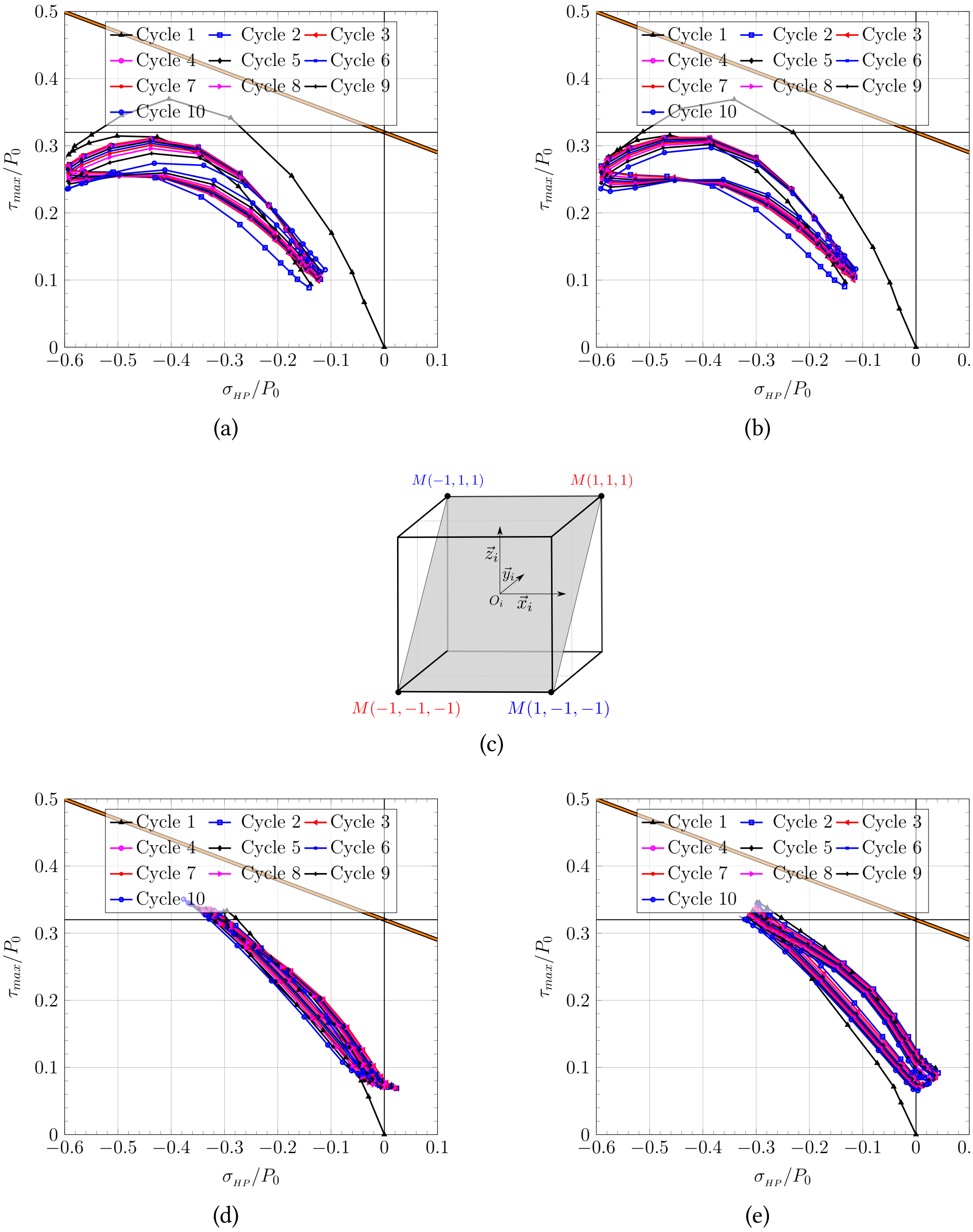

Figure 4.30: Maximum shear stress versus hydrostatic pressure evolution according to rolling cycles: (a) heterogeneity edges point $M(-1,1,1)$; (b) heterogeneity edge point $M(1,1,1)$; (c) heterogeneity referential and edge points locations; (d) heterogeneity edge point $M(-1,-1,-1)$; (e) heterogeneity edge point $M(1,-1,-1)$

4.4.3 EFFECT OF THE FRICTION COEFFICIENT ON THE HEP ROLLING CONTACT BEHAVIOR

Nowadays, advanced machining and finishing processes prevent the rolling elements form failure due to surface asperities. However, even if surface topography has been successfully enhanced prior to commissioning, micro-dents could be created as secondary asperities during the service, by fines hard particles inadequately filtered in the lubricant. Then interruption of lubricant supply or partial lubrication which occurs during transient operating regime, system stop and startup phases, induce a friction torque in the mating surfaces when the film thickness could not fill the valleys. This

situation could be modeled by a relatively low friction coefficient between $f = 0.05$ and $f = 0.1$. Its effect on the rolling contact behavior is compared against the frictionless one ($f = 0$), to provide more accurate estimation of heterogeneity criticality in bearing endurance framework. The subsurface stress strain field is determined by taking into account the Coulomb's shear force due to the friction. For reproducing most unfavorable situations, friction coefficient of $f = 0.15$, $f = 0.2$ and $f = 0.25$ were also simulated.
Fiction leads to snowball effect under some particular condition when heat phenomena and lubricant contamination are not well managed. Cheng [127] showed that heating of the lubricant in the inlet zone of the contact reduces the thickness of the minimum film owing to viscosity decreasing. This reveals some pits created by the lubricant contaminant as indicated by Harris [128]. Depending on the filter rating, the sealing and the thermal insulation, the number of surface defects can increase unrelentingly with the operating time. The new appearing surface asperities result in the increase of the surface friction. The latter is responsible for the additional sliding and shear traction followed by the elevation of the temperature in the contact and end up with the heat transfer (by conduction and convection) to the next arriving lubricant flow. This sustains the surface friction phenomenon depending on the lubrication regime.
First, let's specify that some calculations are stopped during the rolling in purpose not to exceed a plastic strain of 0.05 defined as the limit deformation in agreement with the previous section. Also to avoid convergence issues in the contact solver when updating the surface geometry, because small strain and displacement assumptions no longer hold, since it is well known that frictional contact leads to a high plastic strain at the surface, as shown in Fig.4.31(a). It could be seen Fig.4.32 that when the body is homogeneous, regardless of the friction coefficient, the calculation was not stopped anywhere along the given rolling distance from $-2a$ to $2a$. But in the presence of the heterogeneity, some stops occur for friction coefficient above $f = 0.1$. Thus, the last position reached by the rolling load before ending the calculations, is noted x^{end} and it decreases when f increases. One can mention that the HEP-RC was stopped at the step $x^{end} = 1.2a$ for $f = 0.15$, $x^{end} = 0.6a$ for $f = 0.2$ and $x^{end} = 0.2a$ for $f = 0.25$. Fig.4.31 shows plastic strain maps in the plane $\mathcal{P}(x = 0)$ when the friction coefficient is $f = 0.25$. One can observe that when the body is homogeneous the maximum plastic strain is located at the surface reminding that the load has been moved along all the given distance. However, when the body is heterogeneous the maximum plastic strain is found not only at the surface, but also underneath between the heterogeneity and the surface before the rolling was stopped at $x^{end} = 0.2a$.

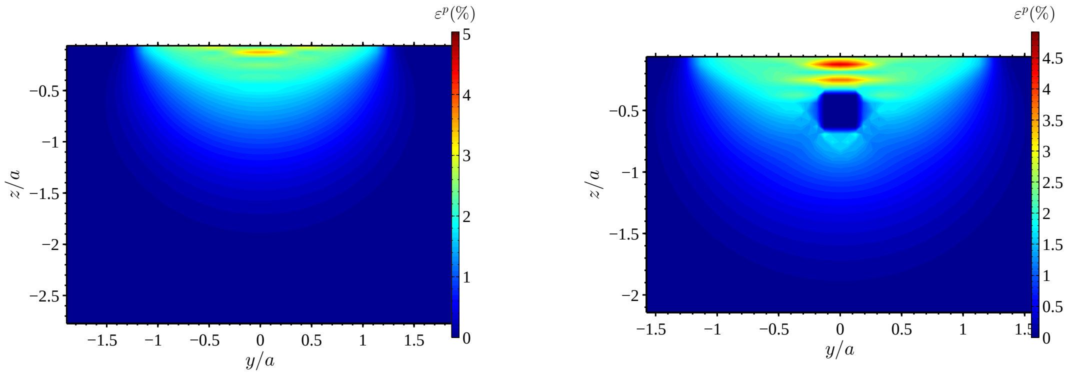

(a) (b)

Figure 4.31: Plastic strain contours in the plane $\mathcal{P}(x = 0)$ when the friction coefficient is $f = 0.25$: (a) Homogeneous material ; (b) Heterogeneous material when the rolling was stopped at $\delta x = 0.2a$

To go deeper in detail, it could be noticed in Fig.4.32(a,b), that the maximum normal pressure decreases slightly when the friction coefficient increases, in the presence of the heterogeneity or not. Then, Fig.4.32(c,d) indicates that for a friction coefficient up to $f = 0.1$ the maximum plastic strain profiles are nearly alike in each homogeneous or heterogeneous case. A marked growth occurs in the maximum plastic strain evolution when the friction coefficient is greater than $f = 0.1$. If the body is homogeneous then the peak of ε^p_{max} triple when switching from $f = 0.1$ to $f = 0.25$. Moreover, when the body is heterogeneous, ε^p_{max} trend changes completely for $f = 0.15$, $f = 0.2$ and $f = 0.25$. These profiles reflect some very sharp increase of the plastic strain before their calculations were stopped. Let's mention that when the friction coefficient increases, the profiles of the maximum plastic strain versus the rolling distance, in Fig.4.32(d), tends to behave similarly as the damage D versus the number of fretting cycles N_{cyc}, in Fig.B.3 from [129], see Appendix. B.3. One can see in Fig.4.32(e,f) that maximum shear stress profiles are almost parallel and shifted by a difference which can be partially attributed to the additional shear stress produced by the Coulomb friction shear force, in each homogeneous or heterogeneous case. Afterwards, the residual stress at the end of the unloading, has the same level when the friction coefficient remains below $f = 0.1$, whatever the body is homogeneous or heterogeneous. It should be specified that, in the heterogeneous case, before calculations were stopped for $f = 0.15$, $f = 0.2$ and $f = 0.25$, the maximum shear stress magnitude changes its slope and get increasing conversely to their trend which normally decreases so far. All considered, the friction coefficient of $f = 0.1$ is found to the lower bound of the severity of the additional plasticity coming from the shear force. Over this limit value, the merging of the friction stress with the heterogeneity reaction stress could aggravate the potential damage.

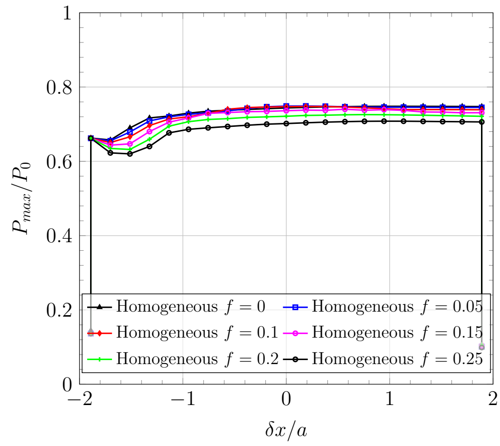

(a)

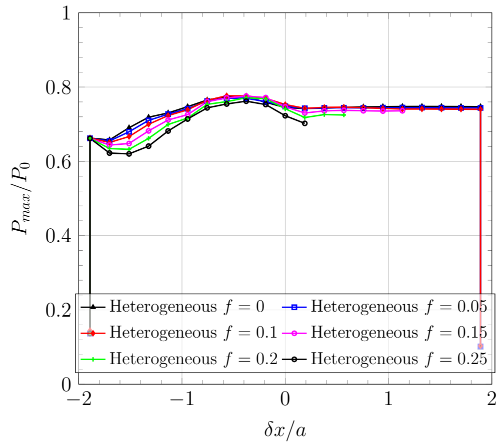

(b)

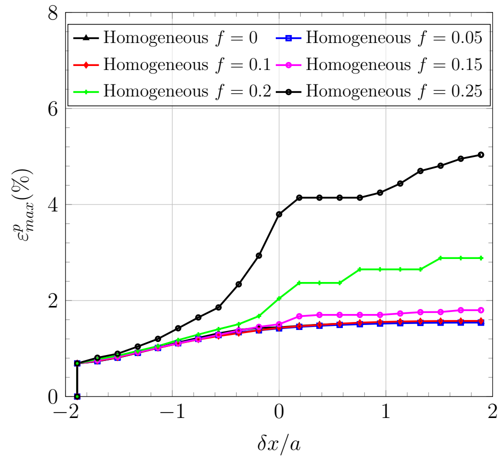

(c)

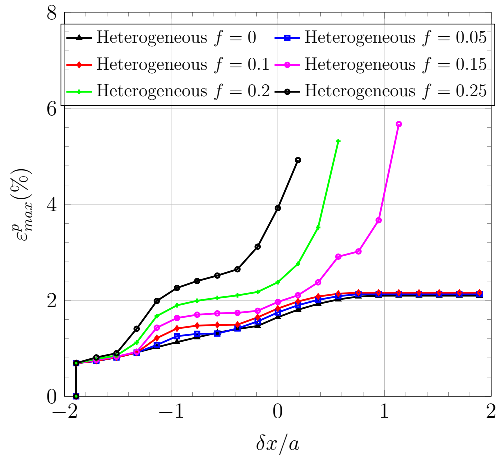

(d)

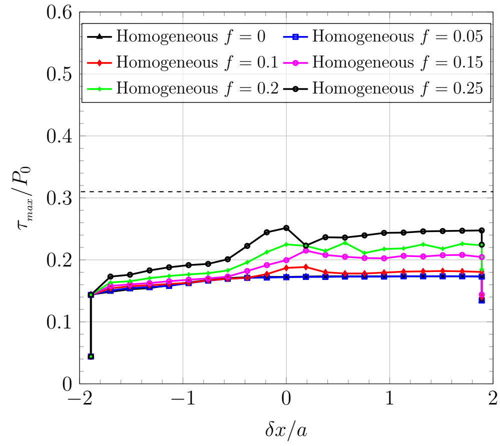

(e)

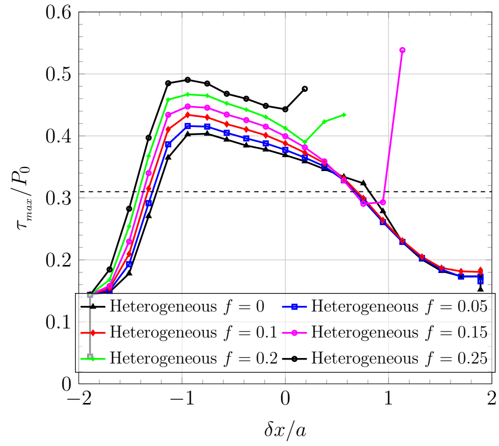

(f)

Parameter	value
Heterogeneity size	$S_i = 0.1a$
Heterogeneity location	$z_i = 0.5a$
Heterogeneity elastic modulus	$E_I = 490GPa$
Friction Coefficient	$f = 0.0$ for full lubricated and non-roughness
Friction Coefficient	$f = 0.1$ for deficient lubrication and low roughness

Figure 4.32: Fields evolution according to friction coefficient: (a) Contact pressure; (b) Equivalent plastic strain; (c) Maximum shear stress

4.5 PARTIAL CONCLUSION

Encouraged by the increase of computer capacities, numerical simulation tools become predominant alternative for a large operating range of investigations. Even if models are limited by some assumptions, they are getting more realistic and essential for understanding complex mechanisms and especially in tribology. The heterogeneous elastic-plastic rolling contact (HEP-RC) analysis has been carried out with a lowered yield strength compared to the real bearing material in purpose to highlight and to amplify the plasticity phenomena. Different fields have been analyzed in order to deepen the knowledge about the mechanical responses of the heterogeneous elastic plastic body subjected to a rolling contact. Hence, the evolution of the contact pressure, plastic strain, shear stress and hydrostatic pressure are fully monitored and recorded during the motion as well as all over the cycles. The HEP-RC model based on semi analytical method proposes a combined study of the role of the size, depth, material properties and distribution of the heterogeneities, along with the contacting surfaces friction properties and their elastic-plastic behavior. Heterogeneity stringers and clusters have been replicated accounting their mutual interaction and density. Investigations have been conducted on the effect of material hardening properties as the plasticity gradient and the initial stress. Throughout this numerical study, the critical effects of heterogeneous inclusions have been characterized and provide the insight of the ensuing bearing life calculation by using the accurate stress-strain magnitude.
Several remarks should be kept, first noted that under the same condition, incompressible heterogeneity produces more plastic strain than porosity. The latter produces more than the considered stiff heterogeneity. It is worth noting that the results obtained when the matrix is assumed elastic, lead to very different ranking of the *overstress* produced by heterogeneity according to their nature. Special care must be taken to the elastic-plastic behavior before calcifying the harmfulness of heterogeneity owing to their type. However, one important finding is that, during the rolling contact, the given smallest porosity studied, regardless of its location in depth, produces more eigenstress than any given larger sized carbide, located at any depth except when the carbide appears at the surface. In addition, fatigue analysis by Dang Van crack initiation criterion more exhibits the severity of porosity and incompressible heterogeneity comparing against a given stiff heterogeneity. Moreover, when many stiff heterogeneities formed a stringer, the material area between them is exposed to a very likely damage risk than the rest of the material mostly when the stringer is vertical. Therefore employed materials should be designed to endure such heterogeneity detrimental effect. Also this paper raises two interesting points. On the one hand, the effect of the surface friction has been found amplified by the presence of stiff heterogeneity. This conclusion should be underlined since it confirms experimental observations that are not supported by conventional elastic analysis, all the more because the plastic strain increases inexorably when the friction exceeds a certain threshold. On the other hand, the critical point is quickly reached in ratcheting regime because the stiff heterogeneity accelerates and sustains the plastic flow even if the stress evolution over cycles indicates a stable closed-loop and its path never cross the Dang Van line. The last success of this study is the fact that it confirms qualitatively the main feature of plasticity phenomena under rolling contact, and to some extent quantitatively the behavior of bearing materials containing multiple heterogeneites.

Part III

ACADEMIC AND INDUSTRIAL APPLICATIONS

Two specific studies are conducted hereafter. Firstly, the semi analytical model is used to investigate the effective elastic-plastic behavior of heterogeneous material subjected to contact loading. Classic homogenization methods are restricted by their own fundamental assumptions when it comes to estimate the overall inelastic and non-linear properties of a representative volume loaded on its free boundary by indentation. Secondly, the micromechanical characterization of M50 and M50NiL is conducted experimentally. The different thermochemical treatments of these materials lead to a graded microstructure and an introduction of compressive residual stress that enhances the RCF resistance. However the non-metallic inclusions precipitated during the thermochemical processes are found to be the responsible of the subsurface damage risk. The rolling contact model is applied to clearly identify the effect for heterogeneity clustering.

5 EFFECTIVE PROPERTY ANALYSIS OF ELASTIC-PLASTIC HALF SPACE CONTAINING HETEROGENEOUS INCLUSIONS UNDER CONTACT LOADING

The objective of this study is to characterize the effects of the presence of multiple heterogeneities on the effective properties of a body under contact loading. First, a heterogeneous elastic-plastic half space is subjected to a contact load and the macroscopic response in terms of load-displacement relation is analyzed. The effective macroscopic elastic-plastic properties are provided by identification on the indentation curve of a homogeneous half-space having equivalent properties, using a reverse Levenberg-Marquadt algorithm. The final effective elastic modulus, yield stress and other effective hardening parameters can indeed be deduced from the load-displacement curve. The role of inclusion size, location and material properties, along with the hardening properties of the indented body are investigated. Special care is devoted to the heterogeneities content and distribution evolution within the representative elementary volume (REV) considered under the contact. A semi analytical method is used for the indentation simulations due to its efficiency to solve contact problems when the contacting bodies are heterogeneous and/or behave plastically. The coupling between the semi-analytical method and the inverse analysis offers the possibility to obtain the nonlinear macroscopic behavior. This method proposes improvements compared to more classical homogenization methods that are (i) used to investigate properties in the elastic domain only and (ii) not accurate for a volume close to a free or loaded surface.

Contents

5.1 INTRODUCTION

Appropriate selection of material to meet specific end-use requirement in a functional system have been one of the principal objectives of research topics in mechanical and civil engineering frameworks from the beginning of these disciplines. During centuries, extensive progress is achieved in the comprehension of the relations between the mechanical properties, chemical compositions, micro/macro structures and the material resistance under a given condition (static or dynamic loading). Materials started to be tailored by mixing different components leading to alloys. Since 1980s powder metallurgy along with forging techniques introduces a manufacturing process that allows to design material approaching the intended properties with very acceptable tolerances. Mix between the host material (the matrix) and carbides, ceramics, borides, oxides or nitrides are the main elements used to compose new alloys having superior properties in comparison to conventional fabrication process [130]. But knowing that tolerances are getting narrow because of economic challenges, international standards and environmental issues, there still is a need of process that can be entirely controlled to achieve perfectly desired properties [131]. Thermo-chemical treatments also contribute to increasing surfaces toughness while maintaining subsurface ductility (plastically graded material PGM). Nowadays innovations in processing routes lead to build materials that can have an alternately layered structure with dense and porous layers. This was experimented for silicon nitride as a strategy to augment strain to failure [132]. Silicon nitride is used in hybrid bearing technology because it was found to offer excellent resistance at high temperature without deterioration even in corrosive environment. But the outstanding mechanical performance of hybrid bearings is affected by the porosity volume fraction contained in the silicon nitride [133, 134].

However, the more heterogeneous the materials become, the more the subsequent effects on the local and global behavior become complex to be completely controllable and predictable. A practice common and widespread in structural mechanics is to replace any encountered heterogeneous constituent by a homogenized fictive material. The effective properties are currently determined by experimental tests. Traditionally, the fatigue strength of steels is usually considered propositional to the hardness and tensile strength. Also the rule of mixture is a well-known law to estimate overall behaviors of heterogeneous bodies. But advancements in experimental methods confirm some of empirical models when others are found obsolete. Therefore designers must be careful when generalizing these laws, since for instance, service condition and environment can significantly influence the most faithful one. Especially for bearing steel, the fabrication process and service conditions influence massively the elements macroscopic property because of the microstructure transformations that occurs de facto at microscopic scales. Even if excellent properties are obtained before commissioning, such as ductility and fracture strength improvement, the accumulation of micro plasticity along with the evolution of grain sizes, are such factors that affect the mechanical properties over rolling cycles. The surface hardness decreases above annealing temperature. In addition, manganese (Mn) content in most of these steels promotes austenitic structure. This leads to $FeMn_3C$ carbides segregation which happened because of an annealing produced by a local heating of the order of 800°C typically in aeronautic mechanisms (turbojet engines). The segregation phenomenon can also occur during cold rolling. Property degradation can be attributed to the dissipated energy in the form of heat escaping from sliding areas around the contact zone [135]. The material macroscopic response is sensitive to any change and any perturbation which occur at microscopic scale. Therefore the homogenization must take into account microstructure aspects such as plasticity, heterogeneity, porosity and damage.

Analytical models provide trusted bounds to frame the effective elastic properties, but with respect to some assumptions limiting their application fields. Some empirical model [136] and classic homogenization techniques such as self-consistency are based on such analytical solutions [137]. Apart from material properties, the unique input of many analytical models is the heterogeneities volume fraction. But this is not a sufficient feature to access realistic effective properties. Investigating on porous material properties, authors found experimentally some relationship between the pores shape [138] and the elastic modulus [139] beside a given volume fraction. The purely analytical models become obsolete and need to be coupled with numerical methods that can, for example, allow to discretize complex heterogeneity forms into multiple simple cells.

The improvement in calculation machines capabilities promoted the establishment of computational homogenization techniques to push forward investigations on global behavior of structures having a nonuniform local behavior. Sophisticated numerical approaches propose solutions incorporating more complex phenomenological aspects (plasticity, creep, eigenstrain from different origins) based on strong micromechanics theories. From the pioneering and famous works of Eshelby [27], Mori T and Tanaka K [140], Hashin and Shtrikman [141], Hill [142], significant progress has been made by Wills [143], Suquet [144, 145], Suresh [146], to integrate inelastic and nonlinear constitutive behavior of the heterogeneous phases. For instance, studies [147, 148] have proposed successfully easy implementable methods to obtain the homogenized properties when the medium repeats a certain periodic pattern. Recent development enhanced this method for modeling sintered porous material in [149]. It was validated by a good agreement with available experimental data. However the analysis is restricted to elastic properties. Also, a representative unit cell (RUC) is considered and it is difficult to correlate these results with a real REV overall behavior because of the structural size ratio between the RUC and the REV. The statistical estimation of the REV size regarding the number of heterogeneity which must be included, has been well studied and documented in[150, 151, 152, 153] to cite a few of the earliest contributions (concerning nonlinear mechanical properties). The influence of the REV choice on the overall property predictions obtained by computational homogenization approaches are discussed in [154]. This influence has been quantified for perfectly periodic heterogeneous material subjected to a dynamic excitation in [155]. In addition, it has been highlighted in [156] that heterogeneity size, distribution and inter-distance have strong impact of the homogenized behavior. The structural and the microstructure sizes effect on the homogenized plastic behavior is described in [157]. Gitman claimed in [158] that the REV size should be generally lager in an elastic-plastic matrix, than for a linear elastic case. However no recommendation exists on REV that will be subject to a strong stress gradient as especially in contact loading condition. Therefore, a new method of REV dimensions determination has been proposed here, taking into consideration the heterogeneity size and distribution.

Computational homogenization techniques are mainly used for the composite constituents having nonlinear behaviors (plasticity [159, 160], thermoelasticity [161]). A numerical homogenization method has been proposed in [162] taking into account the size effects of a hyper-elastic fiber embedded in a hyper-elastic-plastic matrix material but the model is only applied to unidirectional fiber reinforced composite materials. Then the analysis conducted is restricted to two-dimensional domain and the fibers are oriented in the same direction. However the robust Nonuniform Transformation Field Analysis developed by Suquet *et al.* in [163] and improved in [164], enables to obtain the overall constitutive relations of a three-dimensional REV containing randomly oriented fibers. The macroscopic strength solution has been formulated in [165, 166] for ductile porous materials. However the REV is subjected to axisymmetric uniform strain rate boundary conditions. Indeed, thanks to Saint-Venant's principle is often assumed, during homogenization procedures, that an imposed strain at infinity is equivalent to a uniform average strain over the REV, [167]. But, under the Hertzian contact configuration, the contacting bodies are semi-infinite and the generated stress or strain has a strong gradient along the loading direction. If the REV is selected in the vicinity of the contact surface, then nonuniform boundary conditions can be considered on the REV edge. Moreover, by considering a rough surface layer, it has been figured out in [168], that the REV's effective behavior depends on the surface state.

Asymptotic homogenization based on FEM is also one of the numerical approaches used to apply nonuniform boundary conditions on the REV edge [169, 170]. This method has been used in [171] to characterize the effective properties of porous biomaterials. Even if FEM enables integration of the structure design, excessive computational times constitutes a crucial limitation. Yet, solving three dimensional contact problem involving heterogeneity or plasticity with FEM proved by Wang and coworkers [95] has been too time consuming, compared to Semi Analytical Method (SAM), especially when fine mesh is required to capture fields in interesting zones. The efficiency and the fast convergence of SAM is guaranteed by the use of Conjugated Gradient Method (CGM) [50] and Fast Fourier Transform FFT [53] techniques. FFT method demonstrated their efficiency in terms of speed, during effective properties investigations on composite reported in [172], compared to FEM for the same result quality. For two dimensional computation, typical CPU times are roughly 13 minutes with the FFT method against 5 hours with the FEM. In this study the media undergoes non-homogeneous eigenstrain, but the microstructure is considered periodic and homogeneous stress or strain boundary conditions are assumed which means that the applied load is uniformly distributed.

Further enhancement in SAM takes into account the effect of nonlinear behavior as plasticity [37], thermal-elastic-plasticity [99], dynamic effect [55], visco-elasticity [100] along with the presence of heterogeneous inclusion from different origins [66, 41], fretting stick-slip [51, 40] and lubricated plasto-elastohydrodinamic [103]. In a recent study conducted by Hayashi and Koguchi [173] a semi analytical model of elastic-plastic contact has been proposed for anisotropic materials. But the plastic strain and residual stress generate in the subsurface are not calculated and their effect is not integrated in the contact solver. The latter is instead performed by imposing a contact pressure upper limit standing for the effect of the yield stress as a constraint in the CGM. This increases the contact projection area and the yielding region can be identified under the corresponding uniform distribution of the contact pressure. Conceding that the resolution of the contact problem is essential to provide the macroscopic behavior of the contacting bodies in terms of the load displacement, a numerical solver of heterogeneous elastic plastic contact problem has been proposed in [104] by fully coupling contact, plasticity and heterogeneity interactions in the same method. This algorithm is coupled with a minimization technique in the present homogenization method, as in [174]. The overall properties are obtained by optimizing the gap between the heterogeneous material response and that of the actual homogeneous material. The present work is dedicated to bearing industry which engages for high performance (strength, fracture-toughness) material as AISI 52100 steel, M50 and M50 NiL (an improved processing variant of M50 having additional nickel but low-carbon). The latter materials owe their strengthening to the presence of carbides and nitrides together with intermetallic particles. Let's specify that the dimensionless analysis conducted in this study, enables the consideration of different properties of materials (matrix and phases).

5.2 HOMOGENIZATION BY INDENTATION REVERSE ANALYSIS

The investigation on the effective properties of the Representative Elementary Volume (REV) is a widespread topic with purpose to predict the macroscopic behavior of a real structure. However, the existing homogenization methods are limited by some assumptions as the fact that (i) the load is applied far from the interesting zone leading to, by the Saint-Venant principle; (ii) a distributed load quasi uniformly distributed on the REV boundaries as illustrated by Fig. 5.1. In addition (iii) the distribution of the heterogeneous phases is not taken into consideration. Finally (iv) the analysis holds only when the material is assumed to have a linear and elastic behavior.

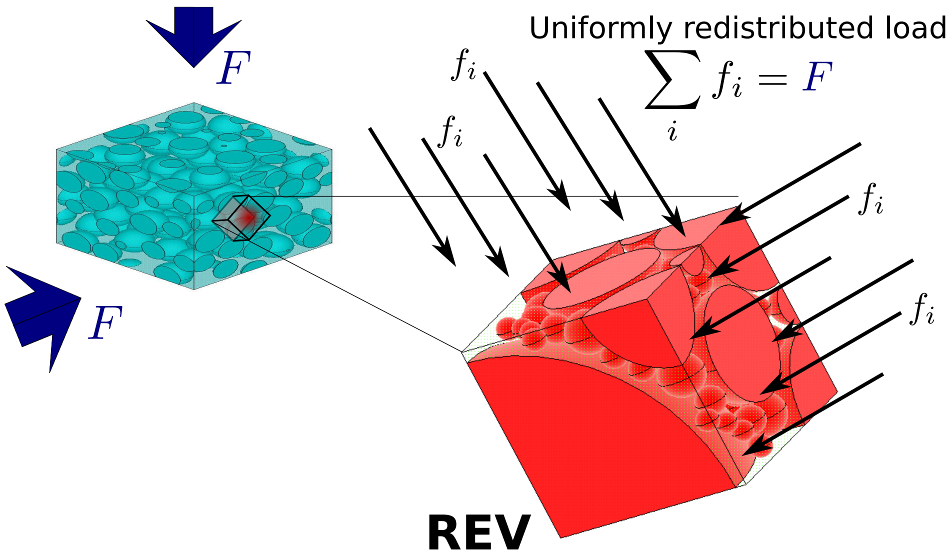

Figure 5.1: Equivalent uniformly redistributed load applied on the Representative Elementary Volume

The homogenization is unavoidable, when sizing materials involved in transmission of load or motion such as gears, wheels/rails, bearings. Indeed, most mechanisms are operated through contacting surfaces (except mechanisms run via gravitational or electro-magnetic forces). Hence in the need of effective properties, designers are constrained by the aforementioned assumptions especially when the bodies mesoscopic behavior is heterogeneous elastic plastic. Fig. 5.2 shows a typical example of a Hertzian contact applied on a free surface leading to a graded stress field inside the REV.

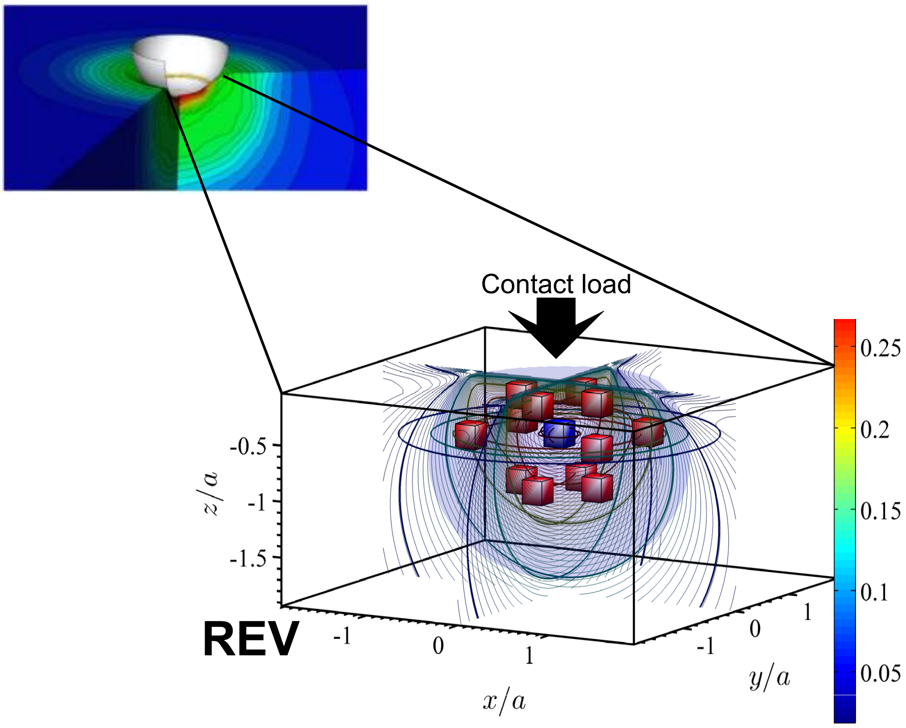

Figure 5.2: Contact load applied on the Representative Elementary Volume

5.2.1 REVIEW OF HOMOGENIZATION METHODS ASSUMING UNIFORMLY LOADED REV

The classic homogenization theoretical background is shortly recalled here. The main assumptions and their consequences on the homogenized solutions are also discussed. Most of the equations are referenced with their corresponding authors or bibliography to provide sources to readers who are seeking more details.

5.2.1.1 Equilibrium equation formulation for heterogeneous material

The solution in terms of displacement, strain and stress $(u, \underline{\varepsilon}, \underline{\sigma})$ within an infinite elastic body, must satisfy the following equilibrium equation:

$$\sigma_{ij,j} + f_i = 0 \tag{5.1}$$

Where f_i is the applied body force. The material behavior is provided by Hooke's law as:

$$\sigma_{ij} = C_{ijkl}\varepsilon^e_{kl} \tag{5.2}$$

Where C_{ijkl} is the fourth order tensor describing the material elastic stiffness properties and ε^e_{kl} the elastic strain tensor which is $\varepsilon^e_{kl} = \dfrac{1}{2}(u_{k,l} + u_{l,k})$. Eq. (5.1) becomes:

$$C_{ijkl}u_{k,lj}(x) + f_i = 0 \tag{5.3}$$

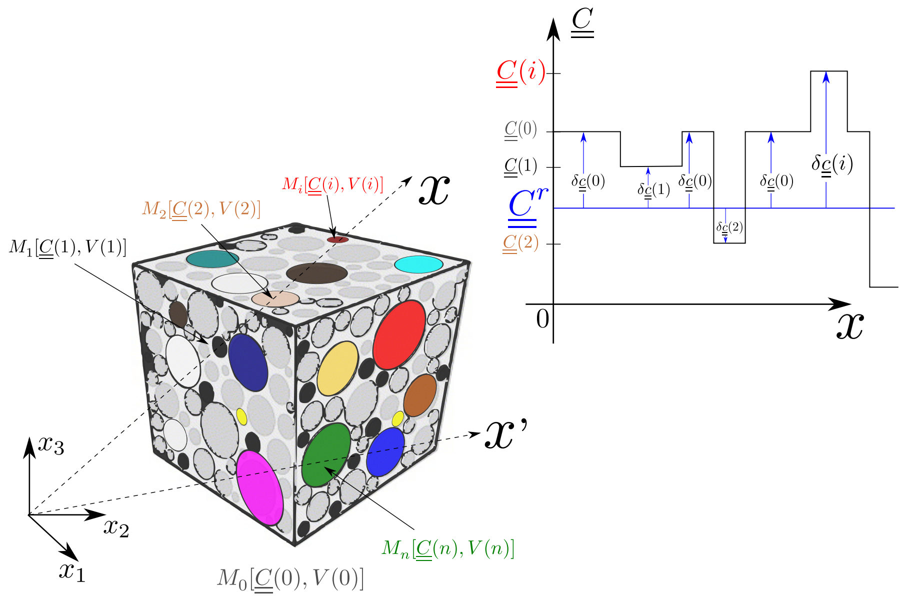

Figure 5.3: Modeling heterogeneous body by a reference homogeneous material containing property fluctuation along any arbitrary direction

Now the stiffness tensor of a heterogeneous body (See Fig. 5.3) can be modeled, by inserting a *homogeneous reference material* of stiffness $\underline{\underline{C}}^r$ and the property fluctuation $\underline{\underline{\delta c}}(x)$, so-called *polarization tensor*, as:

$$C_{ijkl}(x) = C^r_{ijkl} + \delta c_{ijkl}(x) \tag{5.4}$$

Where x is the position vector reflecting the localization of properties within the heterogeneous body. Eq. (5.4) allows Eq. (5.3) to be written into an auxiliary problem as:

$$\begin{aligned} &C^r_{ijkl}u_{k,lj}(x) + \Big[\delta c_{ijkl}(x)u_{k,l}(x)\Big]_{,j} + f_i = 0 \quad \Rightarrow \quad \text{Heterogeneous body} \\ &\text{Let, } \delta f_i(x) = \Big[\delta c_{ijkl}(x)u_{k,l}(x)\Big]_{,j} \text{ and, } f^T_i(x) = \delta f_i(x) + f_i \text{ then} \\ &C^r_{ijkl}u_{k,lj}(x) + f^T_i(x) = 0 \quad \Rightarrow \quad \textit{Homogeneous reference body} \end{aligned} \tag{5.5}$$

Where $f^T_i(x)$ is the total volume force applied to the *Homogeneous reference body* and $\delta f_i(x)$ a fictive body force standing for the heterogeneous body property fluctuation. Let $\delta u_i(x)$ be the displacement field in response to the fictive body force $\delta f_j(x')$ applied on each heterogeneity surface S'.
$\delta u_i(x)$ can be expressed in terms of the elastic Green's function $G_{ij}(x, x')$ integrated around S' as:

$$\delta u_i(x) = \int_{S'} G_{ij}(x, x')\delta f_j(x')dS' \tag{5.6}$$

Where $G_{ij}(x, x')$ is defined as the displacement in the $i-\text{direction}$ at $x-\text{point}$, due to the force in the $j-\text{direction}$ at $x'-\text{point}$. The elastic Green's function existence can be proven by the solution uniqueness of the equilibrium equation: $C_{ijkl}G_{im,jl}(x, x') + \delta_{mk}\delta(x, x') = 0$. Where $\delta(x, x')$ is Dirac's delta function and δ_{nk} is Kronecker's delta

function. The consequence of the Dirac function integration as $\int_{-\infty}^{+\infty} \delta(x, x')g(x')dx' = g(x)$ for a given function g allows to express the entire solution field by knowing a single solution under the elastic linear behavior assumption. In this case $\underline{G}$ only depends on the relative displacement as $G_{ij}(x, x') = G_{ij}(x - x')$.
Writing $\delta f_j = \tau_{jk} n_k$ where τ_{jk} is the so-called the polarization residual stress, Eq. (5.6) becomes:

$$
\begin{aligned}
\delta u_i(x) &= \int_{S'} G_{ij}(x-x')\tau_{jk}n_k(x')dS' \\
\text{then,} \quad \delta u_{i,j}(x) &= \int_{S'} G_{il,j}(x-x')\tau_{lk}(x')n_k dS' \\
\text{with,} \quad \delta\varepsilon_{ij} &= \tfrac{1}{2}(\delta u_{i,j} + \delta u_{j,i}) \\
\delta\varepsilon_{ij}(x) &= \int_{S'} \frac{1}{2}\left[G_{il,j}(x-x') + G_{jl,i}(x-x')\right] n_k \tau_{lk}(x')dS' \\
&= \int_{V} \frac{1}{2}\left[G_{il,jk}(x-x') + G_{jl,ik}(x-x')\right] \tau_{lk}(x')dV' \\
\text{since,} \quad \tau_{kl} &= \delta c_{klmn}\varepsilon_{kl} \\
\text{finally,} \quad \delta\varepsilon_{ij}(x) &= \int_{V} \frac{1}{2}\left[G_{il,jk}(x-x') + G_{jl,ik}(x-x')\right] \delta c_{klmn}(x')\varepsilon_{mn}(x')dV'
\end{aligned}
\tag{5.7}
$$

Let E^r_{ij} be the strain field of the homogeneous reference material, in response to the applied body force f_i from Eq. (5.5). Yet, $\delta\varepsilon_{ij}$ is found to be the solution ensuing from the fictive body force δf_i problem. Under small strain assumption, since, $f^T_i = f_i + \delta f_i$, the general solution in terms of strain yields to $\varepsilon_{ij}(x) = E^r_{ij} + \delta\varepsilon_{ij}(x)$, so-called the *Lippmann-Schwinger integral* equation [175]:

$$
\varepsilon_{ij}(x) = E^r_{ij} - \int_V \Gamma_{ijkl}(x-x')\delta c_{klmn}(x')\varepsilon_{mn}(x')dV' \tag{5.8}
$$

Where $\underline{\underline{\Gamma}}$ is Green's tensor modified by Kröner [176] as $\Gamma_{ijkl} = -\dfrac{1}{2}\left(G_{ik,jl} + G_{jk,il}\right)$. Note that Eq. (5.8) contains its solution within the integral term. Then it cannot be solved explicitly. This constitutes the point of departure of most homogenization procedures. One of the first approach is based on the Neumann series development discussed by Moulinec and Suquet in [177, 144]. Some iterative numerical solutions [178] apply the Fast Fourier Transformation (FFT) to efficiently solve the convolution production from Eq. (5.8). A weak formulation[a] based on Hashin-Shtrikman [141, 179] variational energy principle, has been reformulated into average elastic equivalent work to provide accurate bound of the effective properties by FFT-based numerical method in Brisard and Dormieux (2012) [180] . Otherwise, various homogenization methods have been established since Eshelby's [181] Equivalent Inclusion Method (EIM) presented here.

[a] *Multiplying the initial equation by an arbitrary field and then applying integration on each term of the equation: So-called* Galerkin formulation

5.2.1.2 Equilibrium equation formulation for homogeneous material containing incompatible strain

Let suppose that the homogeneous material contains inclusion (*e.i.* same properties as the matrix) having incompatible strain $\underline{\varepsilon}^*$, so-called eigenstrain (See Fig. 5.4). The elastic strain tensor becomes $\varepsilon^e_{kl} = \frac{1}{2}\left(u_{k,l} + u_{l,k}\right) - \varepsilon^*_{kl}$ in the inclusion.

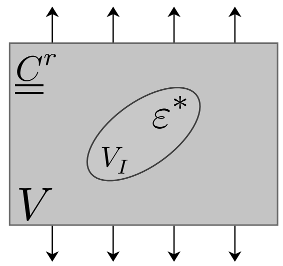

Figure 5.4: Homogeneous reference material containing incompatible strain

The Equilibrium equation Eq. (5.1) is written as:

$$C^r_{ijkl}u_{k,lj}(x) - C^r_{ijkl}\varepsilon^*_{kl,j}(x) + f_i = 0 \quad \Rightarrow \quad \text{Homogeneous body with incompatibility}$$

Let, $f^*_i(x) = C^r_{ijkl}\varepsilon^*_{kl,j}(x)$ and, $f^T_i(x) = -f^*_i(x) + f_i$ then

$$C^r_{ijkl}u_{k,lj}(x) + f^T_i(x) = 0 \quad \Rightarrow \quad \textit{Homogeneous reference body} \tag{5.9}$$

Where $f^T_i(x)$ is once again the total volume force applied to *Homogeneous reference body* and $f^*_i(x)$ a fictive body force reflecting the presence of incompatible strain applied to the inclusion surface S_I.
The homogeneous incompatible problem is written as $C^r_{ijkl}u_{k,lj}(x) - C^r_{ijkl}\varepsilon^*_{kl,j}(x) = 0$.
The solution is constructed by Eshelby [27] using the following four steps of a *"virtual experiment"*.

Step 1

Remove the inclusion and allow it to undergo a stress-free strain: Fig. 5.5

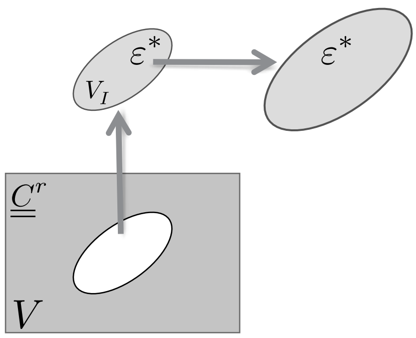

Matrix	Inclusion
$\varepsilon_{ij} = 0$	$\varepsilon_{ij} = \varepsilon^*_{ij}$
$\sigma_{ij} = 0$	$\sigma_{ij} = 0$
$u_i = 0$	$u_i = \varepsilon^*_{ij}x_j$

Figure 5.5: Single inclusion problem: Step 1

Step 2

Apply surface traction to S_I in order to make the inclusion return to its original shape: Fig. 5.6

The inclusion elastic strain should exactly cancel the eigenstrain, then $\varepsilon_{ij}^{el} = -\varepsilon_{ij}^{*}$ and $T_j = \sigma_{ij} n_i = -\sigma_{ij}^{*} n_i$

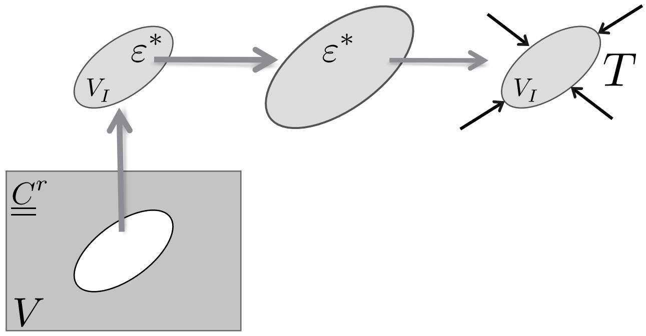

Matrix	Inclusion
$\varepsilon_{ij} = 0$	$\varepsilon_{ij} = \varepsilon_{ij}^{*} + \varepsilon_{ij}^{el} = 0$
$\sigma_{ij} = 0$	$\sigma_{ij} = C_{ijkl}^{r} \varepsilon_{kl}^{el} = -C_{ijkl}^{r} \varepsilon_{kl}^{*} = -\sigma_{ij}^{*}$
$u_i = 0$	$u_i = 0$

Figure 5.6: Single inclusion problem: Step 2

Step 3

Put the inclusion back to the matrix: Fig. 5.7

There is no change on the deformation fields found in Step 2, either in the inclusion or in the matrix.

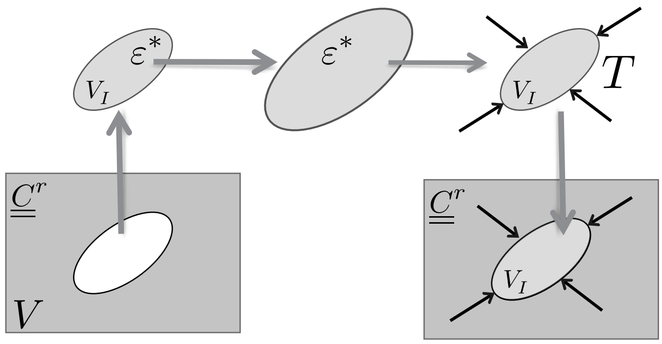

Matrix	Inclusion
$\varepsilon_{ij} = 0$	$\varepsilon_{ij} = \varepsilon_{ij}^{*} + \varepsilon_{ij}^{el} = 0$
$\sigma_{ij} = 0$	$\sigma_{ij} = C_{ijkl}^{r} \varepsilon_{kl}^{el} = -C_{ijkl}^{r} \varepsilon_{kl}^{*} = -\sigma_{ij}^{*}$
$u_i = 0$	$u_i = 0$

Figure 5.7: Single inclusion problem: Step 3

Step 4

Cancel the held surface traction by applying the opposite force $F_j = -T_j = \sigma_{jk}^{*} n_k$ on inclusion: Fig. 5.8

Let $u_i^c(x)$ be the *"constrained"* displacement field in response to the opposite force

$F_j(x')$ applied on the inclusion surface S_I. Hence, $u_i^c(x)$ can be expressed in terms of the elastic Green's function $G_{ij}(x, x')$ integrated around S_I as:

$$
\begin{array}{lrcl}
 & u_i^c(x) & = & \int_{S_I} G_{ij}(x, x')F_j(x')dS \\
 & & = & \displaystyle\int_{S_I} G_{ij}(x - x')\sigma^*_{jk} n_k(x')dS \\
\text{then,} & u_{i,j}^c(x) & = & \displaystyle\int_{S_I} G_{il,j}(x - x')\sigma^*_{lk}(x') n_k dS \\
\text{with,} & \varepsilon^c_{ij} & = & \frac{1}{2}(u^c_{i,j} + u^c_{j,i}) \\
 & \varepsilon^c_{ij}(x) & = & \displaystyle\int_{S_I} \frac{1}{2}\left[G_{il,j}(x - x') + G_{jl,i}(x - x')\right] n_k \sigma^*_{lk}(x')dS \\
 & & = & \displaystyle\int_{V_I} \frac{1}{2}\left[G_{il,jk}(x - x') + G_{jl,ik}(x - x')\right] \sigma^*_{lk}(x')dV \\
\text{since,} & \sigma^*_{kl}(x') & = & \sigma^*_{kl} = C^r_{klmn}\varepsilon^*_{kl} \ \text{ is constant within the inclusion} \\
\text{and replacing Kröner tensor,} & \varepsilon^c_{ij}(x) & = & -\left[\displaystyle\int_V \Gamma_{ijkl}(x - x')dV\right] C^r_{klmn}\varepsilon^*_{mn} \\
\text{then inserting Eshelby tensor,} & S^{Esh}_{ijmn}(x) & = & -\left[\displaystyle\int_V \Gamma_{ijkl}(x - x')dV\right] C^r_{klmn} \\
\text{finally,} & \varepsilon^c_{ij}(x) & = & S^{Esh}_{ijmn}(x)\varepsilon^*_{mn}
\end{array}
\tag{5.10}
$$

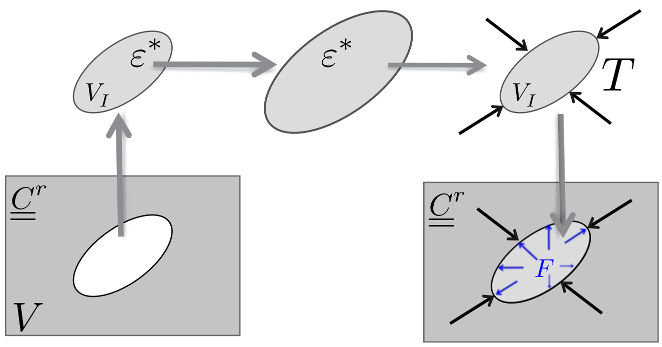

Matrix	Inclusion
$\varepsilon_{ij} = \varepsilon^c_{ij} = S^{Esh}_{ijkl}\varepsilon^*_{kl}$	$\varepsilon_{ij} = \varepsilon^c_{ij} = S^{Esh}_{ijkl}\varepsilon^*_{kl}$
$\sigma_{ij} = \sigma^c_{ij} = C^r_{ijkl}S^{Esh}_{klmn}\varepsilon^*_{mn}$	$\sigma_{ij} = \sigma^c_{ij} - \sigma^*_{ij} = C^r_{ijkl}\left(\varepsilon^c_{kl} - \varepsilon^*_{kl}\right) = C^r_{ijkl}\left(S^{Esh}_{klmn} - \mathcal{I}_{klmn}\right)\varepsilon^*_{mn}$
$u_i = u^c_i$	$u_i = u^c_i$

Figure 5.8: Single inclusion problem: Step 4

Where $\mathcal{I}_{ijkl} = \dfrac{1}{2}\left(\delta_{ik}\delta_{jl} + \delta_{il}\delta_{jk}\right)$ is the symmetric Identity tensor.
Let E^r_{ij} be the strain field of the homogeneous reference material, in response to the applied body force f_i from Eq. (5.5). Yet, ε^c_{ij} is found to be the solution ensuing from the fictive body force f^*_i problem. Under small strain assumption, since $f^T_i = f_i - f^*_i$, the general solution written in terms of strain, yields to $\varepsilon_{ij}(x) = E^r_{ij} - \varepsilon^c_{ij}(x)$ as :

$$\varepsilon_{ij}(x) = E^r_{ij} + \int_V \Gamma_{ijkl}(x - x')C^r_{klmn}(x')\varepsilon^*_{mn}(x')dV' \tag{5.11}$$

For a single ellipsoidal inclusion V_I embedded in infinite matrix V one can assume average fields within the inclusion as $\varepsilon^*_{ij}(x) = \varepsilon^*_{ij}\theta^I(x)$, where θ^I is an indicator function defined as:

$$\theta^I(x) = \begin{cases} 1, & \text{if } x \in V_I \\ 0, & \text{if } x \notin V_I \end{cases} \tag{5.12}$$

Written Eq. (5.11) for the inclusion leads to:

$$\begin{aligned}
\varepsilon^I_{ij} &= E^r_{ij} + \left[\int_{V_I} \Gamma_{ijkl}(x - x')\,dV'\right] C^r_{klmn}\varepsilon^*_{mn} \\
\varepsilon^I_{ij} &= E^r_{ij} + S^{Esh}_{ijkl}\varepsilon^*_{kl} \\
\sigma^I_{ij} &= C^r_{ijkl}\left(\varepsilon^I_{kl} - \varepsilon^*_{kl}\right) \\
\sigma^I_{ij} &= C^r_{ijkl}\left(E^r_{kl} + S^{Esh}_{klmn}\varepsilon^*_{mn} - \varepsilon^*_{kl}\right) \ \text{ let, } \Sigma^r_{ij} = C^r_{ijkl}E^r_{kl} \\
\text{then, } \sigma^I_{ij} &= \Sigma^r_{ij} + C^r_{ijkl}\left(S^{Esh}_{klmn} - \mathcal{I}_{klmn}\right)\varepsilon^*_{mn}
\end{aligned} \tag{5.13}$$

William P. and William D. [182] proved, by reasoning based on energy conservation, that Eshelby's equivalent ellipsoidal inclusion method can be used to find the stress and strain fields in both the matrix and heterogeneity because Eshelby's tensor can always be inverted (its expression is non-singular).

5.2.1.3 Heterogeneous solution with Eshelby tensor

Let's consider a single ellipsoidal heterogeneity (Fig. 5.9) $[V_I, \underline{\underline{C}}^I]$ embedded in an infinite reference matrix $[V, \underline{\underline{C}}^r]$. Note that $\underline{\underline{C}}^I = \underline{\underline{C}}^r + \delta\underline{\underline{c}}^I$ and the strain $\underline{\varepsilon}^I$ field is assumed to be uniform within the heterogeneity.

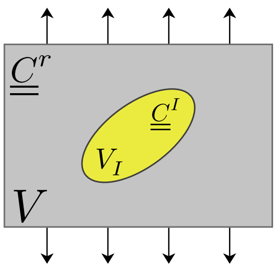

Figure 5.9: Single heterogeneity problem

By writing the Lippmann-Schwinger integral equation Eq. (5.8) for the single ellipsoidal heterogeneity leads to:

$$
\begin{aligned}
\varepsilon_{ij}(x) &= E^r_{ij} - \left[\int_{V_I} \Gamma_{ijkl}(x-x')dV'\right] \delta c^I_{klmn}\varepsilon^I_{mn} \\
\text{defining the heterogeneity average strain as, } \varepsilon^I_{ij} &= \frac{1}{V_I}\int_{V_I}\varepsilon_{ij}(x)dV \\
\text{then, } \varepsilon^I_{ij} &= E^r_{ij} - \left(\frac{1}{V_I}\int_{V_I}\left[\int_{V_I}\Gamma_{ijkl}(x-x')dV'\right]dV\right)\delta c^I_{klmn}\varepsilon^I_{mn} \\
\text{taking, } T^{II}_{ijkl} &= \frac{1}{V_I}\int_{V_I}\left[\int_{V_I}\Gamma_{ijkl}(x-x')dV'\right]dV = S^{Esh}_{ijmn}C^{r^{-1}}_{mnkl} \\
\text{finally, } \varepsilon^I_{ij} &= E^r_{ij} - T^{II}_{ijkl}\delta c^I_{klmn}\varepsilon^I_{mn}
\end{aligned}
\tag{5.14}
$$

From Eq. (5.14), the single heterogeneity problem (Fig. 5.9) is linked to the single inclusion problem (Fig. 5.4) via the Eshelby tensor. Thereby the Eshelby's equivalence principle rises from this result.

5.2.1.4 Equivalence principle

Recognizing that the polarization residual stress $\underline{\tau} = \delta \underline{\underline{c}} \left(\underline{E}^r + \underline{\varepsilon}\right)$ due to the properties fluctuation is equivalent to the eigenstress $\underline{\sigma}^* = \underline{\underline{C}}^r \underline{\varepsilon}^*$ due to the eigenstrain existence, the equivalence principle is described by:

$$
\begin{aligned}
\delta \underline{\underline{c}} \left(\underline{E}^r + \underline{\varepsilon}\right) &= \underline{\underline{C}}^r \underline{\varepsilon}^* \\
\left(\underline{\underline{C}}^r - \underline{\underline{C}}^I\right)\left(\underline{E}^r + \underline{\varepsilon}\right) &= \underline{\underline{C}}^r \underline{\varepsilon}^* \\
\underline{\underline{C}}^I \left(\underline{E}^r + \underline{\varepsilon}\right) &= \underline{\underline{C}}^r \left(\underline{E}^r + \underline{\varepsilon} - \underline{\varepsilon}^*\right)
\end{aligned}
\tag{5.15}
$$

From Eq. (5.15), the eigenstrain becomes the unique unknown of the Equivalent Inclusion Method (EIM). By inserting Eshelby tensor $\underline{\underline{S}}^{Esh}$, the eigenstrain can be explicitly expressed as a function of the heterogeneity stiffness $\underline{\underline{C}}^I$ reference material strain $\underline{E}^r$ and its stiffness $\underline{\underline{C}}^r$ as :

$$
\underline{\varepsilon}^* = -\left[\underline{\underline{S}}^{Esh} + \left(\underline{\underline{C}}^I - \underline{\underline{C}}^r\right)^{-1}\underline{\underline{C}}^r\right]\underline{E}^r \tag{5.16}
$$

5.2.1.5 Multiple heterogeneity problem

Consider a heterogeneous media composed of $N+1$ distinct phases (composites and polycrystals). The property of each phase i of volume $V(i)$ is defined by its stiffness tensor $\underline{\underline{C}}(i)$ represented in Fig. 5.3. The effective stiffness tensor is desired to fulfill this relation:

$$
\underline{\Sigma} = \underline{\underline{C}}^{eff}\underline{E} \tag{5.17}
$$

Where $\underline{\Sigma}$ and $\underline{E}$ are respectively the macroscopic stress and strain defined as the volume average of the local stress $\sigma_{ij}(x)$ and strain $\varepsilon_{ij}(x)$:

$$\begin{aligned} \Sigma_{ij} &= \overline{\sigma}_{ij}(x) &= <\sigma_{ij}(x)> &= \frac{1}{V}\int_V \sigma_{ij}(x)dV \\ E_{ij} &= \overline{\varepsilon}_{ij}(x) &= <\varepsilon_{ij}(x)> &= \frac{1}{V}\int_V \varepsilon_{ij}(x)dV \end{aligned} \tag{5.18}$$

The local strain is related to the macroscopic strain by the localization tensor $A_{ijkl}(x)$ and the local stress is related to the macroscopic stress by the concentration tensor $B_{ijkl}(x)$ as:

$$\begin{aligned} \sigma_{ij}(x) &= B_{ijkl}(x)\Sigma_{kl} \\ \varepsilon_{ij}(x) &= A_{ijkl}(x)E_{kl} \end{aligned} \tag{5.19}$$

If the problem formulation is of the *'applied strain'* type, then the uniformly applied macroscopic strain $\underline{E}$ in Eq. (5.18) is combined with Eq. (5.19) and gives:

$$\begin{aligned} \Sigma_{ij} &= <\sigma_{ij}(x)>=<C_{ijkl}(x)\varepsilon_{kl}(x)>=<C_{ijkl}(x)A_{klmn}(x)E_{mn}>=<C_{ijkl}(x)A_{klmn}(x)>E_{mn} \\ \text{since, } \Sigma_{ij} &= C^{eff}_{ijmn}E_{mn} \\ \text{hence, } C^{eff}_{ijmn} &= <C_{ijkl}(x)A_{klmn}(x)> \end{aligned} \tag{5.20}$$

Else if the problem formulation is of the *'applied stress'* type, then the uniformly applied macroscopic stress $\underline{\Sigma}$ in Eq. (5.18) is combined with Eq. (5.19) leads to:

$$\begin{aligned} E_{ij} &= <\varepsilon_{ij}(x)>=<S_{ijkl}(x)\sigma_{kl}(x)>=<C_{ijkl}(x)B_{klmn}(x)\Sigma_{mn}>=<S_{ijkl}(x)B_{klmn}(x)>\Sigma_{mn} \\ \text{since, } E_{ij} &= S^{eff}_{ijmn}\Sigma_{mn} \\ \text{hence, } S^{eff}_{ijmn} &= <S_{ijkl}(x)B_{klmn}(x)> \end{aligned} \tag{5.21}$$

Where $\underline{\underline{S}} = \underline{\underline{C}}^{-1}$ is the compliance tensor. One can prove that $<\underline{\underline{A}}>=<\underline{\underline{B}}>=\underline{\underline{\mathcal{I}}}$. Finally, $\underline{\underline{A}}$ or $\underline{\underline{B}}$ becomes the unique unknowns of the multiple heterogeneity problem, depending on the applied field.

Back to the $N+1$ phase heterogeneous media (Fig. 5.3), the stiffness distribution field can be modeled as:

$$\begin{aligned} \underline{\underline{C}}(x) &= \underline{\underline{C}}^0\theta^0(x) + \sum_{i=1}^{N}\underline{\underline{C}}^I\theta^I(x) \\ \text{defining, } \Delta\underline{\underline{c}}^I &= \underline{\underline{C}}^I - \underline{\underline{C}}^r \\ \text{then, } \delta\underline{\underline{c}}(x) &= \Delta\underline{\underline{c}}^0\theta^0(x) + \sum_{I=1}^{N}\Delta\underline{\underline{c}}^I\theta^I(x) \end{aligned} \tag{5.22}$$

Where $\underline{\underline{C}}^0$ and $\underline{\underline{C}}^r$ are the matrix and the reference homogeneous media stiffness, respectively. Where again $\theta^I(x)$ is the indicator function defined by Eq. (5.12). Hence, the Lippmann-Schwinger integral equation Eq. (5.8) becomes:

$$\begin{aligned} \underline{\varepsilon}(x) &= \underline{E}^r - \int_{V^0} \underline{\underline{\Gamma}}(x-x') : \Delta\underline{\underline{c}}^0 : \underline{\varepsilon}(x')dV' - \sum_{I=1}^{N} \int_{V^I} \underline{\underline{\Gamma}}(x-x') : \Delta\underline{\underline{c}}^I : \underline{\varepsilon}(x')dV' \\ \text{defining, } \underline{\varepsilon}(x) &= \underline{\varepsilon}^0\theta^0(x) + \sum_{I=1}^{N} \underline{\varepsilon}^I\theta^I(x) \\ \text{hence, } \underline{\varepsilon}(x) &= \underline{E}^r - \int_{V^0} \underline{\underline{\Gamma}}(x-x')dV' : \Delta\underline{\underline{c}}^0 : \underline{\varepsilon}^0 - \sum_{I=1}^{N} \int_{V^I} \underline{\underline{\Gamma}}(x-x')dV' : \Delta\underline{\underline{c}}^I : \underline{\varepsilon}^I \end{aligned} \tag{5.23}$$

Considering the average strain inside any I^{th} phase as: $\underline{\varepsilon}^I = \dfrac{1}{V^I}\displaystyle\int_{V^I} \underline{\varepsilon}(x)dV$, the latter integral equation Eq. (5.23) yields to:

$$\begin{aligned} \underline{\varepsilon}^I &= \underline{E}^r - \sum_{J=0}^{N} \frac{1}{V^I} \int_{V^I}\int_{V^J} \underline{\underline{\Gamma}}(x-x')dV'dV : \Delta\underline{\underline{c}}^J : \underline{\varepsilon}^J \\ \text{defining, } \underline{\underline{T}}^{IJ} &= \frac{1}{V^I} \int_{V^I}\int_{V^J} \underline{\underline{\Gamma}}(x-x')dV'dV \\ \text{hence, } \underline{\varepsilon}^I &= \underline{E}^r - \underline{\underline{T}}^{II} : \Delta\underline{\underline{c}}^I : \underline{\varepsilon}^I - \sum_{\substack{J=0 \\ J\neq I}}^{N} \underline{\underline{T}}^{IJ} : \Delta\underline{\underline{c}}^J : \underline{\varepsilon}^J \end{aligned} \tag{5.24}$$

Where $\underline{\underline{T}}^{IJ}$ is so-called the interaction tensor between any phase I of volume $V^I$and phase J of volume V^J of the heterogeneous media. It can be noticed that $V^I\underline{\underline{T}}^{IJ} = V^J\underline{\underline{T}}^{JI}$. One can also remind from Eq. (5.14) that $\underline{\underline{T}}^{II} = \underline{\underline{S}}^{Esh}\underline{\underline{C}}^{r^{-1}}$. Inserting the strain localization relation $\underline{\varepsilon}^I = \underline{\underline{A}}^I : \underline{E}$ in Eq. (5.24), one can write:

$$\begin{aligned} \underline{\underline{A}}^I : \underline{E} &= \underline{E}^r - \underline{\underline{T}}^{II} : \Delta\underline{\underline{c}}^I : \underline{\underline{A}}^I : \underline{E} - \sum_{\substack{J=0 \\ J\neq I}}^{N} \left(\underline{\underline{T}}^{IJ} : \Delta\underline{\underline{c}}^J : \underline{\underline{A}}^J\right) : \underline{E} \\ \underline{\underline{A}}^I &= \left(\underline{\underline{\mathcal{I}}} + \underline{\underline{T}}^{II} : \Delta\underline{\underline{c}}^I\right)^{-1} : \left[\underline{E}^r : \underline{E}^{-1} - \sum_{\substack{J=0 \\ J\neq I}}^{N} \left(\underline{\underline{T}}^{IJ} : \Delta\underline{\underline{c}}^J : \underline{\underline{A}}^J\right)\right] \end{aligned} \tag{5.25}$$

This induces an implicit determination of the localization tensor since $\underline{\underline{A}}^I$ is a function of itself. Existing homogenization methods come out with particular assumptions and simplification to provide the scheme or algorithm that allows to obtain the localization tensor and then the effective stiffness $\underline{\underline{C}}^{eff}$.

Let's remind that the present study is applied to bearing materials which are plastically graded, owing to multiple carbide inclusions contents along the depth layers. Carbides are typically considered to belong to the same family of stiffness tensor. This leads to a bi-phase media formed by the matrix and the (similar) carbides. Since matrix and carbides are assumed isotropic, there are only two independent elastic constants which expressed the stiffness tensor as $\underline{\underline{C}} = 3K\,\underline{\underline{\mathcal{J}}} + 2G\,\underline{\underline{\mathcal{K}}}$, where K and G are the material bulk modulus and shear modulus, respectively. $\underline{\underline{\mathcal{J}}}$ and $\underline{\underline{\mathcal{K}}}$ are four order tensors defined as $\mathcal{J}_{ijkl} = \frac{1}{3}\delta_{ij}\delta_{kl}$ and $\mathcal{K}_{ijkl} = \mathcal{I}_{ijkl} - \mathcal{J}_{ijkl}$. In this case, it is suitable to write the stiffness tensor like this because its inversion leads to simply express the compliance tensor as $\underline{\underline{S}} = \frac{3}{K}\underline{\underline{\mathcal{J}}} + \frac{2}{G}\underline{\underline{\mathcal{K}}}$.

5.2.1.6 Effective elastic properties: from Eshelby dilute approximation to Mori-Tanaka concentrated scheme

The dilute approximation considers a unique heterogeneity embedded in the matrix m [183]. This equivalent heterogeneity has the sum of volume fractions V_f^I of all N phases as $V_f = \sum_{I=1}^{N} V_f^I$. It is assumed that all phases have the same stiffness. Once the heterogeneity site scheme simplification is made, it is also supposed that $\underline{\underline{T}}^{IJ} \approx \underline{\underline{0}}$ when $I \neq J$. This last assumption is not accurate when heterogeneities are close to each other. The average strain is considered to be the matrix one, $\underline{E} = V_f\underline{\varepsilon}^I + (1 - V_f)\,\underline{\varepsilon}^m \approx \underline{\varepsilon}^m$. This simplification is not accurate for microstructures containing large heterogeneities volume fractions. When the (ellipsoidal) heterogeneity and the matrix are isotropic, the interaction tensor is analytically obtained from Eshelby tensor. Hence, by considering the matrix as the reference homogeneous material, one obtains:

$$\begin{aligned}
\underline{\underline{T}}^{II} &= \underline{\underline{S}}^{Esh}\underline{\underline{C}}^{r^{-1}} \\
\underline{\underline{T}}^{II}_{Esh} &= \underline{\underline{S}}^{Esh}\underline{\underline{C}}^{m^{-1}} \\
\underline{\underline{T}}^{II}_{Esh} &= \frac{1}{3K_m + 4G_m}\left(\underline{\underline{\mathcal{J}}} + \frac{3K_m + 6G_m}{5G_m}\underline{\underline{\mathcal{K}}}\right)
\end{aligned} \tag{5.26}$$

Mura in [56], expressed the Eshelby tensor for some other heterogeneity shapes. One can get the Eshelby's dilute localization tensors, $\underline{\underline{A}}^I_{Esh}$ for the heterogeneity and $\underline{\underline{A}}^m_{Esh}$ from Eq. (5.25) as:

$$\begin{aligned}
\underline{\underline{A}}^I_{Esh} &= \left[\underline{\underline{\mathcal{I}}} + \underline{\underline{T}}^{II}_{Esh} : (\underline{\underline{C}}^I - \underline{\underline{C}}^m))\right]^{-1} \\
\text{since,} \; < \underline{\underline{A}} > &= \underline{\underline{\mathcal{I}}} \\
(1 - V_f)\,\underline{\underline{A}}^m_{Esh} &= \underline{\underline{\mathcal{I}}} - V_f\underline{\underline{A}}^I_{Esh}
\end{aligned} \tag{5.27}$$

Finally, the Eshelby effective stiffness tensor $\underline{\underline{C}}^{eff}_{Esh}$ is obtained by combining Eq. (5.20) with Eq. (5.27), hence:

$$\underline{\underline{C}}^{eff}_{Esh} = \underline{\underline{C}}^m + V_f\left(\underline{\underline{C}}^I - \underline{\underline{C}}^m\right)\underline{\underline{A}}^I_{Esh} \tag{5.28}$$

Thus, the effective bulk modulus K^{eff} and shear modulus G^{eff} can be deducted from Eshelby's dilute approximation as:

$$\begin{aligned} K^{eff} &= K_m + V_f (K_I - K_m) \frac{K_m}{(K_I - K_m)\eta + K_m} \text{ where, } \eta = \frac{3K_m}{3K_m + 4G_m} \\ G^{eff} &= G_m + V_f (G_I - G_m) \frac{G_m}{(G_I - G_m)\varphi + G_m} \text{ where, } \varphi = \frac{6K_m + 12G_m}{15K_m + 10G_m} \end{aligned} \tag{5.29}$$

One can see from Eq. (5.29) that the diluted approximation leads to a linear dependence of the effective modulus on the volume fraction.
Furthermore, Mori T. and Tanaka K. [140] propose their concentrated scheme which reformulate the localization tensor for each individual heterogeneities $I, J, ...N$ of volume fraction $V_f(I, J, ...N)$ based on that of Eshebly as:

$$\begin{aligned} \underline{\underline{A}}^I_{MT} &= \underline{\underline{A}}^I_{Esh} \left(V_f \underline{\underline{J}} + \underline{\underline{A}}_{Esh} \right)^{-1} \\ \text{where, } \underline{\underline{A}}_{Esh} &= \sum_{I=1}^{N} V_f^I \underline{\underline{A}}^I_{Esh} \end{aligned} \tag{5.30}$$

The final Mori-Tanaka effective stiffness is:

$$\underline{\underline{C}}^{eff}_{MT} = \underline{\underline{C}}^m + \sum_{I=1}^{N} V_f^I \left(\underline{\underline{C}}^I - \underline{\underline{C}}^m \right) \underline{\underline{A}}^I_{MT} \tag{5.31}$$

Since each heterogeneity localization tensor is treated separately, Mori-Tanaka concentrated scheme volume fraction could be better than Eshelby dilute approximation one. However, the condition on the interaction tensor ($\underline{\underline{T}}^{IJ} \approx \underline{\underline{0}}$ when $I \neq J$) limits the Mori-Tanaka concentrated scheme in practice when 30% of volume fraction is exceeded because heterogeneities become naturally close to each other inside the considered REV. There are some extensions of Mori-Tanaka by Ferrari [184] and Benveniste [183] taking into account heterogeneities interactions under other assumptions not mentioned here. Hence, the effective bulk modulus K^{eff} and shear modulus G^{eff} can be deducted from Mori-Tanaka concentrated scheme (Benveniste reformulation) as:

$$\begin{aligned} K^{eff} &= K_m + V_f (K_I - K_m) \frac{K_m}{(1 - V_f)(K_I - K_m)\eta + K_m} \text{ where, } \eta = \frac{3K_m}{3K_m + 4G_m} \\ G^{eff} &= G_m + V_f (G_I - G_m) \frac{G_m}{(1 - V_f)(G_I - G_m)\varphi + G_m} \text{ where, } \varphi = \frac{6K_m + 12G_m}{15K_m + 10G_m} \end{aligned} \tag{5.32}$$

5.2.1.7 Effective elastic properties by Hill's self-consistency scheme

The self-consistency method was originally proposed by Hershey (1954) [185] and Kroner (1958) [186], then reviewed and elaborated by Hill (1965) [187]. It suggests choosing the equivalent homogeneous medium as the unknown effective homogeneous medium ($\underline{\underline{C}}^r = \underline{\underline{C}}^{eff}$ then $\underline{E}^r = \underline{E}$). Hence, the effective elastic properties are found by iterative treatment. Once again, the interaction tensor is assumed nil ($\underline{\underline{T}}^{IJ} \approx \underline{\underline{0}}$) when $I \neq J$, restraining the self-consistency scheme to relatively small concentrations of heterogeneities. However, this approximation leads to excellent result compared to the other methods, by enabling numerical approximation of the interaction between different phases even if the analytical interaction tensor is neglected. Because each phase is assumed to be embedded in the effective medium, implying that the other phases are accounted as though they have been already homogenized. The effective bulk modulus K^{eff} and shear modulus G^{eff} can be expressed as:

$$\begin{aligned} K^{eff} &= K_m + \frac{V_f K^{eff}\left(K_I - K_m\right)}{K^{eff} + \eta\left(K_I - K^{eff}\right)} \text{ where, } \eta = \frac{3K_m}{3K_m + 4G_m} \\ G^{eff} &= G_m + \frac{V_f K^{eff}\left(G_I - G_m\right)}{G^{eff} + \varphi\left(G_I - G^{eff}\right)} \text{ where, } \varphi = \frac{6K^{eff} + 12G^{eff}}{15K^{eff} + 10G^{eff}} \end{aligned} \tag{5.33}$$

5.2.1.8 Effective elastic properties by Voigt and Reuss bounds

The original work of Voigt [188] consisted of the minimization of the potential energy for a problem driven by uniform imposed strain. Similarly, Reuss [189] worked on the minimization of the complementary energy for a problem driven by uniform imposed stress. Then, Hill (1952) [190] proved that Voigt and Reuss approximations are upper and lower bounds of the effective stiffness tensor. It was established that:

$$\begin{cases} \underline{E} = & \left(1 - V_f^I\right) \underline{\varepsilon}^m \sum_{I=1}^{N} V_f^I \underline{\varepsilon}^I \\ \underline{\Sigma} = & \left(1 - V_f^I\right) \underline{\sigma}^m \sum_{I=1}^{N} V_f^I \underline{\sigma}^I \end{cases} \tag{5.34}$$

Inserting localization tensor $\underline{\varepsilon}^I = \underline{\underline{A}}^I : \underline{E}$ and concentration tensor $\underline{\sigma}^I = \underline{\underline{B}}^I : \underline{\Sigma}$, Eq. (5.34) leads to:

$$\begin{cases} \underline{\underline{C}}^{eff}_{Voigt} = & \underline{\underline{C}}^m + \sum_{I=1}^{N} V_f^I \left(\underline{\underline{C}}^I - \underline{\underline{C}}^m\right) \underline{\underline{A}}^I_{Voigt} \\ \underline{\underline{S}}^{eff}_{Reuss} = & \underline{\underline{S}}^m + \sum_{I=1}^{N} V_f^I \left(\underline{\underline{S}}^I - \underline{\underline{S}}^m\right) \underline{\underline{B}}^I_{Reuss} \end{cases} \tag{5.35}$$

Voigt bound is found when the strain localization tensor $\underline{\underline{A}}^I_{Voigt} = \underline{\underline{\mathcal{I}}}$ meaning average uniformly imposed strain everywhere inside the heterogeneous media as $\underline{\varepsilon}^m = \underline{\varepsilon}^I = \underline{E}$. Similarly, Reuss bound is found when the stress concentration tensor $\underline{\underline{B}}^I_{Reuss} = \underline{\underline{\mathcal{I}}}$ meaning average uniformly imposed stress everywhere inside the heterogeneous media $\underline{\sigma}^m = \underline{\sigma}^I = \underline{\Sigma}$. For a bi-phase problem one can deduce that:

$$\begin{cases} \underline{\underline{C}}^{eff}_{Voigt} = & V_f^I \underline{\underline{C}}^I + \left(1 - V_f^I\right) \underline{\underline{C}}^m \\ \underline{\underline{S}}^{eff}_{Voigt} = & V_f^I \underline{\underline{S}}^I + \left(1 - V_f^I\right) \underline{\underline{S}}^m \end{cases} \tag{5.36}$$

5.2.1.9 Effective properties by Hashin-Shtrikman bounds

Hashin-Shtrikman [141, 179] variational principles is built on arguments of minimum potential energy. It leads to the lower bound for a problem posed in the form of a uniformly imposed strain. Similarly, the use of the complementary energy leads to the lower bound for a problem posed in the form of a uniformly imposed stress. The effective bulk modulus $K^{eff}_{up/low}$ and shear modulus $G^{eff}_{up/low}$ are:

$$
\begin{aligned}
K^{eff}_{up} &= K_I + \frac{1 - V_f}{\dfrac{1}{K_m - K_I} + \dfrac{3V_f}{3K_I + 4G_I}} \\
K^{eff}_{low} &= K_m + \frac{V_f}{\dfrac{1}{K_I - K_m} + \dfrac{3\,(1 - V_f)}{3K_m + 4G_m}} \\
G^{eff}_{up} &= G_I + \frac{1 - V_f}{\dfrac{1}{G_m - G_I} + \dfrac{6(K_I + 2G_I)V_f}{5G_I\,(3K_I + 4G_I)}} \\
G^{eff}_{low} &= G_m + \frac{V_f}{\dfrac{1}{G_I - G_m} + \dfrac{6(K_m + 2G_m)\,(1 - V_f)}{5G_m\,(3K_m + 4G_m)}} \\
\text{where,} &\quad K_m < K_I \text{ and, } G_m < G_I
\end{aligned}
\tag{5.37}
$$

Note that the effective property bounds are independent of heterogeneity shape and distribution. In practice the upper bound is used when $K_m > K_I$, and lower bound in the opposite case. Hashin-Shtrikman bounds provide a good estimation when the ratio between matrix elastic modulus and embedded phases ones are not too large.

5.2.2 THE HOMOGENIZATION METHOD FOR REV HAVING FREE SURFACE SUBJECTED TO A CONTACT LOAD

The coupling between the semi-analytical method and the inverse analysis offers the possibility to obtain the nonlinear behavior, as the macroscopic yield strength, when most classic homogenization methods are used to determine elastic properties only.

5.2.2.1 Homogenization method by macroscopic response identification

By studying the macroscopic responses of indentation tests, Oliver-Pharr [191] and Herbert [192] have shown that one can capture the reduced[b] $E_{reduced}$ from the unloading part of the load/displacement curves [c] Fig. 5.8(a), assuming that this phase is purely elastic, as :

$$E_{reduced} = \frac{S}{2}\sqrt{\frac{\pi}{A}} \tag{5.38}$$

Where S is the elastic contact stiffness, called the unloading stiffness. A is the projected contact area estimated by the maximum displacement measured during the loading h_{max}, the final plastic depth h_p called indentation print, and the indenter tip geometry (see [193, 194]). Note that $h_{max} < h_e + h_p$,where h_e is the maximum displacement if

[b] *also called equivalent elastic modulus*

[c] *also noted* $P(h)$ *curves*

the contacting bodies are purely elastic. This inequality is attributed to the change of slope during the unloading even if small strain state is guaranteed as on the example illustrated by Fig. 5.8 where the maximum plastic strain is less than 2%. Hence, the earlier the contact stiffness is measured in the unloading step, the more correct its value will be. It could be noticed that the elastic unloading curve is different than the elastic loading one, explaining that $S = \dfrac{dP}{dh}$ must be determined at the beginning of the unloading step when $\text{Slope}_{loading}/\text{Slope}_{unloading} \approx 1$.
The effective elastic modulus E_{eff} is related to the reduced elastic modulus $E_{reduced}$ by:

$$\frac{1}{E_{reduced}} = \frac{1-\nu_{eff}^2}{E_{eff}} + \frac{1-\nu_{tip}^2}{E_{tip}} \tag{5.39}$$

Where the subscript $_{tip}$ stands for the indenter properties. Also, the effective indentation hardness H_{eff} is obtained through the relationship:

$$H_{eff} = \frac{P_{max}}{A} \tag{5.40}$$

Where P_{max} is the maximum indentation load. An isotropic hardening behavior is assumed for the contacting bodies. Then, from H_{eff}, one can access to the effective Yield Strengh (σ_{eff}^{y}), effective Ultimate Tensile Strength (σ_{eff}^{u}) by applying empirical models established by Tabor [195], Cahoon's [196], Pavlina and Van Tyne [197]. The latter models take into consideration the indenter tip shape. However, those models are based on correlations from experimental output data, assuming that the contacting materials are homogeneous, hence they are not appropriated for accurate effective yields stress prediction when the matrix contains multiple particles, inclusions or porosities. In general, those empirical laws tend to overestimate the yield stress value. Furthermore, better yield strength could be obtained, on the proposal of Takakuwa [198], by considering the residual stresses owing to the generated plastic strain during the indentation. But the bodies are assumed still homogeneous. Thus the present study comes with a solution taking to account both plasticity and heterogeneity presence within the contacting bodies. Hence, more accurate σ_{eff}^{y} and σ_{eff}^{u} could be got from the $P(h)$ curve analysis.

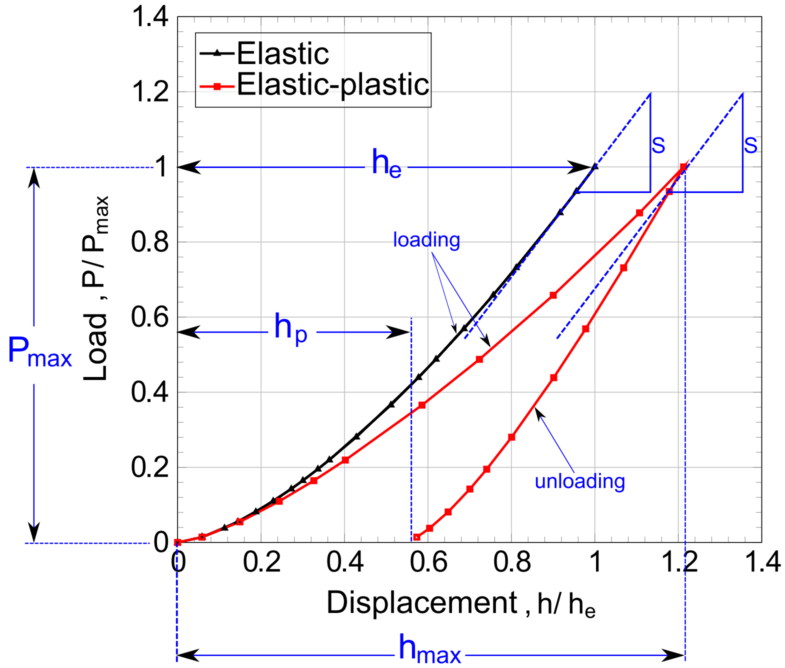

(g)

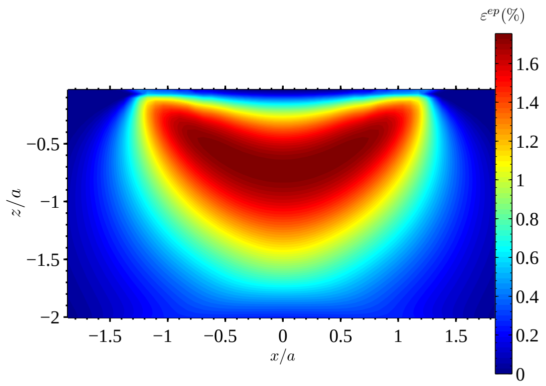

(h)

Figure 5.8: Indentation on homogeneous elastic-plastic body: (a) Load-displacement curve; (b) Equivalent Plastic Strain in the indented body

The Fig. 5.9 describes the reverse analysis algorithm for the identification of the equivalent homogeneous material properties which produce the same macroscopic behavior as the heterogeneous REV. The technique consists, at first, to conduct an indentation on the heterogeneous REV using the SAM. Then the outcomes load-displacement data are stored as the setpoint which must fit with that of the homogenized body at the convergence. The initial properties $[E(0), \sigma^y(0)]$ are used to perform a second indentation simulation using the SAM. It provides the load-displacement curve which is then compared to the setpoint. If both curves match then the initial properties are the solution. Else, the homogeneous body's properties are changed according to the error minimization algorithm of Levenberg-Marquardt. Then another indentation simulation is performed with the optimized properties $[E(i), \sigma^y(i)]$ leading to a new load-displacement curve to be compared. The optimization process is repeated until convergence is reached. Finally, the last properties are considered as the identified effective properties $[E_{eff}, \sigma^y_{eff}]$. Let's recall that the indentation simulations are performed with the heterogeneous elastic plastic contact solver developed in Amuzuga et al. (2015) [104] and the optimization loop is performed with the software Matlab.

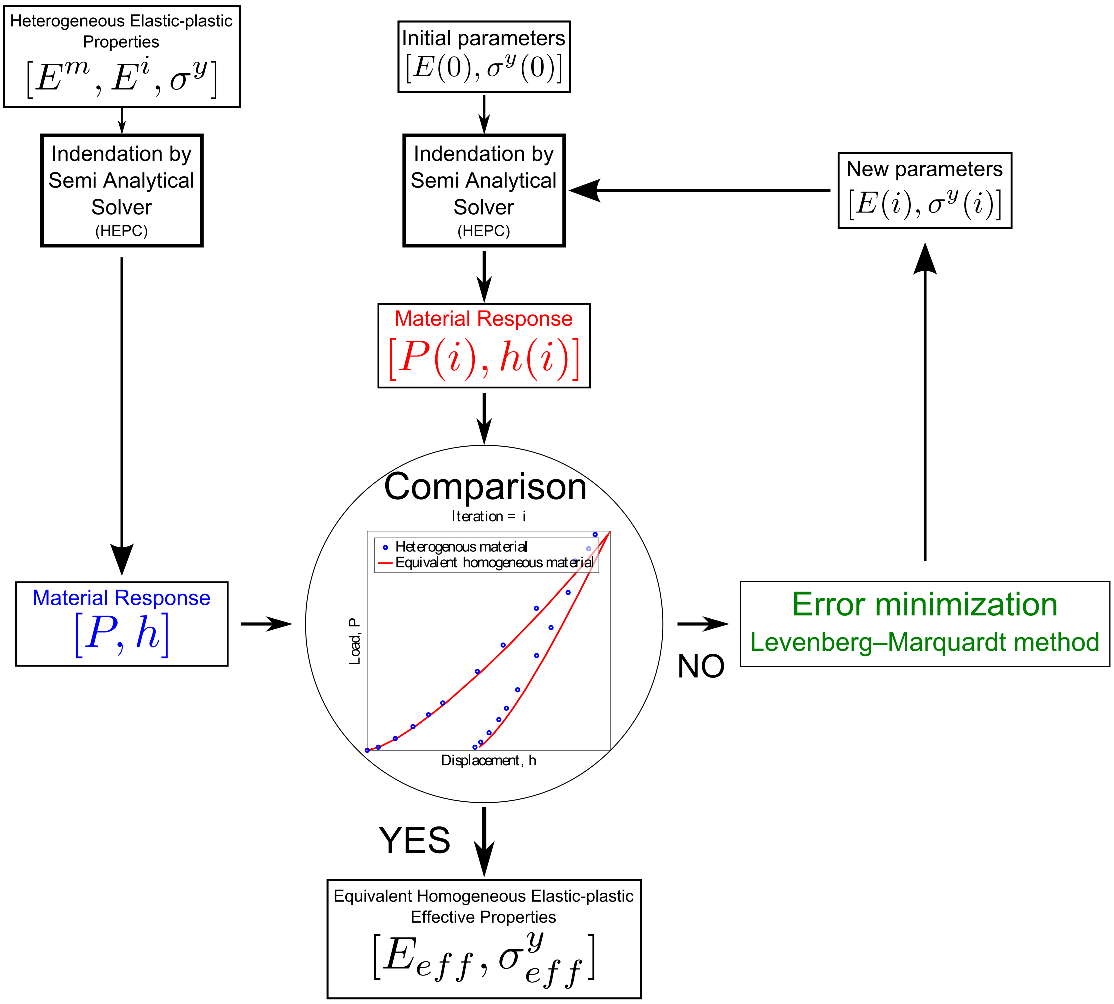

Figure 5.9: Reverse analysis algorithm for the homogenization

5.2.2.2 Contact model validation by nano-indentation tests

The heterogeneous elastic-plastic contact model has been validated by results comparison with a Finite Element Method models in the previous work [104]. Now the contact model is validated experimentally. Nano-indentation tests have been performed on two types of Silicon Nitride ceramics Y1T1700 and Y5T1700 (see [199] for details about the composition of these materials). The porosity content in these ceramics are quasi-nil. The load-displacement curves are compared to the ones obtained by the semi-analytical simulation. One can see in Fig. 5.10, a good agreement between both numerical and experimental results. The simulation parameters are recapped in the Tab. 5.1. The relatively small difference could be attributed to the submicron scales of the experiments. Indeed, Hayashi and Koguchi [173] argued that an increase of the yield stress and the hardness could happen when the distance scales are getting smaller. They found out that the real hardness is influenced by the interdependence between the surface stress and the surface elastic modulus. But this could not be revealed by plotting the evolution of the indentation hardness according to the indentation depth normalized by the indenter radius because it leads to the same profile for different indenters. Note that the surface elastic modulus can be obtained by molecular dynamic method based on Finnis and Sinclair potential [200].

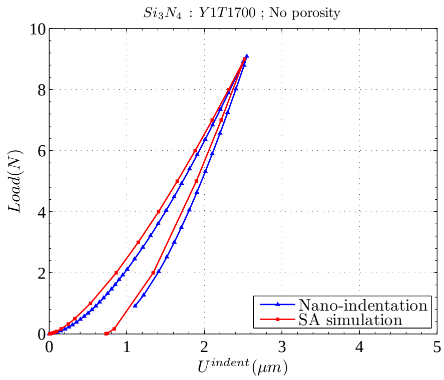

(a)

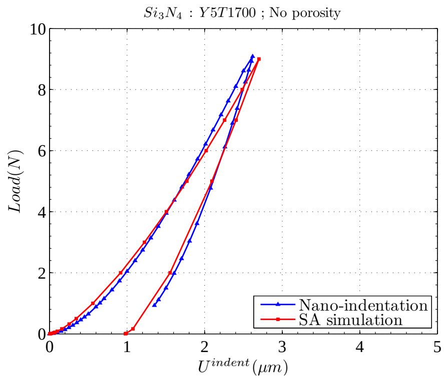

(b)

Figure 5.10: Contact model validation by nanoindentation test

Table 5.1: Value of the simulation parameters used for the contact model validation while it is compared with experimental results obtained by nanoindentation tests

Parameter	Value
Indenter radius	$d = 50\mu m$
Applied indentation load	$f_0 = 9N$
Indenter properties	$E_{tip} = 1141GPa$ (Diamond) ; $\nu_{tip} = 0.07$
1st Silicon nitride matrix elastic properties	$E_m = 335GPa$ (Y1T1700) ; $\nu_m = 0.3$
1st Silicon nitride matrix plastic properties	$\sigma^y = \sigma^y_0 + K\varepsilon^p$ where $\sigma^y_0 = 7.4GPa$ and $K = 5.0e{+}10$
2nd Silicon nitride matrix elastic properties	$E_m = 317GPa$ (Y5T1700) ; $\nu_m = 0.3$
2nd Silicon nitride matrix plastic properties	$\sigma^y = \sigma^y_0 + K\varepsilon^p$ where $\sigma^y_0 = 5.6GPa$ and $K = 4.7e{+}10$

5.2.2.3 Determination of an objective and consistent REV

The aim is to build a REV - representative elementary volume - which must be consistent according to the functions and parameters that drive the REV macroscopic response. The determination of an objective REV is a condition to ensure the accuracy of analysis and comparisons that arise from this study. The essential point is the heterogeneities volume fraction evaluation which is a direct result of the REV dimensions and shape, as well as the heterogeneities size and distribution. However, the parameters that control the description of the heterogeneous phase are the same that constrain the REV dimensions setting. This means that the heterogeneities volume fraction value can be biased by incorrect sizing of the REV, notwithstanding that the actual microstructure configuration (size and distribution of heterogeneities) remains the same. Moreover the REV edges must be set to encounter the minimum region whose response is invariant even if its dimensions increase. Hence to be objective, the REV must provide a volume

fraction which is not flawed by the geometry relations linking the heterogeneity size and distribution as well as the REV length.
Eq. 5.41 along with Tab. 5.2 recaps the parameters involved in the present homogenization method. This equation recalls that the effective property is a function of, on the one hand, the REV nature variables as the properties of the matrix m and the heterogeneous phase I, and in the other hand, the REV structure variables as the heterogeneities size S and distribution D. The volume fraction V_f and the density D_{ensity} are considered as indicator variables that combine the value of S, D, the number of heterogeneities N and the REV boundary dimension B_{REV}. The latter is a rectangular cuboid of $2B_{REV}$ length, $2B_{REV}$ width, B_{REV} depth and whose upper surface is centered on the contact.

$$\begin{aligned} (\mathrm{Property}^{eff}) &= \mathrm{function}\left(S, D, \mathrm{Property}^{I}, \mathrm{Property}^{m}\right) \\ V_f &= \frac{N \times S^3}{4B_{REV}^3} \\ D_{ensity} &= \frac{S}{D} \end{aligned} \tag{5.41}$$

In addition, it should be emphasized that the volume fraction and the number of heterogeneities are obtained by a given set of (S, D, B_{REV}) in Eq. 5.41, meaning that V_f is not directly set as an input data. Also, the density is considered as an indirect input because obtained from the given set of (S, D).

Table 5.2: Determination of a consistent REV

Parameter	Symbol	Description
Size	S	Heterogeneity size
Bound	B_{REV}	REV boundary dimension
Number	N	Number of heterogeneities
Distribution	D	Heterogeneities inter-center gap
Volume fraction	V_f	Heterogeneity content
Density	D_{ensity}	Heterogeneity density [1]

To satisfy requirements related to sizing the REV edges, the heterogeneities distribution and size are fixed, then B_{REV} is varied from a lower value B_{REV}^{low} to an upper value B_{REV}^{up}, arbitrary chosen. It must be ensured that the difference between B_{REV}^{up} and B_{REV}^{low} is greater than the contact radius a. Also B_{REV}^{low} has to be less than a. Then, the volume fraction can be calculated according to B_{REV} as in Fig. 5.11(a). One can see that the volume fraction is oscillating around an average value noted $\mathrm{Mean}(V_f) = 4.343\%$ and its oscillation amplitude decreases when B_{REV} increases. This means that the representative elementary volume becomes relevant for high values of B_{REV} because the volume fraction's oscillation is diminishing and is stabilizing around its average value. But by definition, the correct B_{REV} is the minimum dimension of the REV that is able to reproduce the same behavior as any other greater dimension. However, this minimum

1 The volume fraction must not be confused with the density, see the section Sec. 5.3.1 for the explanation

value must be greater than a to ensure that the REV will frame the contact zone and cover the stress/strain fields generated by the applied load.

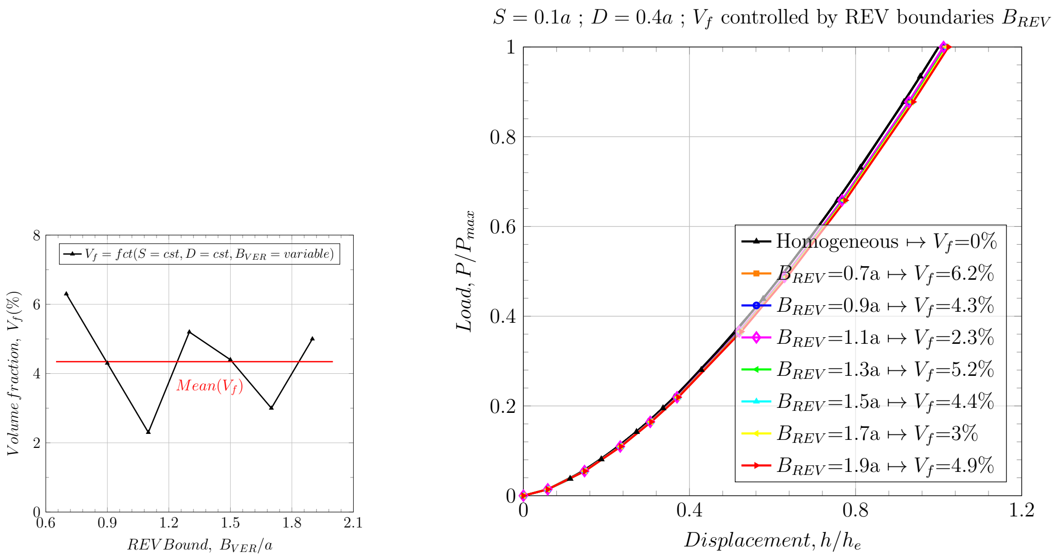

(a) (b)

Figure 5.11: Description of the REV: (a) V_f in function of the REV boundaries B_{REV}; (b) Load-displacement generated by a given $S = 0.1a$ and $D = 0.3a$

Indentation simulations are conducted on a heterogeneous elastic body for the different value of B_{REV} by keeping $S = 0.1a$ and $D = 0.3a$. The heterogeneities are porosities ($E_I = 0GPa$). Fig. 5.11(b) shows the load/displacement ($P(h)$ curves) from these simulations. It is found that for $B_{REV} = 0.9a$, $B_{REV} = 1.5a$ and $B_{REV} = 1.9a$, their corresponding REV have a similar behavior in terms of $P(h)$. It implies that the macroscopic response is sensitive to B_{REV} by the means of the volume fraction, remembering that D and S are constant. Note that when the REV boundary dimension B_{REV} is $0.9a$, $1.5a$ and $1.9a$, then it leads to the volume fraction V_f of 4.3%, 4.4% and 4.9%, respectively. Each of these REV can be considered as a consistent REV since their volume fraction are close to the mean value $Mean(V_f)$ plotted in Fig. 5.11(a). Moreover, these REV have nearly the same load/displacement $P(h)$ profiles. But finally only the REV of $B_{REV} = 1.5a$ will be kept as the relevant one because it frames the contact fields. Moreover Fig. 5.12(c,d) exhibits that the stress field distribution around the heterogeneity when $B_{REV} = 1.5a$, is the more representative. One can see that when the REV edges are extended to $B_{REV} = 1.9a$ in Fig. 5.12(e,f), there isn't any more *overstress* around the additional heterogeneities. But when the REV is reduced to $B_{REV} = 0.9a$ in Fig. 5.12(a,b), there is a lack of heterogeneities which might interfere with the stress field in the places where they are missing.

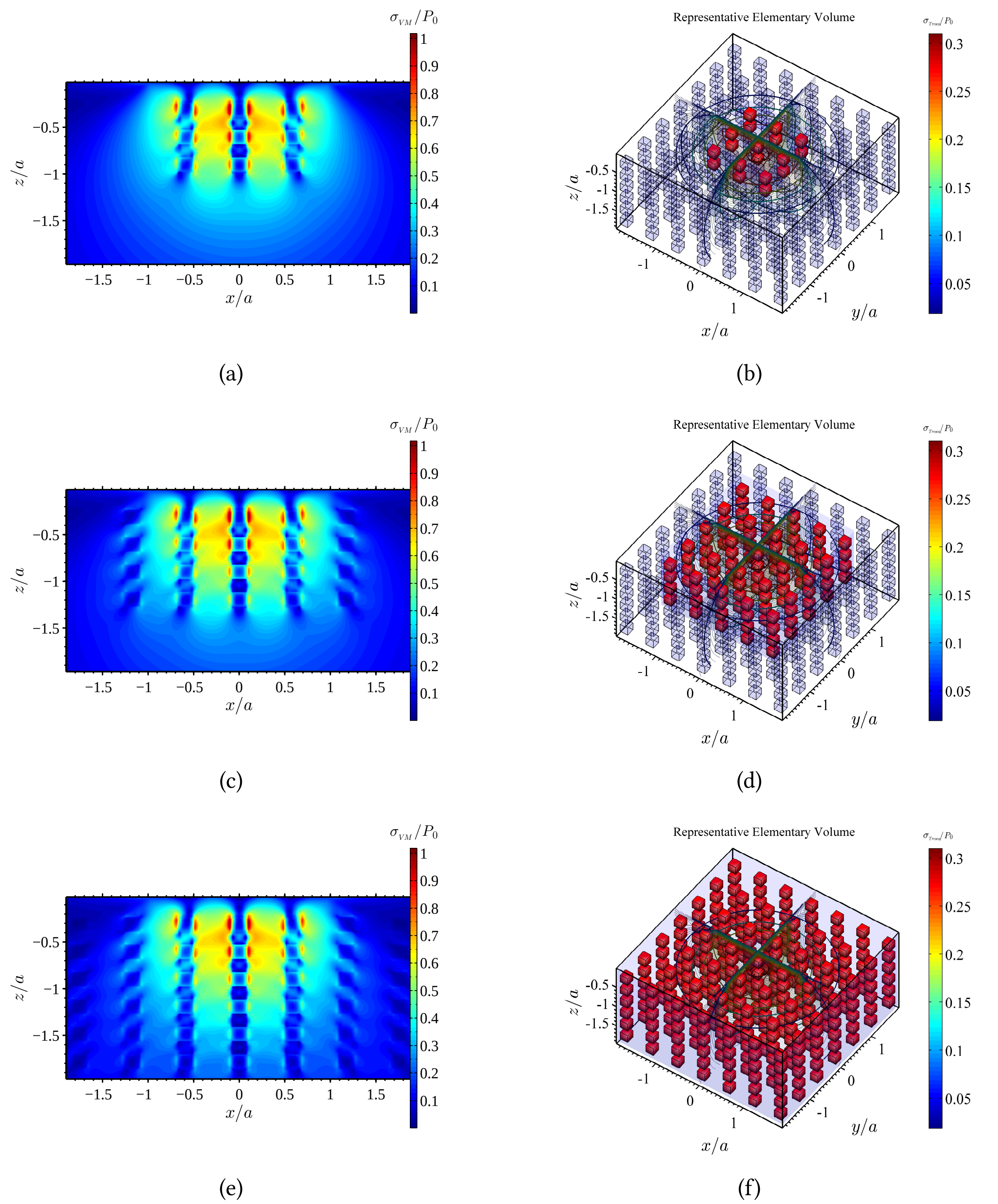

Figure 5.12: Von Mises stress σ_{VM} from the REV generated by $S = 0.1a$; $D = 0.3a$; V_f controlled by REV boundaries B_{REV}: (a-b) $B_{REV} = 0.7a \mapsto V_f = 6.2\%$; (c-d) $B_{REV} = 1.3a \mapsto V_f = 5.2\%$; (e-f) $B_{REV} = 1.9a \mapsto V_f = 5\%$

Fig. 5.12(b,d,f) presents the REV's heterogeneities ranking and the heterogeneities are represented inside the stress field (more precisely the maximum shear stress σ_{Tresca}) to show their position according to the stress gradient. Note that this stress contour is that obtained if the contact loading is applied on the REV while it is assumed homogeneous and elastic. In these representations, the red colored heterogeneities are those contributing to the volume fraction estimation. Those in blue are outside the REV and are plotted solely to distinguish the actual microstructure and the region taken into account in the REV. Fig. 5.12(a,c,e) shows the total Von Mises stress field σ_{VM} corresponding respectively to each REV plotted beside in Fig. 5.12(b,d,f). It should be pointed out that the stress field appearing inside the porosities is due to the fact that since there is a difference of elastic properties between the matrix and porosities, the latter are considered as inclusions in the sense of Eshelby. This leads to an eigenstrain inside each porosity when the REV is loaded. Each eigenstrain produces its eigenstress field, inside and outside the inclusion (porosity). The eigenstress fields are added to the elastic stress field produced by the homogeneous REV having the matrix elastic properties. This explains why the obtained total stress field lets appear a stress field inside each porosity. Nevertheless, this stress field does not actually exist physically. The equivalent stresses σ_{VM} and σ_{Tresca} are normalized by the maximum Hertzian contact pressure applied. The distances x, y, and z are also normalized by their ratio on the contact radius a.

Finally, the REV boundaries dimensions B_{REV} are determined by the technique described above and its volume fraction value of $Mean(V_f)$ is automatically assigned. However, several combinations of D and S can give the same volume fraction, then one needs to couple each V_f with its corresponding density value. It is worth specifying that a considerable error is not committed on the macroscopic response $P(h)$ if the B_{REV} is not perfectly determined, because Fig. 5.11(b) showed that all regarded B_{REV} lead to a similar load/displacement curves. Nonetheless, the interpretations based on V_f may be biased especially when the curves as $E^{eff} = function\,(V_f)$ are compared with other models, since V_f would not have a correct value. Hence it was necessary in the present study not to neglect the step of objective REV determination for comparison purpose.

5.2.2.4 Load-displacement sensitivity to heterogeneities size

The indentation simulation described above is now conducted by varying the heterogeneities (porosities) size S from 0.025 to $0.15a$, when the distribution D and B_{REV} are kept constant. Fig. 5.13(a) shows the heterogeneities volume fraction determined with the technique explained in the Sec. 5.2.2.3. As expected, the volume fraction has a monotonic growth when increasing the heterogeneities size. One can see in Fig. 5.13(b) that the load displacement curve decreases when V_f increases through S augmentation. The matrix is losing in stiffness when its porosities content increases.

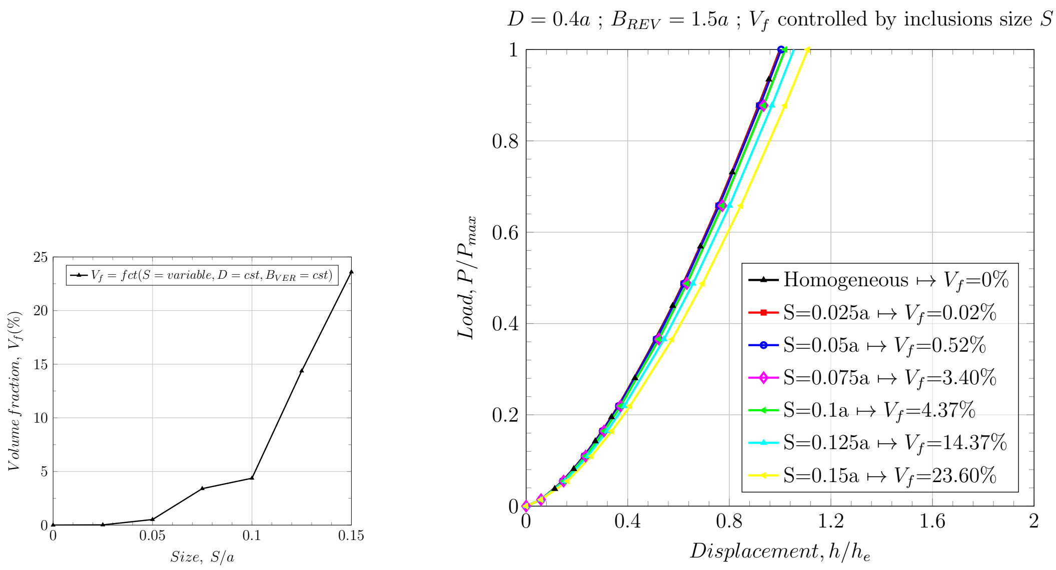

(a) (b)

Figure 5.13: Description of the REV: (a) V_f in function of the heterogeneities size S; (b) Load-displacement generated by a given $B_{REV} = 1.5a$ and $D = 0.3a$

Fig. 5.14(b,d,f) presents the heterogeneities inside the REV, when their size increases. Beside each REV, Fig. 5.14(a,c,e) shows the total Von Mises stress in the plane $\mathcal{P}(y = 0)$ when the contact load is applied. It can be noticed that the stress concentration zone around the porosities is increasing with the porosities size. Since the color scale is identical for the three Fig. 5.14(a,c) and (e), their stress levels indicate that the maximum value reached when $S = 0.075a$, is higher than the one found for $S = 0.15a$. Note that the gradient of the applied stress along with the loading direction, result in a graded distribution of each porosity reaction, according to its position. Also interaction effect between porosities can be seen for a relatively large size as $S = 0.15a$ in Fig. 5.14(e). It confirms that the load distribution inside the REV and the heterogeneity interaction according to their size must be taken into consideration by the homogenization technique. In the present method, these factors affect the $P(h)$ curve. This is the reason why the $P(h)$ curve is used as the representative output reflecting the REV overall response as consequence of the local one.

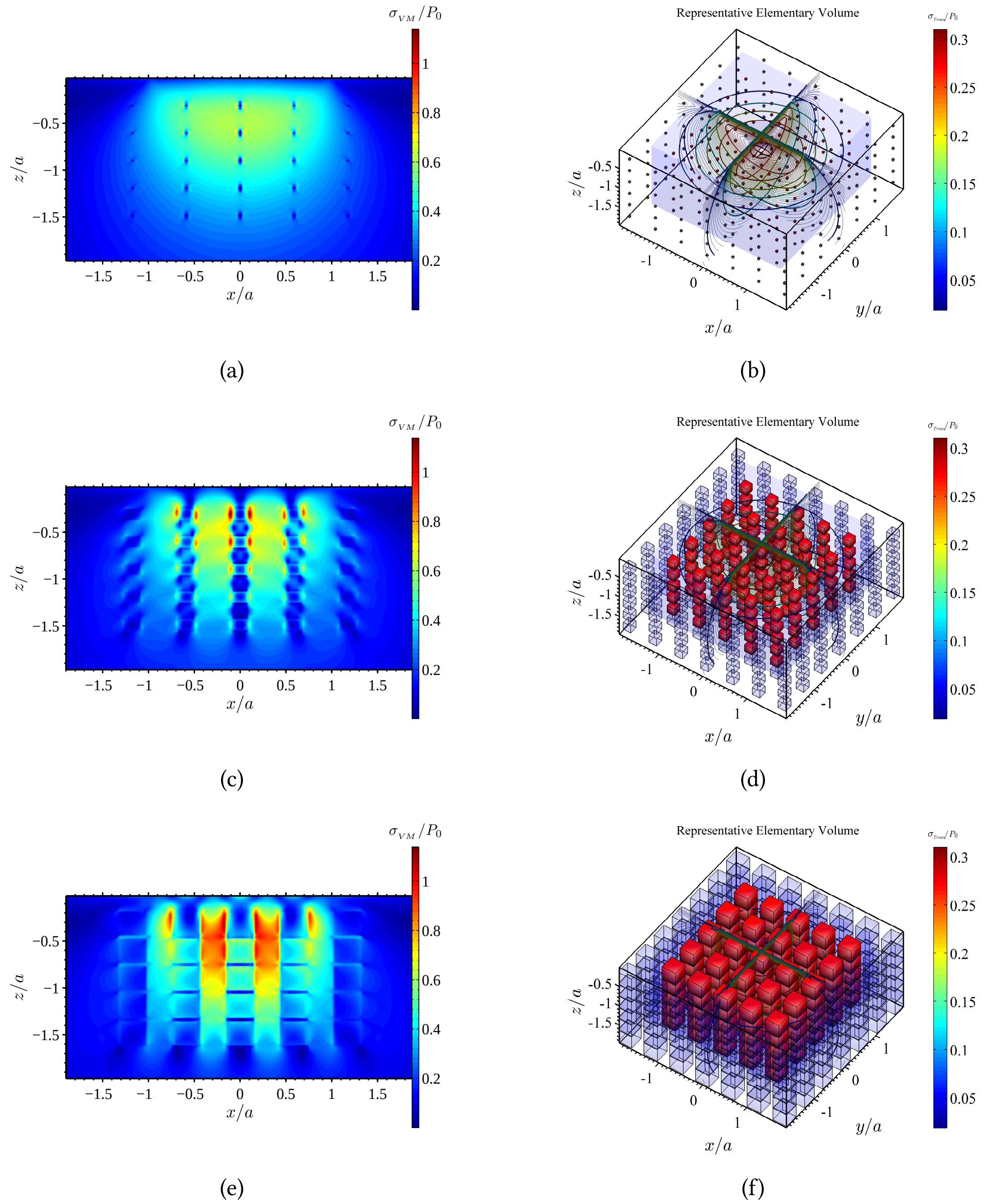

Figure 5.14: Von Mises stress σ_{VM} from REV generated by $D = 0.3a$; $B_{REV} = 1.5a$ and V_f controlled by heterogeneities size S: (a-b) $S = 0.025a \mapsto V_f = 0.02\%$; (c-d) $S = 0.075a \mapsto V_f = 3.40\%$; (e-f) $S = 0.15a \mapsto V_f = 23.60\%$

5.2.2.5 Load-displacement sensitivity to heterogeneities distribution

The indentation simulation described in Sec. 5.2.2.3 is now conducted by varying the heterogeneities (porosities) distribution D from 0.025 to 0.15a, when the size S and B_{REV} are kept constant. As noticed so far, only a regular distribution of heterogeneities along the three space directions, is regarded in the present study. Fig. 5.13(a) shows that the volume fraction diminishes when D increases, remembering that D stands for the distance between heterogeneities. As a consequence, one can see in Fig. 5.13(b) that the body stiffens when D increases (thus the load/displacement curve rises up).

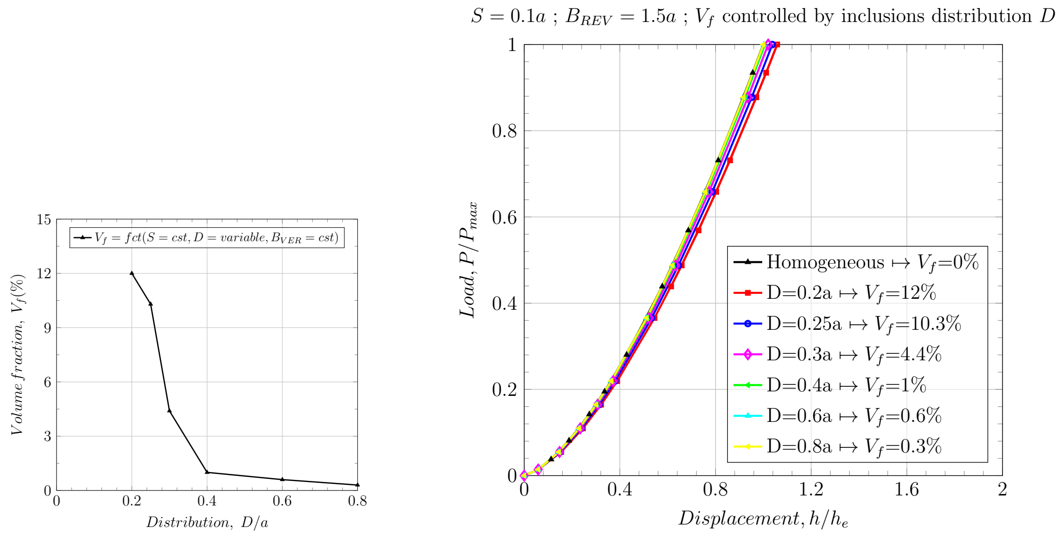

(a) (b)

Figure 5.15: Description of the REV: (a) V_f in function of the heterogeneities distribution D ; (b) Load-displacement generated by a given $B_{REV} = 1.5a$ and $S = 0.1a$

Fig. 5.16(b,d,f) presents the heterogeneities inside the REV, when their distribution increase and Fig. 5.16(a,c,e) shows the effect on the local Von Mises stress field. One can first note that the presence of the porosities at certain regions of the Hertzian stress field depends on D. Since the Hertzian stress magnitude is not uniform, each porosity's eigenstress magnitude will depend in turn on its position. Finally, the total stress in the material depends on the D. This supports the idea that for the same volume fraction, a change of the distribution will lead to a different effective behavior. This phenomenon cannot be taken into account by classic homogenization methods, since the applied load distribution is considered uniform and there is no variable which stands for the heterogeneities distribution. It should be added that the more D increases, the more the stress concentration level is high around each porosity. This agrees with the reasoning argued on the fact that the concentration spreads out when S increases. Indeed, one could hypothesize that, when a heterogeneous media is constituted of porosities, the stress concentration level is sensitive to the dimension of the matrix between them, instead of the gap separating their centers.

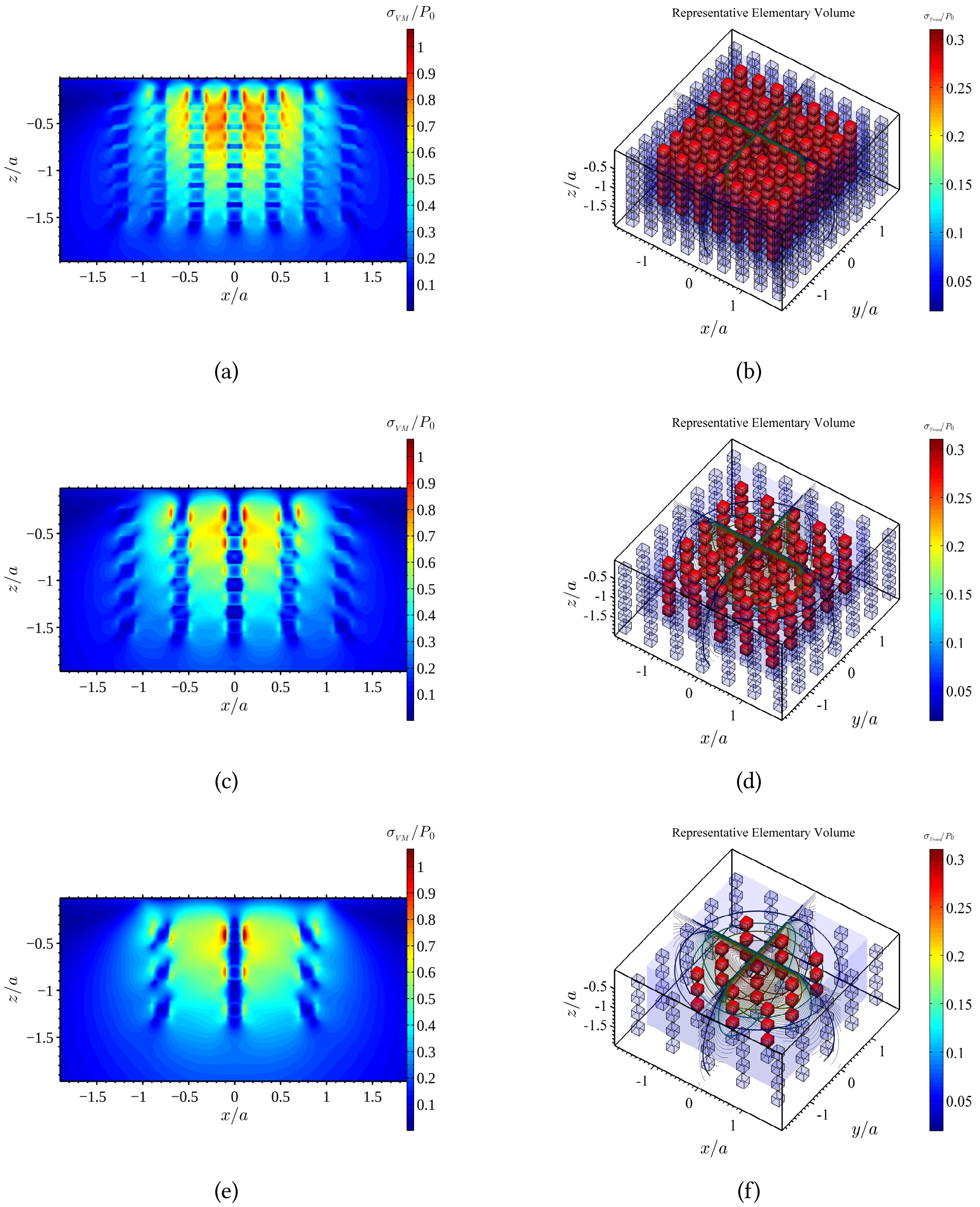

Figure 5.16: Von Mises stress σ_{VM} from REV generated by $S = 0.1a$; $B_{REV} = 1.5a$; V_f controlled by heterogeneities distribution D: (a-b) $D = 0.2a \mapsto V_f = 12\%$; (c-d) $D = 0.3a \mapsto V_f = 4.37\%$; (e-f) $D = 0.4a \mapsto V_f = 1\%$

5.2.2.6 Load-displacement sensitivity to the elastic-plastic parameters

For the purpose of limiting the number of parameters to be identified, tests are performed on the $P(h)$ curve sensitivity to the parameters regulating the reference homogeneous elastic-plastic body behavior. The elastic behavior is described by the Young's modulus E and the Poisson's ratio ν. The plastic behavior is represented by the Swift isotropic hardening law $\sigma^y = B(C + \varepsilon^p)^n$, where σ^y is the yield stress, ε^p the plastic strain, B, n and C are Swift law coefficient, exponent and offset constant, respectively. Even if the used identification program has been validated and proven to provide accurate results, for seeking multiple parameters during reverse analysis conducted in

Richard (1999) [201] , only two parameters will be identified in the present study for uniqueness end of the solution. One parameter is fixed for the elastic behavior and the last one for the plastic behavior. N. Azeggagh demonstrates in [202] that the identification program converges on a unique solution, when each parameter controls a specific part of the $P(h)$ curve, whatever the starting guess value. Thereby, the program is run the first time to identify the elastic parameter, assuming that the body is elastic. Then the elastic parameter is set as a constant in the second execution to determine the plastic parameter, by now considering the body as elastic-plastic.

Table 5.3: Parameters of the reference body sensitivity tests

Parameter	Value
E_0	$210GPa$
ν_0	0.3
B_0	$240MPa$
C_0	4
n_0	0.095

Indentations simulations are performed on homogeneous elastic plastic body. The parameters values are recalled in Tab. 5.3. The chosen material properties simulate the through-hardened M50 steel but its yield stress is lowered (divided by four) in purpose to generate plastic strain under the applied contact pressure of $2GPa$. Fig. 5.17(a) shows the $P(h)$ curve when the Young modulus E is varying around a reference value E_0. One can see at first that the indentation prints h_p are almost similar for all values of E. This is due to the fact that the plastic displacement is more related to the yield stress and the hardening law than the Young modulus. However when E increases, the total displacement h_{max} decreases. As a consequence, the loading part of the $P(h)$ curve is getting close to the unloading part as soon as the Young modulus decreases, because of the conservation of the total energy. This means that the total area under the $P(h)$ curves must be equal for all values of E, since the dissipated energy via plasticity is the same.

Fig. 5.17(b) shows that the indentation print evolves along with the Poisson ratio. Hence, h_p decreases when ν increases. The indentation print minimum is obtained when the body is incompressible ($\nu = 0.5$). Also, note that the $P(h)$ curves unloading part of all regarded ν are parallel with each other. This could be explained by the reason that, during the unloading, plastic flow did not occur and the elastic return is only governed by the Young modulus which is the same for all values of ν.

Now, Fig. 5.17(e) shows that the elastic-plastic response is insensitive to the hardening law parameter C which is varied from $C_0/4$ to $C_0 \times 4$. In contrast h_p is significantly sensitive to the Swift law parameters B and n in Fig. 5.17(c,d). Once again, the $P(h)$ curves unloading part of all regarded B and n are strictly parallel with each other. It sustained that, since plastic flow did not occur during the unloading, only the elastic properties are controlling this phase. Furthermore, when B and n increase which means that the yield stress increases, the total displacement and the indentation print decrease. All in view, the similarity of the profiles of $P(h)$ curves according to parameters B and n could allow to replicate any curve issued from a given B with another curve issued from n, and reciprocally. It is therefore beneficial to the identification program if only one of the parameters B and n, is chosen. However, comparing the growth of $P(h)$ curves with respect to B and n orders of magnitude, one perceives that a better numerical accuracy could be expected by choosing B instead of n, owing to the fact that B is a coefficient and n an exponent.

Observing that the Young modulus can control both loading and unloading parts of the indentation curve, and that the Swift law parameter B controls the indentation print, E and B have been therefore chosen to regulate the identification algorithm. Thus, the effective elastic property is represented by the Young modulus noted E_{eff} on which the identification algorithm converged when the program has been launched for the first time, considering the body as purely elastic. Likewise, the effective plastic property is represented by the effective yield stress σ^y_{eff} through the parameter B on which the identification algorithm converged when the program has been launched the second time, considering lastly the body as elastic-plastic.

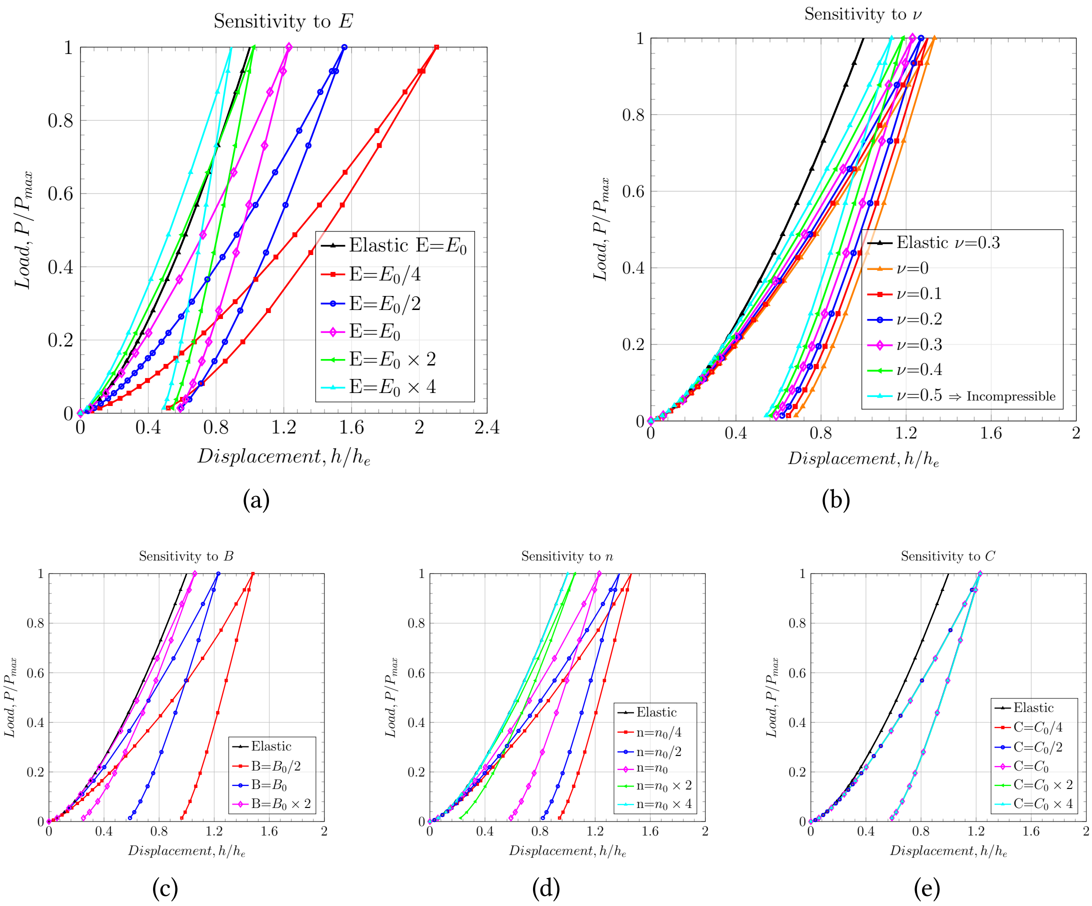

Figure 5.17: Parameters controlling the elastic-plastic behavior: (a) Young modulus E; (b) Poisson coefficient ν; (c) Swift law $\sigma^y = B(C + \varepsilon^p)^n$ coefficient B; (d) exponent n; (e) offset constant C

5.3 APPLICATION OF THE HEPC MODEL FOR THE HOMOGENIZATION

At this stage, one is able to build a consistent REV and to provide trusted parameters to the present homogenization algorithm. The model will be applied in this section to different configurations of REV whose materials constants and loading conditions are summarized in the Tab. 5.4. Two heterogeneities types are studied here. There are porosities represented by $E_I = 0GPa$ and Vanadium carbides having $E_I = 490GPa$ (in this case $E_I/E_m 2.33$). Note that the M50 hardened material is considered as the matrix. The principal aim is to exhibit that the effective properties not only depend on the heterogeneities volume fraction but also on their distribution. Then only two distributions are regarded. Remember that the volume fraction or the density is not input data. They are calculated for given values of the heterogeneities size and distribution, by the technique described in the Sec. 5.2.2.3. Nonetheless, the highest volume fraction generated here is 92%, knowing that in the literature, comparable studies found did not exceed 50% [a] . This limitation is mainly due to preparation routes used in the samples fabrication process.

[a] *up to 24% in Diaz and Hampshire (2004) [203] , 50% in Diaz et al. (2005) [204] and from* 0.1% *to* 30% *in Fritzen et al. (2012) [205]*

Table 5.4: Values of simulations parameters

Parameter description	Symbol and value
Indenter diameter	$d = 29mm$
Applied contact pressure	$P_0 = 3.5GPa$
Indenter elastic properties	$E_{tip} = 310GPa$ (Silicon Nitride) ; $\nu_{tip} = 0.3$
Matrix elastic properties	$E_m = 210GPa$ (M50) ; $\nu_m = 0.3$
Matrix plastic properties	$\sigma^y = B(C + \varepsilon^p)^n$ where $B = 240MPa$, $C = 4$, and $n = 0.095$
Heterogeneity elastic properties	$E_I = 490GPa$ (Vanadium carbide), $E_I = 0GPa$ (Porosity) ; $\nu_I = 0.3$

5.3.1 HOMOGENIZATION OF POROUS MATERIAL

The porous materials are modeled by an elastic matrix containing heterogeneities with a nil Young modulus $E_i = 0$. Fig. 5.21(a) presents the evolution of the density as a function of the volume fraction V_f for two distributions $D = 0.3a$ and $D = 0.4a$. Let's specify that both curves were obtained by varying the heterogeneity size S knowing that the REV boundaries dimension B_{REV} is automatically set by the technique described in Sec. 5.2.2.3. Hence for each S the corresponding volume fraction and density are calculated using the Eq. 5.41 according to the fixed D. It could be seen at first that the density at a small volume fraction ($V_f < 10\%$) is quasi identical for both regarded distributions. However, the more volume fraction increases the more the difference between the densities obtain for both distributions increases. Considering a given volume fraction, the smallest density is obtained for the smallest heterogeneity distribution. This is consistent with the reason that for a given heterogeneity size, the medium having the smallest heterogeneities inter-center gap, is the one having largest volume fraction (Fig. 5.16). It implies that for a given volume fraction, increase the heterogeneities inter-center gap leads to the density augmentation. This is counter-intuitive. Whereas for a given density, increase the heterogeneities inter-center gap leads to the volume fraction diminution. This is more instinctive. Let's specify that the density has been defined as the heterogeneity size S over the inter-center gap D, in order to present the density as a unidimensional representation of the content. Considering S as the material domain occupied by a single heterogeneity and D its available living space, then the ratio $\frac{S}{D}$ could be in turns interpreted as the heterogeneity presence probability. Hence, increase the density is reflected in an increase of the heterogeneity presence probability inclusion, in a mathematical sense. Also, the physical meaning of the density imposes the restrictions $S \geqslant 0$ and $D \geqslant 2S$. The minimum bound of the density prevents the penetration between neighboring heterogeneities.

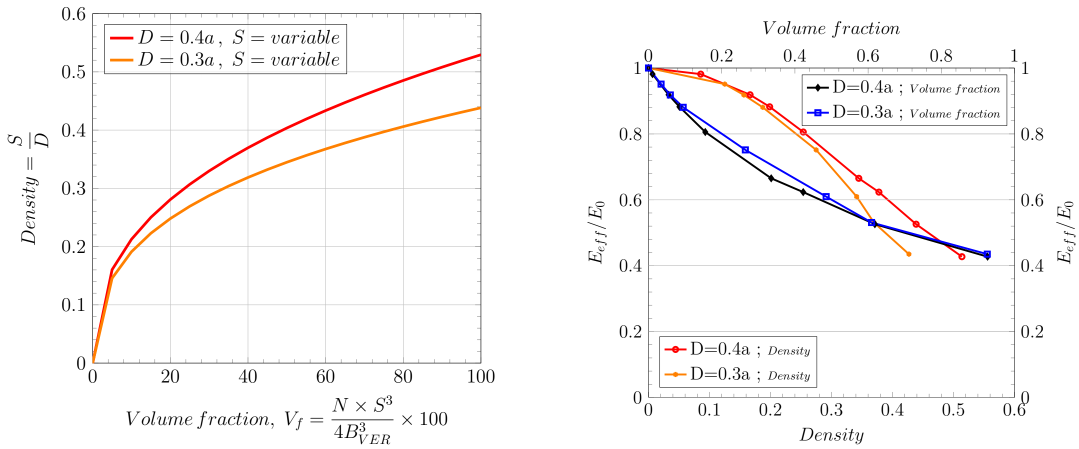

(a) (b)

Figure 5.18: Homogenization of porous material: (a) Density vs Volume fraction ; (b) Effective elastic property properties

The effective Young modulus E_{eff} of a porous material subjected to contact load is presented in Fig. 5.18 as a function of the volume fraction, on the one hand, and the density, on the other hand. Note that two given values of the distribution are analyzed. Remind that the variation of the heterogeneity size controls the volume fraction and the density. One can first found that E_{eff} is sensitive to the distribution. It could be seen that for a small value of volume fraction $V_f < 10\%$ and relatively high value $V_f > 70\%$, both regarded distribution lead to almost identical E_{eff}. It means that the macroscopic response is sensitive to the interaction between heterogeneities. When $V_f < 10\%$, the interaction effect is quite low, then the overall response not depends on the distribution. Otherwise when $V_f > 70\%$, the interaction effect becomes high and begins to saturate then the overall response becomes similar regardless of the volume fraction. However looking at the effective Young modulus depends on the density, one can see that from $D_{ensity} > 0.15$, the difference between E_{eff} relative to both distributions increases with the density. For a considered density value, $E^{D=0.4a}_{eff} > E^{D=0.3a}_{eff}$. Where $E^{D=0.4a}_{eff}$ and $E^{D=0.3a}_{eff}$ are the effectives Young's modulus when the heterogeneities distribution $D = 0.4$ and $D = 0.3$, respectively. In general E_{eff} drops when the volume fraction or density increases, since $E_I < E_m$, whatever the heterogeneities distribution.
Note that in the following section, effective properties will be analyzed only in function

of volume fraction for comparison purposes with other models in the literature since these models do not take into account the density.

5.3.1.1 Comparison with the rule of mixture

It is frequently encountered that, to treat problems involving a presence of heterogeneities, authors make quick homogenization using the rule of mixture for simplification purpose as:

$$\mathrm{Property}^{\mathrm{eff}} = V_f \times \mathrm{Property}^{I} + (1 - V_f) \times \mathrm{Property}^{m} \tag{5.42}$$

One can see that this formulation did not consider the loading type and the distribution of the heterogeneities. This leads to estimation errors depending on the rate of the heterogeneities volume fraction as shown in Fig. 5.19. According to the distribution, the effective property obtained by the rule of mixture can be over-estimated up to a certain value of the volume fraction noted V_f^{lim}, after which it becomes significantly underestimated (or reciprocally). The magnitude of V_f^{lim} also depends on the ratio $\mathrm{Property}^{I}/\mathrm{Property}^{m}$. For instance, if the matrix is stiffer than the heterogeneity which is a porosity here, the more the distance between porosities is smaller, the more the V_f^{lim} is low. Thus $D = 0.3a$ leads to $V_f^{lim} = 20\%$, whereas if $D = 0.4a$ then $V_f^{lim} = 32\%$. The effective Young modulus can't be identified using a simple mixture law when the body is subjected to contact load, more especially when the volume fraction is getting relatively higher.

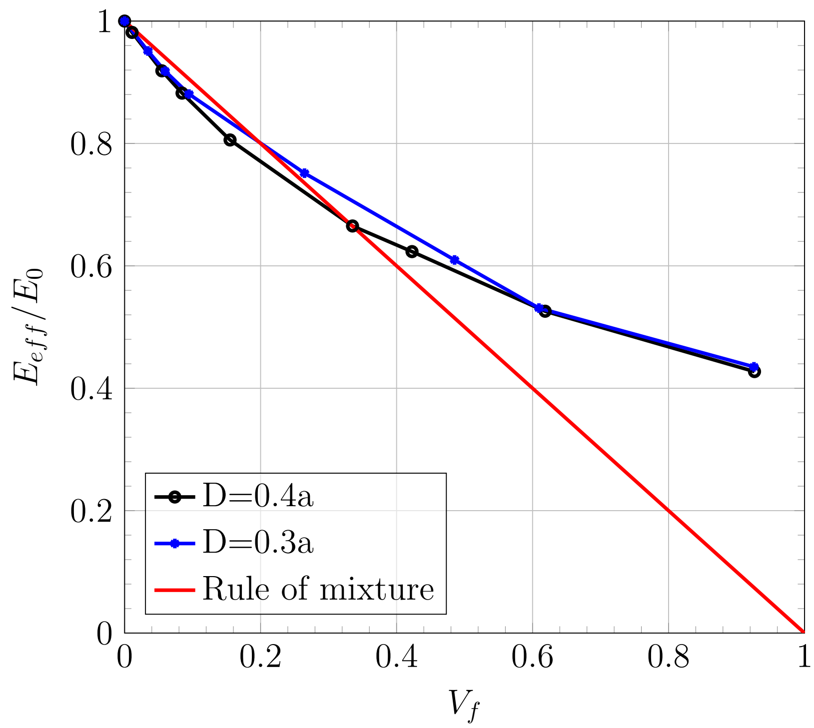

Figure 5.19: Macroscopic E

5.3.1.2 Comparison with Diaz-Hampshire model, Linear law and Exponential law

One can find in the literature several models dealing with the effective elastic property of porous material especially for ceramic materials made by sintering process which consequently lead to micro-porosity inclusions. In this framework, linear and exponential law are mainly established. Also, a power law model is proposed by Diaz and

Hampshire in [203] and was validated for a good prediction up to 24% of porosity content. Fig. 5.20(b) confirms that for a distribution in a range of $D = 0.3a$, one can fit the effective Young modulus by these laws even beyond the limit where Diaz and Hampshire study was stopped. However Fig. 5.20(a) shows that, when $D = 0.4a$ the effective Young modulus is well described up to a volume fraction of about 30%. In all, Diaz-Hampshire model and the exponential law make a good prediction up to 60%, when porosities are closer to each other ($D = 0.3a$).

Law	Parameters
$(1 - aV_f)^n$	$a = 0.076; n = 17.81$
$\exp(-bV_f)$	$b = 1.36$
$1 - hV_f$	$h = 1.32$

Law	Parameters
$(1 - aV_f)^n$	$a = 0.021; n = 52.5$
$\exp(-bV_f)$	$b = 1.1$
$1 - hV_f$	$h = 0.97$

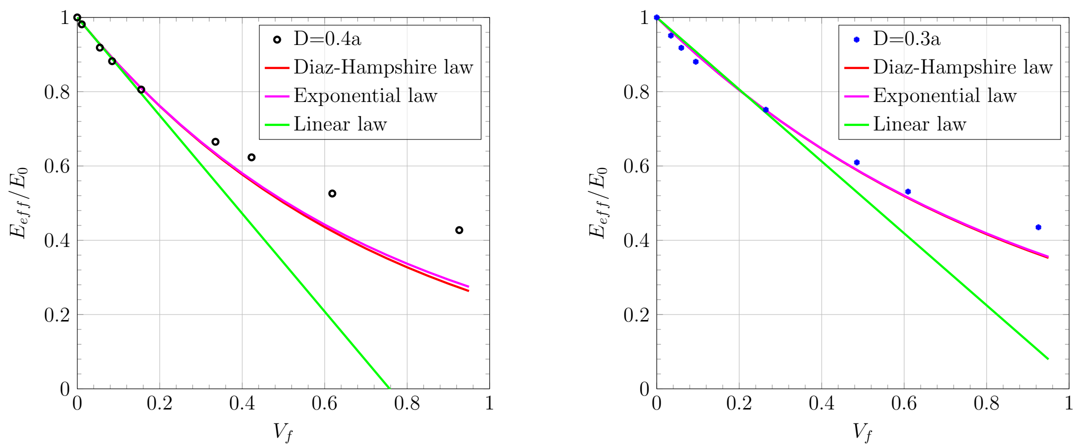

(a) (b)

Figure 5.20: Comparison with Diaz-Hampshire model, Linear law and exponential law: (a) $D = 0.4a$; (b) $D = 0.3a$

5.3.2 HOMOGENIZATION OF MATERIAL CONTAINING CARBIDES PARTICLES

Now, one is interested in the homogenization of matrices containing stiffer heterogeneity ($E_i > E_m$), especially Vanadium carbides ($E_I = 490GPa$). Fig. 5.21 presents the evolution of the effective Young modulus and effective yield stress according to the carbide volume fraction for the distributions $D = 0.4a$ and $D = 0.3a$. As expected, both the effective Young modulus and the yield stress, increase with the volume fraction in general. But their evolution profiles depend on the regarded distribution. Once again this mismatch between effective properties profiles which held according to each distribution is attributed to the effect of carbide interactions. It is worth noticing that, even if the carbides are considered purely elastic ($\sigma_I^y/\sigma_I^m = +\infty$), the effective yield stress could not be increased by 50% of the matrix yield stress, when the volume fraction which reached to about $V_f = 90\%$ with $D = 0.3a$. But, with the same carbide volume fraction and distribution, the effective Young modulus has been doubled, recalling that $E_i/E_m = 2.33$.

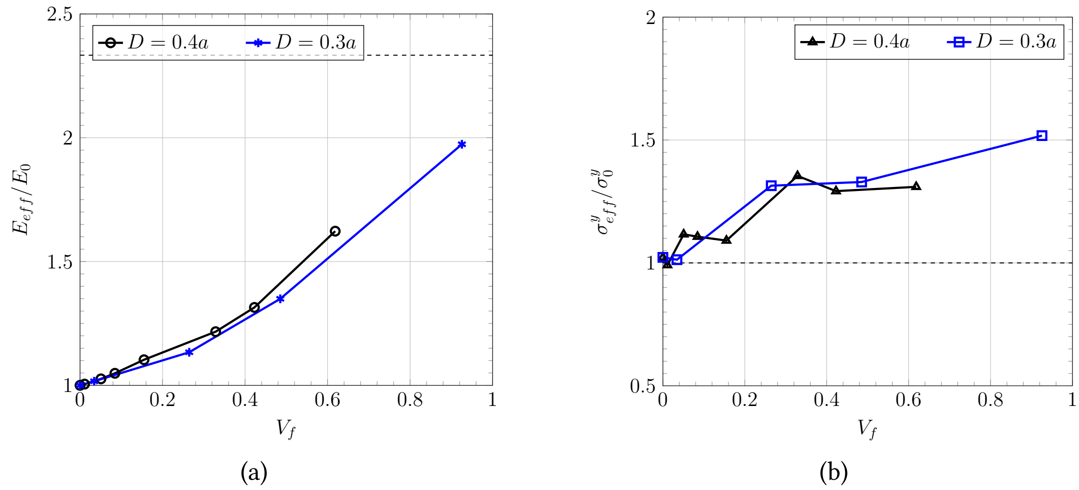

Figure 5.21: Effective properties of material containing carbides particles: (a) Young's modulus ; (b) Yield stress

Effective Young modulus comparison with classic homogenization methods

The effective Young modulus of elastic bodies containing Vanadium carbides is studied here for two values of distribution ($D = 0.3a$ and $D = 0.4a$) when the volume fraction is varying. Fig. 5.22 presents the comparison of these results with the predictions made by classic homogenization methods reviewed in Sec. 5.2.1. It could be seen at first that the classical method does not take into account the carbides distribution. It is interesting to find that the present method gives solutions which are close to the classic one. In particular when the $D = 0.3a$ the effective Young modulus E_{eff} is framed by the Voigt and the Reuss solutions proved as the effective property upper and lower bounds; respectively. But when $D = 0.4a$ one can see that E_{eff} profile is under the Reuss bound. This is more noticeable for high volume fraction of $V_f = 90\%$. This leads to argue that when the load is applied on the REV free surface, the classic homogenization methods over estimates the homogeneous solution for relatively large heterogeneities inter-center gap ($D = 0.4a$) with large heterogeneities size. More distributions must be studied in other to confirm this argument. Also for the regarded distributions, the present solution is not contained between Hashin-Shtrikman bounds. Fig 5.22(b) shows that the Mori-Tanaka and Self-Consistency are quite similar. In addition, one can note that Eshelby's diluted scheme overestimates the E_{eff} when the volume fraction is less than a threshold noted $V_f^{lim}(D)$ which depends on the distribution D. Then E_{eff} is underestimated above this threshold. It could be observed in Fig. 5.22(b) that $V_f^{lim}(D = 0.4a) = 44\%$ and $V_f^{lim}(D = 0.3a) = 56\%$

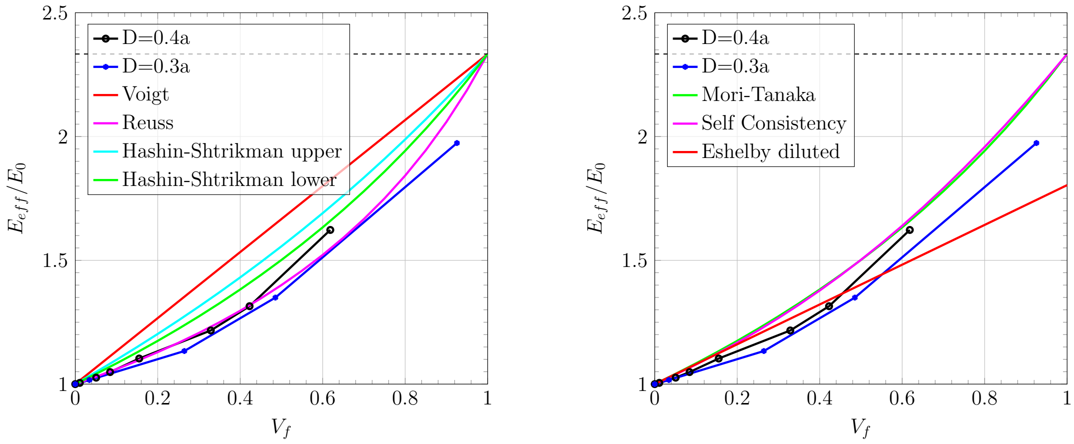

(a) (b)

Figure 5.22: Effective Young modulus comparison with classic homogenization methods: (a) Voigt Reuss and Hashin-Shtrikman bounds ; (b) Mori-Tanaka, Self consistency and diluted Eshelby

5.4 PREDICTION OF THE MACROSCOPIC ELASTIC MODULUS AND YIELD STRESS

The purpose of this section is to build a general law describing the evolution of the macroscopic elastic and plastic behaviors for a particular distribution of heterogeneities ($D = 0.4a$).

5.4.1 HETEROGENEOUS MATERIAL ELASTIC BEHAVIOR LAW ESTABLISHMENT

Fig. 5.24 presents the general trend of macroscopic Young modulus for a fixed distribution of $D = 0.4a$ when heterogeneity Young modulus E_I and the volume fraction V_f are varying. One can notice that there are two distinguishable trends according to the V_f value. When $V_f < 50\%$ the trend is called here, a dominant matrix macro behavior and when $V_f > 50\%$ the trend can then be called a dominant heterogeneous phase macro behavior. The dominant matrix macro behavior brings up a concave shape of the effective Young modulus E_{eff} evolution when a tangent is laid at the point $E_{eff} = E_i = E_m$ in Fig. 5.24(a). Where E_m is the matrix Young modulus. But this curve becomes convex for the prevailing heterogeneous phase macro behavior in Fig. 5.24(b). These observations bring to set up a rheological model that can catch E_{eff} evolution.

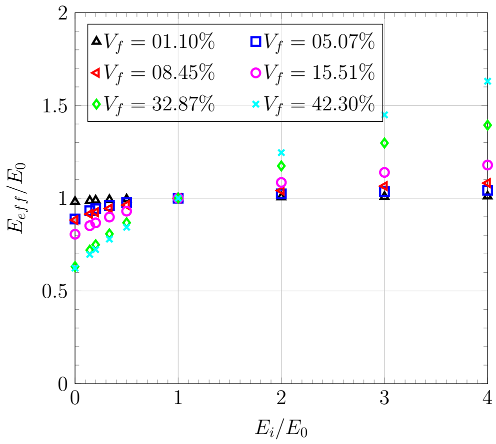

(a)

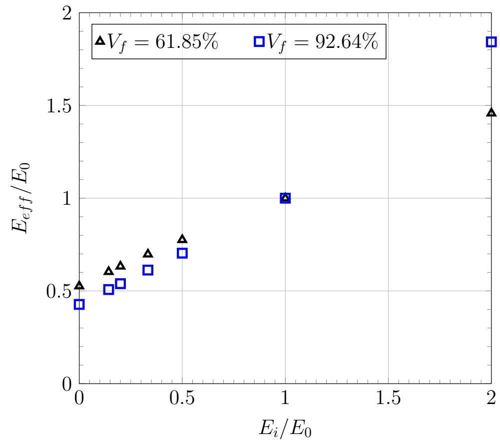

(b)

Figure 5.23: Effective Young modulus of heterogeneous elastic material subjected to contact loading: Behavior law establishments (a) when $V_f < 50\%$; (a) when $V_f > 50\%$

The effective Young modulus is fitted by four parameters power law curve (Appendix. B.2) as:

$$\frac{E_{eff}}{E_m} = p_1 + p_2\left(p_3 + \frac{E_I}{E_m}\right)^{p_4} \tag{5.43}$$

One can see that the parameter p_1 is considering as the E_{eff} threshold to prevent it from negative value. The parameter p_3 is offsetting E_I to avoid E_{eff} to be nil. Those two parameters are expected to depend only on the matrix Young's modulus but not sensitive to the heterogeneities volume fraction. But Fig. 5.24 shows that after the curve fitting, p_1 and p_3 vary relatively to V_f. One can also see that the rheo-coefficient $p_2 = 0$ when $V_f = 0$ implying $E_{eff} = E_I$ because $p_1 = 1$. This is consistent with the fact that in absence of heterogeneity the macroscopic behavior is the matrix one. Let's specify that the problem complexity leads us to propose a four parameters model which is able to represent the effective behavior because below this number, tested models do not strictly produce all the cases.

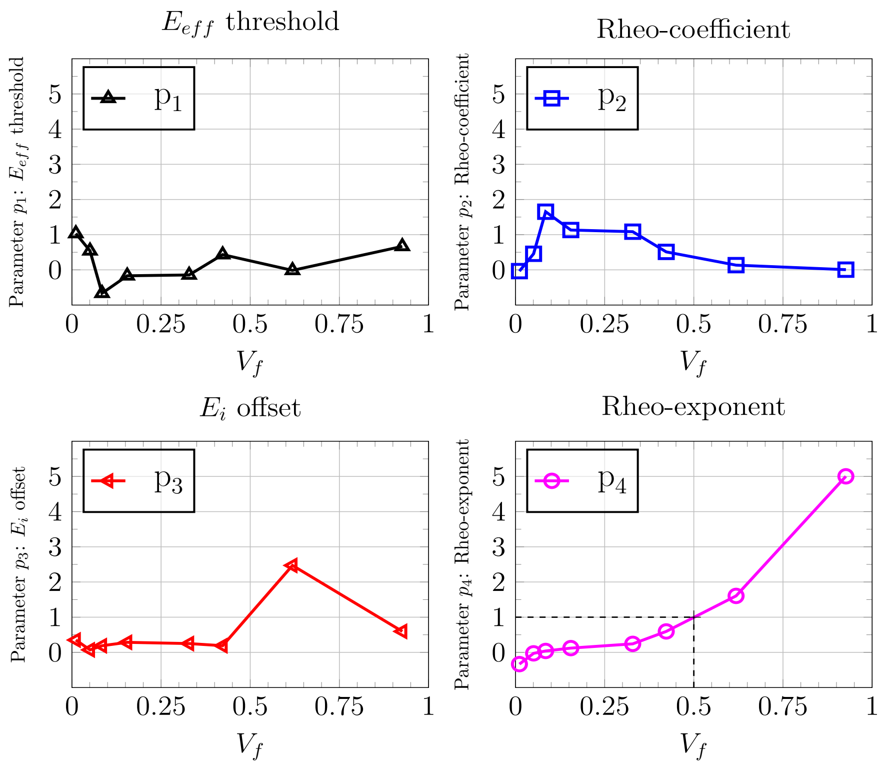

Figure 5.24: Evolution of parameters p_1 , p_2 , p_3 , p_4

It could be observed that the rheo-exponent p_3 is less than 1 when $V_f < 50\%$ and $p_3 > 1$ when $V_f > 50\%$ explaining the concave and the convex shape of E_{eff}, respectively. Hence for a given heterogeneity elastic property, one can predict the homogenized elastic property, depending on the distribution, whatever the volume fraction by finding those rheological parameters. However, even if a general law could find to fit the E_{eff} trend according to E_I and V_f, one must be aware that the parameters used to describe E_{eff} evolution are non-independent. The homogeneous elastic behavior is complex to be fully described and generalized by simple laws when heterogeneities parameters such as density, distribution and the mutual influence must be taken into account. Thus, numerical model is proven still essential to obtain correct and accurate effective properties of the heterogeneous elastic plastic bodies under contact.

5.4.2 EFFECTIVE YIELD STRESS ANALYSIS OF THE HETEROGENEOUS ELASTIC-PLASTIC BODY

The macroscopic yield stress σ^y_{eff} obtained for a fixed distribution $D = 0.4a$ is presented in Fig. 5.25 when E_I and V_f are varying. The heterogeneities are considered elastic meaning $\sigma^y_I = +\infty$. It could be noticed that when the heterogeneity Young modulus increases, the effective yield stress increases for $E_I < E_0$ and decreases for $E_I > E_0$. One can explain this by the fact that when the difference $|E_I - E_0|$ increases, it leads to raise the overstress around heterogeneities then the plastic flow occurs earlier than expected which gives insight to have the effective yield stress dropping. This phenomenon is emphasized by the mutual interaction between heterogeneities when their size is increasing, even more, when they are getting close to each other.

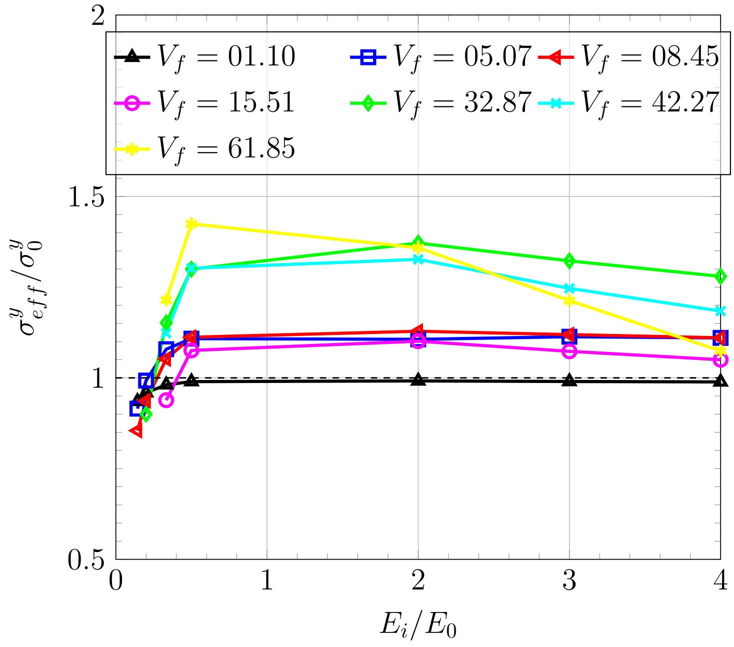

Figure 5.25: Heterogeneous material plastic behavior trend

5.5 PARTIAL CONCLUSION

Encouraged by the increasing of computer capacities, numerical simulation tools become predominant alternative for a large operating range of investigations. Even if models are limited by some assumptions, they are getting more realistic and essential for understanding complex mechanisms, particularly in tribology. Throughout the present work, a three-dimensional heterogeneous elastic-plastic contact model based on semi analytical method, proposes a combined study of the role of the size, location, material properties and distribution of the heterogeneities and their elastic-plastic behavior. Investigations have been conducted on the effect of heterogeneities content and density on the macroscopic behavior of a body subjected to contact loading. The mutual influence of heterogeneities according to their distribution, has been characterized and provide the insight to ensuring bearings material sizing by involving the accurate effective elastic-plastic properties. Several remarks should be kept from this study. Firstly, one must be aware that classical homogenization models are inadequate when strong gradient of stress distribution is issued from the REV boundary conditions as contact loading in the present case. Also, mutual influence between heterogeneities is not accounted in most used classical techniques, especially when the matrix is allowed to yield plastic behavior. In addition this study raises two interesting points. On the one hand, the elastic effective property such as the Young's modulus cannot be identified using a simple mixture law. But the Diaz-Hampshire model and the exponential law make a good prediction when the porosities are closer to each other. On the other hand, the plastic effective property such as the yield stress is increased when the embedded elastic heterogeneities are stiffer than the matrix whatever the volume fraction. This conclusion should be underlined since it confirms experimental observations that could not be described by conventional elastic analysis. However, one important finding is that, even if the numerical simulation allows to analyze materials with high heterogeneity contents, the homogeneous elastic behavior is complex to be fully described and generalized by simple laws when the heterogeneities parameters such as density, distribution and the mutual influence must be taken into account. Knowing that an employed material under contact mechanisms should be designed by considering such parameters, therefore, numerical model is proven still essential to obtain correct and accurate effective properties of the heterogeneous elastic plastic bodies under contact. The last success of this study is the fact that it confirms qualitatively three major advantages of semi analytical method for treating inelastic and nonlinear behaviors, making:

- Very robust contact computation and full coupling of contact/heterogeneous/-plastic problems.
- Large number of simulations for specific heterogeneities distributions is easily affordable in relatively low computation time.
- Good agreement with experimental results and other computational methods.

Finally, two main applications of the present method is the homogenization of porous materials (in bio-tribology: *bone/cartilage*) and the overall property of heterogeneous plastically graded materials (*M50, M50NiL, M50 obtained from Powder Metallurgical Process*) subjected to contact loading.

6

INFLUENCE OF HETEROGENEITIES AND HARDENING PROPERTIES ON PLASTICALLY GRADED BEARING MATERIALS: M50 AND M50NIL

In service, the active component surfaces of aerospace bearings are subjected to alternate high pressure due to successive passage of rolling elements on the raceway. This may end up by fatigue damage marked through material spalling or etching. After initiation in the subsurface, the main features grow toward the surface, which results in the loss of the bearings initial properties. The bearing loses its initial properties. The material imperfections and the presence of non-metallic inclusions such as carbides aid to ease crack nucleation. All these considering, investigating on the damage mechanisms need a complete knowledge of the material microstructure, and their consequence on the behavior under an applied stress field. The microstructure characterization is conducted with scanning electron microscope (SEM), coupled with hardness measurements. In situ SEM tensile tests are performed to determinate the local mechanical behavior after thermomechanical treatments (nitriding and carburizing) and evaluate the behavior of microstructure features such as small cracks and carbides during the deformation. Observations and material properties resulting from tested specimens are used as input of a semi-analytical heterogeneous elastic-plastic rolling contact model for numerical simulations.

Contents

6.1 INTRODUCTION

The superior resistance to rolling contact fatigue (RCF) of high strength bearing steels is significantly enhanced by surface treatment technologies such as plasma nitriding [206], carburizing [207, 208], thermal-spraying [209, 210, 211], shot peening [212, 213] etc. These processes can be combined to tailor the material for attaining some very special targeted properties. Hardening (carburizing or through-hardening) followed by gaz nitriding seem to be the best-known coupling to achieve remarkable properties with taking into account economic constrains. The hardening+nitriding treatments are particularly relevant to two prevailing aeroengine bearing steels designated as M50 and M50NiL. The chemical composition of the alloy leading to the traditional M50 base material is described in [214]. But for the M50NiL, nickel is included to prevent from ferrite formation, in the same alloy as the M50 except that the initial carbon content is significantly lowered and the silicon is also reduced. Hence, since M50 base material disposes of a sufficient quantity of carbon, the conventional hardening treatment phase is a through-hardening (quenching/tempering). In contrary, the M50NiL base material has initially low carbon, then it needs carbon intake by case-hardening following the carburizing.

The beneficial effect of the carburizing for work pieces is well known in material engineering [215, 216, 217, 218, 219]. The thermochemical treatments lead to (i) a hard surface enabling good resistance to wear and pitting; (ii) residual compressive stress linking the surface to the subsurface and enhancing the toughness under rolling contact fatigue; (iii) ductile core allowing the material efficiently dissipating high applied deformation energy in the form of plasticity. The initial compressive stress tends to close the micro-cracks so to delay their propagation. This explained why cracks size could be related to the probability of failure [220]. But the accumulation of plasticity during rolling cycles generates residual tensile stress in a sufficient amount to cancel the existing compressive stress. Tensile stress is then more developed and damage mechanisms are accentuated. Residual tensile stress can also be introduced when the surface layer decarburization is provoked. Carbon depletion is a known source of fatigue life reduction in bearing industry, [221]. However optimal conditions are needed for the hardening+nitriding process to meet the requirements enabling resistance to the RCF, as studied for M50 and M50NiL in [222], because of the competitive kinetic of nitrogen and carbon elements [223].

Lately, Xie [224] pointed out that the nitrided steel can withstand higher applied contact stress and reduce the likelihood of plastic strain in comparison to the untreated material. The nitrided steel advanced resistance to the wear is also claimed in [225]. Moreover, Sun [226] pointed out that the introduction of rare earth elements as additives-catalysts [227] during plasma nitriding enhances significantly the case-hardened M50NiL properties (hardness, wear resistance). Surface treatments have been proven to increase the outlying layer hardness which then gradually decreases according to the distance from the surface [228]. It should be specified that surface alloying could lead to two distinguishable material types. On the one hand, functionally graded materials (FGM) which is the term standing when the elastic property such as Young's modulus evolves with respect to the depth [105]. In the other hand plastically graded material (PGM) which is the term suiting when the plastic property such as hardness evolves with respect to the depth [229, 230]. For martensitic and austenitic steels, FGM are mainly obtained by coatings and PGM by thermochemical treatments.

The bearing steels performance continues to be awarded to the outermost surface layer hardness [231, 232], loading conditions [233, 234, 235], lubricant chemistry [15] and the subsurface microstructure characteristics such as cleanness, unmelted particles [236], initial stresses [237] etc. Despite all these aspects, it is accepted that, within ductile matrix, cracks appear when the plastic strain locally outgrows the material fracture strain [238]. Observing large number of failed bearings [81, 239], evidence is provided that micro-cracks initiated from non-metallic inclusions [240] and from micro-defects, grow randomly [241], connected to each other and finally coalesce to create the principal cracks [79, 242]. Also, with the development of fractography techniques [243] and examination by dye-penetrants [244], damage evolution could be investigated. Non-destructive procedures are used to follow cracks propagation. A quasi-exhaustive listing is made in Márquez's review [245] fully devoted to wind turbines. For bearings, in-situ cracks detections could be investigated by acoustics emission [246, 247, 248] and vibrations signal [249], since the first signs of fatigue damage.

Nowadays, the high efficiency of hybrids bearing involving Si_3N_4 and high-strength steels is more and more claimed. The tenacity in front of severe operating pressures and the reliability in a high temperature environment such as in aircraft engines are ones of the factors often appreciated for this technology. This is justified by the important difference between the expansion coefficients of both materials. However the present study does not take into account thermo-elastic effects [250, 251] even if it has been figured out that contact pressure increases when temperature gradient increased between the contact surfaces, [252]. Nevertheless, failure analysis of bearing races surfaces is often attributed to macro-pits and spalls related to the presence of carbides in the vicinity of the outlying layer. Cracks issued from extremely brittle carbides can rapidly reach the surface during cyclic rolling under excessive contact load [253]. The chemical composition of carbides, strongly impacts their resilience under the stress field transmitted through the matrix. Vanadium [254] and molybdenum [255] are mainly known as responsible for the quantity of supersaturated carbons during segregation phases preceding carbide formations. In the literature, Klecka [254] exposes an inventory of carbide types present in bearing materials as those used in the aerospace framework.

Of course numerous factors are at the origin of component failures [256] during rolling contact, but one must emphasize that stress raisers reduce the fatigue life significantly below the prediction obtained when referring to smooth samples [257]. Due to the fact that analytical modeling of rolling contact problem requires too many assumptions and simplifications [258], their use for fatigue life prediction could be questionable. Numerical methods become a good compromise. Finite element method (FEM) is intensively used by many researchers thanks to its flexibility to solve the problem of structure involving complex geometries. But the computation burden is increased drastically when large number of elements is needed to mesh the structure [259]. A three-dimensional semi-analytical method (SAM) [52], based on influence coefficients [260] derived from Boussinesq-Cerruti integral equations [261, 262], offers the alternative to be faster by combining the Conjugate Gradient Method (CGM) [263, 264] with the discrete convolution and fast Fourier transform (DC-FFT) algorithm [53]. New features are progressively integrated to the SAM solvers throughout the following publications: [265, 112, 266, 267, 268, 269] . Recent developments [104] allows to perform heterogeneous elastic plastic rolling contact (HEP-RC) simulations. The numerical part of the present work is an application of the HEP-RC models as a tool to understand the influence of the microstructure, in particular the carbide distribution, on the bearing lifetime. Therefore an experimental part is needed to identify the microstructure and to determine the mechanical properties of different phases. Since the studied materials are heterogeneous, it is needed to follow in-situ the deformation during loading, at microscopic scale in order to detect the brittlest zones of the microstructure where the material are likely to crack.

The twofold focus of the present work are: (i) the micromechanical characterization of M50 and M50NiL materials; (ii) the consequence of their microstructure on the mesoscopic behavior through numerical rolling contact models. The first point aims to explore the local heterogeneous elastic-plastic properties related to the thermochemical treatments experienced by the concerned materials (M50 and M50NiL). The purpose of the second point is to investigate the influence of carbide population (size, location and distribution) on the overall elastic-plastic properties of a representative elementary volume embedded in the substrate as clusters or stringers. The results presented herein, have been sustained and commented by comparison with other works.

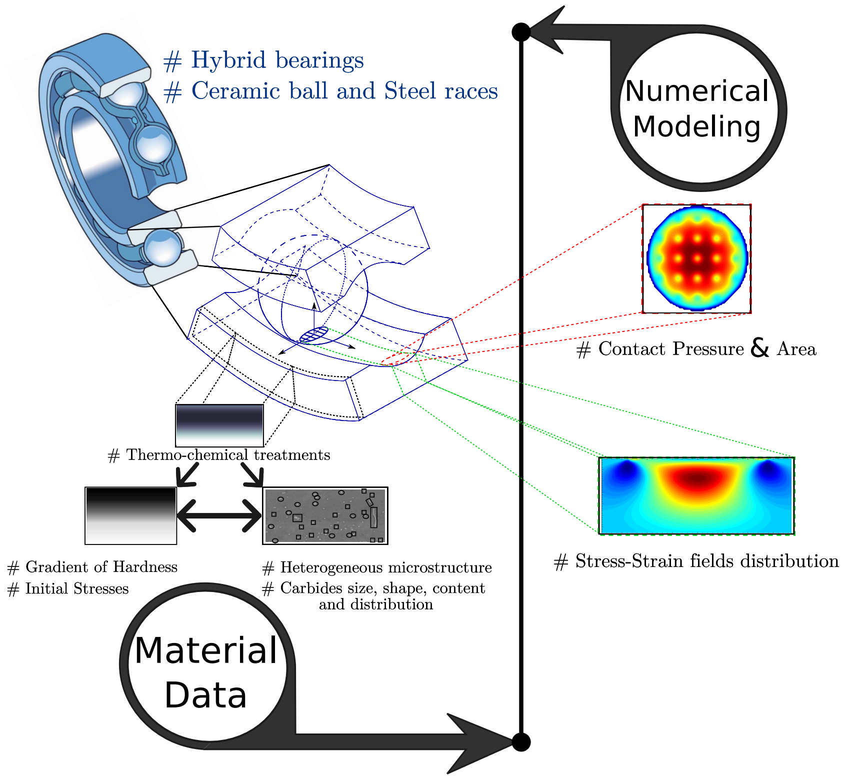

Figure 6.1: General context of the rolling contact on graded heterogeneous elastic-plastic material

Fig. 6.1 presents the general context of the rolling contact on graded heterogeneous elastic-plastic material which experienced a thermochemical treatment. The latter introduces initial compressive stress and hardness gradient along the depth.

6.2 MATERIALS AND METHODS

Statistical analysis of heterogeneities along the depth axis, reveals that the gradient of property is a direct consequence of the heterogeneity distribution. The microstructure characterization is an essential ingredient to create a numerical model capable of reproducing the material behavior during the simulations. The versatile quality of the semi-analytical method allows to investigate on the consequence of different microstructure patterns. The surface contact pressure and area, as well as the subsurface stress-strain fields will be the output for a thorough, hence used to identify the factors that influence the material RCF resistance.

6.2.1 MATERIALS

M50NiL is the enhanced version of M50 with nickel addition and low carbon (see Tab. 6.1). The purpose of this section is to reconstruct these material microstructures in order to simplify their modeling for numerical simulations.

Table 6.1: Chemical composition (mass fraction)(wt.%) of the M50 in [270] and M50NiL in Sun, Zhang, and Yan (2014) [226]

Element	C(%)	Si(%)	Mn(%)	P(%)	S(%)	Cr(%)	Mo(%)	V(%)	Ni(%)	Fe
M50	0.78-0.88	0.20-0.60	0.15-0.45	MAX 0.030	MAX 0.30	3.75-4.50	3.90-4.75	0.80-1.25		Balance
M50NiL	0.13	0.18	0.13	0.012	0.002	4.10	4.20	1.20	3.40	Balance

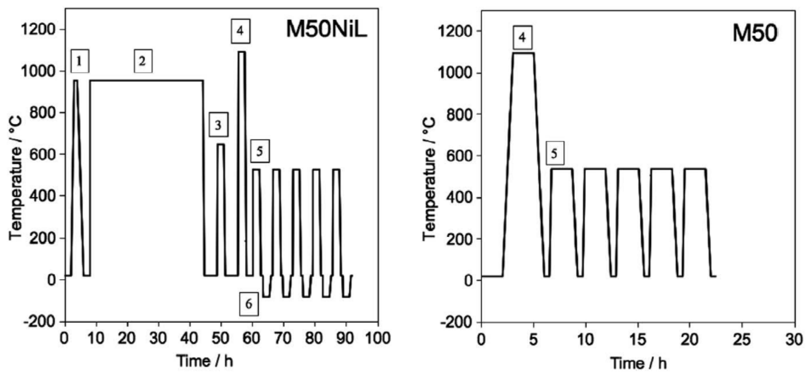

Figure 6.2: Typical heat treatments for M50 and M50NiL steels described in [271] where the numbers in the squares are relative to different stages of the treatments as: (1) oxidation; (2) carburizing; (3) stress relief; (4) solution treatment and quenching; (5) tempering; (6) sub-zero cooling

Fig. 6.2 presents a typical heat treatment experienced by M50 and M50NiL steels. The heating+cooling temperatures and duration are the fundamental variables that control the final microstructure features such as the grain size, the carbide precipitation (size, location, chemistry, distribution, clustering, stiffness), the gradient of hardness and the initial compressive stress. On the one hand, the M50 has a high amount of C and carbides will form during tempering (0.80 wt%). It has thus been first quenched, then tempered and finally nitrided. On the other hand, the M50NiL contains much less carbon. It has been carburized before quenched. This intake of carbon via the specimen surface allows to control the quantity of diffused carbon at high temperature. Then carbide precipitations are controlled during the quenching and tempering process. Finally, the M50NiL is also nitrided. The nitriding process crates a very hard surface layer with initial compression stress profile owing to thermoplastic deformation inside grains.

METALLOGRAPHIC SPECIMEN PREPARATION PROCEDURE

The specimen preparation procedure for Optical Microscopy (OM) and Scanning Electron Microscopy (SEM) explained in [272], is adopted. Tab. 6.2 recaps the polishing sequence route of M50 and M50NiL before microscopic observations. Polishing was performed on an automated polishing Buehler device. After polishing, specimens are etched by Nital solution composed by 95% ethanol and 5% nitric acid in volume proportion.

Table 6.2: Polishing sequences route of M50 and M50NiL

Step	Abrasive paper's grit sizes $(P - grade)$	Grinding force (N)	Head speed (rpm)	Base speed (rpm)	Duration (min)
1	P180	45	-60	+400	3
2	P320	45	-60	+400	5
3	P600	20	-60	+400	5
4	P1200	20	-30	+200	5
5	$3\mu m$ Diamond fluid	10	-30	+120	5
6	$1\mu m$ Diamond fluid	10	-30	+120	10
7	$0.5\mu m$ Diamond fluid	5	-30	+60	15

6.2.2 OBSERVATION TECHNIQUE

For magnification lower than $\times 500$, samples were observed on conventional optical microscopy. For higher magnification measurements, microstructure observations were performed on a ZEISS Supra 55 VP FEG Scanning Electron Microscope, operated between 10 and 15 kV, and equipped with a $80mm^2$ Oxford Instrument SDD EDX detector.

XRay Tomography experiments were performed at 160kV using the v|tome|x device of GE Sensing & Inspection Technologies Phoenix X|ray. The voxel resolution is $3\mu m \times 3\mu m \times 3\mu m$. Tomography test is performed on the M50 sample of dimensions: length $= 1560\mu m$, width $= 1560\mu m$ and height $= 1852\mu m$. The sample is sliced beneath the surface along the property gradient direction to be consistent with observations on microscopy images.

MATERIALS MICROSTRUCTURE IMAGES PROCESSING

In order to reconstruct the material microstructure, the particles and defects must be sorted by categories. The carbides have to be isolated according to their surface area and the ratio $width/length$ by making the threshold to the microscopy images. In addition statistical study have to be conducted to investigate on the effective property related to the carbides content, type, size, shape, location and distribution. The flowchart presented in Fig. 6.3 is inspired by the one used in [273] for magnetic nanoparticles analysis. The commercial software Matlab was chosen here because of its useful and powerful library of functions in Image Processing Toolbox. Matlab Statistic tools used here has been testing and validated by Jana Salacova [274].

```
procedure INITIALIZE VARIABLES
    f_i ← Current image file ; Im ← Current image ; N_f ← Total number of images    % Counters
    diskImOpen (pixel) ← Disk areas    % Delete particles less than diskImOpen
    diskImClose(pixel) ← Disk areas    % Fill inner voids less than diskImClose
    diskImBackground (pixel) ← Disk areas    % Background and Adjustment
    coefGrayThresh ← Coefficient    % Convert into binary And Threshold gray scale
    median2D (pixel) ← 2-D median filtering    % 2 − D median filtering
    deleteLessXpixel (pixel) ← Disk areas    % Delete particles less than deleteLessXpixel
    lowerBound (pixel) ← Disk areas    % Sort particles less than lowerBound
    upperBound (pixel) ← Disk areas    % Sort particles larger than lowerBound
    imConcat (char) ← Horizontally or Vertically    % Multiscanned images concatenation layout according to storage order
end procedure
```

```
procedure PRE-PROCESSING
    for f_i = 1 : N_f do
        Im = imcomplement(rgb2gray(imread(f_i)))    % Read, convert color map to grayscale and get image complement
        Im = adapthisteq(Im)    % Enhances the contrast of the grayscale image
        Im = imopen(Im, strel('disk', diskImOpen))    % Perform morphological opening on the grayscale
        Im = imclose(Im, strel('disk', diskImClose))    % Perform closing with a disk structuring elements of diskImClose
        ImBackground = imopen(Im, strel('disk', diskImBackground))    % Background adjustment
        Im = imsubtract(Im, ImBackground)    % Subtract one image from another
        Im = imadjust(Im)    % Adjust image intensity values in grayscale
    endfor
end procedure
```

```
procedure CORE
    for f_i = 1 : N_f do
        Im = im2bw(Im, 1 − coefGrayThresh × graythresh(Im))    % Convert to binary image by threshold grayscale
        Im = medfilt2(Im, [median2Dmedian2])    % Perform median filtering of a binary image in two dimensions
        Im = imfill(Im, 4, 'holes')    % Fill all the hole: Two-dimensional connectivity value 4 for connecting neighborhood
        Im = bwareaopen(Im, deleteLessXpixel)    % Delete particles less than deleteLessXpixel
        ImParticles = regionprops(Im, 'Area')    % Measure properties (Area) of image regions
        ImParticlesArea = [ImParticles.Area]    % Return measured region area
    endfor
end procedure
```

```
procedure POST-PROCESSING
    if imConcat = 'Vertically' then
        ImScan = vertcat(Im{1 : N_f})    %
    elseif imConcat = 'Horizontally' then
        ImScan = [Im{1 : N_f}]    %
    endif
    allImScan = bwlabel(ImScan)    %
    REV = regionprops(ImScan, 'Area')    %
    smallParticles = find([REV.Area] < lowerBound)    %
    midParticles = find([REV.Area] >= lowerBound&[REV.Area] <= upperBound)    %

    largeParticles = find([REV.Area] > upperBound)    %
    smallParticlesIm = ismember(allImScan, smallParticles)    %
    midParticlesIm = ismember(allImScan, midParticles)    %
    largeParticlesIm = ismember(allImScan, largeParticles)    %
    smallParticlesRegion = regionprops(smallParticlesIm, 'Area')    %
    midParticlesRegion = regionprops(midParticlesIm, 'Area')    %
    largeParticlesRegion = regionprops(largeParticlesIm, 'Area')    %
    R = 0 ; G = 0 ; B = 1    % Blue color for small particles
    smallParticlesColor = cat(3, smallParticlesIm × R, smallParticlesIm × G, smallParticlesIm × B)    %
    R = 1 ; G = 1 ; B = 0    % yellow color for medium particles
    midParticlesColor = cat(3, midParticlesIm × R, midParticlesIm × G, midParticlesIm × B)    %
    R = 1 ; G = 0 ; B = 0    % red color for large particles
    largeParticlesColor = cat(3, largeParticlesIm × R, largeParticlesIm × G, largeParticlesIm × B)    %
    ColoredREV = smallParticlesColor + midParticlesColor + largeParticlesColor    %
end procedure
```

Figure 6.3: Image processing flowchart for multi-scanned images

Let's remember that the objective of automatic images treatment is to deal with tomography or multi-scanning microscopy images, with a large number of images to be simultaneously treated. At this step, one need to test it on representative images samples chosen randomly in order to calibrate the variables. If the result obtained by the post-processing procedure is acceptable as the example shown in Fig. 6.3 relative to setting in Tab Tab. 6.3, then the algorithm can be executed on the entire microstructure images stack. The pre-processing procedure intended to convert the images into matricial objects in order to perform contrast, intensity and morphological adjustments before the real processing which will be held in the Core procedure. The pre-processing procedure can also allow to reveal some particular aspects of the microstructure (as porosity) and take them into account.

Table 6.3: Value of parameters used in the flowchart of Fig .6.3 to obtain the processed images of Fig .6.4

Parameter	Value
1pixel (px)	292nm
diskImOpen	1px
diskImClose	1px
diskImBackground	210px
coefGrayThresh	0.9
median2D	7px
deleteLessXpixel	1px
lowerBound	20px
upperBound	100px
imConcat	'Horizontally'

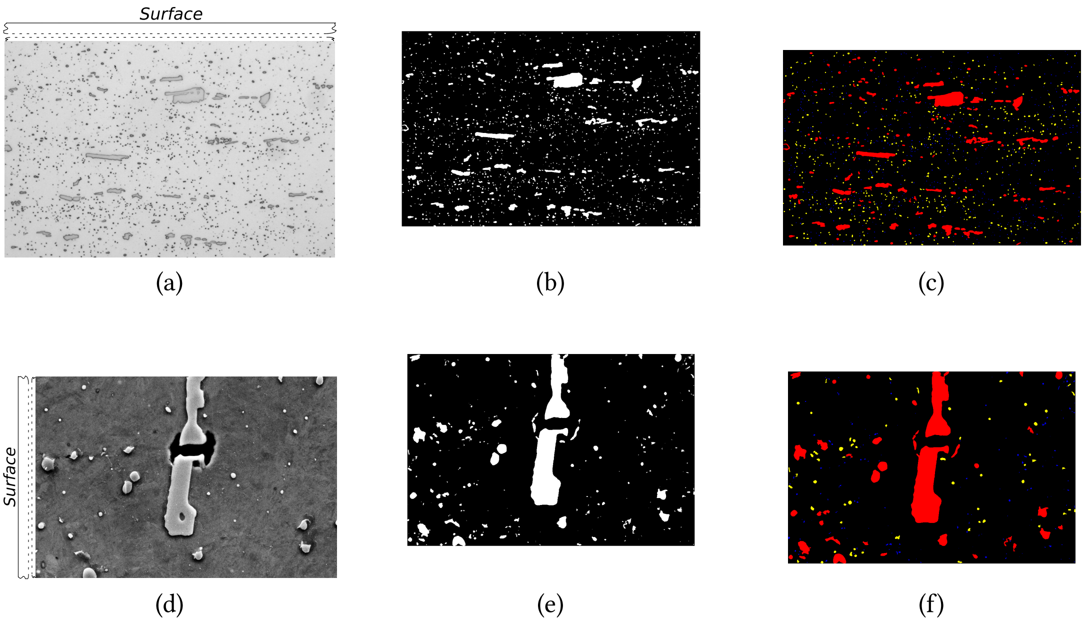

Figure 6.4: Image processing outputs carried out on the quenched/tempered and nitrided M50 microstructures selected inside the hardened layer of: (a) the M50 obtained by powder metallurgy technology and (d) the M50 obtained by VIM-VAR

Fig. 6.4(b,e) shows the binary images obtained from the Core procedure related to the initial images Fig. 6.4(a,d), respectively. One can see that the microstructure is accurately preserved. The post-processing procedure offers the possibility to create three families of particles according to their size. In Fig. 6.4(c, f) the relatively tiny carbides are colored in blue then can be homogenized in the numerical REV. The large carbides are colored in red when the medium-size ones are colored in yellow. This classification is made with respect to the variables *lowerBound* and *upperBound* set. The output file consists of the size of large carbides considered critical for the RCF, their distribution and their volume fraction. These data are directly used to simulate the REV for the modeling part.

6.2.3 MECHANICAL PROPERTIES DETERMINATION

The macroscopic mechanical properties were made using micro tensile samples, to measure the mechanical properties of the different layer, assuming there were homogeneous. Those measures are supplemented with micro and nano and micro indentation tests are conducted to check the values found in the literature, for the different layers and the carbide phases.

6.2.3.1 Mechanical characterization by micro-indentation

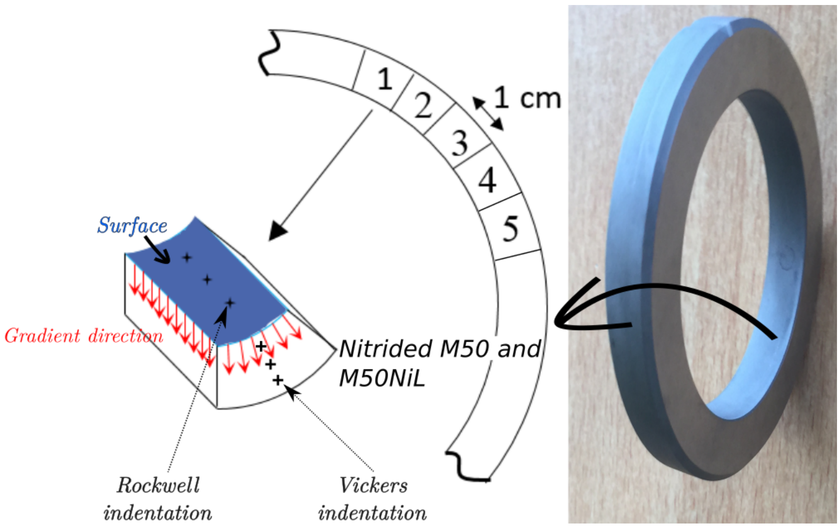

Figure 6.5: Nitrided M50 and M50NiL samples slicing for micro-indentation tests. The surface and the hardness gradient direction are indicated. The Rockwell indentation is performed on the surface while the Vickers indentation is performed on the subsurface.

Micro-indentation tests are performed on nitrided M50 specimens. Fig. 6.5 presents sectioned sample geometries with respect to the entire bearing race structure. Rockwell indentations are conducted normal to the property gradient direction for qualitative analysis of the overall behavior when the bulk material is subjected to contact load. Since the Rockwell indenter tip is spherical, these tests permit to reproduce the severity of the indentation caused by hard spherical particles during the RCF (such as debris which are not yet led to the oil filtration device). The purpose is to analyze the macroscopic surface cracks produced, according to the loading force and the hard particle equivalent diameter. Vickers indentations are performed for quantitative analysis of the local behavior at different depths along the applied stress gradient direction. Vickers indentation is chosen here, because the hardness value provided can be used to estimate the material yield strength via existing models in the literature (Tabor (2000) [195] , Cahoon, Broughton, and Kutzak (1971) [196] , Pavlina and Van Tyne (2008) [197]). One can then reconstruct the gradient of the material plastic properties. For instance, Tabor's rule is used in [275] to convert Vikers hardness to yield stress in order to obtained plastic response along the depth of graded materials without the need for tension or compression tests.

6.2.3.2 Specimens preparation for the micro-tensile tests

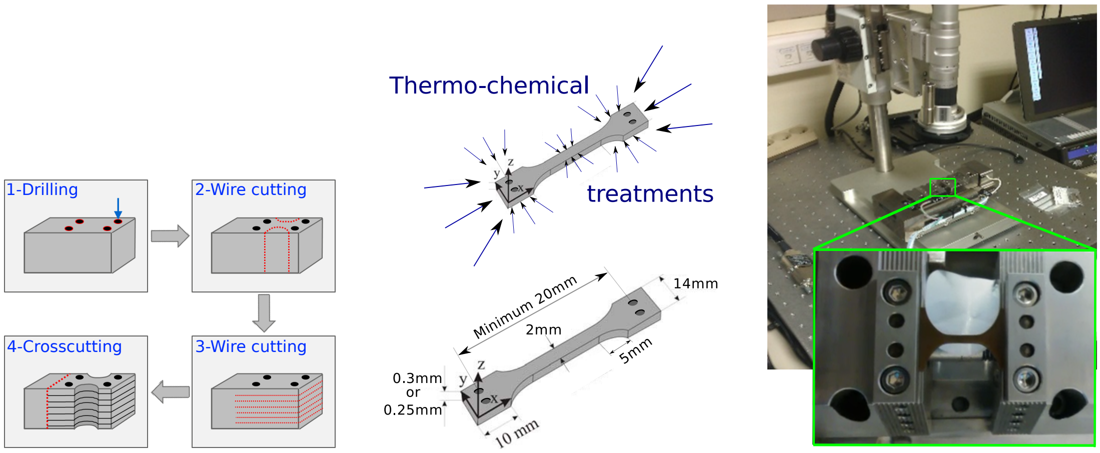

(a) (b) (c)

Figure 6.6: In-situ micro-tensile test setup: (a) Specimens preparation (b) Specimen final geometry after thermochemical treatments; (c) Loading stage with a mounted specimen. The micro-tensile tests are performed on the M50 material. The samples are treated after the step *(4-Crosscutting)* of (a)

The aim of micro-tensile tests is, first, to measure the tensile properties of the different layers, assuming homogeneous layers. The specimens are sectioned by wire-cutting process before the thermochemical treatments, Fig. 6.6(a). Then the whole samples were cemented or nitrided. Three states were then tested for each composition: bulk metal, cemented and nitrided.
As this micro-tensile device is designed for SEM in situ measurements, the second objective was to follow the crack apparition and propagation in situ in the SEM, and to correlate its path with the local microstructure.
Fig. 6.6shows the setup of the in situ micro tensile tests on M50 materials. Micro-tensile tests were performed using a 2kN Deben commercial micro-tensile stage. The loading device requires the specimens sizing described in Fig. 6.6(b). The thickness is calculated knowing that the maximum achievable force is 2kN.

6.3 RESULTS

6.3.1 MICROSTRUCTURE CHARACTERIZATION

6.3.2 THE THROUGH-HARDENED AND NITRIDED M50

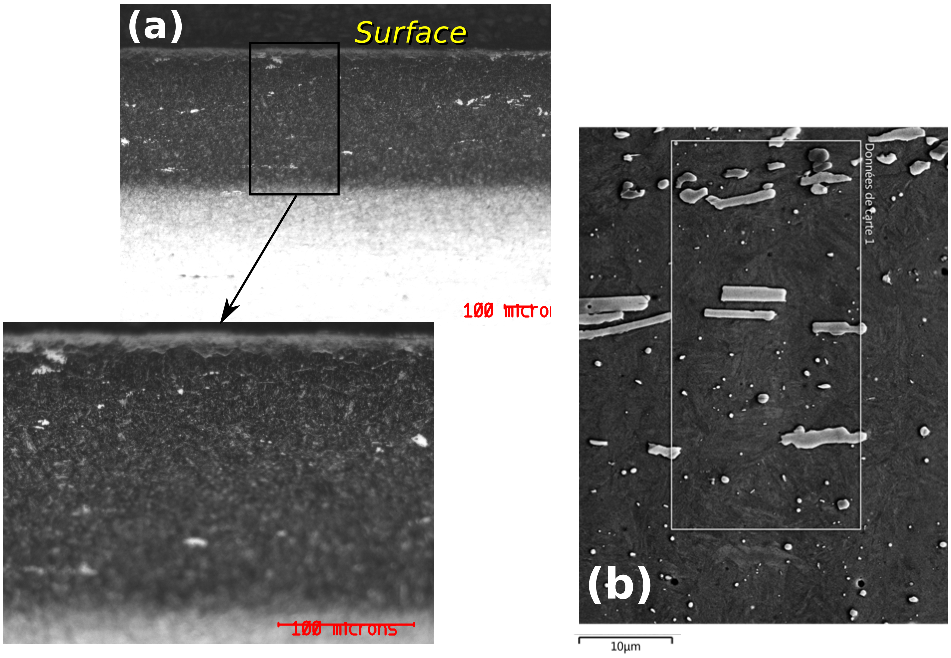

Figure 6.7: Microstructure of M50 alloy (Quenched/Tempered and Nitrided) from (a) Optical microscopy and (b) SEM observations

Fig. 6.7 presents the microstructure of M50 alloy from (a) Optical Microscopy (OM) and (b) SEM observations. The nitrided layer appears darker on the OM image, and its length is around 200µm. The hardened layer is found to be 2000µm.

Some fine and elongated gray contrast are close to the surface. It is reported as *'angel hair'* carbides in GIRODIN (2008) [117] . Micrometric spherical carbides are also observed in the nitrided layer.

In the bulk metal, some large rectangular cuboid particles (10µm in length, 2µm large) are visible, identified as carbides from EDX measurements. They are oriented parallel to the surface along the rolling/forging direction and align as long stringer chains. They can be close to each other along their width side but they leave a minimum gap of about 5µm along the length side which corresponds to the stringer direction. The relevant direction frequently observed is the one parallel to the surface along with the rolling direction. The effect of carbide stringer is studied by a numerical model presented in the section 6.4.1.

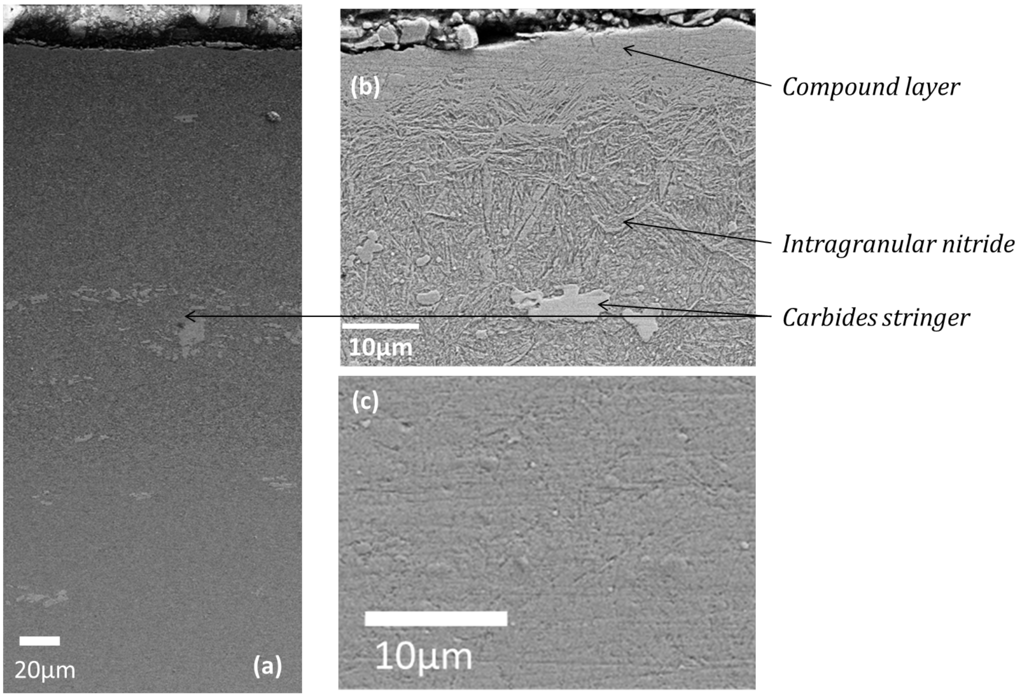

Figure 6.8: SEM observations of the through-hardened and nitrided M50 microstructure: (a) an overview; (b) the nitrided zone; (c) the through-hardened zone

Smaller spherical shaped particles, identified as carbides from EDX measurements are also present in the through-hardened zone as shown in Fig. 6.8(c). The composition of carbide stringers found in Fig. 6.8(b) was measured by EDX. Carbon content could not be quantified, but the carbides contain mostly molybdenum, together with vanadium and chromium and some iron.

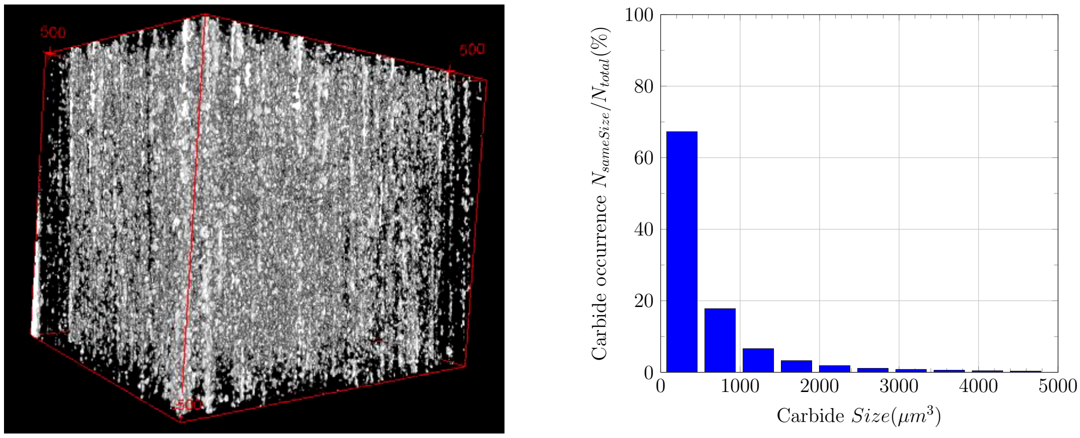

(a) (b)

Figure 6.9: Characterization of beneath layers: (a) M50 microstructure [$Voxel = 3 \times 3 \times 3(\mu m^3)$]; (b) Histogram of carbides inside the REV obtained by tomography [REV $=$L1560$\times$W1560$\times$H1852.2(μm^3) and carbide content $=$ 4.6046% in the REV]

It is well known that the large rectangular cuboid carbides play an important role on the material mechanical behavior during the RCF (Nélias et al. (1999) [4] , Bhadeshia and Solano-Alvarez (2015) [276]). In order to get a quantitative description of the size distribution and space repartition of those carbides, a 3D X-Ray Tomography analysis was performed, see Fig. 6.9. Thanks to the absorption difference of the matrix and of those carbides, a clear contrast is observed. Fig. 6.9(b) confirms the continuous distribution of M50 carbides. The carbide volume fraction obtained from the image processing is 4.6%. One can also see that about 85% of the carbides size is less than $1000\mu m^3$. But less than 2% of the carbides are larger than $3000\mu m^3$ and that occurrence is constant up to $5000\mu m^3$.

6.3.3 THE CASE-HARDENED AND NITRIDED M50NIL

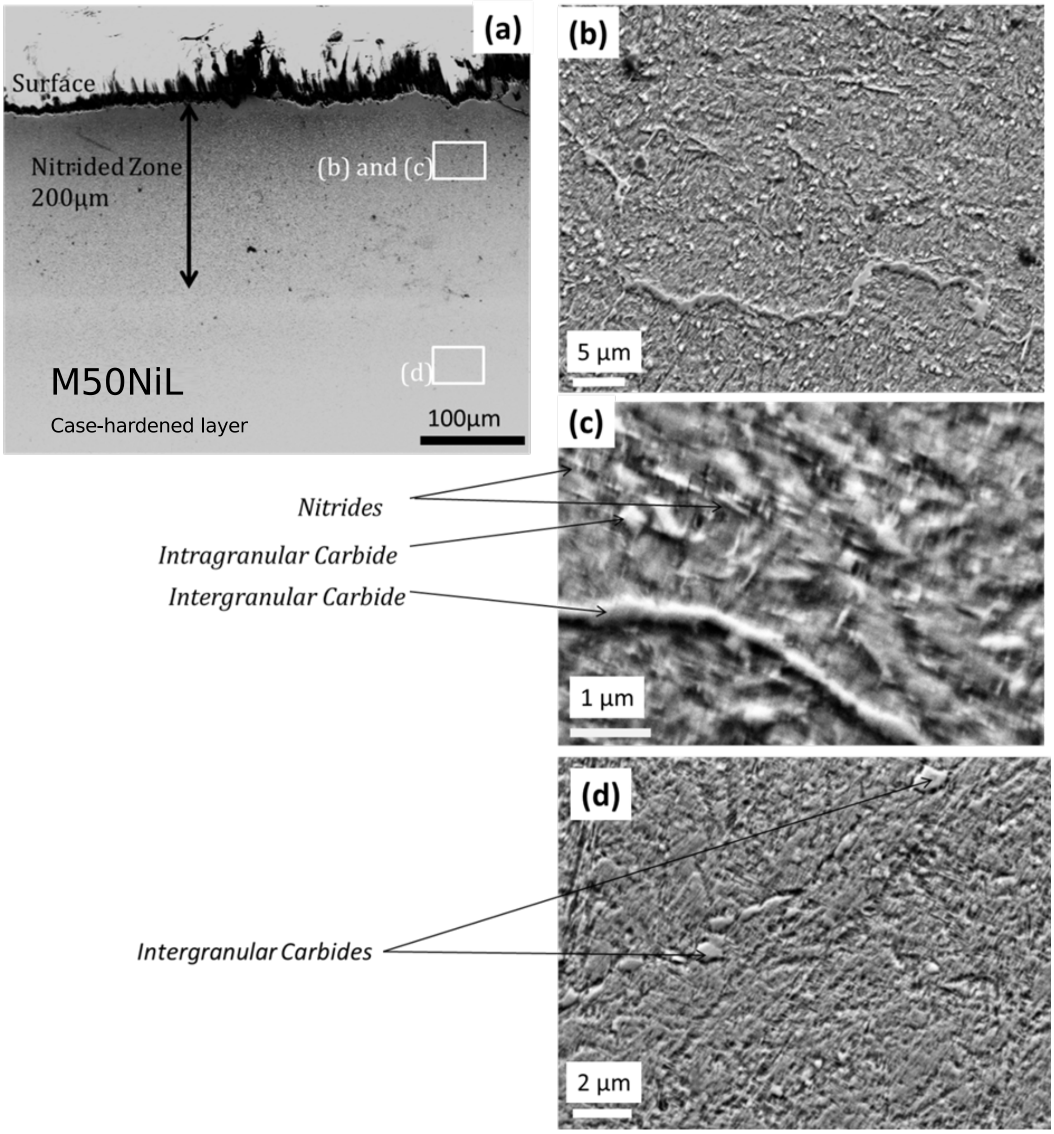

Figure 6.10: SEM observation presenting: (a) Global view of the M50NiL; (b) and (c) closer view of the nitrided zone; (d) closer view of the case-hardened zone

On SEM images, the nitrided layer appears darker than the core material. Its width is around $200\mu m$. In the nitride zone, *'angel hair'* carbides are present such as in the case of the M50 sample, but slightly larger, and present at higher depth in the sample. Nanometric needle shaped nitrides are also present in the grains, together with coarser spherical shaped carbides, with diameters close to $500nm$. In the case-hardened zone, micrometric spherical shaped carbides are visible and aligned at what seems to be former austenitic grain boundaries, while smaller spherical carbides are present inside the grains, see Fig. 6.11.

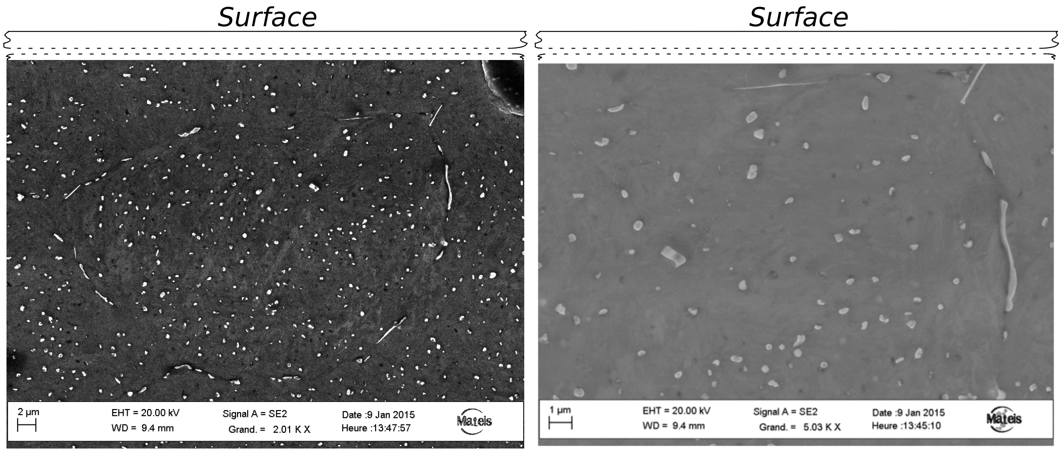

Figure 6.11: Inter and intra-granular carbides inside the hardened layer of the M50NiL Case-hardened Quenched/Tempered and Nitrided

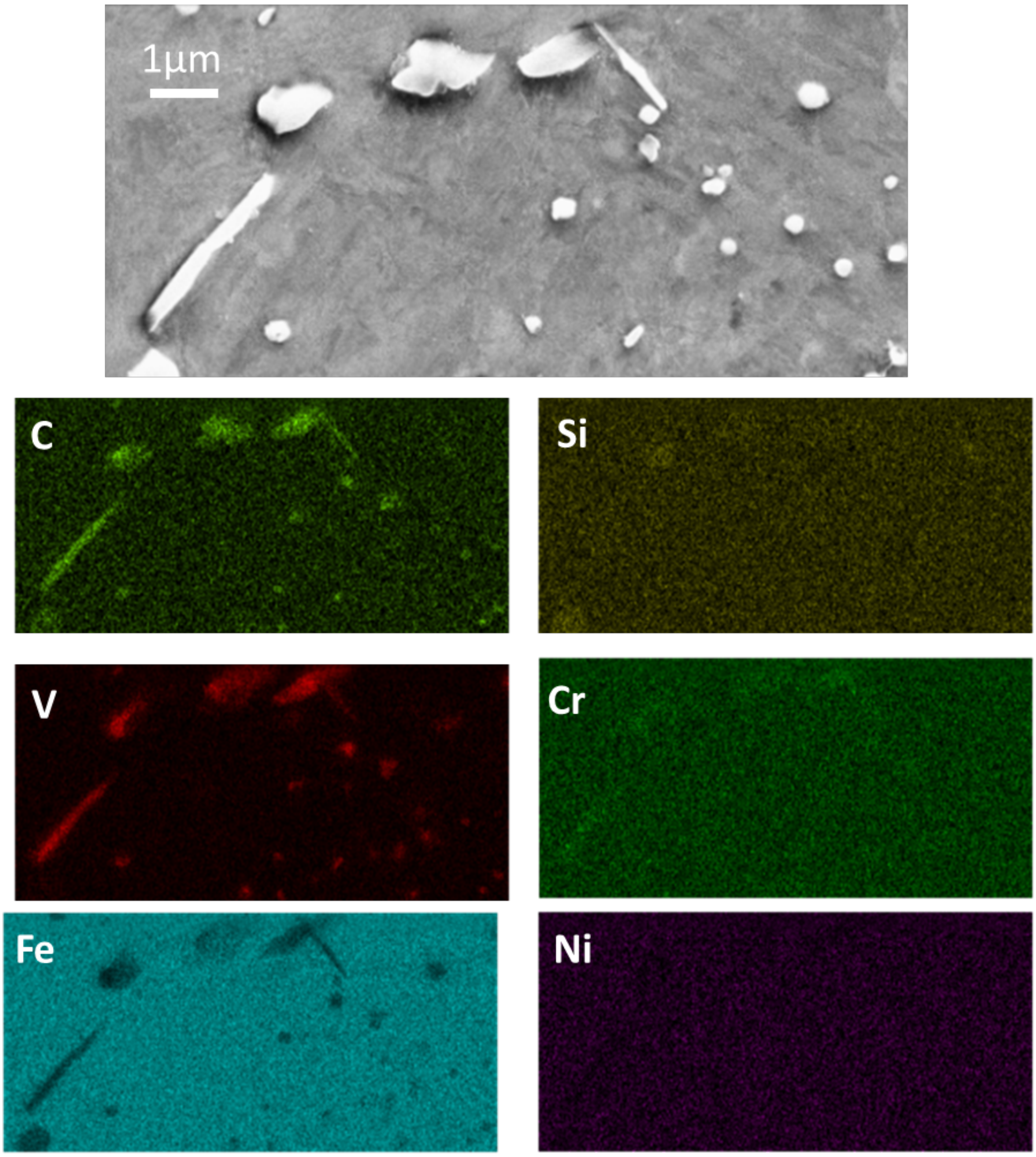

Figure 6.12: EDX map showing the chemistry of carbides in the core material of the M50NiL. Carbides contain C, Cr, Mo V, and some Si

Table 6.4: Chemical composition (% at) of targeted intergranular carbides of M50NiL nitrided layer

Si	V	Cr	Mn	Fe	Mo	Ti	Ni	N	Total
1.02	29.22	11.55	0.79	15.69	41.58	0.15	0	0	100

Fig .6.10 presents the intergranular carbides in the M50NiL nitrided layer by EDX analysis. These carbides can have two distinguishable forms. Some of them are almost spheroidal with a diameter equivalent to approximately 1µm as in Fig .6.10(d). The others have subatomic thickness but their length is about 5µm. The latter are curved as in Fig .6.10(c). All these carbides are found between grain boundaries of the nitrided layer. This can be explained by the fact that the nitriding diffusion drains the old intergranular carbides resulting from the case-hardening. These carbides are then blocked between the grain boundaries. These carbides form stringers oriented by the grain boundary directions. The length of these stringers depends on the grain boundary size. One will observe during the micro-tensile tests that longer a carbide stringer is, more it is able to generate long cracks. Thus it is preferable to control the heat treatments in purpose to obtain small grains. Moreover, the Tab. 6.4 shows the chemical composition (% at) of a targeted intergranular carbides M50NiL nitrided layer. It can be seen an absence of silicon inside the intergranular carbide whereas the studied nitrides contain silicon. But vanadium and molybdenum are found to be the predominant amount elements inside the intergranular carbide with an uncertainty of the EDX measurements of about 1%. It is interesting to specify that the carbides containing a high quantity of vanadium and molybdenum are likely to break in a ductile matrix submitted to tensile stress. This fact can predispose the nitrided layer to crack initiations when there are strong stress concentrations in tensile due to plastic strains in areas where resides these carbides. This point will be developed in the section devoted to micro-tensile tests.

MODELING OF THE MATERIALS MICROSTRUCTURES AFTER THERMO-CHEMICAL TREATMENTS

Fig. 6.13 recaps the main characteristics of the microstructures of M50 from M50NiL. One can see that the nitrogen diffusion layer of both materials have similar thickness, as the nitriding parameter are similar for the two compositions. In both cases, *'angel hair'* carbides with thicknesses of few hundreds of nanometers at grain boundaries are observed, together with smaller carbides. In the M50NiL nanometric nitrides are present while large carbides are observed in the case of the M50.

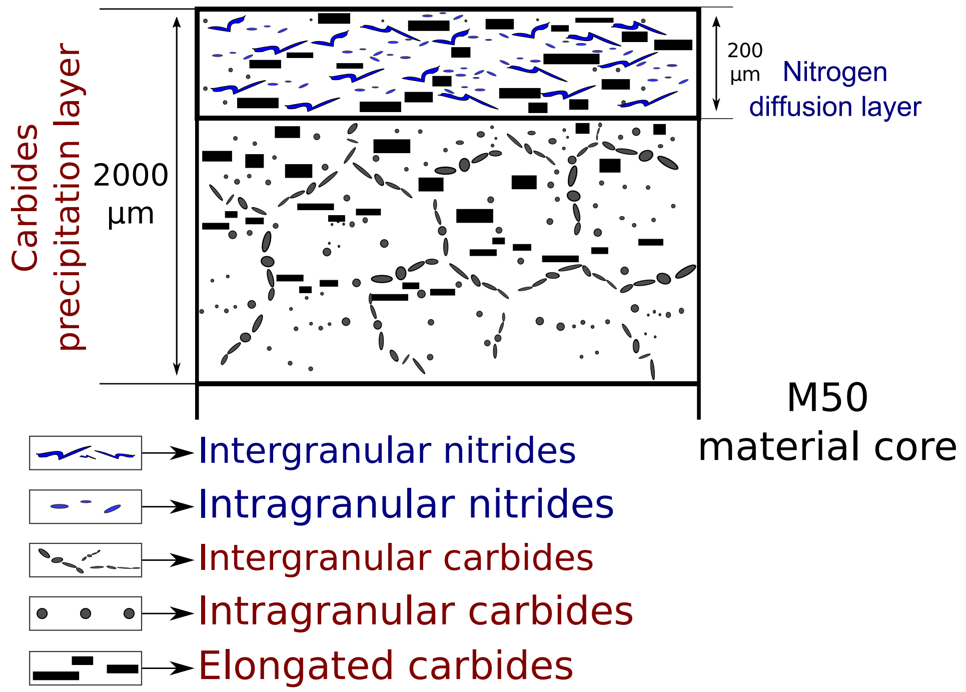

(a)

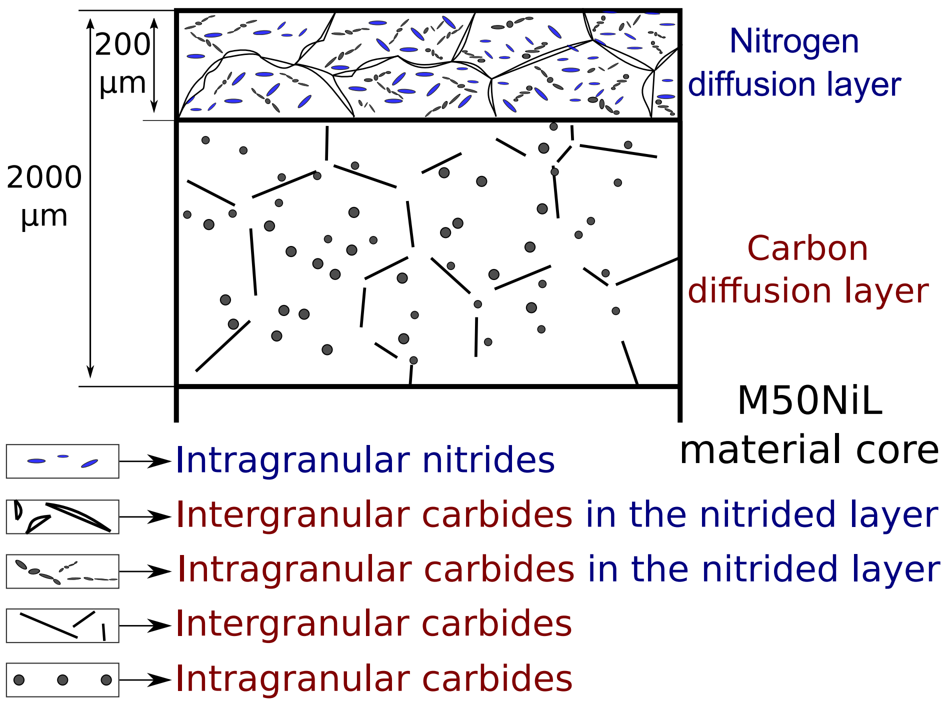

(b)

Figure 6.13: Modeling of the materials microstructures after thermo-chemical treatments: (a) M50 Quenched/Tempered and Nitrided; (b) M50NiL Case-hardened Quenched/Tempered and Nitrided

It should be mentioned that the martensitic structure created during the quench/tempering process is conserved in the hardened layer. It means that the material core remains ductile compared to the hardened layer which is more brittle. Concerning the hardened layer, one can see that only M50NiL presents intra and inter granular carbides. In the M50 hardened layer, large carbides are rather organized as clusters and stringers. The effect of stringer orientation and cluster density along with carbides mu-

tual influence is studied numerically in the section sec:StringerCluster.
The carbides and nitrides presence in M50 and M50NiL materials resulting from the carburizing and nitriding have been characterized. Now the mechanical behavior related to the local microstructure is investigated at nano and micro scales.

MECHANICAL BEHAVIOR

6.3.3.1 Mechanical characterization by Nano-indentations

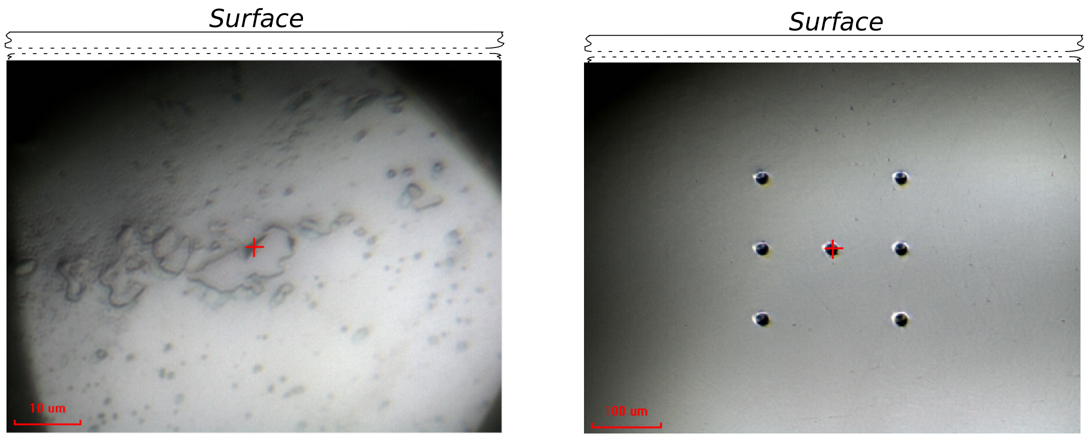

(a) (b)

Figure 6.14: Mechanical characterization by nano-indentation tests performed in the M50: (a) through-hardened material zone with presence of high carbide clusters population; (b) material matrix

The Young modulus of the M50 matrix and carbides is determined through nano-indentation tests thanks to the nanoindenter Aligent G200. This machine has been used in [202]. A Berkovich tip has been used for the carbides and a spherical tip for the matrix because of the difference in hardness between the nature of both materials. Only the largest carbides could be analyzed. From the load/displacement curve provided by the nano-indentation test, the elastic plastic behavior of the carbides could also be identified. Note that the measured Young modulus error is less than 10%.

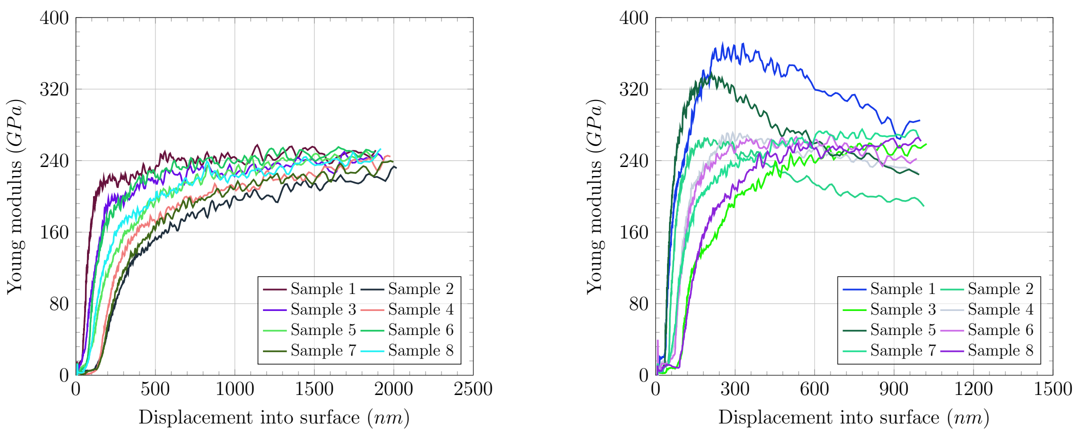

(a) (b)

Figure 6.15: Young's modulus obtained by nano-indentation tests performed in the M50: (a) material matrix; (b) through-hardened material zone with presence of high carbide clusters population

Fig. 6.15 presents the Young's modulus obtained by the nano-indentation tests. It could be seen in Fig. 6.15(a) that the effective Young modulus of the M50-through-hardened matrix is tending toward the value of 240GPa. Klecka, Subhash, and Arakere (2013) [254] estimated the M50-through-hardened matrix modulus to be 210 ± 10GPa, close to the mean value of 215GPa found here (Tab. 6.5). The maximum values of carbide Young's modulus are extracted from Fig. 6.15(b) and presented in Tab. 6.6. Mean modulus is not relevant for carbides owing to their tiny thickness because the indenter tip drill the carbide material and touch the matrix material below. The scattered values of modulus could lead to argue that there are different families of carbides. More tests have to be performed in order to have more data for statistics classification of carbide families. In addition one can estimate the carbide thickness by measuring the distance covered by the indenter before the modulus dropped to the matrix modulus mean value. So far these carbides Young modulus values agreed with that provided in [254] where carbides found in M50-through-hardened have Young's modulus of $290 \pm 15\mathrm{GPa}$.

Table 6.5: Young modulus of nitrided M50 matrix from nano-indentation Fig. 6.15(a)

Sample	Average Young Modulus (GPa)	Max Young Modulus (GPa)
1	241.2	257.4
2	181.1	233.5
3	227.2	249.9
4	199.5	245.6
5	218.0	250.5
6	236.7	255.2
7	195.3	239.8
8	218.9	253.5
Mean	214.7	248.1721

Table 6.6: Young modulus of nitrided M50 carbides from nano-indentation Fig. 6.15(b)

Sample	Max Young Modulus (GPa)
1	370.8
2	265.1
3	259.4
4	271.0
5	337.2
6	269.1
7	275.0
8	265.9

6.3.3.2 Rockwell indentation on nitrided M50

In order to analyze the cracks, Rockwell indentation has been performed at different loads with different sizes of indenters as referenced in Tab. 6.7. Note that the indents are separated by at least $g = 1.5\mathrm{mm}$ to avoid interactions between each stamp residual fields (displacement, stress, strain). This held since the contact print radius is ten times less than the gap g regardless of the load and the tip size.

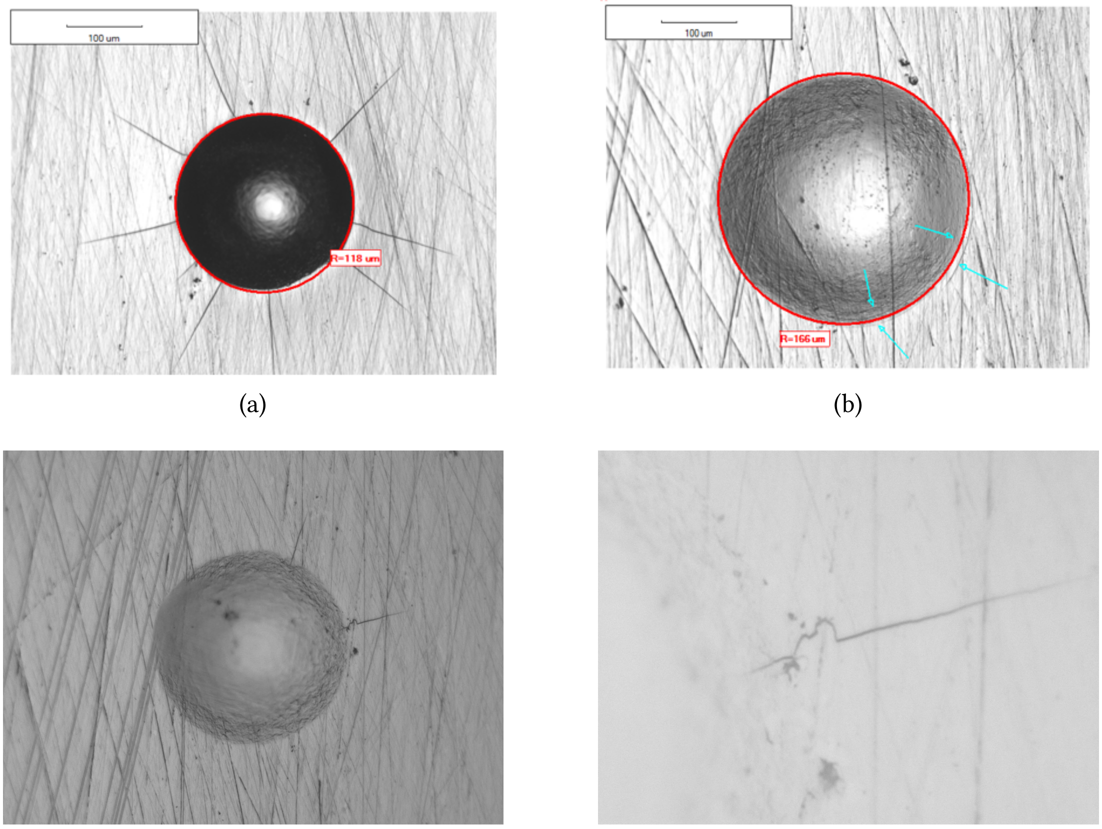

(a) (b) (c) (d)

Figure 6.16: Cracks observed during the Rockwell indentation on nitrided M50 surface: (a) radial cracks of $120\mu m$ length; (b) circumferential cracks; (c) radial crack bifurcation by an emerged carbide ($\times 20$ optical magnification); (d) radial crack bifurcation by an emerged carbide ($\times 100$ optical magnification)

Two cracking modes are observed as presented in Fig.6.16. Radial cracks named *start crack* located at the indents edges. The circumferential cracks located at the indents edges and inside the indentation print. On the one hand, the typical *start cracks* in Fig. 6.16(a), occurred when the indenters tip is less than $400\mu m$ under $50daN$ applied force. However when the load is diminished to $10daN$, the material stopped cracking. On the other hand, the typical circumferential cracks in Fig. 6.16(b), occurred when the applied force is higher than $50daN$ under the tip of $600\mu m$. Note that the presence of emerging carbides located at the print edge can create a radial crack when circumferential cracks are holding, typically in Fig. 6.16(c). In this configuration, the carbide forks the radial crack propagation but its initial trajectory is recovered after a certain distance as shown in Fig. 6.16(d).
It should be specified that the corresponding maximum contact pressure could be calculated for all configurations. But for an equivalent maximum contact pressure the cracking modes could be different according to the applied force and the indenter size. For that reason the surface toughness and cracking modes should be analyzed regarding both the applied force and the indenter size instead of only the maximum contact pressure.

Table 6.7: Indents dimensions from Rockwell indentations on nitrided M50

Indentation N°	Load (daN)	Tip radius (μm)	Indent radius (μm)	Crack observed
1	10	200	61	No
2	50	200	118	Radial
3	50	400	121	Radial
4	50	600	166	Circumferential
5	100	600	128	Circumferential

In order to confirm that the heterogeneous microstructure of the M50 Nil sample generates a hardness gradient, Vickers Hardness measurements were performed.

6.3.3.3 Vickers indentation on the nitrided M50NiL

Micro indentation tests are performed on nitrided M50NiL sample, along the rolling direction and along the depth; see Fig. 6.17. The purpose is to obtain the yield stress σ^y distribution as a function of the depth. Existing models (Pavlina and Van Tyne (2008) [197] , Tabor (2000) [195] , Ashby and Jones (1980) [277]) allow to relate the yield stress and the ultimate tensile stress to the hardness value. For most metallic materials, in particular steels, the Cahoon's [196] relationship $\sigma^y = \frac{H_V}{3}(0.1)^{m-2}$ is often used. H_V is the Vickers hardness in daN/mm^2 and m is the Mayers's hardness coefficient [216]. For accurate estimation of σ^y, Takakuwa, Kawaragi, Soyama, et al. (2013) [198] propose a model that takes into account the effect of residual compressive stress resulting from thermal process, on the hardness.

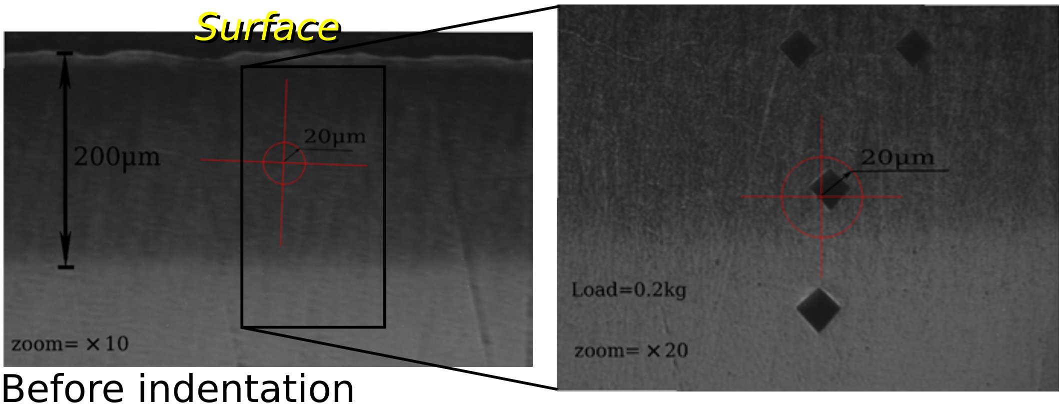

Figure 6.17: Vickers indentations on the nitrided M50NiL subsurface. Global view of indents location inside the case-hardened and the nitrided layers

The Tab. 6.8 presents the mean values of Vickers hardness obtained at different depths as $H_V = hv_{mean} = 1/n \sum_{i=1}^{i=n} hv_i$, where n the number of tests perform at a given depth. As expected, the hardness decreased from $1018 daN/mm^2$ at the outlying layer to $451 daN/mm^2$ in the substrate material, with respect to the trend described in Fig. 6.24(a). Similar values of the hardness are obtained in Sun, Zhang, and Yan (2014) [226] and in Ooi and Bhadeshia (2012) [214] .

Table 6.8: Vickers micro indentation

Depth $z(\mu m)$	Hardness $H_V(daN/mm^2)$
60	1018
120	945
200	790
240	451

6.3.3.4 Tensile properties of M50 sample, with and without surface treatments

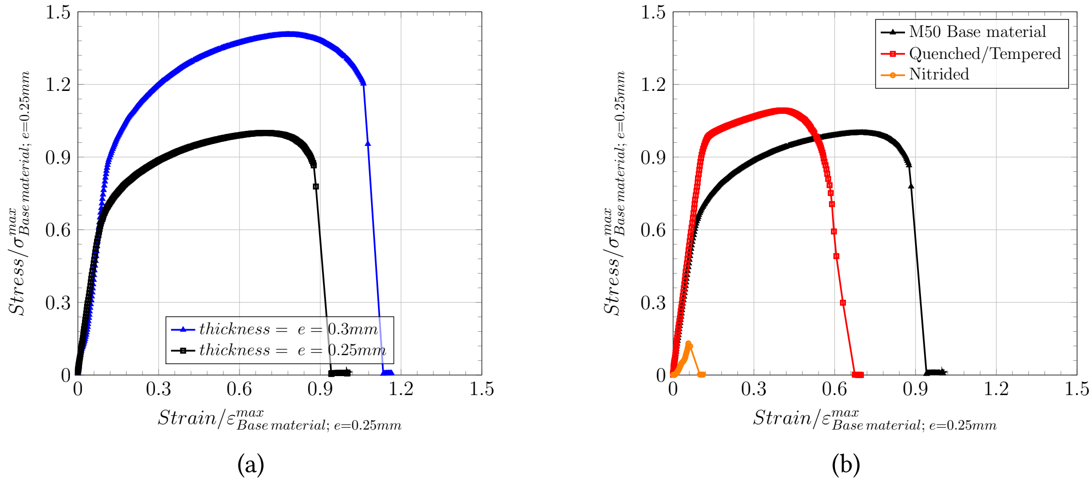

Figure 6.18: Stress-Strain curves: (a) Influence of M50 base material specimens thickness; (b) Effect of quenched/tempering and nitriding

The stress and strain curves from micro-tensile tests performed on M50 sample, under optical microscopy after thermochemical treatments are presented in Fig. 6.18. Micrographs were acquired regularly during the tensile tests, and image correlation could be performed to extract the correct stress/strain behavior. The axes are normalized by the maximum value obtained when the base material sample thickness is $e = 250\mu m$. The maximum values are $\sigma^{max}_{Base\,material;\,e=0.25mm} = 366.5MPa$ and $\varepsilon^{max}_{Base\,material;\,e=0.25mm} = 0.022$. The results of Fig. 6.18(a) are obtained when two samples ($e = 250\mu m$ and $e = 300\mu m$) of the untreated M50 material are pulled. It could be seen that the elastic slope is not affected by the samples thickness but the plastic part and the fracture point were influenced. The sample of $e = 250\mu m$ m is arbitrarily chosen for the thermochemical treatments. Fig. 6.18(b) shows that the elastic slope of the quenched/tempered M50 and that of the base material are perfectly superimposed, meaning that both elastic modulus are equal. However the yield stress has been increased by the case-hardening. Moreover one can observe that the plastic flow part of the quenched/tempered M50 and that of the base material are almost parallel. This allows to model the gradient of plastic property of the treated M50 by a unique hardening law weighted with a variable coefficient in function of the depth. The hardening law parameters could be obtained from any chosen layer. Hereafter the plastic behavior of the treated M50 is represented by Swift hardening law $\sigma^y = B(C + \varepsilon^p)^n$, where only the coefficient B depends on the depth. Even if the elastic modulus is not affected, one can note that the ductility has been decreased by the through-hardening. Then the total strain before the fracture point is also decreased by the case-hardening. Through hardened M50 can still undergo large applied deformation energy because of its ductile core which remains soft. This hold with respect to a particular size ratio between the subtract (core) and the treated layer. This ductility is an important factor for the fatigue resistance at low-cycle with relatively heavy load. But the hardened layer is still ductile compared to the nitrided one. It has been shown in previous sections that the nitrided layer is $200\mu m$ when the case hardening one is $2000\mu m$, then since sample thickness is $250\mu m$ or $300\mu m$, it implies that there is no gradient inside the sample because the treatment is done from the two sides of the samples, and the whole volume is affected. Gradient should appear when the thickness is more than $400\mu m$ at least. Then the nitrided sample is fully nitrided and it represents the M50 nitrided layer. Fig. 6.18(b) shows that this layer is very brittle. The nitriding significantly decreased the elastic property. It should be specified that on a real structure, the nitrided layer is sustained by the substrate, so that the overall behavior accounts the subsurface elastic-plastic property. Furthermore, from the in-situ footage, the total strain of the nitrided specimens have been measured by the image correlation tool developed in [278]. It is found to be barely 0.15% at the fracture point. This confirms the extremely brittle behavior of the nitrided layer.

DEFORMATION MECHANISM OF M50 SAMPLE

Now M50 samples are characterized by in-situ micro-tensile tests. Tests were performed in situ in the SEM to follow the deformation behavior of the matrix and of the carbides. More precisely, cracks onset and propagation modes are investigated under tensile tests. Note that one can correlate the tensile stress with that of compression stress which is the loading configuration undergone by the bearing material during rolling contact. An external compression load applied on material free surface leads in stress field which can get a positive sign (tensile) at some locations within the material. This is called an indirect-tensile. It is known that tensile stress is one of the factors that promote crack nucleation and propagation [221]. The effect of localized tensile stress is studied hereafter, in particular at the vicinity of carbide stringer and cluster. Note that only a small fraction of the cracks that are present in the sample is visible, as most of them appear in the volume and do not reach the surface at first.

The following observations were made:

- All specimens tested failed for applied stress under $\sigma_{max} = 2GPa$. This value could be considered as a stress limit in tensile or indirect-tensile of the M50 hardened layer at micro-scale.
- It should be noticed that all cracks observed in the case-hardened M50 material are located nearby carbide clusters and stringers, except obviously in the fractured section of the specimen.
- A good cohesion between carbides and the matrix before the tests; see for example Fig. 6.19. In this case, the debonding between carbides and matrix is a consequence of crack initiation. It should be specified that imperfections and flaws at inclusion-matrix interfaces, attributed to the metallurgic process, are often the precursors of debonding even for high-strength steels in very high cycle fatigue regime [279].

- Fig. 6.22 investigates on the composition in molybdenum and vanadium of cracked carbide *Spectre 12* versus the non-cracked *Spectre 15*. Considering EDX measurement errors, and the effect of the thickness on the measurement, there is not much difference in the precipitate concentrations. The size, orientation and distribution of the particles should then be determinant factor that controls the crack ability of the carbide.
- In addition, Fig. 6.21 highlights that the crack length varies with the carbide size. Moreover, only stringers have been cracked. Clusters stayed undamaged. This could imply that particular grouping is favorable for cracking.
- It could be seen from Fig. 6.21(a) that isolated elongated carbides are also likely to crack. In this case the crack is located in the middle of the carbide in the direction of the largest axis, almost perpendicular to the traction direction. Relatively small cracks take sources from the largest crack and rip the elongated carbide in multiple parts. Fig. 6.21(b) shows that the carbide cracking leads to the cleavage of its underground matrix. This implies that secondary cracks could be initiated out of the principal crack plane.

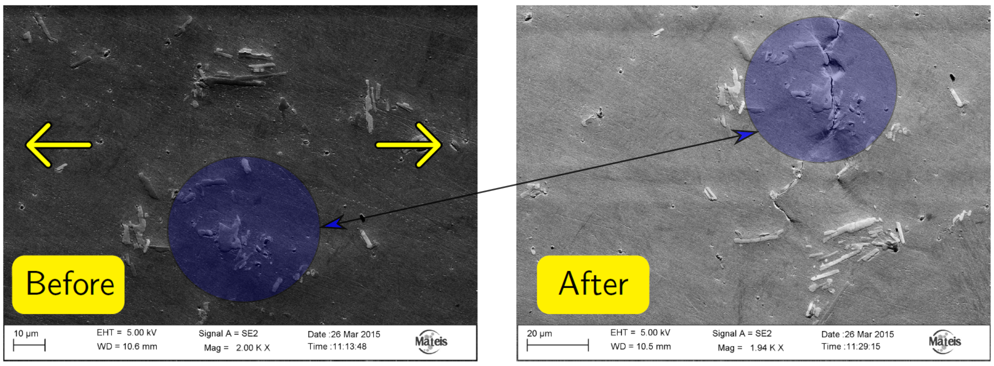

Figure 6.19: Mechanical characterization by micro-tensile tests

Fig 6.20 reveals that cracks appear preferentially inside aligned carbides which form *stringers*. From Fig 6.21, it can be seen that there is an influence of the orientation of those stringers toward the tensile direction. In this area, stringers are oriented perpendicular of parallel to the tensile direction, and one can see that the crack appears in the perpendicular family of carbides. As a result, cracks are oriented perpendicular to the applied tensile direction, such as cracks are quasi parallel to each other and parallel to the fractured section. It could be argued that in presence of multiple carbides (in form of a cluster), the principal crack will follow the line connecting carbides in a way to remain perpendicular to the applied tensile direction. This can also explain the orientation of butterfly wingspan cracks observed around non-metallic inclusions after rolling contact fatigue (RCF) tests when the load was strictly moving in one way. In deed the areas where the mean stress is in tensile around the inclusion are inclined perpendicularly regarding of the butterfly wing, [280].

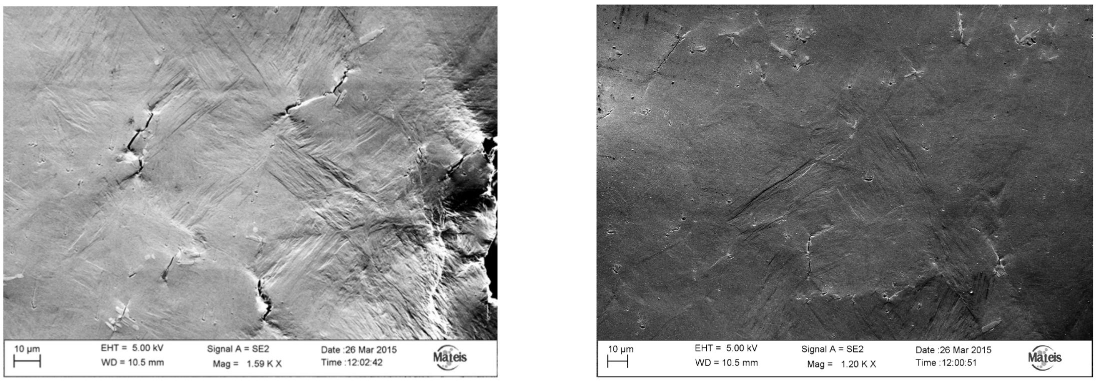

(a) (b)

Figure 6.20: Cracks and dislocation activities after micro-tensile tests: (a) zone close to the fractured section; (b) zone far from the fractured section

It is observed that the crack dimensions depends on a combination of the stringer length and location according fractured section. Hence, Fig. 6.21 shows that the cracks C_4 and C_5 have the same lengths but the crack C_5 is thinner than the crack C_4. It could be explained by the fact C_4 closer to the fractured section. However, the width of the crack C_2 is larger than that of the crack C_1 even if the stringer associated to C_1 is the closest to the fractured section. In that case, the stringer associated to C_2 is longer than that of C_1. Both the location and the length of the stringer seem to affect the crack dimension. From C_3, it is held that, for far from rupture and short stringers, crack dimensions remain small.

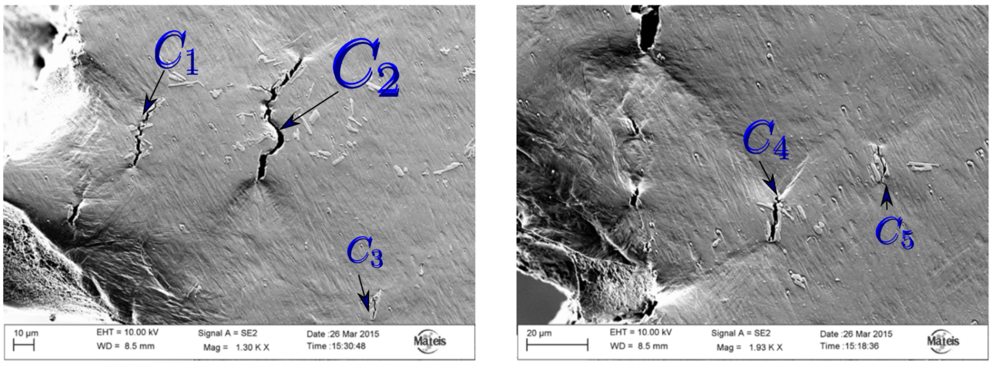

Figure 6.21: Cracks issued from the micro-tensile tests

The view of dominant dislocation activities informs about a prevalent plastic behavior. A certain degree of ductility is preserved in the M50 case-hardened layer. In Fig. 6.20, dislocation activity ceases in the matrix in areas situated beyond 10mm away from the fractured section, however, cracks still happen there. This supports the argument that cracks are initiated from carbides, being more brittle.

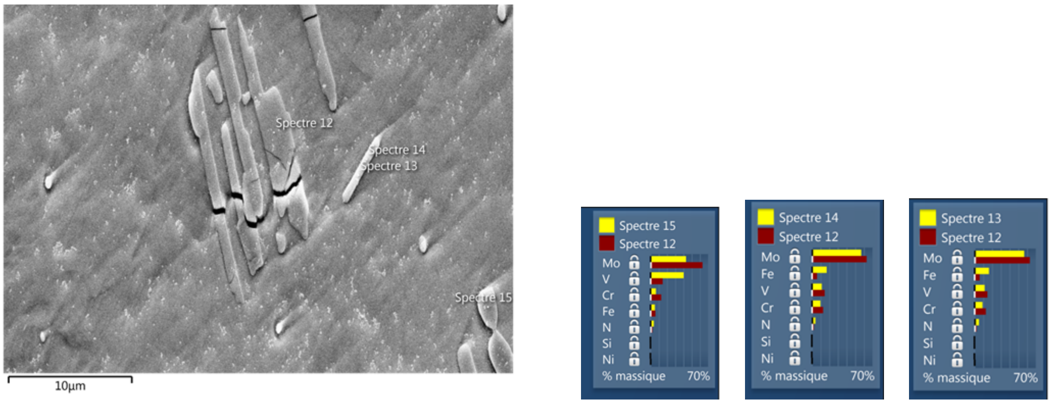

(a) (b) (c) (d)

Figure 6.22: Spectroscopy of cracked and non-cracked carbides

Fig. 6.21 also shows that there are non-cracked carbides situated in some zones beside cracked carbides stringers. This could be explained by stress relaxation induced ahead the crack. In addition, one can see two dark shades, inclined 45°, indicating a relief left by permanent deformation at each crack front. The plasticity happened owing to high stress concentration when the carbide crack encountered the elastic-plastic matrix. The material yielding is diffused in the direction where the cracks might be supposed to propagate, because those regions undergone stress peaks that did not exceed the fracture limit. Note that regardless of the stringer crack dimensions and orientation, the two plastic zones at a crack front are oriented at 45° and −45° relative to the applied tensile direction. Hence, an angle of 90° is always conserved between the two plastic zones, see Fig. 6.21 and Fig. 6.20(a). One can make the hypothesis that in RCF situation of through-hardened M50, the early cracking of carbides led to plastic strain in the surrounding material. In the meantime, during cycles, material resistance is decreasing due to microstructure degradation promoted by carbides. Then the overstress produced by primary cracks becomes sufficient enough to provoke further nucleation followed by other cracks departure. The coalescence and propagation of those cracks inside the material could be responsible for the spalling failure.

All considered, carbide parameters that affect the treated M50 behavior can be summarized as:

- size
- alignment
- orientation
- environment

These parameters will be included in the numerical modeling.

6.4 MODELING

APPROACH FOR INTEGRATION OF EXPERIMENTAL DATA TO NUMERICAL MODELS

Fig. 6.23 illustrates how the experimental data coupled with numerical models are used to meet fabrication process objectives. First, the treatment is performed on some specimens and the value of the parameters used to control the process is stored. The general evolution laws of the hardness and residual stress profiles are built by analyzing the observed trends along with the variables and constant data identified on these latter profiles. Now the numerical model of rolling contact fatigue is performed based on the general evolution laws. Once strong correlations could be established between the process input parameters and those of the numerical model, simulation set is launched by varying the model parameters. Subsequently, a meta-analysis is conducted on the results issued from simulation set in order to extract the best qualified numeral model setup which led to fulfill the objectives initially defined. Then the corresponding setup of the parameters that might control the process is obtained by reverse correlation. Validation procedures are finally needed to examine whether the material obtained by the selected setup is confirming the objective list experimentally.

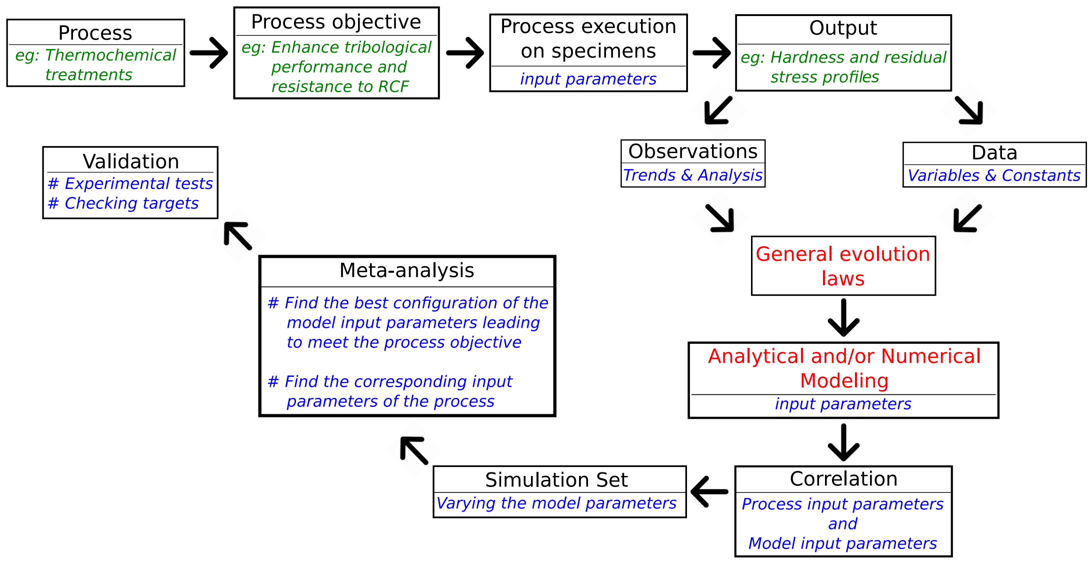

Figure 6.23: Flowchart to determine optimal parameters of a process by numerical modeling and simulation set

Particularly for martensitic steel, the positions of $t_{1,2,\ldots,\infty}$, presented in Fig. 6.24, depend on the thermochemical treatment parameters and conditions such as furnace time, temperature, catalyst nature and quantity, etc. However the general trends of the residual stress profiles remain similar [224]. This also holds for the yield stress profiles in [216] or the hardness profiles in [226, 214]. This allows the establishment of correlations between the process input parameters and those of the numerical model.

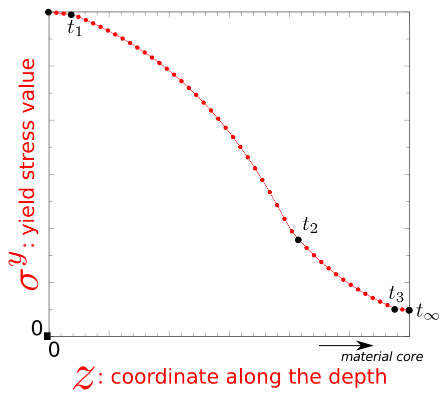

(a)

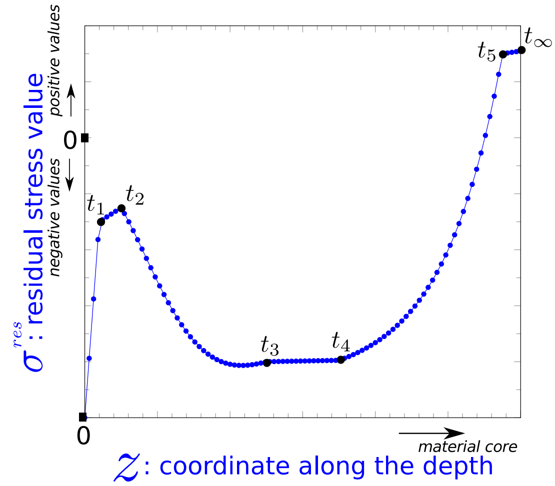

(b)

Figure 6.24: Modeling the distribution of (a) initial stress and (b) yield stress after thermochemical treatments by analytical expressions involving a set of parameters depending on: $t_{1,2,\ldots,\infty}$

The typical gradient of the yield stress obtained after case hardening and/or nitriding is modeled as a function of the coordinate along the depth z, by this following set of equations :

$$\sigma^y(z) = \begin{cases} \sigma^y_{\text{surface}} + z\left(\sigma^y_{t_1} - \sigma^y_{\text{surface}}\right)/z_{t_1} & \text{, if } z \leqslant z_{t_1} \\ \sigma^y_{t_1} + C_1^{YS}\left(1 - \exp\left(c_1^{ys}\left(z - z_{t_1}\right)\right)\right) & \text{, if } z_{t_1} < z \leqslant z_{t_2} \\ \sigma^y_{t_3} + C_2^{YS}\left(\exp\left(c_2^{ys}\left(z_{t_3} - z\right)\right) - 1\right) & \text{, if } z_{t_2} < z \leqslant z_{t_3} \\ \sigma^y_{t_3} & \text{, if } z_{t_3} < z \leqslant z_{t_\infty} \end{cases} \tag{6.1}$$

Where, $\sigma^y_{\text{surface}}$ is the yield stress value at the surface layer; $\sigma^y_{t_1}$ and $\sigma^y_{t_2}$ are the yield stress values at specific transition points; $\sigma^y_{t_3}$ and $\sigma^y_{t_\infty}$ are the yield stress values of the substrate material; C_1^{YS} and C_2^{YS} are constant coefficients to identify for different input distributions of the yield stress; c_1^{ys} and c_2^{ys} are constant to ensure the continuity of each portion of the curve between t_1, t_2 and t_3 as:

$$\begin{aligned} c_1^{ys} &= \log\left(\left(\sigma^y_{t_1} - \sigma^y_{t_2} + C_1^{YS}\right)/C_1^{YS}\right)/\left(z_{t_2} - z_{t_1}\right) \\ c_2^{ys} &= \log\left(\left(\sigma^y_{t_2} - \sigma^y_{t_3} + C_2^{YS}\right)/C_2^{YS}\right)/\left(z_{t_3} - z_{t_2}\right) \end{aligned} \tag{6.2}$$

In practice the yield stress is inferred from the Vickers hardness as aforementioned in Sec. 6.3.3.3. The typical profile of the residual stress distribution obtained after hardening and/or nitriding is modeled as a function of the depth z, by this following set of equations :

$$\sigma^{res}(z) = \begin{cases} \sigma^{res}_{surface} + z\left(\sigma^{res}_{t_1} - \sigma^{res}_{surface}\right)/z_{t_1} & , \text{if } z \leqslant z_{t_1} \\ \sigma^{res}_{t_1} + (z - z_{t_1})\left(\sigma^{res}_{t_2} - \sigma^{res}_{t_1}\right)/(z_{t_2} - z_{t_1}) & , \text{if } z_{t_1} < z \leqslant z_{t_2} \\ \sigma^{res}_{t_3} + C^{RS}_1\left(\exp\left(c^{rs}_1 (z_{t_3} - z)\right) - 1\right) & , \text{if } z_{t_2} < z \leqslant z_{t_3} \\ \sigma^{res}_{t_3} + (z - z_{t_3})\left(\sigma^{res}_{t_4} - \sigma^{res}_{t_3}\right)/(z_{t_4} - z_{t_3}) & , \text{if } z_{t_3} < z \leqslant z_{t_4} \\ \sigma^{res}_{t_4} + C^{RS}_2\left(1 - \exp\left(c^{rs}_2 (z - z_{t_4})\right)\right) & , \text{if } z_{t_4} < z \leqslant z_{t_5} \\ \sigma^{res}_{t_5} + (z - z_{t_5})\left(\sigma^{res}_{t_\infty} - \sigma^{res}_{t_5}\right)/(z_{t_\infty} - z_{t_5}) & , \text{if } z_{t_5} < z \leqslant z_{t_\infty} \end{cases} \tag{6.3}$$

Where, $\sigma^{res}_{surface}$ is the residual stress value at the surface layer; $\sigma^{res}_{t_1}$, $\sigma^{res}_{t_2}$, $\sigma^{res}_{t_3}$, $\sigma^{res}_{t_4}$ and $\sigma^{res}_{t_5}$ are the residual stress values at particulars transition points; $\sigma^{res}_{t_\infty}$ is the residual stress value in the core of the substrate material; C^{RS}_1 and C^{RS}_2 are constants that remain to be identified for different input distributions of the residual stress; c^{rs}_1 and c^{rs}_2 are constant to ensure the continuity of each portion of the curve between t_1, t_2, t_3, t_4 and t_5 as:

$$\begin{aligned} c^{rs}_1 &= \log\left(\left(\sigma^{res}_{t_2} - \sigma^{res}_{t_3} + C^{RS}_1\right)/C^{RS}_1\right)/(z_{t_3} - z_{t_2}) \\ c^{rs}_2 &= \log\left(\left(\sigma^{res}_{t_4} - \sigma^{res}_{t_5} + C^{RS}_2\right)/C^{RS}_2\right)/(z_{t_5} - z_{t_4}) \end{aligned} \tag{6.4}$$

The parameters of the above analytical models Eq. 6.1 and Eq. 6.3, are identified for the yield stress and the initial residual stress profiles coming from real samples of through-hardened and nitrided M50 presented in Fig. 6.25. The yield stress dependency on the depth and the hardening law consistency evoked in Sec. 6.3.3.4, lets to model the gradient of plastic property of the case-hardened and nitrided M50 with the values recapitulated in Tab. 6.9. The distribution of the initial residual stress is fitted by the values listed in Tab. 6.10.

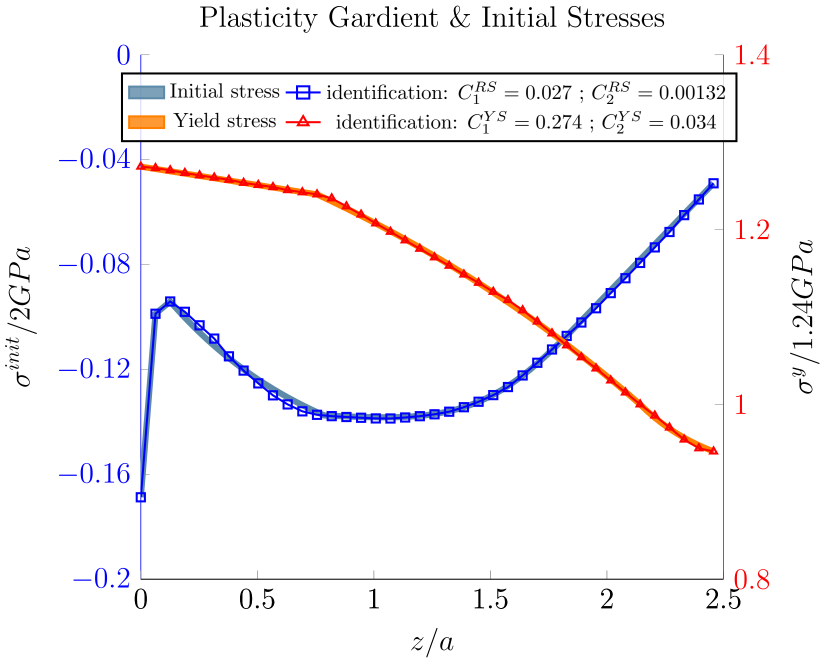

Figure 6.25: Fitting the model on profiles coming from nitrided M50

Table 6.9: Value of variables and constants modeling the yield stress profiles coming from nitrided M50 presented in Fig. 6.25

Parameter	Value
$\sigma^y_{surface}$	1.272
$\sigma^y_{t_1}$	1.240
$\sigma^y_{t_2}$	1.0
$\sigma^y_{t_3}$	0.946
z_{t_1}	0.756
z_{t_2}	2.142
z_{t_3}	2.457
C_1^{YS}	0.274
C_2^{YS}	0.034

Table 6.10: Value of variables and constants modeling the residual stress profiles coming from nitrided M50 presented in Fig. 6.25

Parameter	Value
$\sigma^{res}_{surface}$	-0.169
$\sigma^{res}_{t_1}$	-0.099
$\sigma^{res}_{t_2}$	-0.094
$\sigma^{res}_{t_3}$	-0.138
$\sigma^{res}_{t_4}$	-0.138
$\sigma^{res}_{t_5}$	-0.107
$\sigma^{res}_{t_\infty}$	-0.049
z_{t_1}	0.063
z_{t_2}	0.126
z_{t_3}	0.788
z_{t_4}	0.788
z_{t_5}	1.827
z_{t_∞}	2.457
C_1^{RS}	0.027
C_2^{RS}	0.00132

6.4.1 APPLICATION OF THE HETEROGENEOUS ELASTIC PLASTIC CONTACT MODEL

The numerical model based on the semi-analytical method developed in [104], is used to simulate an indentation and a rolling contact on nitrided M50. The model is supplied by the material data brought in by experimental investigations presented in previous sections.

6.4.1.1 Model validation

The semi-analytical model is first validated by comparison with results obtained by the finite element method in terms of contact pressure and plastic strain. The heterogeneous elastic plastic contact model is presented in Fig. 6.26. The gradient of properties and initial residual stress described in Fig. 6.25 are taken into account. The contact load is first applied to indent the body, then the load is moved in one direction to simulate pure rolling contact. As cuboidal shape particles are mostly observed in the above M50 microscopic images, the carbides are represented by cubes. This eases the numerical model in such a way to create heterogeneities which coincide with the matrix mesh. For dimensionless analysis, the carbide size r_i is reported on the Hertzian contact radius a introducing new variable $\beta = r_i/a$. The carbide location is represented by $\alpha = z_i/a$, where z_i is the coordinate along the depth of its center. The carbide property is involved via the parameter $\gamma = E^i/E^m$, where E^i and E^m are the carbide and matrix Young's modulus, respectively.

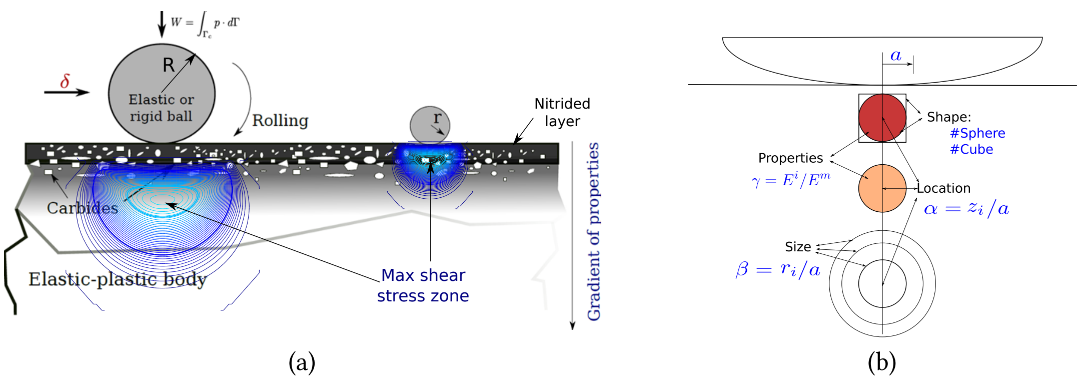

Figure 6.26: Indentation and rolling contact on nitrided M50: (a) Problem presentation; (b) Heterogeneity variables

It is noteworthy that the thicknesses of the case-hardened and the nitrided layers must be controlled in accordance with the domain of distribution of the applied energy. As in Fig .6.26(a), for the same quantity of applied energy by a given sized sphere, the Hertzian stress field could be concentrated in the case-hardened layer. But a smaller sized sphere leads to stress peak that is located in the nitrided layer. In consequence, the resistance to the RCF will be different for each of the two configurations.

Comparison with FEM

The indentation model used for the numerical validation is an assumed rigid sphere with a radius of $R_{tip} = 2.78mm$ in contact with a heterogeneous elastic plastic half-space in frictionless state. Note that in rolling contact, the contact pressure may very slightly increase when increasing the friction coefficient [281]. The indenter material is a silicon nitride Si_3N_4 which properties are a Young's modulus $E = 310GPa$ and Poisson's ratio $\nu = 0.3$. The half-space matrix material elastic properties are $(E, \nu)_m = (210GPa, 0.3)$ when that of the carbides are $(E, \nu)_I = (305GPa, 0.3)$. A normal Hertzian pressure distribution of $P_{max} = 4GPa$ is applied on $a = 63.5\mu m$ when the computational domain is discretized into a $65dx \times 65dy \times 35dz$ uniform cubic elements of $dx = dy = dz = 4\mu m$. Note that, for validation purpose, material yield stresses are lowered in order to produce the plastic flow under this applied pressure. The used plastic properties and hardening law of the matrix and carbide are listed in Tab. 6.11.

Table 6.11: Numerical model parameters

Contact	Carbide	Matrix
$P_{max} = 4GPa$; $a = 63.5\mu m$; $(E, \nu)_{sphere} = (310GPa, 0.3)$; $(E, \nu)_m = (210GPa, 0.3)$; $R_{tip} = 2.78mm$; $dx = dy = dz = 4\mu m$; Rolling distance $X = 288\mu m$	Perfect plasticity $\sigma_I^y = 1GPa$; $(E, \nu)_I = (305GPa, 0.3)$; size $\beta = 0.1a$; position $\alpha = 0.3a$	Swift law $\sigma_m^y = B(C + \bar{\varepsilon}^p)^n$ with $(B, C, n) = (350MPa, 4, 0.095)$ then $\sigma_m^y = 730MPa$

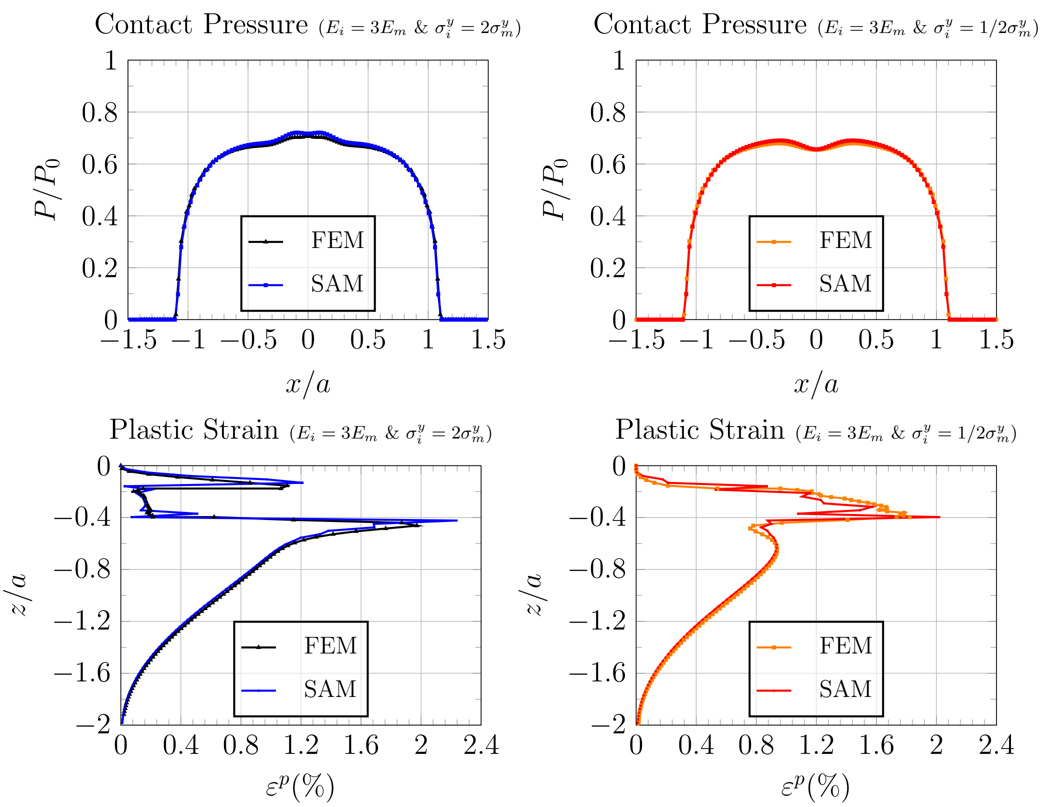

Figure 6.27: Numerical validation of the heterogeneous elastic plastic contact

Fig. 6.27 presents the comparison of SAM and FEM contact pressures at the surface when the space coordinate $y = 0$ and their corresponding plastic strains induced along the axisymmetric line z. Distances and pressures are normalized by the Hertzian contact radius a and maximum contact pressure P_0, respectively. Two configurations are presented. The blue and black plots are obtained when the value of the carbide yield stress is twice that of the matrix, $\sigma_i^y = 2\sigma_m^y$. The red and orange plots are obtained when the value of the carbide yield stress is half the one of the matrix, $\sigma_i^y = 1/2\sigma_m^y$. In all cases carbide is three times stiffer than the matrix $E_i = 3E_m$. It is interesting to note that very good agreement is obtained for both SAM and FEM results.

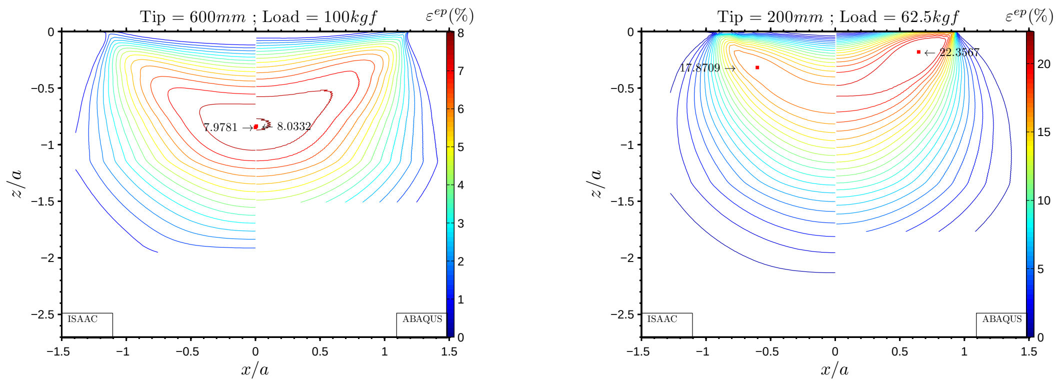

(a) (b)

Figure 6.28: Comparison of the plastic strain distribution: (a) the indenter radius is $600\mu m$ when the load is $100daN$; (b) the indenter radius is $200\mu m$ when the load is $65.5daN$

Moreover the plastic strain distribution is compared in absence of carbide to validate the semi-analytical model capability to describe plastic strain over 2%. It can be seen in Fig. 6.28 that the plastic strain distributions are quite similar for both SAM and FEM. However a difference between maximum values starts appearing when the accumulated plastic strain exceeds 15%, see Fig. 6.28(b).

Comparison with experimental result: surface displacement produce by a spherical particle entrapped in the contact

The elastic plastic response of the nitrided M50 in terms of surface displacement produced by a spherical particle entrapped in the contact is shown in Fig. 6.29. The particle has a radius of $100\mu m$ and was pressed at $50daN$. Remember that the one goal of the nitriding is to enhance the surface resistance to pitting caused by entrapped hard particles. The elastic plastic effective properties of the nitrided layer have been provided by homogenization.

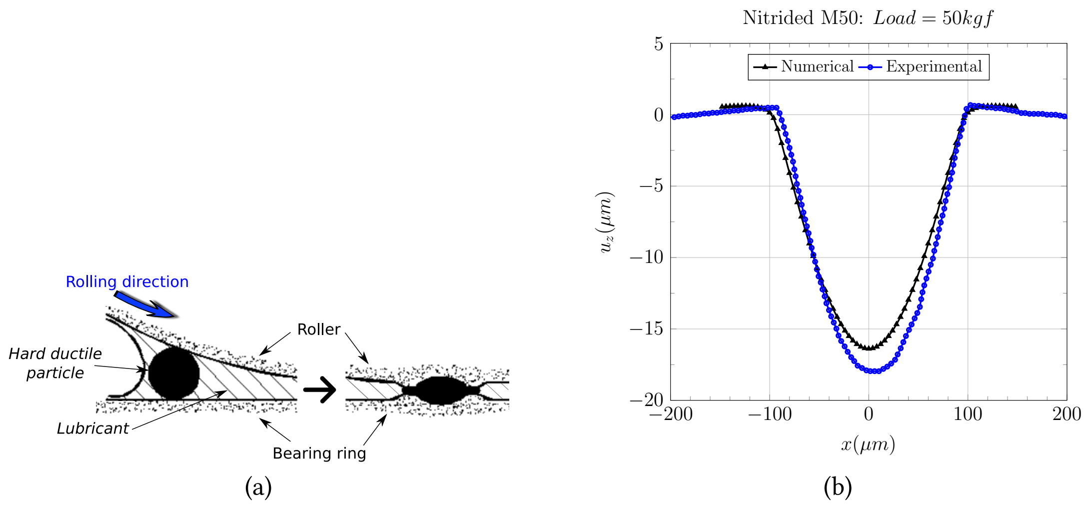

Figure 6.29: Experimental validation: (a) Hard particle entrapment problem; (b) Surface displacement u_z comparison

Fig. 6.29(b) presents the displacement in z direction obtained from the indentation simulation against that provided by a profilometer for a Rockwell indented a nitrided M50 sample (in the same conditions as the simulation). A good agreement can be noticed between the numerical and experimental results. It is interesting to observe that the height of the flash and the stamp diameter are well captured by the simulation result. The topology of the residual imprint is important because it informs about the material hardening type (isotropic or kinematic). It could be related to the maximum plastic strain rate yielded inside the material by empirical laws. This is why residual imprint data are often used to predict the resistance of surface layers. Note that soft particles can also be dangerous when they completely become entrapped between contacting bodies. Since the particle becomes full plastic, it is considered incompressible. Hence, by load transmission, the pressure between the contacting surfaces becomes extremely high according to the final size of the particle. This phenomenon has been studied by Nelias and Antaluca in [112].

6.4.2 HETEROGENEOUS ELASTIC PLASTIC ROLLING CONTACT

Now the contact is moved to simulate pure rolling contact. This approach is formulated in the quasi-static point of view, or steady-state. A new contact problem is solved at each displacement time-step. The total distance of the motion is $228\mu m$ with an increment of $12\mu m$ when the domain is discretized into a $195dx \times 65dy \times 35dz$. The material properties and the loading configuration are the same as in Tab. 6.11. Let's remember that carbides are assumed elastic perfectly plastic and their elastic limit is $1GPa$ when the matrix yield stress is $0.73GPa$. The chosen properties simulate the through-hardened M50 steel and its carbides but the yield stress is lowered in purpose to emphasize the plastic strain generated under the applied contact pressure of $4GPa$.

6.4.2.1 Rolling contact on carbides stringer

Rolling contact simulations are performed on stringers composed of three carbides. The middle carbide center is located at the depth of $z_i = 0.3a$ underneath the surface. The stringers are inclined by an angle θ with respect to the rolling direction. The effect of the stringer orientation is studied when θ is varying from $-45°$ to $45°$. The stringers are centered in the symmetric plan $\mathcal{P}(y = 0)$. The distance between carbide centers is d_i and each carbide size is S_i in terms of semi-width. One set $d_i = 2S_i$ so that the carbides touch each other. The contact pressure peaks, the stress and plastic strain maxima are recorded during the load first passage and are presented hereafter. Let's specified that metallic materials, especially steels are weaker in shear than tension and more than compression [282, 283]. This is the reason why only the shear component of the stress is regarded here. This corresponds to Tresca's stress. In contrast ceramic materials are even weaker in tension than in compression [220]. Since compression is applied via the rolling contact, one will not present the stress field in the silicon nitride ball used to perform the following simulations.

Contact pressure

Fig. 6.30 shows that the contact pressure peaks P_{max} are lower than the maximum Hertzian pressure P_0 applied. This means that the contact areas increased and also that one part of the applied deformation energy has been dissipated by plasticity occurrence in the subsurface. However one can observe that P_{max} augments when the load is arriving on the top of the stringer, then diminishes and reaches the steady value ($0.86P_0$), whatever the orientation θ. Also the maximum values of P_{max} are almost equal for all regarded θ. But the distance along which the pressure increase is proportional to the projected length of the stringer on the motion axis. Henceforth, the pressure is increased over a long distance when the stringer is parallel to the motion axis as one can see for $\theta = 0°$. Note that δ_x is the relative distance between the load and the stringer. $\delta_x = x_i - x_c$, where x_c is the contact center and x_i middle carbide center location in the motion direction.

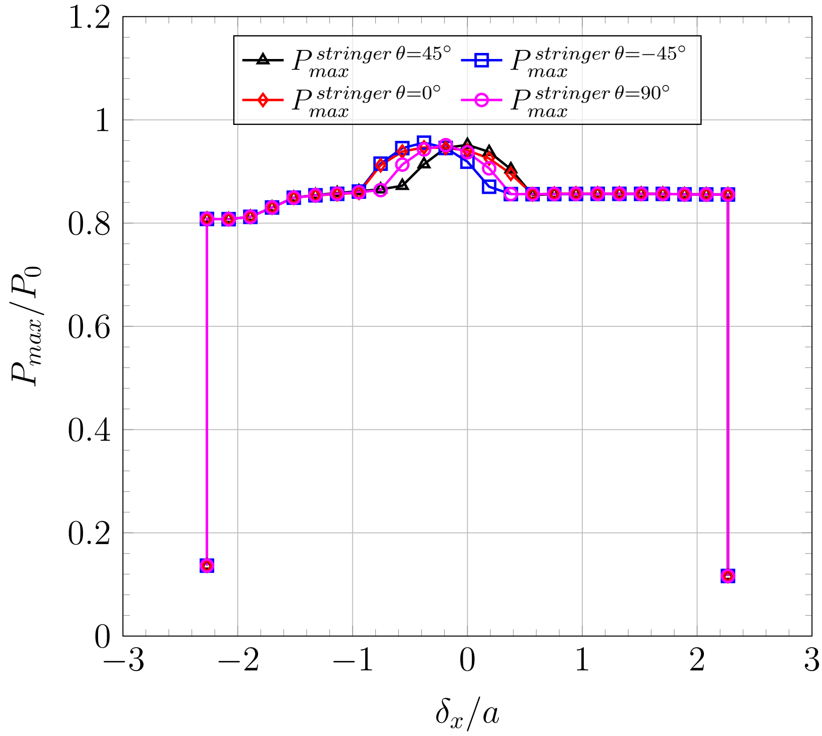

Figure 6.30: Maximum contact pressure during rolling contact on a stringer of carbides

Shear stress

Fig. 6.31 shows maximum shear stress during rolling contact on carbide stringers. The total shear stress is noted σ^{tot} when the shear component of overstress also called eigen-stress produced by the carbides is noted σ^*.

It could be clearly seen that the total shear stresses are almost equal for all considered stringer orientations. Nonetheless in the literature one can find out on sliced samples after RCF tests that some particular stringer orientations lead the carbides to be favorable for crack initiations, than other orientations. This was also confirmed on microscopy images obtained after the micro-tensile tests in Sec. 6.3.3.4.

Henceforth, one investigates on the eigen-stress, not as the unique responsible for the stress that increases the likelihood of cracking. This vision could help improve crack initiation criteria by including the eigen stress σ^* in RCF models. It is now distinguishable that when the stringer is oriented at $\theta = -45°$ the overstress undergone by the carbides is more important than that of the other orientation. In addition Fig. 6.31 allows the determination of the relative position of the eigen maximum shear stress according to the load situation through δ_x. Hence, the moment when, and the location where, σ^* gets its highest value can also be used to predict the crack point of departure in relative time and relative space for long carbide stringer. Furthermore, one can see from Fig. 6.31 that, the residual part of σ^* after the unloading, depends on the stringer orientation θ but difference is not noticeable on the residual σ^{tot} since all curves land on the same value.

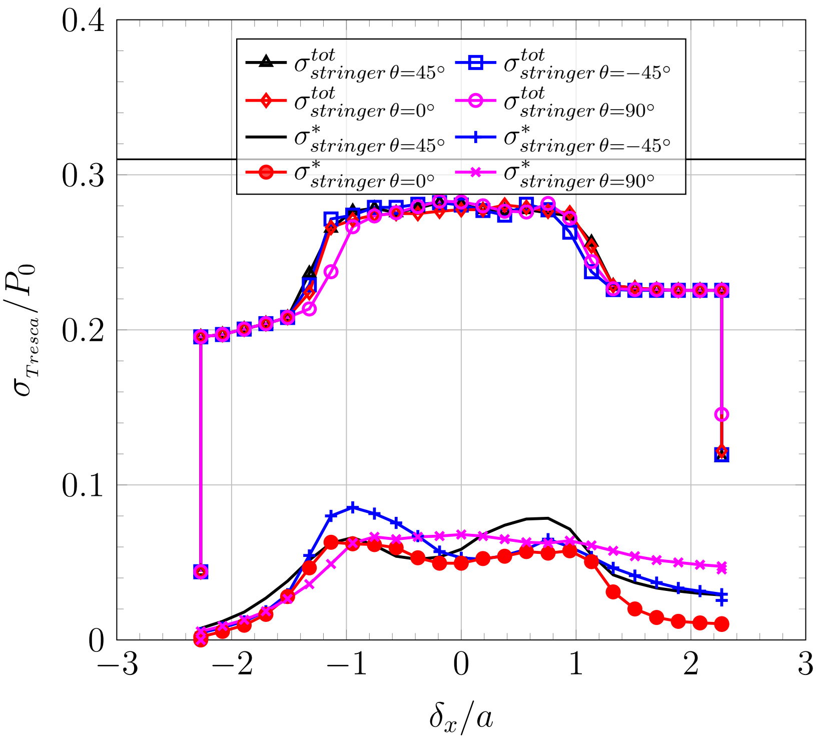

Figure 6.31: Maximum shear stress during rolling contact on carbide stringer
s

Fig. 6.32 shows the distribution of the total maximum shear stress inside the body at $\delta_x = 0$. One can notice that the highest magnitudes are located at the carbides edges perpendicular to the rolling direction. But this figure frames correspond to only one rolling time-steps in the quasi-static point of view. Actually from $\delta_x = -a$ to $\delta_x = a$ the highest magnitude of τ_{max} rides along the entire stringer boundary. This period can promote the loss of cohesion between the matrix and the carbide. Therefore, this period is referred as the potential decohesion moment.

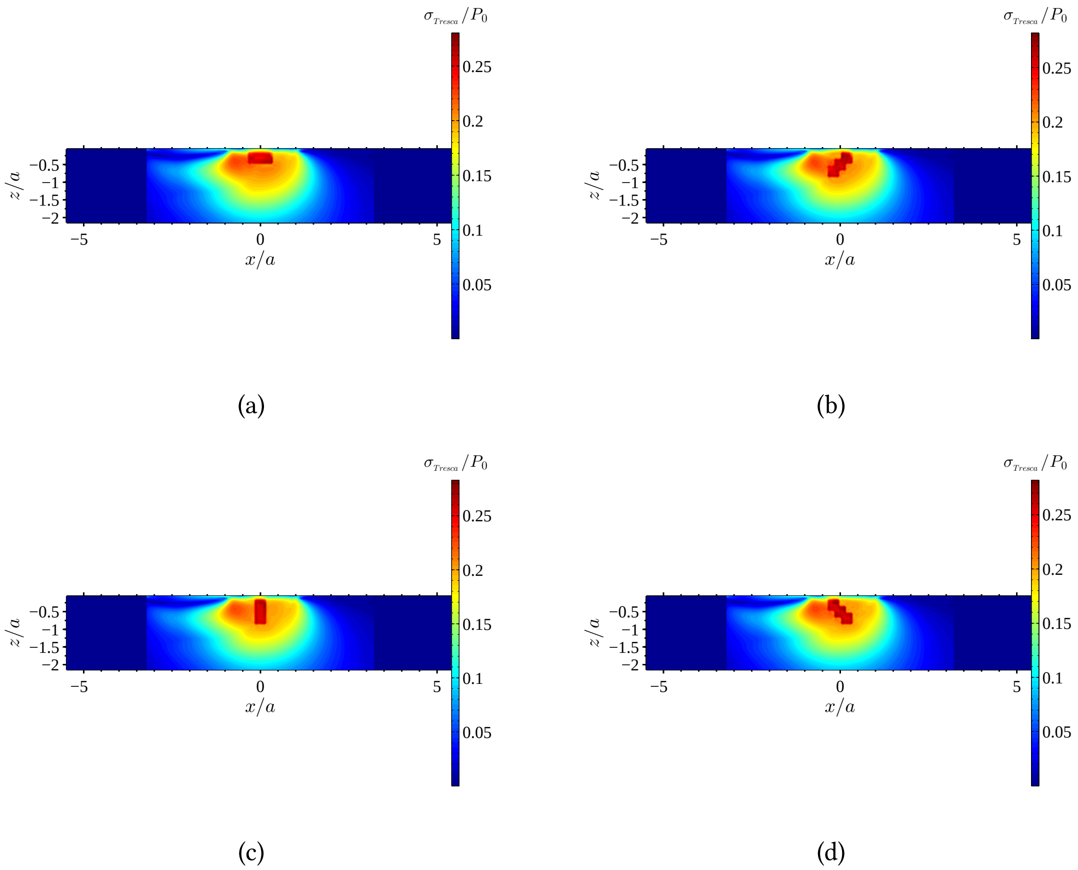

Figure 6.32: Total shear stress distribution during rolling contact on carbide stringer s

Fig. 6.33 shows the distribution of the eigen maximum shear stress inside the body when the load is situated at the position where σ^* is higher for each θ respectively. It could be seen that the highest magnitudes are located along the stringer diagonal following the rolling direction. This instant is favorable to the carbides internal cracks, as located at the stringer middle in Fig . 6.21(a) or at a single carbide middle in Fig. 6.21(b). Knowing that carbides are brittle materials, fracture can occur locally when the imposed deformation through σ^* exceeds their nominal strain at the break. Therefore, this instant is referred as the potential carbide fracture moment.

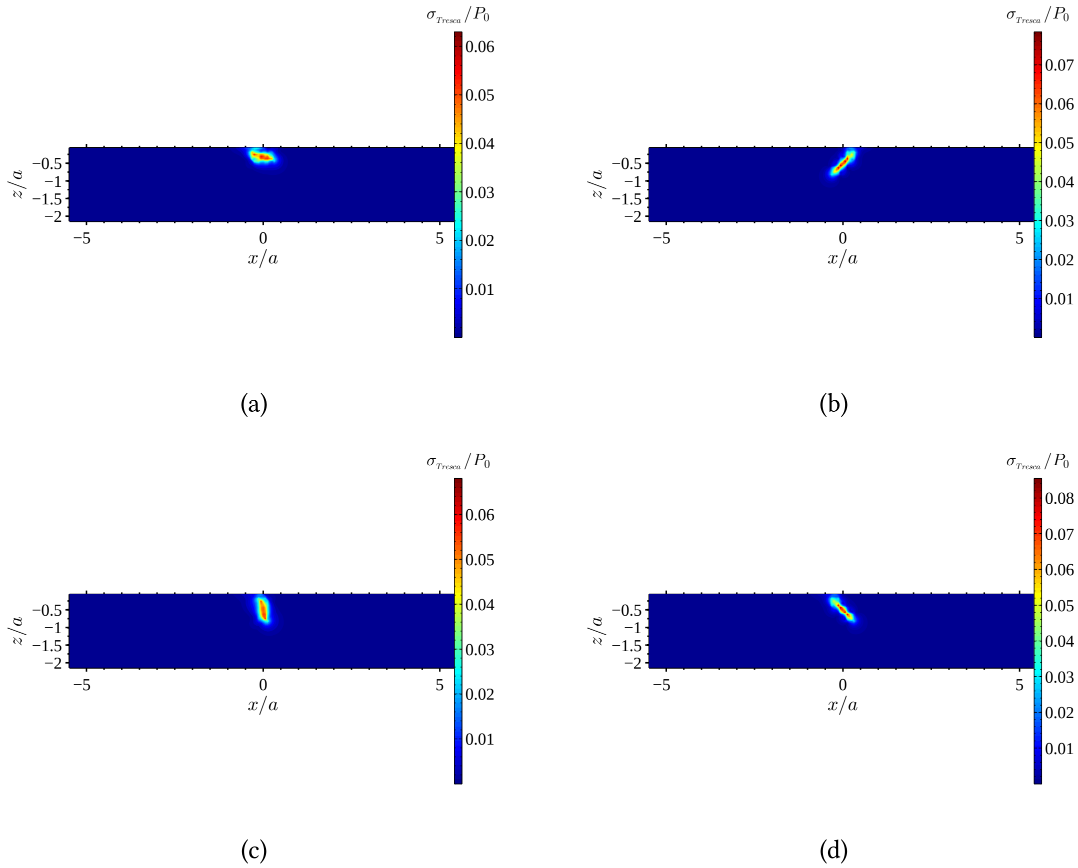

Figure 6.33: Eigen shear stress distribution during rolling contact on carbide stringer
s

Correlations can be established from this analysis and the cracks observed during the micro-tensile test. One can argue that the decohesion noticed in Fig. 6.20 occurred due to damage mechanisms attributed to the period when there is high stress concentration at carbide interfaces. Then in Fig. 6.21, the fractures occurrence inside carbides could be associated to the instants when the eigen maximum shear stress reach the carbide nominal strain at the break at the middle of the stringer.

Equivalent plastic strain

Fig. 6.34 presents the maximum accumulated equivalent plastic strain during rolling contact on carbide stringers. The elevated value of the plastic strain is obtained when the stringer is horizontal. However by observing the plastic strain distribution in Fig. 6.35(a), one can figure out that the plastic strain is more concentrated and elevated in the matrix region below the horizontal stringer. Moreover, the level of the plastic strain inside the carbides of the horizontal stringer is the smallest in comparison with the other orientations. In contrast, the vertical stringer produced the minimum plastic strain in the material but the value reached inside, is higher than that inside the other stringers regarded. The plastic strain generated by the stringer oriented at $\theta = -45°$ and at $\theta = 45°$ are almost confounded. These results yield to argue that the capacity of the material to dissipate the applied energy in form of plasticity is influenced by the stringer orientation. Hence, under a given total stress as in Fig. 6.31, the plastic flow evolves differently according to θ. As consequence, the more the material plastic behavior is susceptible to change by the stringer orientation, the more the effective ductility of a representative volume embedding the stringer could be controlled.

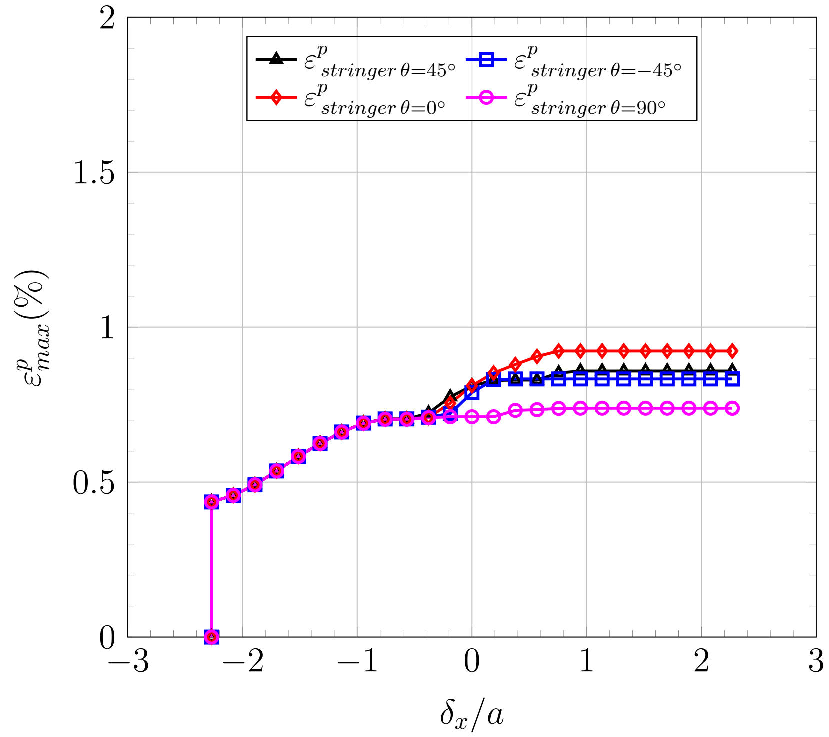

Figure 6.34: Maximum accumulated equivalent plastic strain during rolling contact on carbide stringer

s

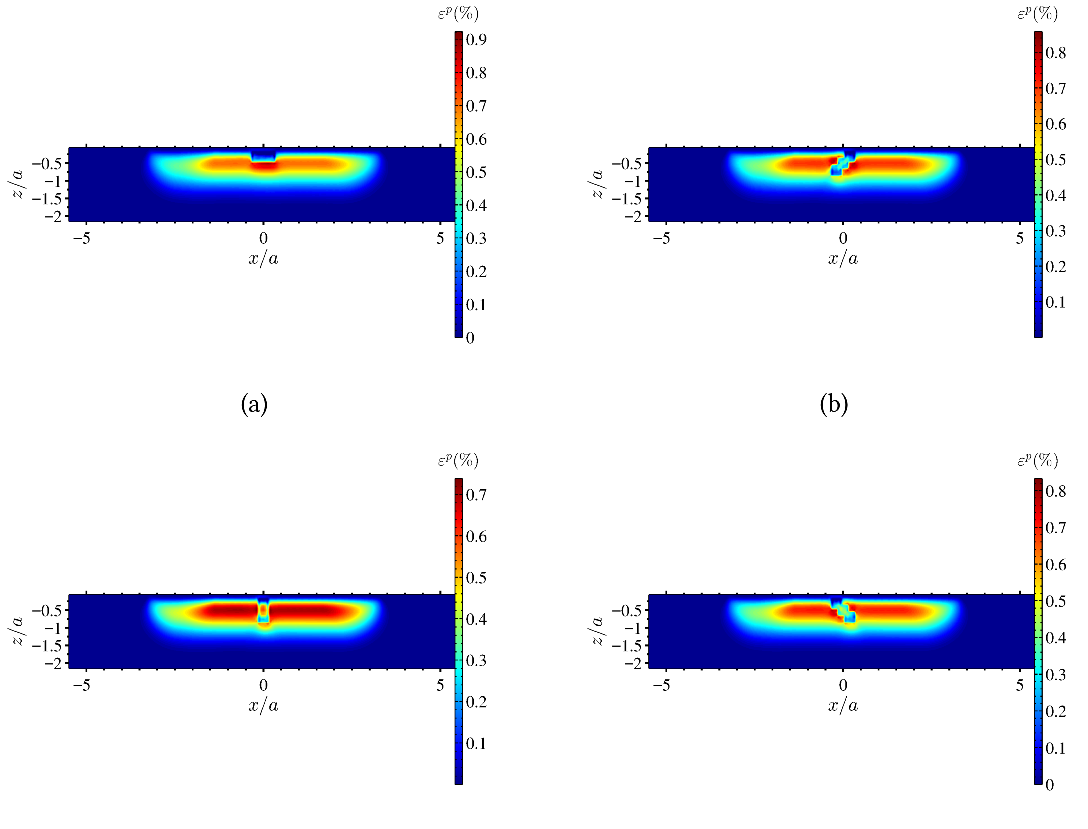

(a) (b)

(c) (d)

Figure 6.35: Accumulated equivalent plastic strain during rolling contact on carbide stringer s

6.4.2.2 Rolling contact on carbide clusters

Rolling contact simulations are performed on two clusters of carbides and a single carbide. The carbides size S_i, number N_i and separation distance d_i are set in such way to ensure equivalent density for both clusters (see value in Tab. 6.12). The single carbide occupied the same domain as the other clusters, therefore its volume fraction is considered 100% facing to $V_f^{Cluster1} = 42\%$ and $V_f^{Cluster2} = 67\%$ for the *Cluster1* and *Cluster2*, respectively.

Table 6.12: Cluster setting

Designation	*Cluster1*	*Cluster2*	*singleCarbide*
Number of carbide	$N_i = 3 \times 3 \times 3$	$N_i = 7 \times 7 \times 7$	$N_i = 1$
Carbide size	$S_i = 0.1a$	$S_i = 0.05a$	$S_i = 0.4a$
Distance between carbide centers	$d_i = 3S_i$	$d_i = 3S_i$	

The clusters as well as the single carbide are centered in the symmetric plans $\mathcal{P}(y = 0)$ and $\mathcal{P}(x = 0)$, at the depth of $z_i = 0.3a$ underneath. The gap between clusters carbides centers is set to $d_i = 3S_i$ so that carbides could not touch each other. The effect of the presence of matrix material between the multiple carbides is analyzed. The influence of clusters volume fractions along with the density is studied. The contact pressure peaks, the stress and plastic strain maxima are recorded during the load first passage and are presented hereafter.

Contact pressure

Fig. 6.36 shows maximum contact pressure P_{max} during rolling contact on the considered clusters and the single carbide. The evolution of P_{max} is quite identical for both clusters and the single carbide. However one must note that the pressure peak increased when the load is passing on the carbides top. In accordance with analysis mentioned above in Sec. 6.4.2.1, the distance along which the pressure increase is the same for the clusters and the single carbide because their projections on the contact surface are equal.

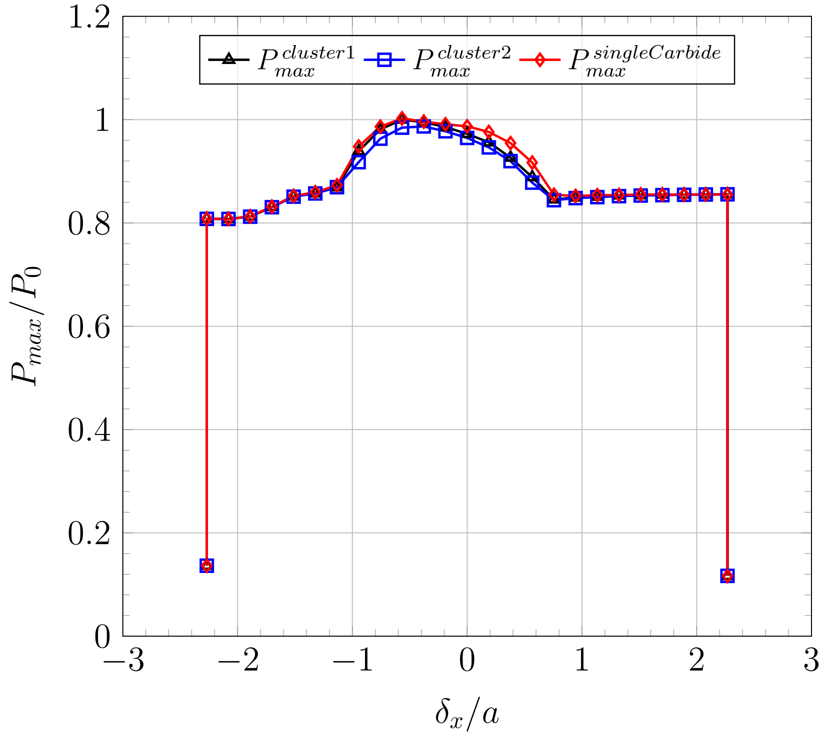

Figure 6.36: Maximum contact pressure during rolling contact on carbide cluster s

Shear stress

The maximum shear stress during rolling contact on carbide clusters and the single carbide are presented in Fig. 6.37. Once again, the total maximum shear stress σ^{tot} are similar for the two clusters and the single carbide even if there is a significant difference between their volume fractions. Knowing that the two clusters have equivalent density, it could be argued that σ^{tot} is more sensitive to the density, than to the volume fraction. However the evolution of eigen maximum shear stress σ^* allows to eliminating the hypothesis that the carbide reactions would be proportional to their volume fraction, because $max(\sigma^*_{Cluster2}) < max(\sigma^*_{Cluster1}) < max(\sigma^*_{singleCarbide})$ but $V_f^{Cluster1} < V_f^{Cluster2} < V_f^{singleCarbide}$. But one can notice that the peak of σ^* grows with the carbides size, since $S_i^{Cluster2} < S_i^{Cluster1} < S_i^{singleCarbide}$. The consequence of the carbides size on the eigen maximum shear stress peak lead to confirm that having smaller carbides, even if they are numerous, will contribute to the increase the resistance to RCF of the treated M50. Moreover, the magnitude of the total and eigen residual stresses, generated by the plasticity inside and outside the *Cluster2*, are relatively lower than that of the other cases.

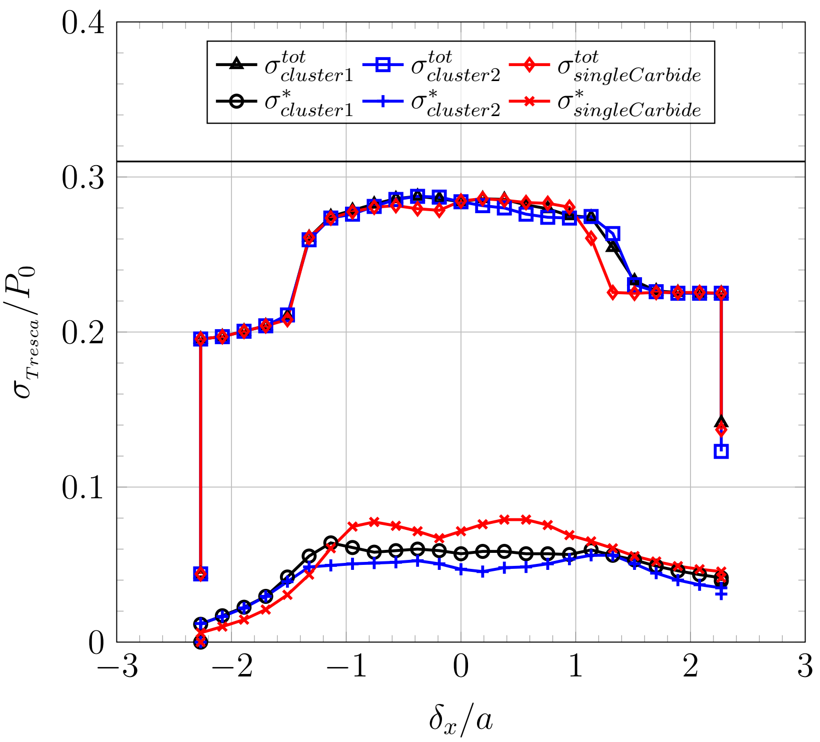

Figure 6.37: Maximum shear stress during rolling contact on carbide cluster
s

It could be seen from Fig. 6.38 that the distribution of the total shear stress in the matrix outside of the clusters is identical to that of the single carbide. But very high stress concentration could be noted inside the area filling by the clusters of carbides. Herewith the matrix material between the multiple carbides is subjected to important stress rising because of mutual interactions held between carbides. Hence, these areas are conducive to the damage.

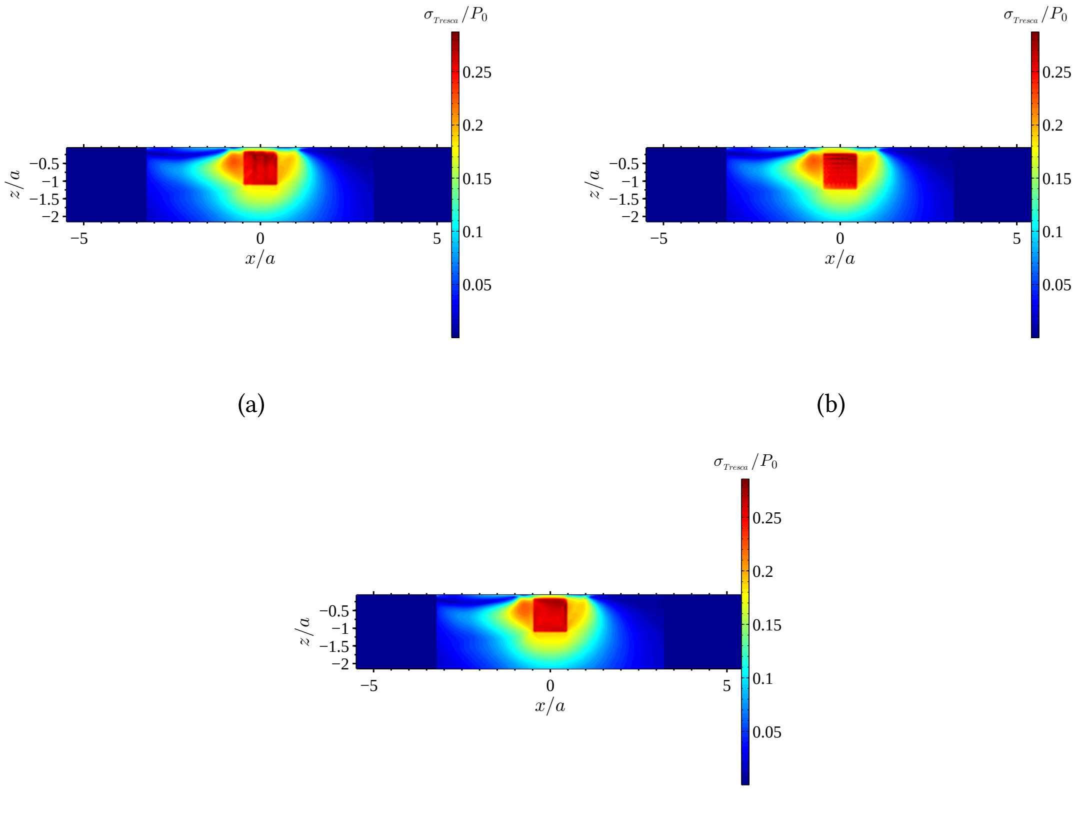

(a) (b)

(c)

Figure 6.38: Total shear stress distribution during rolling contact on carbide cluster
s

Fig. 6.39 presents the eigen shear stress distribution during rolling contact at the instant when the highest value of eigenstress is reached on carbide clusters and the single carbide. It was found out that at this particular instant, the eigen stress is concentrated along the diagonal of each carbide, as one can clearly see in Fig. 6.39(a, c). In addition the magnitude of the peak grows with the carbide size. Also, the peak is located at the corners of edges aligned diagonally. These corners belong to the interface carbide-matrix. The eigen stress concentration spreads into the material via the edges along the carbide diagonal. This finding is suggesting a close relationship between the concentration along the extended axis of carbide diagonal and the apparition of fatigue butterflies wings which usually being located there.

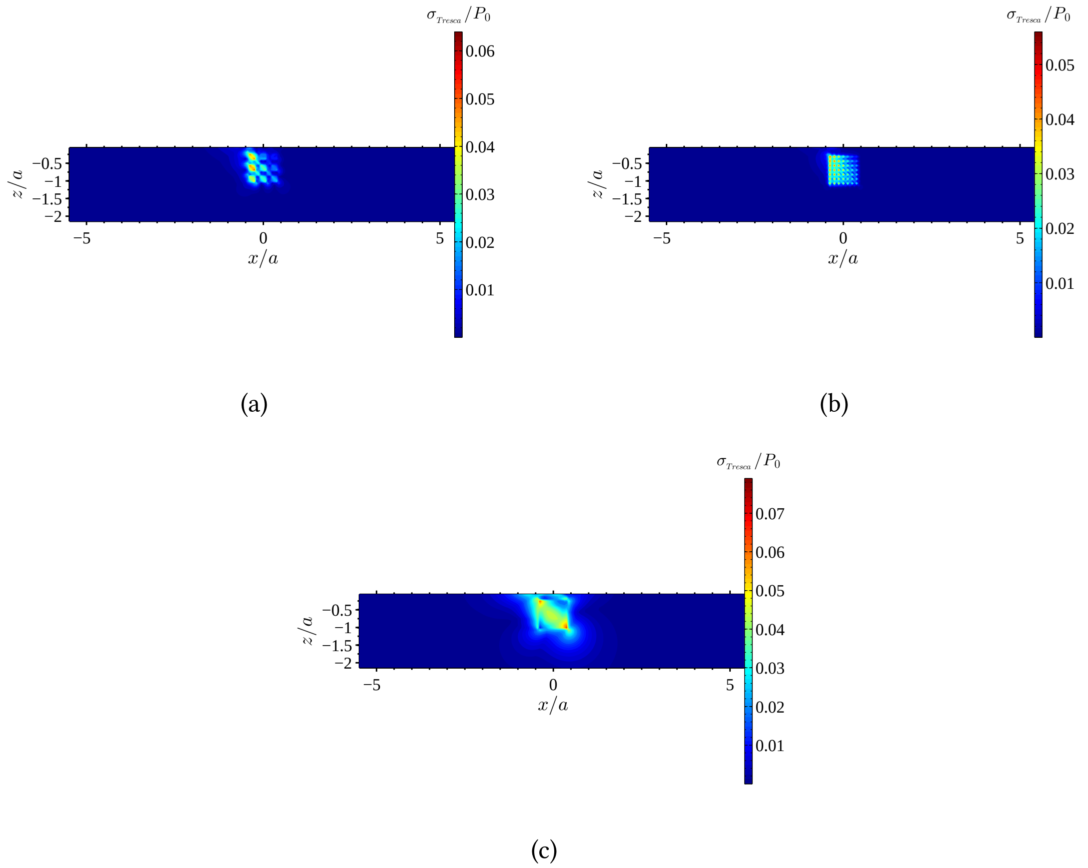

Figure 6.39: Eigen shear stress distribution during rolling contact on carbide cluster
s

Equivalent plastic strain

The maximum accumulated equivalent plastic strain recorded during rolling contact on carbide clusters and the single carbide is plotted in Fig. 6.41. One can see that the plastic strain peak is the same for all regarded cases. The distribution of the plastic strain in Fig. 6.41 reveals that the peaks are achieved in the matrix material because the matrix yield stress is less than that of the carbides. Yet there is no plasticity, or at least a little plastic strain, in the material between those carbides, compared to the rest of the matrix, as shown in Fig. 6.41. The carbides composing the *Cluster1* have the same elastic limit, the same elastic properties and the same size as those of stringers in Fig. 6.35, but the plastic strain yielded is lower inside the *Cluster1* carbides than that inside any of the stringers studied above. Hence, the clustering of carbide leads to less plastic strain than the ranking in form of stringer. Remember from Fig. 6.21 that, even if no plasticity activity is noticeable in the matrix, cracks appear along stringers when clusters remain undamaged. Therefore the overall elastic limit has been artificially increased in the representative volume embedded the carbides. The augmentation of the effective yield stress has been explained in Chap. 5. However one can observe from Fig. 6.41 that the magnitude of the plastic strain is higher inside the single carbide than in the *Cluster1* and even more than in the *Cluster2*. Finally, the plastic strain level reached inside the carbides would strongly depend on their size and their spatial arrangement. This always brings back to the effect of the mutual influence between the carbides, in grouping situation.

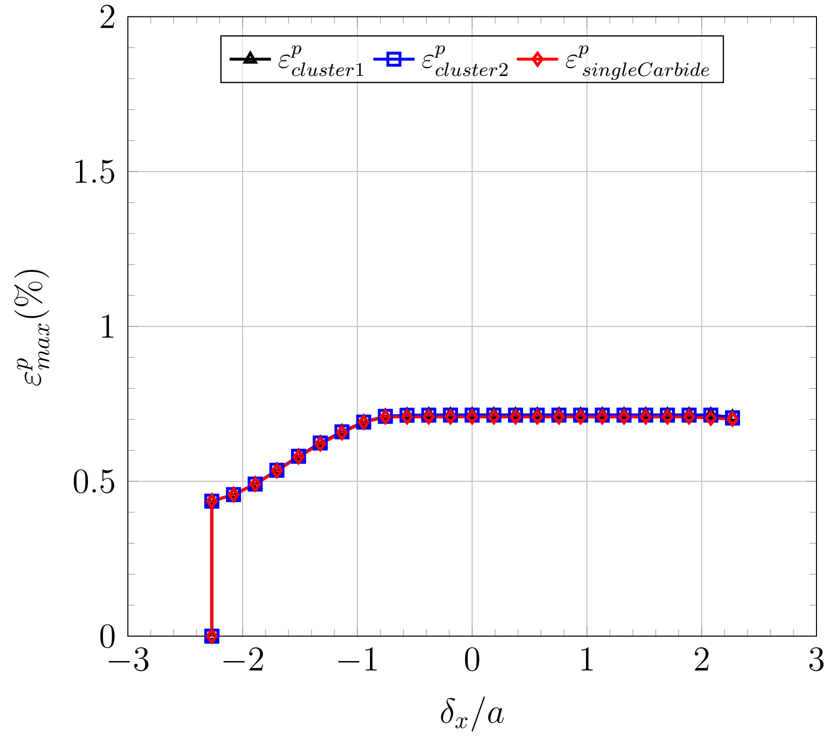

Figure 6.40: Maximum accumulated equivalent plastic strain during rolling contact on carbide cluster

s

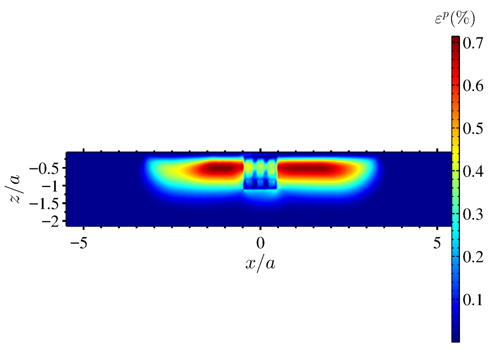

(a)

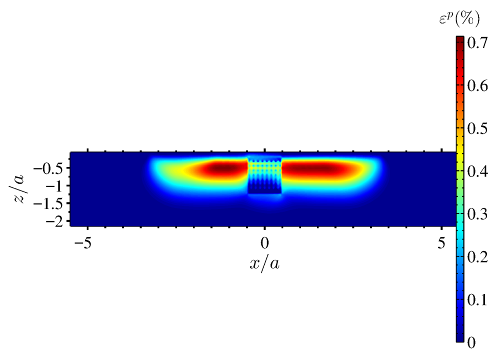

(b)

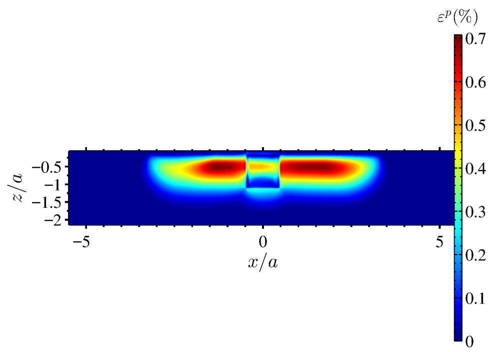

(c)

Figure 6.41: Accumulated equivalent plastic strain during rolling contact on carbide cluster

s

6.5 PARTIAL CONCLUSION

The micromechanical characterization of two plastically graded rolling bearing materials (M50 and M50NiL) has been conducted in purpose to investigate on the effects of microstructures and hardening properties resulting from thermochemical treatments. In summary, the microstructure difference of both materials lies mainly in carbide size, shape, distribution and properties. It is important to realize that for both M50/M50NiL, nitriding lead to the same results in terms of the affected thickness and formed nitrides. However there is still a presence of large carbides in the M50 nitrided layer, and intragranular carbides in the M50NiL nitrided layer. The small carbides have been drained by the nitriding diffusion front. This is the reason of absence of small carbides in both M50 or M50NiL nitrided layers. Nevertheless, knowing that nitrides are hard but brittle compounds, the issue is to figure out whether their presence could prevent or postpone the spalling phenomena by resistance to the crack initiation and propagation. This can also explain somewhere the increased life of nitrided bearings. The micro-tensile tests raised some interesting observations about the carbide rupture. It was found that vanadium and molybdenum are elements having the largest concentration in the cracked carbides. From spectroscopy outputs, it seems like molybdenum is responsible for the carbide brittleness when vanadium enhances its resilience. However, stringers of carbides cracked much more than clusters. This could imply that particular grouping is favorable for cracking. Moreover, the shorter and farther from the fractured section the cracked stringer is, the smaller the crack dimensions are. Nearby all observed stringers, plasticity happened when the carbide crack encountered the elastic-plastic matrix. In the second part of this study, a three-dimensional heterogeneous elastic-plastic contact model allows to reproduce the surface displacement of the indent left by a hard particle entrapped in hybrid contact (Si_3N_4 on nitrided M50). Very good agreement is obtained by comparing the displacement component along the depth direction against that provided by measurements on an indented nitrided M50 sample. The numerical model takes into account the heterogeneous microstructure, the gradient of plastic property as well as the initial compressive stress. All considered, the present work suggests controlling the heating stages of the hardening+carburizing to ideally avoid the formation of elongated carbide stringers, found by the micro-tensile tests as well by numerical analysis, to be detrimental for the material resistance to cracking.

7 GENERAL CONCLUSION

A robust, fast and versatile model using a semi-analytical method (SAM) has been developed for a fully coupled analysis of contact pressure, contact area and subsurface stress-strain fields for accurate damage prediction. The main advantages of the SAM are its performances in computation time, the non-necessity to mesh the boundary conditions and the fact that the meshed volume can be limited to the zone of interest like the plastic zone. The models developed can be directly applied for contact mechanisms working in severe conditions such as gears and rolling bearings when high contact pressure occurs in service transition phases or overloading conditions (e.g. loss of the structure balance). The main potential applications consist to evaluate the criticality of the presence of heterogeneities (manufacturing best-practices).

Contents

7.1 DISCUSSIONS AND SUMMARIES

The present work has aimed at developing a fast and versatile tool for studying damage mechanisms related to plastic strain and residual stresses induced by rolling contact loading on a heterogeneous elastic-plastic body. The model has the capability to solve a three-dimensional contact problem between two half-spaces having a gradient of properties and containing initial residual stresses. The effect of multiple heterogeneities has been analyzed studying the influence of their position, size, mechanical properties and distribution beneath the contact surface.

The Heterogeneous Elastic Plastic Contact solver (Chap. 3) was the first approach developed. Based on the theoretical background exposed in Chap. 2, a fully coupled algorithm of the contact, the plasticity and the heterogeneity problems have been developed. The distribution of the contact pressure and area above the heterogeneity is one of the main output. It is known that the contact pressure decreases when the material starts to yield, but the presence of a hard elastic heterogeneity increases the maximum pressure according to its location and size.

Moreover in the subsurface, the residual stresses generated by the plastic strain tend to decrease the elastic stress field due to the applied contact, but once again the heterogeneity eigenstress raises the total stress at its vicinity. When the heterogeneity is harder than the matrix, the stress concentration reaches its maximum inside the heterogeneity. But, if the matrix is harder than the heterogeneity, then the stress concentration peak is observed at their interface. This could explain the likely debonding between heterogeneity and the matrix, or, even more, a crack initiation if the heterogeneity is considered as a void.

Finally looking at the highest principal stress location and orientation around hard heterogeneity, one can predict crack initiation directions, that should be perpendicular to the principal stress direction for the mode I in a fracture mechanics point of view. Hence it was found that locations favorable to crack are the heterogeneity bottom and upper corners.

The Heterogeneous Elastic Plastic Rolling Contact solver (Chap. 4) has been an extension of the HEPC solver. It consists to move the contact loading along a given direction on the surface. The presented rolling contact model is a three-dimensional analysis based on the quasi-static displacement of the loading which reproduces the motion observed in ball bearings. Interesting conclusions have been drawn from numerical simulations with different types of inclusions according to the Dang Van damage criteria. It was found that an incompressible heterogeneity [a] will generate more damage than a porosity and even more than a vanadium carbide which is 2.33 times stiffer than the M50NiL matrix. However the critical effect of these heterogeneities is significantly decreased by introducing an initial compressive stress of $-0.14P_0$ from the depth -0.5 to $1.5a$ beneath the surface, where P_0 and a are the applied maximum Hertzian contact pressure and Hertzian contact radius, respectively.

[a] *for instance a porosity filled by a low viscosity lubricant oil that entered via emerged crack network*

It is well known that over a certain number of rolling fatigue cycles, even if the applied nominal stress did not exceed the material yield stress, plastic deformed layer appears. This may be caused by the elastic plastic property degradation attributed to the damage mechanism initiated at microscopic scale. Further plasticity growth is generally prevented by the residual beneficial stress developed during the self-balanced phenomena known as the shakedown. However, if the system is submitted to extremely high-cycle fatigue and/or if the material's behavior is particularly influenced by the presence of heterogeneities, then the shakedown limit can be exceeded. This promotes a progressive accumulation of plastic deformation known as ratcheting. Shakedown and ratcheting phenomena have been studied over a simulated multi-cycle rolling contact, in presence of vanadium carbide when the material is assumed to have an isotropic hardening behavior. It was found that the contact pressure at the surface reaches a quasi shakedown regime from the second rolling pass, while the maximum sheer stress in the subsurface, continues to increase during ten rolling cycles. Yet, without the presence of the vanadium carbide the maximum shear stress level was constant for twenty cycles. Thus heterogeneity disrupts the shakedown establishment and could cause an earlier ratcheting than in homogeneous body. The severity of the heterogeneity on the accumulated plastic strain over cycles was also studied. During twenty cycles, the maximum plastic strain level has barely increased by 10% for the homogeneous body, whereas this level has more than doubled in only ten cycles for the heterogeneous body.

Finally, the evolution of the plastic strain distribution inside the heterogeneous body reveals that after the 10th cycle, the region located between the heterogeneity upper edge and the contact surface experienced a severe elevation of the plastic strain maximum, about three times the nominal value obtained at the Hertzian depth. It is well known that the more the level of the plastic strain increases, the harder the material becomes. The hardening means the loss of ductility. This situation leads to potential cracks occurrence, even more, since the plastic zone is located near the surface where contact stress is very high. The present chunk of material created by cracks network will be snatched at a forthcoming rolling pass by letting appear a spalling.

The effective property analysis of elastic-plastic half space containing heterogeneous inclusions under contact loading is the academic and industrial application of the HEPC solver. It is often found that the homogenized properties predicted by classical methods diverge according to the inclusion density and especially for indentation loading. The source of this inaccuracy is the assumptions that underpin the classical methods which are briefly reviewed in the Chap. 5. The presented study proposes an alternative method consisting in a reverse identification of effective properties by fitting the heterogeneous body behavior with that of a homogeneous body.

The results from homogenization simulations, raised some noteworthy points. The first most important is that a single model is not sufficiently efficient to describe the effective properties while indicating the heterogeneities distribution and their volume fraction. This is due to the fact that, depending on the heterogeneities number and size, several distributions could be established while maintaining the same volume fraction, and vice versa. The homogenized property sensitivity to the heterogeneity distribution rather than only the volume fraction could partly explain the divergence of classic methods. It is also imperative to specify that classic methods are not appropriate for high densities of heterogeneity even more when a contact load is applied on the REV boundary leading to a strong gradient of stresses. However, in case of a relatively low volume fraction and a quasi-uniformly distributed stress field on the REV, the distribution has an insignificant effect on the macroscopic response. Then the classic methods become faster and more suitable.

In addition, it should be noticed that the elastic property of the heterogeneity influences the effective plastic property of the homogenized body. It was figured out that the overall yield stress decreases when the absolute value of the difference between the matrix and heterogeneity stiffness $|E_I - E_m|$ increases, for a fixed volume fraction.But in general, the overall yield stress increased with the heterogeneity volume fraction because they are firstly considered as purely elastic which implies that their individual elastic limit is infinite. However this evolution is nonlinear, since the mutual influence between heterogeneities and their interaction with the surrounding plastic zone highly depends on many factors discussed in Chap. 4. Finally, the overall Young's modulus increases when the ratio between the matrix and heterogeneity stiffness increases, for a given volume fraction.

The influence of heterogeneities and hardening properties on plastically graded bearing materials (M50 and M50NiL) was the final part (Chap. 6) that combined experimental data with simulation results in an industrial application. Micromechanical and microstructure characterization have been conducted to highlight the effect of the carburizing and the nitriding on the material behavior. The carbide precipitation, the gradient of hardness and the compressive stress introduced were analyzed trough indentations and micro-tensile tests. Two analytical models were proposed to fit the data (the profiles of the hardness gradient and the initial stress). Rolling contact simulations were performed on a typical M50 material containing stringer and clusters of carbides. The evolution of the contact pressure peaks and the distribution of the shear stress and plastic strain maxima have been the subject of numerical studies.

The microstructure characterization has shown a very close relationship between the carbide shape and size in both M50 and M50NiL treated materials in accordance with the heat treatment procedures. However, it has been observed and quantified that the sizes of carbides in M50 are larger than those in M50NiL. Also, the M50NiL carbides population could be sorted into two families depending on when they have been formed during the heat treatment procedures. One family of very small and spherical intragranular carbides and the other family of a relatively larger elongated intergranular carbides. The nitrogen diffusion layer of both materials have similar thicknesses, implying that the initial microstructures do not inhibit or promote the nitriding process. But the absence of small carbides inside the nitrided layer suggests that they have been drained down during the nitriding diffusion front progression.

The micro-tensile tests revealed that M50 carbide stringers are likely to crack, more than carbide clusters. The crack dimensions are related to the stringer position. Hence, the shorter and farther from the fractured section the cracked stringer is, the smaller the crack dimensions are. In addition to carbides distribution, their chemical composition influences the crack likelihood. EDX analysis showed that vanadium and molybdenum are elements having the largest concentration inside the cracked carbides. However, molybdenum may be linked to the carbide brittleness when vanadium enhances its resilience.

Furthermore, nearby all cracked stringers, high plastic deformation was observed when the carbide crack encountered the matrix. This point suggests that even if carbides are fragile, their surroundings matrix remains ductile[b] . This difference of behavior explains the two scenarios of rupture found during the micro-tensile tests. These are cleavage fractures and debonding.

[b] *meaning that it can still allow yielding (plasticity) in reaction to high stress concentrated by the carbide*

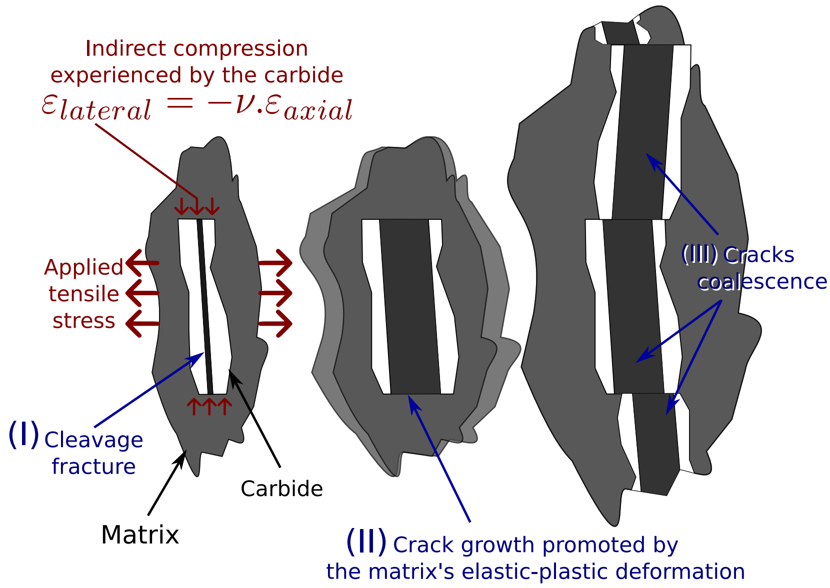

Figure 7.1: Carbides cracks by cleavage during the micro-tensile tests [16]

Fig. 7.1, describes cleavage fractures which is the most frequent rupture observed here. Firstly, the elongated carbides crack when the lateral deformation exceeds their elongation at rupture. The crack is perpendicular to the tensile stress direction, i. e. parallel to the direction of the indirect compression experienced by the carbide along its longest axis. Secondly, the cleavage is growing because of the matrix's elastic-plastic deformation. Finally, when the dimensions of each cracked carbide are sufficiently large, a connection is established between neighboring cracks. The coalescence of multiple cracks along the carbides stringer enables the main crack propagation.

Rupture by carbide debonding is also observed during the micro-tensile test. Due to the weakness of the matrix/carbide interface, the tensile stress could generate a loss of cohesion along one of longest edge of the elongated carbide, as presented in Fig 7.2. Afterwards, the created void growth will be promoted by the surrounding matrix's elastic-plastic deformation. Once again, a main crack is started by the coalescence of neighboring debonded carbides that composing the stringer.

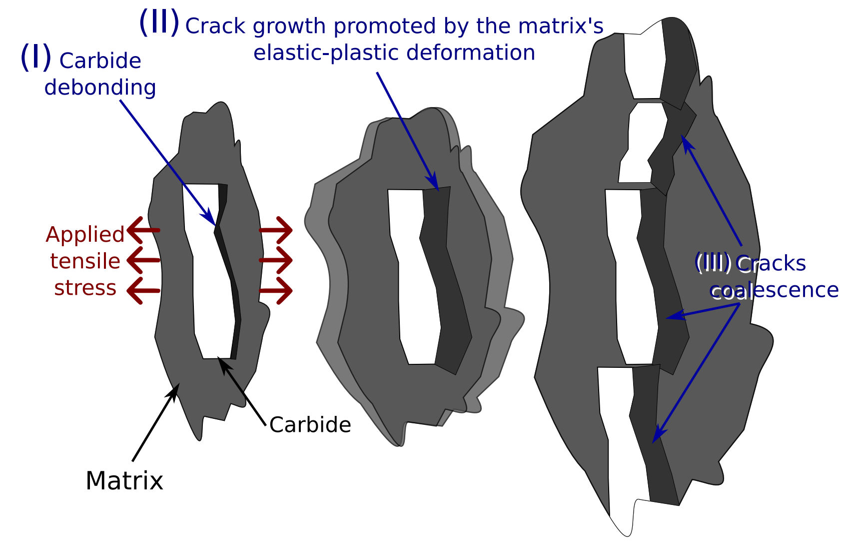

Figure 7.2: Carbides cracks by dedonding during the micro-tensile tests [16]

In the scheme of all analysis conducted in the present work, it can be argued that, although heterogeneities (such as carbides or nitrides) are responsible for the high resistance of the studied materials, some of them (those whose length exceeds tens of micrometer or those which form stringers in a particular direction) become, over fatigue cycles, the main sources of damage, from their local scale up to the macroscopic failure of the structure.

7.2 PERSPECTIVES

The heterogeneous elastic-plastic contact solver offers the possibility to explore several problems mentioned above. The analysis conducted in the academic and industrial contexts, constitutes a major point of differentiation from others three-dimensional numerical solvers based on finite elements method. The difficulty comes when the resolution requires fine meshing of boundary conditions. All these factors lead to expensive computational resources for the contact resolution. Some perspectives of the application of the HEPC solver are exposed hereafter.

7.2.1 EFFECTIVE ELASTIC-PLASTIC PROPERTIES OF RANDOMLY DISTRIBUTED HETEROGENEITIES

The homogenization method presented in Chap. 5 was only applied to cases where the heterogeneities have the same shapes, sizes and regular distribution inside the considered REV. However, isotropic materials have random distribution of heterogeneities as in Fig. 7.3. The preferential distribution imposed to the hetrogeneities in the present work, can lead to an induced anisotropic behavior. This will change the effective properties when the applied contact force is a combination of normal and tangential components. Therefore the induced anisotropic behavior must be studied considering the type of distribution (regular and random).

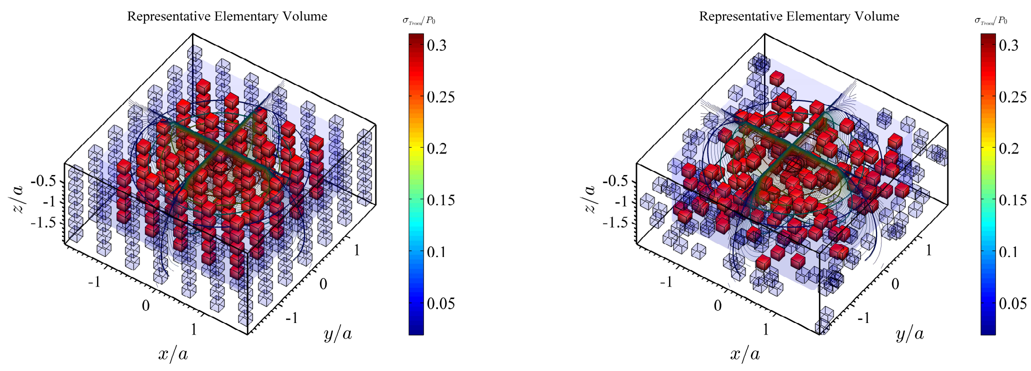

(a) (b)

Figure 7.3: Heterogeneities distribution in present work: (a)Regular distribution; (b) Random distribution

7.2.2 DAMAGE MECHANISMS OF THE SILICON NITRIDE ROLLER

Remembering that the aim of the present work was to investigate the hybrid bearing (ceramic on steel), it may be noted that the study focused only on the steel ring, whereas the ceramic could also be studied as a porous elastic-plastic material. It was noticed in hybrid bearing that the ceramic rollers have a higher RCF resistance than the steel races. A procedure for evaluating the probability of survival of the hybrid ball bearings has been presented in [220]. However a static damage analysis is proposed for only the silicon nitride roller. The porosities are the principal heterogeneities found in ceramic materials for reasons linked to the manufacturing process[a] . The plastic behavior of ceramics was proved by the permanent stamp left by indentation test as in Fig. 7.4(b).

[a] *Chemical Vapor Deposition (CVD), Hot Isostatic Pressing (HIP), Sintering, etc.*

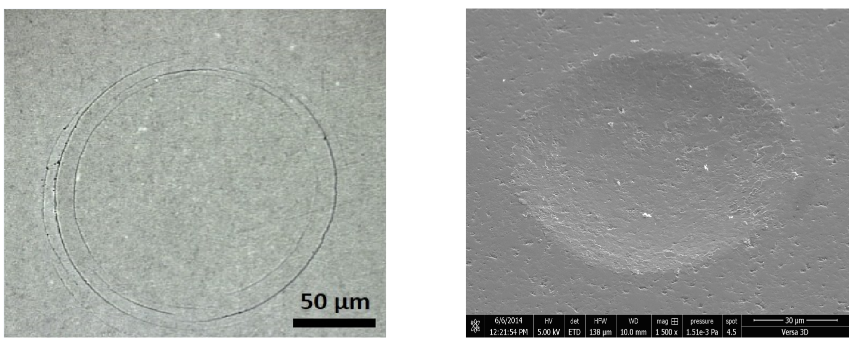

(a) (b)

Figure 7.4: Indentation conducted on a silicon nitride [202]: (a)circumferential crack (a) raceway; (b) plastic deformation of the surface

However, the ceramic materials are weaker in tension than in compression. This explains the initiation of circumferential cracks observed in Fig. 7.4(a) at the contact flange where the tensile component of the stress tensor is greater than the others. But, knowing that the ultimate tensile strength (UTS) of ceramics are relatively high, the circumferential cracks that occurred at a tensile stress lower than the UTS, can be attributed to the presence of porosities which weaken the effective UTS of a representative elementary volume (REV) located at the contact edge. Indeed, the apparent decrease of the UTS inside the considered REV, is due to the fact that the level of stress is raised by the porosities. The matrix is therefore subjected to a more elevated stress in comparison to what it would experience without porosities. Fig. 7.5 presents the concentration of the equivalent Von Mises stress around porosities. It can be seen that the stress is almost doubled around the porosities close to the surface, and even more when the porosity is close to the Hertzian depth.

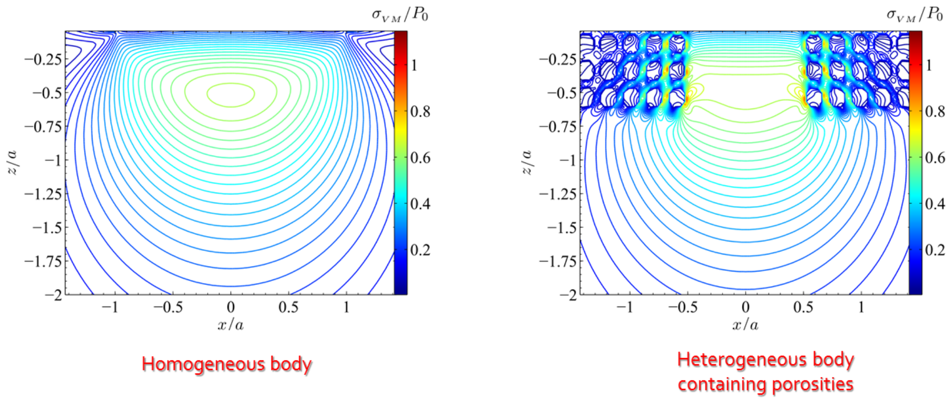

Figure 7.5: Concentration of the equivalent Von Mises stress in a representative volume containing porosities compared to the stress level in a homogeneous matrix

The consequence of the presence of subsurface porosities on the radial component of the stress tensor at the surface outermost layer is reported in Fig. 7.6. It is well established that the radial stress is positive outside the contact circle and has its maximum value at the edge of the contact patch when $x/a = 1$; where a the elastic homogeneous contact radius and x one of the Cartesian coordinates of the axisymmetric referential centered on the contact. Note that the partial cone cracks (so-called c-cracks) observed on silicon nitride balls after RCF, result from a combining effect of the oblique impact velocity and the maximum radial stress at the contact periphery, [284].

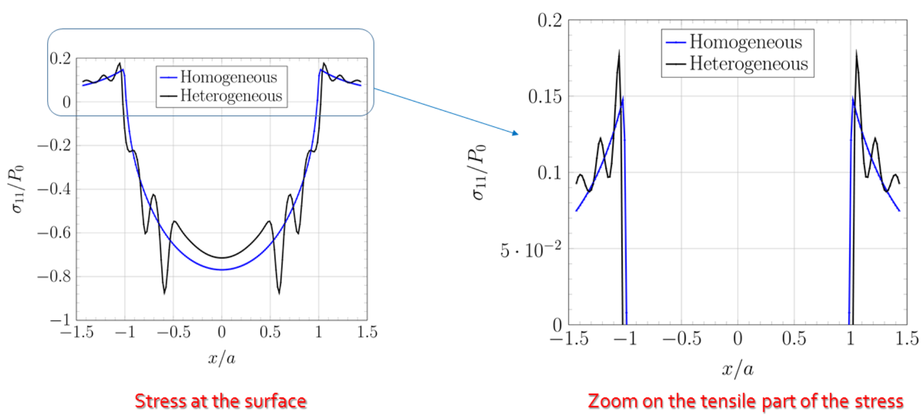

Figure 7.6: Distribution of radial stress at the surface outermost layer of the porous body compared to that of the homogeneous body

From Fig. 7.6, it can be noted that the contact size is a little increased by the presence of porosities and that the peak of the tensile radial stress is also increased compared to that of the homogeneous body. The magnitude of this peak depends on the porosities sizes, shapes, locations and distribution.

Fig. 7.7 describes the static damage analysis that could be conducted on the silicon nitride roller. The objective is to correlate the circumferential crack radius a_{crack}, provided by an indentation test, with the contact size a^* determined numerically by the heterogeneous elastic-plastic contact model. From the critical stress level obtained at the vicinity of representative porosities micro scale damage criteria could be established. The prediction of the ceramic's breaking point will be an excellent application of the HEPC model for a deeper understanding of the hybrid bearing fatigue resistance.

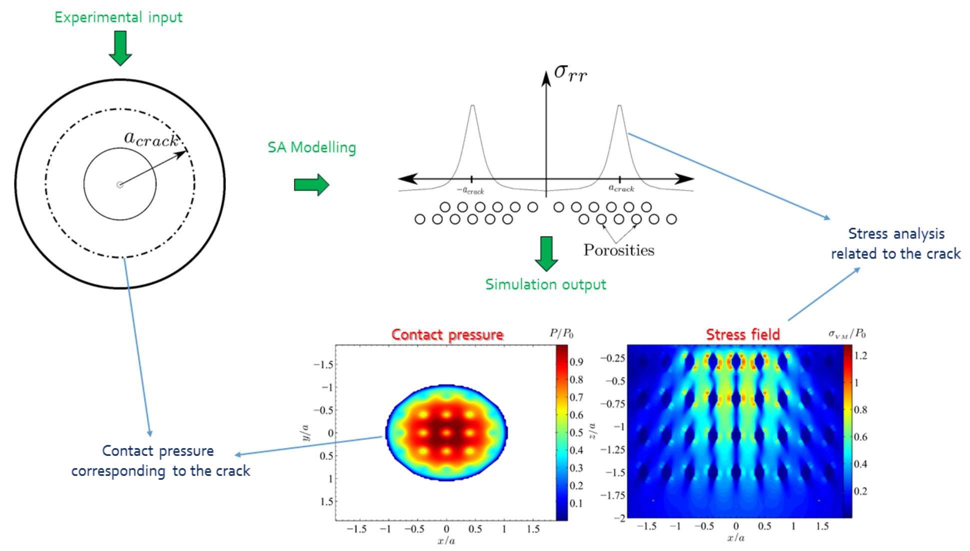

Figure 7.7: Static damage analysis of the silicon nitride roller

7.2.3 SIMULATION OF BUTTERFLY WING FORMATION AROUND CARBIDE

The multi-cycles rolling contact model developed in Chap. 4 could be extended to simulate Butterfly Wing Formation (BWF) around nonmetallic inclusions found in the high-strength steels, as illustrated by Fig. 7.8. The aim is to predict and distinguish the total fatigue life from the life before the BWF and beyond. Flatwasher fatigue tests can be conducted to obtain material data for the numerical model. With the development of in-situ monitoring facilities, information such as stress fluctuations and the number of rolling cycles could be captured directly on the test bench to validate the numerical model predictions, by detecting and following in-time the BWF evolution during the tests. Recently, Barkhausen noise[b] measurements have been used to detect the early stages of SAE52100 bearing steel material's microstructural alterations during RCF [285].

[b] *perturbations in the magnetic signals from a ferromagnetic material*

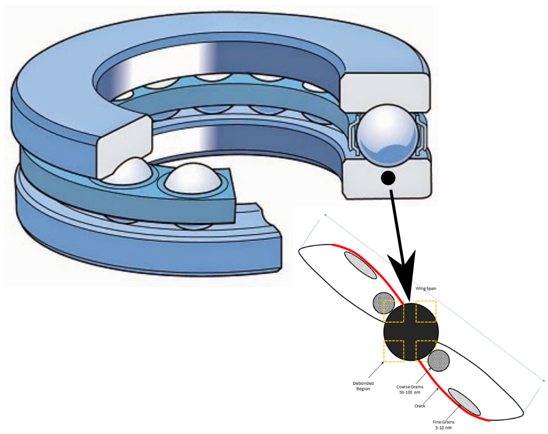

Figure 7.8: Rolling Contact Fatigue on flatwasher for BWF investigations

The numerical fatigue damage model is a coupling of the HEP rolling contact solver with the damage law proposed in Moghaddam et al. (2015) [280] . It is postulated that the formation of butterfly wings is related to cyclic damage accumulation at the vicinity of the inclusion. This type of damage accumulation is manifested physically by the alteration of the material microstructure, implying a degradation of its properties such as stiffness. This is sustained by many observations of serial sectioned worn bearing raceway [79, 286, 81] and pioneering research works [287] referred to RCF since the middle of the last century. It is assumed in Moghaddam et al. (2015) [236] that martensite decaying to ultrafine ferritic grains occurs when the damage reaches a critical value of 0.1. This value allowed to reproduce the microstructural changes accompanying the stress history over rolling cycles inside a defined REV around the inclusion. The damage evolution rate is given by the following expression as:

$$\frac{dD}{dN} = \left(\frac{\tau_{amplitude} + |\tau_{mean}|}{\sigma_r (1 - D)} \right)^m \tag{7.1}$$

Where D is the damage variable, N the number of rolling cycles, $\tau_{amplitude}$ the amplitude of shear stress, τ_{mean} the mean shear stress, m the damage law exponent which depends on the material and σ_r the resistance stress standing for the material's ability to resist to fatigue damage accumulation. Note that σ_r and m can be obtained from $S - N$ curves of fatigue tests [288] or torsion fatigue experiments [82].

However numerical resolution of high cyclic rolling contact needs extremely long computational time. A *Jump-in-cycles* technique can therefore be used with respect to recommendations outlined in Lemaitre (1992) [289] , in order to accelerate the damage evolution. But a damage increment ΔD must be set to relate the simulation number of cycle N_s to the theoretical number of cycle N_t permitted by the *Jump-in-cycles* technique [10]. Therefore, the more the assumed damage increment ΔD is small, the more the theoretical number of cycle N_t will be close to the real number of cycles N.

The fatigue damage solver is based on a scheme composed by three blocks of computation: (i) an initialization block for allocating the starting values of material data and numerical parameters; (ii) a simulation block consisting of the semi-analytical HEP rolling contact resolution; (iii) a looping block used to update the Young modulus of the material as $E^i = (1 - D^i)E^{i-1}$ and to launch a next simulation block until the damage converges to the value set in the initialization block (*e.g.* 0.1 in this case, to reproduce the BWF). The superscript i designates the current cycle. Then D^i is calculated from the previous stress history ($\tau^{i-1}_{amplitude}$, τ^{i-1}_{mean}) and the previous damage state D^{i-1}. Damage calculation using the *Jump-in-cycles*, has been well detailed in Warhadpande et al. (2012) [9] .

Fig .7.9 illustrates a qualitative result concerning a three-dimensional reconstitution of BWF obtained from the fatigue damage solver described above. It can be seen that the microstructural transformation starts from the interface inclusion/matrix and then propagates along a direction forming 45° with the opposite rolling direction. The next stage of the application of the fatigue damage solver would be to conduct parametric study by varying the inclusion and the matrix initial properties and also the loading conditions, in order to obtain quantitative output such as the evolution of the effective degraded material volume according to the number of fatigue cycle.

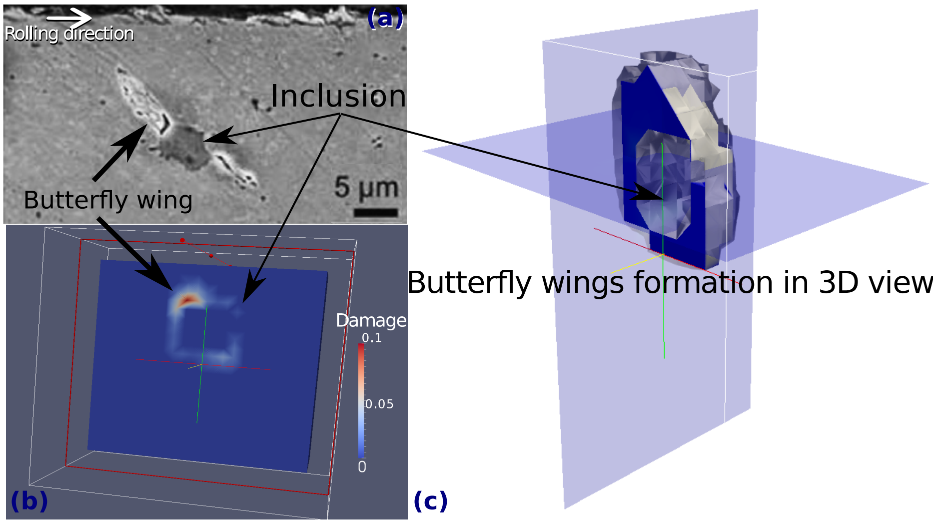

Figure 7.9: Simulation of Butterfly Wing Formation around nonmetallic inclusion. (a) [79]

7.2.4 SIMULATION OF ETCHING AREAS APPEARANCE IN PRESENCE OF CARBIDES

Another microstructural transformation during RCF is known as White Etching Area (WEA). The development of a WEA generally leads to a White Etching Crack (WEC) which connects to the surface as shown in Fig .7.10(b)-(c). It can be a precursor of spalling. Inclusions are mostly found at the source of crack propagation in a WEA. However the WEA features are related to the occurrence of local micro-plastic deformations that relax to some extent the high stress concentration undergone over continued cycling. This phenomenon is discussed in [290], highlighting one variant associated with WEA called Dark Etching Areas (DEA) found in the subsurface regions at the depth of the maximum Hertzian stress. Therefore, investigating on the DEA, WEA and WEC requires a full coupling of the fatigue damage solver with that of heterogeneous elastic plastic rolling contact. One interesting application would be to explore the protective role of the nitrided layer on the propagation of a WEA. As one can see in Fig .7.10(a), the evolution of a WEA seems to be blocked and/or diverted when it encounters the nitrided layer.

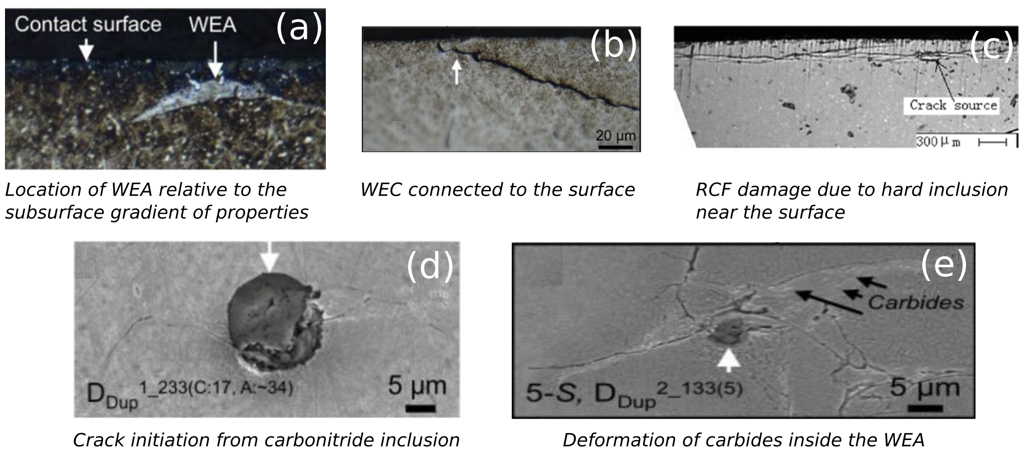

Figure 7.10: Bearing rings subsurface risk [78]

To be able to replicate the etching regions also described as the RCF affected zones in Bhattacharyya, Subhash, and Arakere (2014) [291] , Eq. 7.1 is modified to a fatigue plastic damage model consisting in the degradation of the material plastic properties. The present damage noted D_{pd} will decrease the elastic limit instead of the Young modulus, in a representative volume surrounding the Hertzian zone and the inclusion. The plastic damage evolution rate can be expressed as:

$$\frac{dD_{pd}}{dN_{pd}} = \left(\frac{|\tau_{pd}|}{\sigma_{pd}(1 - D_{pd})} \right)^{m_{pd}} \tag{7.2}$$

Where $\tau_{pd} = max\left(\tau_{max}(t) + a_{DV}.\sigma_{HP}(t) - b_{DV}\ ,\ 0\right)$ representing the stress responsible for plastic properties degradation. The script $_{pd}$ stands for plastic damage. Note that τ_{pd} is an equivalent stress corresponding to the gap between the Dang Van stress and the material fatigue line described in Chap. 4. It is 0 when the stress trajectory never crosses the fatigue line during the regarded rolling cycle. a_{DV} and b_{DV} are material constants related to the Dang Van fatigue criteria. N_{pd}, σ_{pd} and m_{pd} are the plastic damage parameters, counterparts of that of the elastic damage responsible for BWF. But here, σ_{pd} is closely related the material yield strength. Hence, the fatigue elastic plastic damage solver is constructed on the same scheme as in the above Sec. 7.2.3, by adding the plastic damage model into the simulation block.

Fig .7.11 illustrates a qualitative result concerning a three-dimensional reconstitution of RCF affected zones obtained from the fatigue elastic plastic damage solver described above. It can be seen that the layer where the equivalent stress responsible for elastic plastic properties degradation corresponds to the etching regions on both sides of the Hertzian depth. The stress is more concentrated inside and around the inclusion[c] . This could explain why in practice, etching regions are observed more accentuated in the vicinity of inclusions, but seem to be homogeneous elsewhere, in reference to Fig .7.10(d)-(e). In addition, a potential butterfly wing formation was found nearby the inclusion.

[c] *in the present case the inclusion is harder than the matrix*

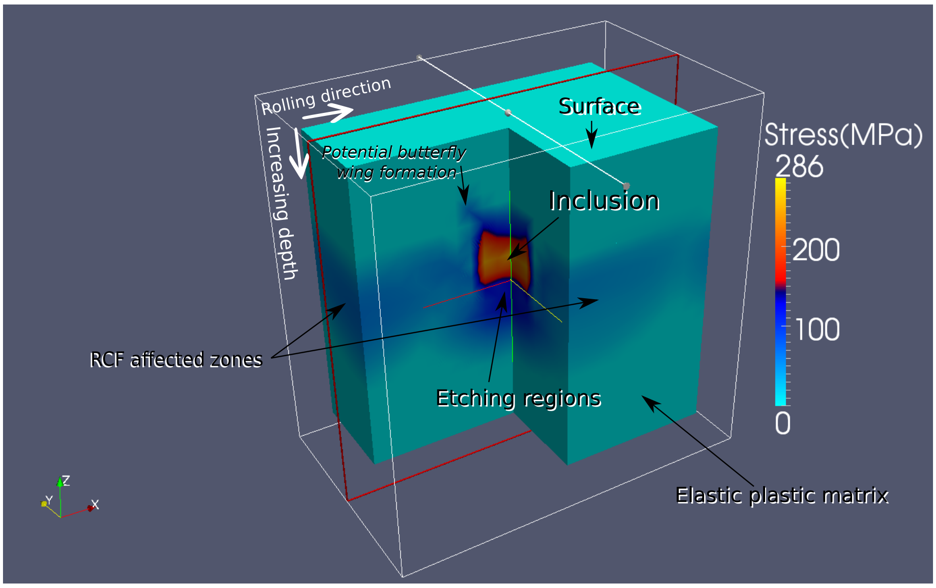

Figure 7.11: Description of plastic layer over rolling fatigue cycles in presence of nonmetallic inclusion

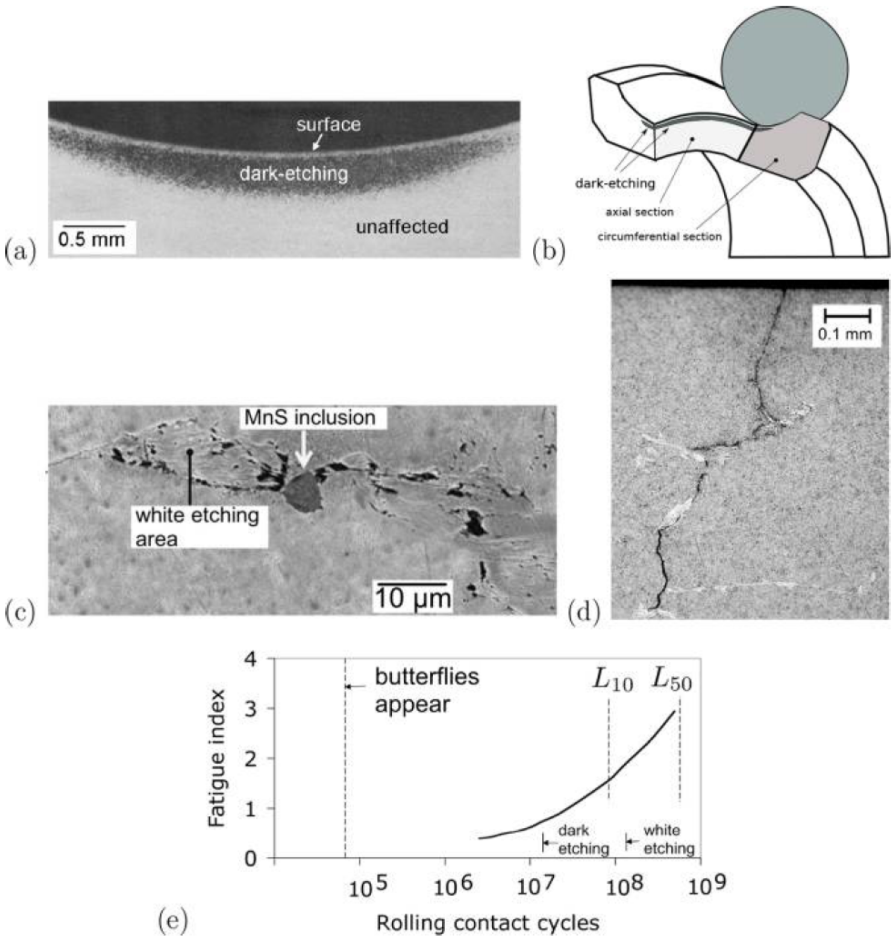

Figure 7.12: BWF, DEA and WEA is discussed in Bhadeshia and Solano-Alvarez (2015) [276] by reporting results from experimental studies

Fig .7.12 presents BWF, DEA and WEA is discussed in Bhadeshia and Solano-Alvarez (2015) [276] by reporting results from experimental studies. But no numerical model has been found in the literature proposing a full description combining these three phenomena. (a) Uniform layer of dark etching region on the circumferential section, following 10^7 rotations while subjected to contact stress of 3.3GPa at $70°$C. Micrograph courtesy of T. B. Lund. (b) Three-dimensional form of dark etching microstructures. (c) White etching regions emanating from inclusion in Evans et al. (2013) [79] . (d) Irregular white etching regions associated with axial crack on bearing. Micrograph courtesy of R. Errichello, GEARTECH. (e) Typical sequence of damage evolution. Fatigue index is a measure of heterogeneous strains within material. The fatigue elastic plastic damage solver can allow a theoretical bearing life prediction accounting plasticity and heterogeneity interactions. This suggests investigation on the:

- Influence of material data m, σ_r, σ_{pd} and m_{pd}
- Influence of heterogeneity shape, size, location and stiffness
- Consequences related to the initial compressive stress and the gradient of hardness
- Evolution of the stress concentration around heterogeneity and the subsurface plastic zone
- Effect of loading variables such as the amplitude of the contact pressure, the friction coefficient

In the scheme of things, the interaction of the microstructural alterations (BWF, WEA, DEA) result in microcavities and cracks which coalescence lead to the bearing failure. A control of the design parameters (loads sizing, microstructures tailoring, manufacturing procedures etc.) which contribute to acting on the microstructural alterations, is an excellent alternative to improve the bearings operating performance. The bearing engineering practice in perspective of the present work will be to delay the fatigue cracks and to ensure a realistic prediction of their occurrence then to enable a more accurate planning of maintenance operations.

Part IV

APPENDIX

This part is dedicated to the comprehension elements that sustain the models developed above in the study. Details are given about the influences coefficients necessary to solve the heterogeneous elastic plastic contact. The scripts of the computational code are not mentioned. The reader is directed to the flowchart referred in second part, if need to reproduce the semi analytical model

A

INFLUENCE COEFFICIENTS RELATIVE TO THE HETEROGENEOUS ELASTIC PLASTIC PROBLEM

The semi-analytical method is based on the numerical summation of elementary analytical solutions. The latter are obtained by solving an applied unit force problem. A normal force applied on the surface leads to the Boussinesq solution when a tangential force leads to the Cerruti solution. The combination of both solutions are sufficient to have influence coefficients for any given distribution of contact pressure. A normal force applied on a volume element within infinite space leads to the elastic or the plastic or the heterogeneous problem influence coefficients according to the resolution of the equilibrium equation. These influence coefficients are exposed here below.

Contents

A.1 ESHELBY TENSOR

The results presented here are limited to a uniform eigenstrain, therefore, only the calculation of the tensor D_{ijkl} is performed.

$$D_{ijkl} = \frac{1}{8\pi(1-\nu)}[\Psi_{,ijkl} - 2\nu\delta_{kl}\phi_{,ij} - (1-\nu)(\delta_{kl}\phi_{il} + \delta_{ki}\phi_{,jl} + \delta_{jl}\phi_{,ik} + \delta_{li}\phi_{,jk})] \tag{A.1}$$

$$\Psi(x) = \int_\Omega |x - x'|dx'$$

$$\phi(x) = \int_\Omega \frac{1}{|x - x'|}dx'$$

The harmonic potential $\phi(x)$ and the biharmonic potential $\Psi(x)$ can be expressed as a function of the elliptical integrals $E(\theta', k)$ and $F(\theta', k)$ [292] , where:

$$E(\theta', k) = \int_0^{\theta'} (1 - k^2 \sin w)^{1/2} dw$$

$$F(\theta', k) = \int_0^{\theta'} \frac{1}{(1 - k^2 \sin w)^{1/2}} dw$$

$$\theta' = \sin^{-1}\left(1 - \frac{a_3^2}{a_1^2}\right)^{1/2}$$

$$k = \frac{3(a_1^2 - a_2^2)}{(a_1^2 - a_3^2)}$$

Assuming that $a_1 > a_2 > a_3$, with a_1,a_2,a_3 the semi-axes of the ellipsoidal inclusion. The Eshelby's tensor S_{ijkl} is obtained from Eq. (A.1) as:

$$S_{ijkl} = D_{ijkl}(x^I)$$

where $x^I = (x_1^I, x_2^I, x_3^I)$ represents the position of the inclusion center in Cartesian reference frame.

A.2 STRESSES WITHIN A HALF-SPACE SUBMITTED TO A NORMAL PRESSURE UNIFORM OVER A RECTANGULAR PATCH

An isotropic half-space is submitted to a uniform normal pressure σ^n discretized over a rectangular element of size $2\Delta x_1 \times 2\Delta x_2$ at the center point $P(x_1', x_2', 0)$. The stress at an observation point $Q(x_1, x_2, x_3)$ is given by [293]:

$$\sigma_{ij}(x_1, x_2, x_3) = M_{ij}(x_1 - x_1', x_2 - x_2', x_3)\sigma^n(x_1, x_2)$$

$$\begin{aligned}\sigma_{ij}(x_1, x_2, x_3) =& \frac{\sigma^n}{2\pi}[h_{ij}(\xi_1 + \Delta x_1, \xi_2 + \Delta x_2, \xi_3) - h_{ij}(\xi_1 + \Delta x_1, \xi_2 - \Delta x_2, \xi_3) \\ &+ h_{ij}(\xi_1 - \Delta x_1, \xi_2 - \Delta x_2, \xi_3) - h_{ij}(\xi_1 - \Delta x_1, \xi_2 + \Delta x_2, \xi_3)]\end{aligned}$$

where

$$\xi_i = x_i - x_i'.$$

The functions $h_{ij}()$ in Eq.(B1) are defined by

$$h_{11}(x_1,x_2,x_3) = 2\nu\tan^{-1}\frac{x_2^2+x_3^2-\rho x_2}{x_1x_3} + 2(1-\nu)\tan^{-1}\frac{\rho-x_2+x_3}{x_1} + \frac{x_1x_2x_3}{\rho(x_1^2+x_3^2)},$$

$$h_{22}(x_1,x_2,x_3) = h_{11}(x_2,x_1,x_3),$$

$$h_{33}(x_1,x_2,x_3) = \tan^{-1}\frac{x_2^2+x_3^2-\rho x_2}{x_1x_3} - \frac{x_1x_2x_3}{\rho}\left(\frac{1}{x_1^2+x_3^2}+\frac{1}{x_2^2+x_3^2}\right),$$

$$h_{12}(x_1,x_2,x_3) = -\frac{x_3}{\rho} - (1-2\nu)\log(\rho+x_3),$$

$$h_{13}(x_1,x_2,x_3) = -\frac{x_2x_3^2}{\rho(x_1^3+x_3^2)},$$

$$h_{23}(x_1,x_2,x_3) = h_{13}(x_2,x_1,x_3),$$

where

$$\rho = \sqrt{x_1^2+x_2^2+x_3^2}.$$

A.3 NORMAL DISPLACEMENT AT THE SURFACE SUBJECTED TO NORMAL PRESSURE (K^N)

The contact between a sphere and an elastic half-space having respectively elastic constants (E_1,ν_1) and (E_2,ν_2), where the surface $x_3 = 0$ is discretized into rectangular surface elements $2\Delta_1 \times 2\Delta_2$, is now considered. The initial contact point coincides with the origin of the Cartesian coordinate system (x_1,x_2,x_3). The relationship between the normal displacement at an observation point $P(\xi_1,\xi_2,0)$ and the pressure uniformly distributed to an elementary surface element centered at $Q(\xi_1',\xi_2',0)$ is built using the following functions K^n.

$$K^n(c_1,c_2) = \left[\frac{1-\nu_1^2}{\pi E_1}+\frac{1-\nu_2^2}{\pi E_2}\right]\sum_{p=1}^{4}K_p^n(c_1,c_2),$$

$$K_1^n(c_1,c_2) = (c_1+\Delta_1)\log\left(\frac{(c_2+\Delta_2)+\sqrt{(c_2+\Delta_2)^2+(c_1+\Delta_1)^2}}{(c_2-\Delta_2)+\sqrt{(c_2-\Delta_2)^2+(c_1+\Delta_1)^2}}\right),$$

$$K_2^n(c_1,c_2) = (c_2+\Delta_2)\log\left(\frac{(c_1+\Delta_1)+\sqrt{(c_2+\Delta_2)^2+(c_1+\Delta_1)^2}}{(c_1-\Delta_1)+\sqrt{(c_2+\Delta_2)^2+(c_1-\Delta_1)^2}}\right),$$

$$K_3^n(c_1,c_2) = (c_1-\Delta_1)\log\left(\frac{(c_2-\Delta_2)+\sqrt{(c_2-\Delta_2)^2+(c_1-\Delta_1)^2}}{(c_2+\Delta_2)+\sqrt{(c_2+\Delta_2)^2+(c_1-\Delta_1)^2}}\right),$$

$$K_4^n(c_1,c_2) = (c_2-\Delta_2)\log\left(\frac{(c_1-\Delta_1)+\sqrt{(c_2-\Delta_2)^2+(c_1-\Delta_1)^2}}{(c_1+\Delta_1)+\sqrt{(c_2-\Delta_2)^2+(c_1+\Delta_1)^2}}\right),$$

where

$$c_1 = \xi_1-\xi_1' \quad\text{and}\quad c_2 = \xi_2-\xi_2'$$

A.4 RESIDUAL STRESSES IN AN INFINITE BODY

The influence coefficients giving the residual stresses generated in an infinite space by a cuboid of uniform strain ϵ^p_{ij} $(i,j = 1,2,3)$ are recalled here [67]. The source of the displacements is a cuboid of a uniform strain of dimensions $\Delta x \times \Delta y \times \Delta z$ with its center located at the origin of the coordinate system $(x,y,z) = (0,0,0)$. The calculation point M is at (x,y,z). It should be recalled here that the body is considered infinite, thus the origin of the coordinate system has no importance. ν is the Poisson's ratio of the body. The vectors linking the corners of the cuboid to the observation point are first defined as follows:

$$C_1 = \left(x - \frac{\Delta x}{2}, y - \frac{\Delta y}{2}, z - \frac{\Delta z}{2}\right) = \left(c_1^1, c_2^1, c_3^1\right)$$

$$C_2 = \left(x + \frac{\Delta x}{2}, y - \frac{\Delta y}{2}, z - \frac{\Delta z}{2}\right) = \left(c_1^2, c_2^2, c_3^2\right)$$

$$C_3 = \left(x + \frac{\Delta x}{2}, y + \frac{\Delta y}{2}, z - \frac{\Delta z}{2}\right)$$

$$C_4 = \left(x - \frac{\Delta x}{2}, y + \frac{\Delta y}{2}, z - \frac{\Delta z}{2}\right)$$

$$C_5 = \left(x - \frac{\Delta x}{2}, y + \frac{\Delta y}{2}, z + \frac{\Delta z}{2}\right)$$

$$C_6 = \left(x - \frac{\Delta x}{2}, y - \frac{\Delta y}{2}, z + \frac{\Delta z}{2}\right)$$

$$C_7 = \left(x + \frac{\Delta x}{2}, y - \frac{\Delta y}{2}, z + \frac{\Delta z}{2}\right)$$

$$C_8 = \left(x + \frac{\Delta x}{2}, y + \frac{\Delta y}{2}, z + \frac{\Delta z}{2}\right)$$

For a cuboid with constant unit normal plastic strain, i.e. $\epsilon^p_{11} = 1$ and $\epsilon^p_{ij} = 0|(i,j) \neq (1,1)$, the elastic strains at the observation point M are given by:

$$\epsilon_{1111} = \frac{1}{8\pi^3} \sum_{m=1}^{8} \left[D^m_{,1111} + \frac{2-\nu}{1-\nu}\left(D^m_{,1111} + D^m_{,1133}\right)\right] - H(M)$$

$$\epsilon_{2211} = -\frac{1}{8\pi^3} \sum_{m=1}^{8} \left[-D^m_{,1122}\right] + \frac{\nu}{1-\nu}\left(D^m_{,2222} + D^m_{,2233}\right)$$

$$\epsilon_{3311} = -\frac{1}{8\pi^3} \sum_{m=1}^{8} \left[-D^m_{,1133}\right] + \frac{\nu}{1-\nu}\left(D^m_{,2233} + D^m_{,3333}\right)$$

$$\epsilon_{1211} = \frac{1}{8\pi^3} \sum_{m=1}^{8} \left[\frac{\nu}{1-\nu} D^m_{,1112}\right] + \frac{1+\nu}{1-\nu}\left(D^m_{,2221} + D^m_{,3312}\right)$$

$$\epsilon_{1311} = \frac{1}{8\pi^3} \sum_{m=1}^{8} \left[\frac{\nu}{1-\nu} D^m_{,1113}\right] + \frac{1+\nu}{1-\nu}\left(D^m_{,3331} + D^m_{,2213}\right)$$

$$\epsilon_{2311} = \frac{1}{8\pi^3}\sum_{m=1}^{8}\left[\frac{\nu}{1-\nu}\left(D^m_{,2233} + D^m_{,3332}\right)\right]$$

For a cuboid with a constant unit shear plastic strain, i.e. $\epsilon^p_{12} = \epsilon^p_{21} = 1$ and $\epsilon^p_{ij} = 0|(i,j) \neq (1,2),(2,1)$, the elastic strains at the observation point M are given by:

$$\epsilon_{1112} = \frac{1}{8\pi^3}\sum_{m=1}^{8}\left[\frac{-2\nu}{1-\nu}D^m_{,1112}\right] + 2\left(D^m_{,2221} + D^m_{,3312}\right)$$

$$\epsilon_{2212} = \frac{1}{8\pi^3}\sum_{m=1}^{8}\left[\frac{-2\nu}{1-\nu}D^m_{,1222}\right] + 2\left(D^m_{,1112} + D^m_{,3312}\right)$$

$$\epsilon_{3312} = \frac{1}{8\pi^3}\sum_{m=1}^{8}\left[\frac{-2\nu}{1-\nu}D^m_{,3312}\right]$$

$$\epsilon_{1212} = \frac{1}{8\pi^3}\sum_{m=1}^{8}\left[\frac{-2\nu}{1-\nu}D^m_{,1122} + D^m_{,1111} + D^m_{,2222} + D^m_{,1133} + D^m_{,2233}\right] - H(M)$$

$$\epsilon_{1312} = \frac{1}{8\pi^3}\sum_{m=1}^{8}\left[-\frac{1+\nu}{1-\nu}D^m_{,1123}\right] + D^m_{,2223} + D^m_{,3332}$$

$$\epsilon_{2312} = \frac{1}{8\pi^3}\sum_{m=1}^{8}\left[-\frac{1+\nu}{1-\nu}D^m_{,2213}\right] + D^m_{,1113} + D^m_{,3331}$$

If the point M is located inside the cuboid, $H(M) = 1$ and $H(M) = 0$ otherwise. The functions $D^m_{,ijkl}$ $(m = 1\ldots8)$ are defined as following:

$$\begin{aligned} D^m_{,1111} =& 2\pi^2(\arctan\left(\frac{c_2^m c_3^m}{c_1^m R}\right) \\ &- \frac{c_1^m c_2^m c_3^m}{2R}\left(\frac{1}{\left(c_1^m\right)^2 + \left(c_2^m\right)^2} + \frac{1}{\left(c_1^m\right)^2 + \left(c_3^m\right)^2}\right)) \end{aligned}$$

$$\begin{aligned} D^m_{,1112} =& -\pi^2(\mathrm{sign}\left(c_3^m\right) \\ &\times \ln\left(\frac{R + \left|c_3^m\right|}{\sqrt{\left(c_1^m\right)^2 + \left(c_2^m\right)^2}} - \frac{\left(c_1^m\right)^2 c_3^m}{\left(\left(c_1^m\right)^2 + \left(c_2^m\right)^2\right)R}\right)) \end{aligned}$$

$$D^m_{,1122} = \frac{\pi^2 c_1^m c_2^m c_3^m}{\left(\left(c_1^m\right)^2 + \left(c_2^m\right)^2\right)R}$$

$$D^m_{,1123} = -\frac{\pi^2 c_1^m}{R}$$

where

$$R = \sqrt{\left(c_1^m\right)^2 + \left(c_2^m\right)^2 + \left(c_3^m\right)^2}$$

The other $D^{m}_{,ijkl}$ functions are obtained by circular permutations of the subscripts. Similar permutation allows to determine the elastic strain components at the observation point M generated by other plastic strain components. At last the use of the traditional Hooke's law allows to calculate the elastic stresses generated by the plastic strains from the elastic strains.

A.5 RESIDUAL SURFACE DISPLACEMENT GENERATED BY A CUBOID OF UNIFORM EIGENSTRAIN

The influence coefficients giving the residual displacements at the surface of a half-space generated by a cuboid of uniform eigenstrain are recalled here. The solution for the displacement normal to the surface was first given by Chiu [72] in an integral form and later by Jacq et al. [37] in an analytical form. The extension to the tangential displacements along the x and y directions was made by Fulleringer et al. [41] to couple the effects of both plasticity and tangential effects for use in semi-analytical models. The source of the displacements is a cuboid of a uniform strain of dimensions $\Delta x \times \Delta y \times \Delta z$ with its center C at (x, y, z). The calculation point A is located at the surface of the body, at the origin of the coordinate system $(x, y, z) = (0, 0, 0)$. ν is the Poisson's ratio of the body.

A.5.1 RESIDUAL DISPLACEMENT IN THE Z DIRECTION

The residual displacement in the direction normal to the surface (z or 3) is given by:

$$u_z^{res}(A) = \varepsilon_{ij}^{p} D_{3ij}(A, C) \,|\, (i, j) = 1, 2, 3$$

The function D_{3ij} was analytically integrated by Jacq et al. [37] and is given by:

$$\begin{aligned}
D_{3ij}(A, C) = & F_{3ij}\left(x + \frac{\Delta x}{2}, y + \frac{\Delta y}{2}, z + \frac{\Delta z}{2}\right) - F_{3ij}\left(x + \frac{\Delta x}{2}, y + \frac{\Delta y}{2}, z - \frac{\Delta z}{2}\right) \\
& - F_{3ij}\left(x + \frac{\Delta x}{2}, y - \frac{\Delta y}{2}, z + \frac{\Delta z}{2}\right) - F_{3ij}\left(x - \frac{\Delta x}{2}, y + \frac{\Delta y}{2}, z + \frac{\Delta z}{2}\right) \\
& + F_{3ij}\left(x + \frac{\Delta x}{2}, y - \frac{\Delta y}{2}, z - \frac{\Delta z}{2}\right) + F_{3ij}\left(x - \frac{\Delta x}{2}, y - \frac{\Delta y}{2}, z + \frac{\Delta z}{2}\right) \\
& + F_{3ij}\left(x - \frac{\Delta x}{2}, y + \frac{\Delta y}{2}, z - \frac{\Delta z}{2}\right) - F_{3ij}\left(x - \frac{\Delta x}{2}, y - \frac{\Delta y}{2}, z - \frac{\Delta z}{2}\right)
\end{aligned}$$

with:

$$F_{311}(x, y, z) = \frac{1}{\pi}\left(-\nu x \ln(y + R) - (1 - 2\nu) z \arctan\left(\frac{y + z + R}{x}\right)\right)$$

$$F_{322}(x, y, z) = \frac{1}{\pi}\left(-\nu y \ln(x + R) - (1 - 2\nu) z \arctan\left(\frac{x + z + R}{y}\right)\right)$$

$$F_{333}(x, y, z) = \frac{1}{\pi}\left((1 - 2\nu)\left(2z \arctan\left(\frac{x + y + R}{z}\right) + x \ln(R + y) + y \ln(R + x)\right) + \frac{z}{2} \arctan\left(\right.\right.$$

$$F_{312}(x, y, z) = \frac{1}{\pi}\left(-2\nu R - (1 - 2\nu) z \ln(z + R)\right)$$

$$F_{313}(x, y, z) = \frac{1}{\pi}\left(2x \arctan\left(\frac{y + z + R}{x}\right) + y \ln(z + R)\right)$$

$$F_{323}(x,y,z) = \frac{1}{\pi}\left(2y\arctan\left(\frac{x+z+R}{y}\right) + x\ln(z+R)\right)$$

with $R = \sqrt{x^2+y^2+z^2}$.

A.5.2 RESIDUAL DISPLACEMENT IN THE X DIRECTION

The residual displacement in the direction parallel to the surface (x or 1) is given by:

$$u_x^{res}(A) = \varepsilon_{ij}^{p} D_{1ij}(A,C)\,|\,(i,j) = 1,2,3$$

The function D_{1ij} was analytically integrated by Fulleringer et al. [41] and is given by:

$$\begin{aligned}
D_{1ij}(A,C) = {} & F_{1ij}\left(x+\frac{\Delta x}{2}, y+\frac{\Delta y}{2}, z+\frac{\Delta z}{2}\right) - F_{1ij}\left(x+\frac{\Delta x}{2}, y+\frac{\Delta y}{2}, z-\frac{\Delta z}{2}\right)\\
& - F_{1ij}\left(x+\frac{\Delta x}{2}, y-\frac{\Delta y}{2}, z+\frac{\Delta z}{2}\right) - F_{1ij}\left(x-\frac{\Delta x}{2}, y+\frac{\Delta y}{2}, z+\frac{\Delta z}{2}\right)\\
& + F_{1ij}\left(x+\frac{\Delta x}{2}, y-\frac{\Delta y}{2}, z-\frac{\Delta z}{2}\right) + F_{1ij}\left(x-\frac{\Delta x}{2}, y-\frac{\Delta y}{2}, z+\frac{\Delta z}{2}\right)\\
& + F_{1ij}\left(x-\frac{\Delta x}{2}, y+\frac{\Delta y}{2}, z-\frac{\Delta z}{2}\right) - F_{1ij}\left(x-\frac{\Delta x}{2}, y-\frac{\Delta y}{2}, z-\frac{\Delta z}{2}\right)
\end{aligned}$$

with:

$$\begin{aligned}
F_{111}(x,y,z) = {} & \frac{1}{2\pi}(z\ln(R+y) + y\ln(R+z) + 2x\arctan\left(\frac{y+z+R}{x}\right) + x\arctan\left(\frac{yz}{xR}\right)\\
& + (1-2\nu)\left(2x\arctan\left(\frac{y+z+R}{x}\right) + z\ln(R+y) + \frac{1}{2}y\ln(R+z) - \frac{zy}{2(R+z)}\right))
\end{aligned}$$

$$F_{122}(x,y,z) = \frac{1}{2\pi}\left(-y\ln(R+z) + (1-2\nu)\,y\left(\frac{z}{2(R+z)} + \frac{1}{2}\ln(R+z)\right)\right)$$

$$F_{133}(x,y,z) = \frac{1}{2\pi}\left(-2\nu z\ln(R+y) + (1-2\nu)\,y\left(2x\arctan\left(\frac{R+y+z}{x}\right) + y\ln(R+z)\right)\right)$$

$$F_{112}(x,y,z) = \frac{1}{\pi}\left(2y\arctan\left(\frac{x+z+R}{y}\right) + z\ln(R+x) + \frac{1-2\nu}{2}\left(x\ln(R+z) + \frac{xz}{R+z}\right)\right)$$

$$F_{113}(x,y,z) = \frac{1}{\pi}\left(2z\arctan\left(\frac{x+y+R}{z}\right) + y\ln(R+x)\right)$$

$$F_{123}(x,y,z) = \frac{-R}{\pi}$$

with $R = \sqrt{x^2+y^2+z^2}$. For residual displacement along the y or 2 direction, the solutions for F_{2ij} can be found easily by circular permutations of the indices.

B

IDENTIFICATION OF OVERALL BEHAVIOR

Identification algorithm is executed to find parameters need to describe the overall behavior of a heterogeneous elastic plastic representative volume. The identification is based on Levenberg-Marquardt algorithms implemented in matlab code MIC2M. The evolution of the ratcheting during multi-cycles rolling contact is fitted. The homogenized elastic bodies are found to follow some rheological behaviors according to the ratio between heterogeneity and matrix Young's modulus.

Contents

B.1 RATCHETING RATE CURVE FITTING

The Fig.B.1 presents the identification of parameters needed to describe the evolution of plastic strain during rolling cycles when ratcheting regime primed (see section 4.4.2) by curve fitting made through data points using least-square method.

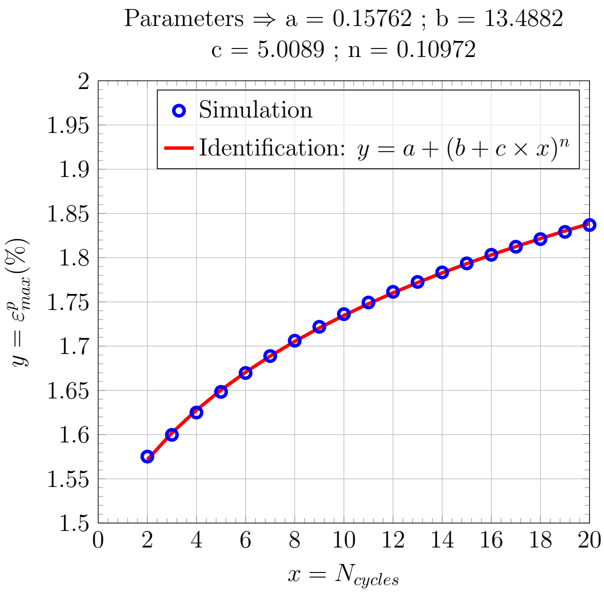

Figure B.1: Ratcheting rate curve fitting

B.2 RHEOLOGY LAW PARAMETERS IDENTIFICATION OF THE HOMOGENIZED BODY ELASTIC BEHAVIOR

The results presented here are the identification of parameters needed to describe the elastic macroscopic behavior of the heterogeneous elastic media for a fixed distribution $D = 0.4a$. The effective Young's modulus E_{eff} is obtained in function of the heterogeneity Young's modulus E_I relatively to each volume fraction V_f. In Fig. B.2 E_{eff} as well as E_I are normalized by the matrix Young's modulus E_m.

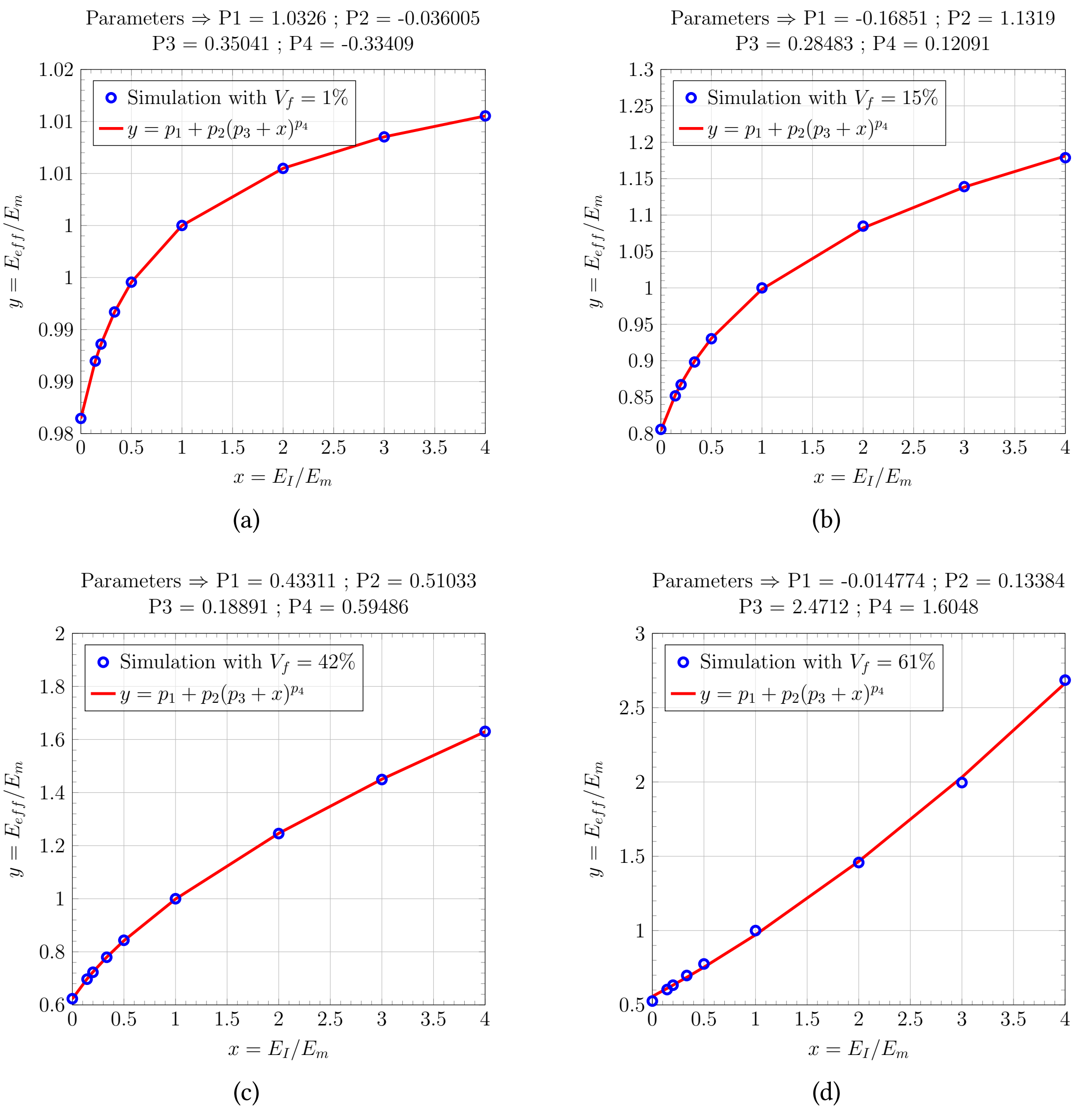

Figure B.2: Rheology law parameters identification: (a) $V_f = 1\%$; (b) $V_f = 15\%$; (c) $V_f = 42\%$; (d) $V_f = 61\%$

B.3 DAMAGE EVOLUTION ACCORDING TO FRICTION COEFFICIENT

Working on contact problems involving coated surfaces subject to fretting fatigue loading Jerbi *et al.* [129] propose an elastic damageable model, base on semi analytical algorithms, to describe the damage evolution according to friction coefficients. The profiles of the damage D versus the number of fretting cycles N_{cyc}, in Fig.B.3, tends to behave similarly as the maximum plastic strain ε^p_{max} versus the rolling distance δx, in Fig.B.3, when the friction coefficient, noted μ, increases. A link could be made between both studies, since N_{cyc} could be likened to δx and the coating was modeled by multiple heterogeneities. Also D could be correlated to ε^p_{max} because the damage criteria used and its evolution is analog to the plastic strain one. The damage integration is described by a set of relations as:

$$
\begin{aligned}
f(\varepsilon, D) &= \tilde{\varepsilon} - K(D) \\
f &< 0 \Leftrightarrow \text{Elastic behavior} \\
f &= 0 \Leftrightarrow \text{Damage flow} \\
D &= \frac{\tilde{\varepsilon} - \varepsilon_{d0}}{\varepsilon_R - \varepsilon_{d0}} \\
\sigma &= (1 - D)E_0\varepsilon
\end{aligned}
$$

f	damage yield function
$\tilde{\varepsilon}$	Mazars's equivalent strain modified
$K(0) = \varepsilon_{d0}$	damage threshold for virgin material
ε_{d0}	limit strain beyond which damage occurs
ε_R	strain to failure
E_0	Initial Young's modulus

Those relations reminds the plasticity yield function equations used to determine ε^p_{max}.

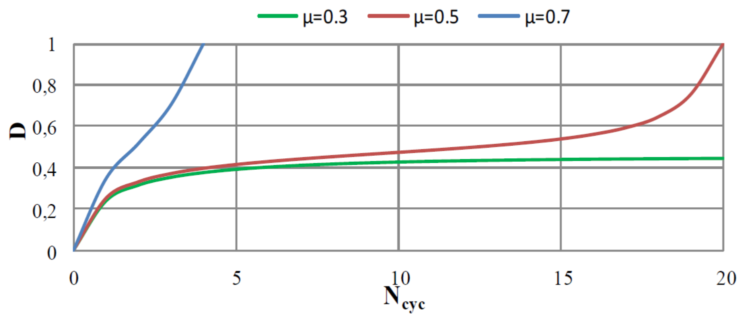

(a)

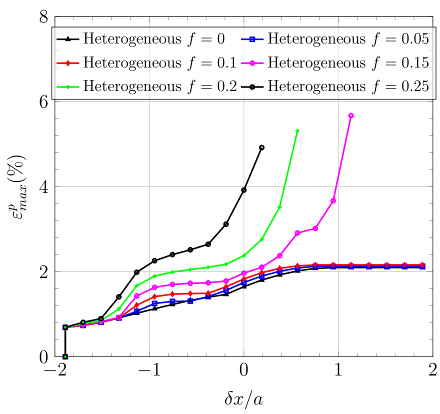

(b)

Figure B.3: Damage evolution according to friction coefficient: (a) Typical evolution of the damage as a function of the number of cycles according to friction coefficient, see [129] for more details on the calculation input data. (b) Evolution of the plastic strain as a function of the rolling distance according to the friction coefficient

[1] Leonardo Da Vinci. *The notebooks of Leonardo da Vinci*. Vol. 1. Courier Corporation, 2012.

[2] Lewis Rosado, Nelson H Forster, Kevin L Thompson, and Jason W Cooke. "Rolling contact fatigue life and spall propagation of AISI M50, M50NiL, and AISI 52100, Part I: experimental results." In: *Tribology Transactions* 53.1 (2009), pp. 29–41.

[3] Farshid Sadeghi, Behrooz Jalalahmadi, Trevor S Slack, Nihar Raje, and Nagaraj K Arakere. "A review of rolling contact fatigue." In: *Journal of Tribology* 131.4 (2009), p. 041403.

[4] DMLFADR Nélias, ML Dumont, F Champiot, A Vincent, D Girodin, R Fougeres, and L Flamand. "Role of inclusions, surface roughness and operating conditions on rolling contact fatigue." In: *Journal of tribology* 121.2 (1999), pp. 240–251.

[5] Tibor E Tallian. "The Failure Atlas For Hertz Contact Machine Elements." In: *Mechanical Engineering* 114.3 (1992), p. 66.

[6] TE Tallian. "Simplified contact fatigue life prediction model—Part II: New model." In: *Journal of tribology* 114.2 (1992), pp. 214–220.

[7] Daniel Nelias and Fabrice Ville. "Detrimental effects of debris dents on rolling contact fatigue." In: *Journal of Tribology* 122.1 (2000), pp. 55–64.

[8] Gang Xu and Farshid Sadeghi. "Spall initiation and propagation due to debris denting." In: *Wear* 201.1 (1996), pp. 106–116.

[9] Anurag Warhadpande, Farshid Sadeghi, Michael N Kotzalas, and Gary Doll. "Effects of plasticity on subsurface initiated spalling in rolling contact fatigue." In: *International Journal of Fatigue* 36.1 (2012), pp. 80–95.

[10] Trevor Slack and Farshid Sadeghi. "Explicit finite element modeling of subsurface initiated spalling in rolling contacts." In: *Tribology International* 43.9 (2010), pp. 1693–1702.

[11] Clarence Zener. "A theoretical criterion for the initiation of slip bands." In: *Physical Review* 69.3-4 (1946), p. 128.

[12] K Tanaka and T Mura. "A theory of fatigue crack initiation at inclusions." In: *Metallurgical Transactions A* 13.1 (1982), pp. 117–123.

[13] Nihar Raje, Farshid Sadeghi, and Richard G Rateick. "A statistical damage mechanics model for subsurface initiated spalling in rolling contacts." In: *Journal of Tribology* 130.4 (2008), p. 042201.

[14] Zaretsky Erwin. *How to Determine Bearing System Life.*

[15] Pawel Rycerz, Amir Kadiric, Rihard Pasaribu, Guillermo Morales Espejel, and Andy V Olver. "EFFECT OF ADDITIVES ON SURFACE PERFORMANCE." In: ().

[16] Dominique François. *Endommagement et rupture de matériaux*. EDP sciences, 2012.

[17] WJ Davies and KL Day. "Surface fatigue in ball bearings, roller bearings, and gears in aircraft engines." In: *Applied Mechanics Group, Symposium on Fatigue in Rolling Contact, The Institution of Mechanical Engineers, London, England.* 1963.

[18] RF Johnson and JR Blank. "Fatigue in rolling contact: some metallurgical aspects." In: *Symposium on Fatigue in Rolling Contact.* 1963.

[19] RF Johnson and JF Sewell. "The bearing properties of 1% C-Cr steel as influenced by steelmaking practice." In: *Journal of the Iron and Steel Institute* 196.Part IV (1960), p. 414.

[20] S Stewart and R Ahmed. "Rolling contact fatigue of surface coatings—a review." In: *Wear* 253.11 (2002), pp. 1132–1144.

[21] YP Chiu, TE Tallian, and JI McCool. "An engineering model of spalling fatigue failure in rolling contact: I. The subsurface model." In: *Wear* 17.5 (1971), pp. 433–446.

[22] TE Tallian and JI McCool. "An engineering model of spalling fatigue failure in rolling contact: II. The surface model." In: *Wear* 17.5 (1971), pp. 447–461.

[23] XZ Jin and NZ Kang. "A study on rolling bearing contact fatigue failure by macro-observation and micro-analysis." In: *Wear of Materials 1989.* 1 (1989), pp. 205–213.

[24] A.P. Voskamp. "Material response to rolling contact loading." In: *Journal of Tribology* 107.3 (1985), pp. 359–364.

[25] D. Nelias, M.-L. Dumont, F. Champiot, A. Vincent, D. Girodin, R. Fougeres, and L. Flamand. "Role of inclusions, surface roughness and operating conditions on rolling contact fatigue." In: *Journal of Tribology* 121.2 (1999), pp. 240–251.

[26] Yukitaka Murakami and M. Endo. "Effects of defects, inclusions and inhomogeneities on fatigue strength." In: *International Journal of Fatigue* 16.3 (1994), pp. 163–182.

[27] J.D. Eshelby. "The determination of the elastic field of an ellipsoidal inclusion, and related problems." In: *Proceedings of the Royal Society of London. Series A. Mathematical and Physical Sciences* 241.1226 (1957), pp. 376–396.

[28] J.D. Eshelby. "The elastic field outside an ellipsoidal inclusion." In: *Proceedings of the Royal Society of London. Series A, Mathematical and Physical Sciences* 252 (1959), pp. 561–569.

[29] T. Mura and R. Furuhashi. "The elastic inclusion with a sliding interface." In: *Journal of Applied Mechanics* 51.2 (1984), pp. 308–310.

[30] Zissis Andrew Moschovidis and T. Mura. "Two-ellipsoidal inhomogeneities by the equivalent inclusion method." In: *Journal of Applied Mechanics* 42.4 (1975), pp. 847–852.

[31] Julien Leroux. "Modélisation numérique du contact pour matériaux composites." PhD thesis. INSA-Lyon, 2013.

[32] Elena Kabo and Anders Ekberg. "Fatigue initiation in railway wheels - a numerical study of the influence of defects." In: *Wear* 253.1-2 (2002), pp. 26–34.

[33] Joel Courbon, Gerard Lormand, Gilles Dudragne, P. Daguier, and Alain Vincent. "Influence of inclusion pairs, clusters and stringers on the lower bound of the endurance limit of bearing steels." In: *Tribology International* 36.12 (2003), pp. 921–928.

[34] G.R. Miller and L.M. Keer. "Interaction between a rigid indenter and a near-surface void or inclusion." In: *Journal of Applied Mechanics* 50.3 (1983), pp. 615–620.

[35] Chang-Hung Kuo. "Stress disturbances caused by the inhomogeneity in an elastic half-space subjected to contact loading." In: *International Journal of Solids and Structures* 44.3 (2007), pp. 860–873.

[36] Julien Leroux, Benjamin Fulleringer, and Daniel Nelias. "Contact analysis in presence of spherical inhomogeneities within a half-space." In: *International Journal of Solids and Structures* 47.22 (2010), pp. 3034–3049.

[37] Christophe Jacq, Daniel Nelias, Gerard Lormand, and Daniel Girodin. "Development of a three-dimensional semi-analytical elastic-plastic contact code." In: *Journal of Tribology* 124.4 (2002), pp. 653–667.

[38] D. Nelias, V. Boucly, and M. Brunet. "Elastic-plastic contact between rough surfaces: Proposal for a wear or running-in model." In: *Journal of Tribology* 128.2 (2006), pp. 236–244.

[39] Thibaut Chaise. "Mechanical simulation using a semi analytical method: from elasto-plastic rolling contact to multiple impacts." PhD thesis. INSA-Lyon, 2011.

[40] Julien Leroux and Daniel Nelias. "Stick-slip analysis of a circular point contact between a rigid sphere and a flat unidirectional composite with cylindrical fibers." In: *International Journal of Solids and Structures* 48.25 (2011), pp. 3510–3520.

[41] Benjamin Fulleringer. "Semi-analytical modeling of complex mechanical contacts: application to inclusions and swear of coated surfaces." PhD thesis. INSA-Lyon, 2011.

[42] D. Nelias and F. Ville. "Detrimental effects of debris dents on rolling contact fatigue." In: *Journal of Tribology* 122.1 (2000), pp. 55–64.

[43] JR Barber and M Ciavarella. "Contact mechanics." In: *International Journal of solids and structures* 37.1 (2000), pp. 29–43.

[44] Anup S. Pandkar, Nagaraj Arakere, and Ghatu Subhash. "Microstructure-sensitive accumulation of plastic strain due to ratcheting in bearing steels subject to Rolling Contact Fatigue." In: *International Journal of Fatigue* 63 (2014), pp. 191–202.

[45] Kun Zhou, W. Wayne Chen, Leon M. Keer, and Q. Jane Wang. "A fast method for solving three-dimensional arbitrarily shaped inclusions in a half space." In: *Computer Methods in Applied Mechanics and Engineering* 198.9 (2009), pp. 885–892.

[46] Shuangbiao Liu and Qian Wang. "Elastic fields due to eigenstrains in a half-space." In: *Journal of Applied Mechanics* 72.6 (2005), pp. 871–878.

[47] Shuangbiao Liu, Xiaoqing Jin, Zhanjiang Wang, Leon M. Keer, and Qian Wang. "Analytical solution for elastic fields caused by eigenstrains in a half-space and numerical implementation based on FFT." In: *International Journal of Plasticity* 35 (2012), pp. 135–154.

[48] Raymond D. Mindlin and David H. Cheng. "Thermoelastic stress in the semi-infinite solid." In: *Journal of Applied Physics* 21.9 (1950), pp. 931–933.

[49] Christophe Fond, Arnaud Riccardi, Robert Schirrer, and Frank Montheillet. “Mechanical interaction between spherical inhomogeneities: An assessment of a method based on the equivalent inclusion.” In: *European Journal of Mechanics - A/Solids* 20.1 (2001), pp. 59–75.

[50] I.A. Polonsky and L.M. Keer. “A numerical method for solving rough contact problems based on the multi-level multi-summation and conjugate gradient techniques.” In: *Wear* 231.2 (1999), pp. 206–219.

[51] L. Gallego, D. Nelias, and S. Deyber. “A fast and efficient contact algorithm for fretting problems applied to fretting modes I, II and III.” In: *Wear* 268.1 (2010), pp. 208–222.

[52] Christophe Jacq, Daniel Nelias, Gérard Lormand, and D Girodin. “Development of a three-dimensional semi-analytical elastic-plastic contact code.” In: *Journal of Tribology* 124.4 (2002), pp. 653–667.

[53] Shuangbiao Liu, Qian Wang, and Geng Liu. “A versatile method of discrete convolution and FFT (DC-FFT) for contact analyses.” In: *Wear* 243.1 (2000), pp. 101–111.

[54] Juan C. Simo and Robert Leroy Taylor. “Consistent tangent operators for rate-independent elastoplasticity.” In: *Computer Methods in Applied Mechanics and Engineering* 48.1 (1985), pp. 101–118.

[55] Thibaut Chaise, Daniel Nelias, and F Sadeghi. “On the effect of isotropic hardening on the coefficient of restitution for single or repeated impacts using a semi-analytical method.” In: *Tribology Transactions* 54.5 (2011), pp. 714–722.

[56] Toshio Mura. *Micromechanics of defects in solids.* Vol. 3. Springer, 1987.

[57] A. Giraud, Q.V. Huynh, D. Hoxha, and D. Kondo. “Application of results on Eshelby tensor to the determination of effective poroelastic properties of anisotropic rocks-like composites.” In: *International Journal of Solids and Structures* 44.1112 (2007), pp. 3756–3772. ISSN: 0020-7683. DOI: http://dx.doi.org/10.1016/j.ijsolstr.2006.10.019. URL: http://www.sciencedirect.com/science/article/pii/S0020768306004252.

[58] James G. Berryman. “Generalization of Eshelby’s formula for a single ellipsoidal elastic inclusion to poroelasticity and thermoelasticity.” In: *Physical Review Letters* 79.6 (1997), pp. 1142–1145.

[59] Koffi Espoir Koumi, Thibaut Chaise, and Daniel Nelias. “Rolling contact of a rigid sphere/sliding of a spherical indenter upon a viscoelastic half-space containing an ellipsoidal inhomogeneity.” In: *Journal of the Mechanics and Physics of Solids* 80 (2015), pp. 1–25.

[60] Caroline Bagault, Daniel Nelias, Marie-Christine Baietto, and Timothy C Ovaert. “Contact analyses for anisotropic half-space coated with an anisotropic layer: Effect of the anisotropy on the pressure distribution and contact area.” In: *International Journal of Solids and Structures* 50.5 (2013), pp. 743–754.

[61] Caroline Bagault, Daniel NĂŠlias, and Marie-Christine Baietto. “Contact analyses for anisotropic half space: effect of the anisotropy on the pressure distribution and contact area.” In: *Journal of tribology* 134.3 (2012), p. 031401.

[62] Yang Gao, Suenne Kim, Si Zhou, Hsiang-Chih Chiu, Daniel Nélias, Claire Berger, Walt De Heer, Laura Polloni, Roman Sordan, Angelo Bongiorno, et al. “Elastic coupling between layers in two-dimensional materials.” In: *Nature materials* 14.7 (2015), pp. 714–720.

[63] Albert Giraud, Quoc Vu Huynh, Dashnor Hoxha, and Djimedo Kondo. “Application of results on Eshelby tensor to the determination of effective poroelastic properties of anisotropic rocks-like composites.” In: *International journal of solids and structures* 44.11 (2007), pp. 3756–3772.

[64] James G Berryman. “Generalization of Eshelby’s formula for a single ellipsoidal elastic inclusion to poroelasticity and thermoelasticity.” In: *Physical review letters* 79.6 (1997), p. 1142.

[65] Julien Leroux, Benjamin Fulleringer, and Daniel Nelias. “Contact analysis in presence of spherical inhomogeneities within a half-space.” In: *International Journal of Solids and Structures* 47.22 (2010), pp. 3034–3049.

[66] Koffi Espoir Koumi, Daniel Nelias, Thibaut Chaise, and Arnaud Duval. “Modeling of the contact between a rigid indenter and a heterogeneous viscoelastic material.” In: *Mechanics of Materials* 77 (2014), pp. 28–42.

[67] Y.P. Chiu. “On the stress field due to initial strains in a cuboid surrounded by an infinite elastic space.” In: *Journal of Applied Mechanics* 44.4 (1977), pp. 587–590.

[68] Linzhi Wu and Shanyi Y. Du. “The Elastic Field Caused by a Circular Cylindrical Inclusion?Part II: Inside the Region x12+ x22> a2, -8< x3<8 Where the Circular Cylindrical Inclusion is Expressed by x12+ x22=a2,- h= x3= h.” In: *Journal of Applied Mechanics* 62.3 (1995), pp. 585–589.

[69] Yuji Nakasone, Hirotada Nishiyama, and Tetsuharu Nojiri. “Numerical equivalent inclusion method: a new computational method for analyzing stress fields in and around inclusions of various shapes.” In: *Materials Science and Engineering: A* 285.1 (2000), pp. 229–238.

[70] T. Mura and P.C. Cheng. “The elastic field outside an ellipsoidal inclusion.” In: *Journal of Applied Mechanics* 44.4 (1977), pp. 591–594.

[71] K. Seo and T. Mura. “The elastic field in a half space due to ellipsoidal inclusions with uniform dilatational eigenstrains.” In: *Journal of Applied Mechanics* 46.3 (1979), pp. 568–572.

[72] Y.P. Chiu. “On the stress field and surface deformation in a half space with a cuboidal zone in which initial strains are uniform.” In: *Journal of Applied Mechanics* 45.2 (1978), pp. 302–306.

[73] Gregory J. Rodin. “Eshelby’s inclusion problem for polygons and polyhedra.” In: *Journal of the Mechanics and Physics of Solids* 44.12 (1996), pp. 1977–1995.

[74] W. Wayne Chen, Shuangbiao Liu, and Q. Jane Wang. “Fast Fourier transform based numerical methods for elasto-plastic contacts of nominally flat surfaces.” In: *Journal of Applied Mechanics* 75.1 (2008), pp. 011022–1–11.

[75] Michael A Klecka, Ghatu Subhash, and Nagaraj K Arakere. “Microstructure–property relationships in M50-NiL and P675 case-hardened bearing steels.” In: *Tribology Transactions* 56.6 (2013), pp. 1046–1059.

[76] KR Eldredge and D Tabor. “The mechanism of rolling friction. I. The plastic range.” In: *Proceedings of the Royal Society of London A: Mathematical, Physical and Engineering Sciences*. Vol. 229. 1177. The Royal Society. 1955, pp. 181–198.

[77] AW Crook. "Simulated gear-tooth contacts: some experiments upon their lubrication and subsurface deformations." In: *Proceedings of the Institution of Mechanical Engineers* 171.1 (1957), pp. 187–214.

[78] M-H Evans, AD Richardson, L Wang, RJK Wood, and WB Anderson. "Confirming subsurface initiation at non-metallic inclusions as one mechanism for white etching crack (WEC) formation." In: *Tribology International* 75 (2014), pp. 87–97.

[79] M-H Evans, AD Richardson, L Wang, and RJK Wood. "Effect of hydrogen on butterfly and white etching crack (WEC) formation under rolling contact fatigue (RCF)." In: *Wear* 306.1 (2013), pp. 226–241.

[80] Farshid Sadeghi, Nick Weinzapfel, and Alexander Liebel. "A Damage Mechanics Approach to Simulate Butterfly Wing Formation Around Nonmetallic Inclusions." In: ().

[81] MH Evans. "White structure flaking (WSF) in wind turbine gearbox bearings: effects of 'butterflies' and white etching cracks (WECs)." In: *Materials Science and Technology* 28.1 (2012), pp. 3–22.

[82] M-H Evans, AD Richardson, L Wang, and RJK Wood. "Serial sectioning investigation of butterfly and white etching crack (WEC) formation in wind turbine gearbox bearings." In: *Wear* 302.1 (2013), pp. 1573–1582.

[83] MA Guler, Y Alinia, and S Adibnazari. "On the rolling contact problem of two elastic solids with graded coatings." In: *International Journal of Mechanical Sciences* 64.1 (2012), pp. 62–81.

[84] Gustaf Lundberg and Arvid Palmgren. "Dynamic capacity of rolling bearings." In: *JOURNAL OF APPLIED MECHANICS-TRANSACTIONS OF THE ASME* 16.2 (1949), pp. 165–172.

[85] E Ioannides and TA Harris. "A new fatigue life model for rolling bearings." In: *Journal of Tribology* 107.3 (1985), pp. 367–377.

[86] TA Harris, John Skiller, and Ronald F Spitzer. "On the fatigue life of M50 NiL rolling bearings." In: *Tribology transactions* 35.4 (1992), pp. 731–737.

[87] Gabriel Popescu, Antonio Gabelli, Guillermo Espejel, and Benny Wemekamp. "Micro-plastic material model and residual fields in rolling contacts." In: *Bearing Steel Technology-Advances and State of the Art in Bearing Steel Quality Assurance: 7th Volume*. ASTM International, 2007.

[88] C Richard Liu and Youngsik Choi. "Rolling contact fatigue life model incorporating residual stress scatter." In: *International Journal of Mechanical Sciences* 50.12 (2008), pp. 1572–1577.

[89] C Richard Liu and Youngsik Choi. "A new methodology for predicting crack initiation life for rolling contact fatigue based on dislocation and crack propagation." In: *International Journal of Mechanical Sciences* 50.2 (2008), pp. 117–123.

[90] Arnab Ghosh, Neil Paulson, and Farshid Sadeghi. "A fracture mechanics approach to simulate sub-surface initiated fretting wear." In: *International Journal of Solids and Structures* 58 (2015), pp. 335–352.

[91] S Bogdanski, M Olzak, and J Stupnicki. "Numerical stress analysis of rail rolling contact fatigue cracks." In: *Wear* 191.1 (1996), pp. 14–24.

[92] Yongming Liu, Liming Liu, and Sankaran Mahadevan. "Analysis of subsurface crack propagation under rolling contact loading in railroad wheels using FEM." In: *Engineering fracture mechanics* 74.17 (2007), pp. 2659–2674.

[93] Yanyao Jiang and Huseyin Sehitoglu. "A model for rolling contact failure." In: *Wear* 224.1 (1999), pp. 38–49.

[94] KD Vo, A Kiet Tieu, HT Zhu, and Prabuono Buyung Kosasih. "A 3D dynamic model to investigate wheel–rail contact under high and low adhesion." In: *International Journal of Mechanical Sciences* 85 (2014), pp. 63–75.

[95] Qinghua Zhou, Lechun Xie, Xiaoqing Jin, Zhanjiang Wang, Jiaxu Wang, Leon M Keer, and Qian Wang. "Numerical Modeling of Distributed Inhomogeneities and Their Effect on Rolling-Contact Fatigue Life." In: *Journal of Tribology* 137.1 (2015), p. 011402.

[96] Alan RS Ponter, HF Chen, M Ciavarella, and G Specchia. "Shakedown analyses for rolling and sliding contact problems." In: *International journal of solids and structures* 43.14 (2006), pp. 4201–4219.

[97] Chung Lun Pun, Qianhua Kan, Peter J Mutton, Guozheng Kang, and Wenyi Yan. "An efficient computational approach to evaluate the ratcheting performance of rail steels under cyclic rolling contact in service." In: *International Journal of Mechanical Sciences* 101 (2015), pp. 214–226.

[98] Zefeng Wen, Xuesong Jin, Xinbiao Xiao, and Zhongrong Zhou. "Effect of a scratch on curved rail on initiation and evolution of plastic deformation induced rail corrugation." In: *International Journal of Solids and Structures* 45.7 (2008), pp. 2077–2096.

[99] Vincent Boucly, Daniel Nelias, Shuangbiao Liu, Q Jane Wang, and Leon M Keer. "Contact analyses for bodies with frictional heating and plastic behavior." In: *Journal of tribology* 127.2 (2005), pp. 355–364.

[100] G Carbone and C Putignano. "Rough viscoelastic sliding contact: theory and experiments." In: *Physical Review E* 89.3 (2014), p. 032408.

[101] Qinghua Zhou, Xiaoqing Jin, Zhanjiang Wang, Jiaxu Wang, Leon M Keer, and Qian Wang. "An efficient approximate numerical method for modeling contact of materials with distributed inhomogeneities." In: *International Journal of Solids and Structures* 51.19 (2014), pp. 3410–3421.

[102] Chang-Hung Kuo. "Stress disturbances caused by the inhomogeneity in an elastic half-space subjected to contact loading." In: *International journal of solids and structures* 44.3 (2007), pp. 860–873.

[103] Tao He, Jiaxu Wang, Zhanjiang Wang, and Dong Zhu. "Simulation of Plasto-Elastohydrodynamic Lubrication (PEHL) in Line Contacts of Infinite and Finite Length." In: *Journal of Tribology* (2015).

[104] Kwassi Amuzuga, Chaise Thibaut, Nelias Daniel, and Duval Arnaud. "Fully coupled resolution of heterogeneous elastic-plastic contact problem." In: *Journal of Tribology* 201.2 (2015), pp. 238–249.

[105] Mehmet A Guler, Saeed Adibnazari, and Yadolah Alinia. "Tractive rolling contact mechanics of graded coatings." In: *International Journal of Solids and Structures* 49.6 (2012), pp. 929–945.

[106] K Dang Van, G Cailletaud, JF Flavenot, A Le Douaron, and HP Lieurade. "Criterion for high-cycle fatigue failure under multiaxial loading." In: *ICBMFF2*. 2013.

[107] George Sines and George Ohgi. "Fatigue criteria under combined stresses or strains." In: *Journal of Engineering Materials and Technology* 103.2 (1981), pp. 82–90.

[108] Anders Ekberg. "Rolling contact fatigue of railway wheels." In: *Chalmers University of Technology, Goteborg, Sweden* (2000).

[109] Felix Hofmann, Gratiela Bertolino, Andrei Constantinescu, and Mohamed Ferjani. "Numerical exploration of the Dang Van high cycle fatigue criterion: application to gradient effects." In: *Journal of Mechanics of Materials and Structures* 4.2 (2009), pp. 293–308.

[110] GM Hamilton et al. "Plastic flow in rollers loaded above the yield point." In: *Proceedings of the Institution of Mechanical Engineers* 177.1 (1963), pp. 667–675.

[111] G Peridas, AM Korsunsky, and DA Hills. "The relationship between the Dang Van criterion and the traditional bulk fatigue criteria." In: *The Journal of Strain Analysis for Engineering Design* 38.3 (2003), pp. 201–206.

[112] Eduard Antaluca and Daniel Nélias. "Contact fatigue analysis of a dented surface in a dry elastic–plastic circular point contact." In: *Tribology Letters* 29.2 (2008), pp. 139–153.

[113] PE Bold, MW Brown, and RJ Allen. "Shear mode crack growth and rolling contact fatigue." In: *Wear* 144.1-2 (1991), pp. 307–317.

[114] DI Fletcher, P Hyde, and A Kapoor. "Investigating fluid penetration of rolling contact fatigue cracks in rails using a newly developed full-scale test facility." In: *Proceedings of the Institution of Mechanical Engineers, Part F: Journal of Rail and Rapid Transit* 221.1 (2007), pp. 35–44.

[115] S Bogdanski. "A rolling contact fatigue crack driven by squeeze fluid film." In: *Fatigue & Fracture of Engineering Materials & Structures* 25.11 (2002), pp. 1061–1071.

[116] Sebastien Jegou, Laurent Barrallier, and Marcel AJ Somers. "Evolution des contraintes residuelles dans la couche de diffusion d un acier modele Fe-Cr-C nitrure." In: *Traitements & Materiaux* 411 (2011), pp. 21–27.

[117] Daniel GIRODIN. "Deep nitrided 32CrMoV13 steel for aerospace bearings applications." In: *TECHNICAL REVIEW* (2008).

[118] Marion Le, Fabrice Ville, Xavier Kleber, and Laurence Briançon. "Effect of intergranular cementite arrays in nitrided alloyed steels on gear rolling contact fatigue." In: *1st Porto-Lyon Tribology Workshop*. 2013, CD–ROM.

[119] Tedric Harris. "Rolling Bearing Analysis." In: *John Wiley and Sons, Inc.(United States), 1991,* (1991), p. 1013.

[120] Kenneth Langstreth Johnson. *A shakedown limit in rolling contact*. Division of Engineering, Brown University, 1962.

[121] K Ls Johnson and JA Jefferis. "Plastic flow and residual stresses in rolling and sliding contact." In: *Proc. Inst. Mech. Eng. Symp. on Rolling Contact Fatigue*. Institution of Mechanical Engineers London. 1963, pp. 50–61.

[122] DA Hills and DW Ashelby. "The influence of residual stresses on contact-load-bearing capacity." In: *Wear* 75.2 (1982), pp. 221–239.

[123] DA Hills and A Sackfield. "Yield and shakedown states in the contact of generally curved bodies." In: *The Journal of Strain Analysis for Engineering Design* 19.1 (1984), pp. 9–14.

[124] Joseph Edward Shigley. *Shigley's mechanical engineering design*. Tata McGraw-Hill Education, 2011.

[125] JE Merwin, KL Johnson, et al. "An analysis of plastic deformation in rolling contact." In: *Proceedings of the Institution of Mechanical Engineers* 177.1 (1963), pp. 676–690.

[126] NC Welsh. "Structural changes in rubbed steel surfaces." In: *Proc. Conf. Lubrication and Wear*. 1957, pp. 701–706.

[127] HS Cheng. "A numerical solution of the elastohydrodynamic film thickness in an elliptical contact." In: *Journal of Lubrication Technology* 92.1 (1970), pp. 155–161.

[128] Tedric A Harris and Roger M Barnsby. "Tribological performance prediction of aircraft gas turbine mainshaft ball bearings." In: *Tribology transactions* 41.1 (1998), pp. 60–68.

[129] Hana Jerbi, Daniel Nelias, and Marie-Christine Baietto. "Etude et modelisation de l endommagement du contact revetu soumise des sollicitations de fretting-fatigue." In: *S21 Endommagement et rupture* (2015).

[130] S Aamani, SK Pandey, R Nagalakshmi, and KS Pandey. "Effect of Homogenization &Quenching Media on the Mechanical Properties of Sintered Hot Forged AISI 9250 P/MSteel Preforms." In: ().

[131] Darrel W Smith and Stephen J Mashl. "Pore-free density of powder forged steel: comparison of measured and calculated values." In: *International journal of powder metallurgy* 28.3 (1992), pp. 271–278.

[132] Tatsuki Ohji, Yasuhiro Shigegaki, Tatsuya Miyajima, and Shuzo Kanzaki. "Fracture resistance behavior of multilayered silicon nitride." In: *Journal of the American Ceramic Society* 80.4 (1997), pp. 991–994.

[133] Yasuhiro Shigegaki, Manuel E Brito, Kiyoshi Hirao, Motohiro Toriyama, and Shuzo Kanzaki. "Strain tolerant porous silicon nitride." In: *Journal of the American Ceramic Society* 80.2 (1997), pp. 495–498.

[134] Yoshiaki Inagaki, Naoki Kondo, and Tatsuki Ohji. "High performance porous silicon nitrides." In: *Journal of the European Ceramic Society* 22.14 (2002), pp. 2489–2494.

[135] MZ Huq and J-P Celis. "Expressing wear rate in sliding contacts based on dissipated energy." In: *Wear* 252.5 (2002), pp. 375–383.

[136] EA Dean and JA Lopez. "Empirical dependence of elastic moduli on porosity for ceramic materials." In: *Journal of the American Ceramic Society* 66.5 (1983), pp. 366–370.

[137] EA Dean. "Elastic Moduli of Porous Sintered Materials as Modeled by a Variable-Aspect-Ratio Self-Consistent Oblate-Spheroidal-Inclusion Theory." In: *Journal of the American Ceramic Society* 66.12 (1983), pp. 847–854.

[138] DN Boccaccini, M Romagnoli, E Kamseu, Paolo Veronesi, C Leonelli, and GC Pellacani. "Determination of thermal shock resistance in refractory materials by ultrasonic pulse velocity measurement." In: *Journal of the European Ceramic Society* 27.2 (2007), pp. 1859–1863.

[139] Anthony P Roberts and Edward J Garboczi. "Elastic properties of model porous ceramics." In: *Journal of the American Ceramic Society* 83.12 (2000), pp. 3041–3048.

[140] T Mori and K Tanaka. "Average stress in matrix and average elastic energy of materials with misfitting inclusions." In: *Acta metallurgica* 21.5 (1973), pp. 571–574.

[141] ZSHTR Hashin and S Shtrikman. "A variational approach to the theory of the elastic behaviour of polycrystals." In: *Journal of the Mechanics and Physics of Solids* 10.4 (1962), pp. 343–352.

[142] Rodney Hill. "Elastic properties of reinforced solids: some theoretical principles." In: *Journal of the Mechanics and Physics of Solids* 11.5 (1963), pp. 357–372.

[143] JR Willis. "The structure of overall constitutive relations for a class of nonlinear composites." In: *IMA Journal of Applied Mathematics* 43.3 (1989), pp. 231–242.

[144] H Moulinec and P Suquet. "A numerical method for computing the overall response of nonlinear composites with complex microstructure." In: *Computer methods in applied mechanics and engineering* 157.1 (1998), pp. 69–94.

[145] PM Suquet. "Overall potentials and extremal surfaces of power law or ideally plastic composites." In: *Journal of the Mechanics and Physics of Solids* 41.6 (1993), pp. 981–1002.

[146] JR Brockenbrough, Subra Suresh, and HA Wienecke. "Deformation of metal-matrix composites with continuous fibers: geometrical effects of fiber distribution and shape." In: *Acta metallurgica et materialia* 39.5 (1991), pp. 735–752.

[147] Edward J Garboczi and James G Berryman. "Elastic moduli of a material containing composite inclusions: effective medium theory and finite element computations." In: *Mechanics of Materials* 33.8 (2001), pp. 455–470.

[148] AP Roberts and Edward J Garboczi. "Computation of the linear elastic properties of random porous materials with a wide variety of microstructure." In: *Proceedings of the Royal Society of London A: Mathematical, Physical and Engineering Sciences*. Vol. 458. 2021. The Royal Society. 2002, pp. 1033–1054.

[149] AV Manoylov, Feodor M Borodich, and Henry Peredur Evans. "Modelling of elastic properties of sintered porous materials." In: *Proceedings of the Royal Society of London A: Mathematical, Physical and Engineering Sciences*. Vol. 469. 2154. The Royal Society. 2013, p. 20120689.

[150] Felix Fritzen, Thomas Böhlke, and Eckart Schnack. "Periodic three-dimensional mesh generation for crystalline aggregates based on Voronoi tessellations." In: *Computational Mechanics* 43.5 (2009), pp. 701–713.

[151] Mark W Jessell, Paul D Bons, Albert Griera, Lynn A Evans, and Christopher JL Wilson. "A tale of two viscosities." In: *Journal of Structural Geology* 31.7 (2009), pp. 719–736.

[152] Kamel Madi, Samuel Forest, Patrick Cordier, and Michel Boussuge. "Numerical study of creep in two-phase aggregates with a large rheology contrast: implications for the lower mantle." In: *Earth and Planetary Science Letters* 237.1 (2005), pp. 223–238.

[153] G Cailletaud, S Forest, D Jeulin, F Feyel, I Galliet, V Mounoury, and S Quilici. "Some elements of microstructural mechanics." In: *Computational Materials Science* 27.3 (2003), pp. 351–374.

[154] Andrea Vigliotti, Vikram S Deshpande, and Damiano Pasini. "Non linear constitutive models for lattice materials." In: *Journal of the Mechanics and Physics of Solids* 64 (2014), pp. 44–60.

[155] Kim Pham, Varvara G Kouznetsova, and Marc GD Geers. "Transient computational homogenization for heterogeneous materials under dynamic excitation." In: *Journal of the Mechanics and Physics of Solids* 61.11 (2013), pp. 2125–2146.

[156] Julie Diani and Pierre Gilormini. "Using a pattern-based homogenization scheme for modeling the linear viscoelasticity of nano-reinforced polymers with an interphase." In: *Journal of the Mechanics and Physics of Solids* 63 (2014), pp. 51–61.

[157] LH Poh, RHJ Peerlings, MGD Geers, and S Swaddiwudhipong. "Towards a homogenized plasticity theory which predicts structural and microstructural size effects." In: *Journal of the Mechanics and Physics of Solids* 61.11 (2013), pp. 2240–2259.

[158] IM Gitman, H Askes, and LJ Sluys. "Representative volume: existence and size determination." In: *Engineering fracture mechanics* 74.16 (2007), pp. 2518–2534.

[159] Laurence Brassart, Laurent Stainier, Issam Doghri, and Laurent Delannay. "A variational formulation for the incremental homogenization of elasto-plastic composites." In: *Journal of the Mechanics and Physics of Solids* 59.12 (2011), pp. 2455–2475.

[160] Huan Chen, Yi Liu, Xuefeng Zhao, Yoram Lanir, and Ghassan S Kassab. "A micromechanics finite-strain constitutive model of fibrous tissue." In: *Journal of the Mechanics and Physics of Solids* 59.9 (2011), pp. 1823–1837.

[161] I Temizer and Peter Wriggers. "Homogenization in finite thermoelasticity." In: *Journal of the Mechanics and Physics of Solids* 59.2 (2011), pp. 344–372.

[162] Konstantinos Poulios and Christian F Niordson. "Homogenization of long fiber reinforced composites including fiber bending effects." In: *Journal of the Mechanics and Physics of Solids* 94 (2016), pp. 433–452.

[163] Jean-Claude Michel and Pierre Suquet. "Nonuniform transformation field analysis." In: *International journal of solids and structures* 40.25 (2003), pp. 6937–6955.

[164] Jean-Claude Michel and Pierre Suquet. "A model-reduction approach in micromechanics of materials preserving the variational structure of constitutive relations." In: *Journal of the Mechanics and Physics of Solids* 90 (2016), pp. 254–285.

[165] Kokou Anoukou, Franck Pastor, Philippe Dufrenoy, and Djimedo Kondo. "Limit analysis and homogenization of porous materials with Mohr–Coulomb matrix. Part I: Theoretical formulation." In: *Journal of the Mechanics and Physics of Solids* 91 (2016), pp. 145–171.

[166] F Pastor, K Anoukou, J Pastor, and D Kondo. "Limit analysis and homogenization of porous materials with Mohr–Coulomb matrix. Part II: Numerical bounds and assessment of the theoretical model." In: *Journal of the Mechanics and Physics of Solids* 91 (2016), pp. 14–27.

[167] Sébastien Brisard, Karam Sab, and Luc Dormieux. "New boundary conditions for the computation of the apparent stiffness of statistical volume elements." In: *Journal of the Mechanics and Physics of Solids* 61.12 (2013), pp. 2638–2658.

[168] P Mohammadi, LP Liu, P Sharma, and RV Kukta. "Surface energy, elasticity and the homogenization of rough surfaces." In: *Journal of the Mechanics and Physics of Solids* 61.2 (2013), pp. 325–340.

[169] F Devries, H Dumontet, G Duvaut, and F Léné. "Homogenization and damage for composite structures." In: *International Journal for Numerical Methods in Engineering* 27.2 (1989), pp. 285–298.

[170] José Miranda Guedes. *Nonlinear computational models for composite materials using homogenization*. 1990.

[171] Zhibin Fang, Binil Starly, and Wei Sun. "Computer-aided characterization for effective mechanical properties of porous tissue scaffolds." In: *Computer-Aided Design* 37.1 (2005), pp. 65–72.

[172] JC Michel, H Moulinec, and P Suquet. "Effective properties of composite materials with periodic microstructure: a computational approach." In: *Computer methods in applied mechanics and engineering* 172.1 (1999), pp. 109–143.

[173] Takao Hayashi and Hideo Koguchi. "Contact Analysis Considering Surface Stress and Surface Elasticity: Increase of Indentation Hardness and Yield Stress." In: *ASME 2012 International Mechanical Engineering Congress and Exposition*. American Society of Mechanical Engineers. 2012, pp. 207–214.

[174] Fengwen Wang, Ole Sigmund, and Jakob Søndergaard Jensen. "Design of materials with prescribed nonlinear properties." In: *Journal of the Mechanics and Physics of Solids* 69 (2014), pp. 156–174.

[175] E Kröner. "Bounds for effective elastic moduli of disordered materials." In: *Journal of the Mechanics and Physics of Solids* 25.2 (1977), pp. 137–155.

[176] E Kröner. "On the physics and mathematics of self-stresses." In: *Topics in Applied Continuum Mechanics*. Springer, 1974, pp. 22–38.

[177] Herve Moulinec and Pierre Suquet. "A fast numerical method for computing the linear and nonlinear mechanical properties of composites." In: *Comptes rendus de l'Académie des sciences. Série II, Mécanique, physique, chimie, astronomie* 318.11 (1994), pp. 1417–1423.

[178] Hervé Moulinec and Pierre Suquet. "Comparison of FFT-based methods for computing the response of composites with highly contrasted mechanical properties." In: *Physica B: Condensed Matter* 338.1 (2003), pp. 58–60.

[179] Zvi Hashin and Shmuel Shtrikman. "A variational approach to the theory of the elastic behaviour of multiphase materials." In: *Journal of the Mechanics and Physics of Solids* 11.2 (1963), pp. 127–140.

[180] Sébastien Brisard and Luc Dormieux. "Combining Galerkin approximation techniques with the principle of Hashin and Shtrikman to derive a new FFT-based numerical method for the homogenization of composites." In: *Computer Methods in Applied Mechanics and Engineering* 217 (2012), pp. 197–212.

[181] JOHN D Eshelby. “The determination of the elastic field of an ellipsoidal inclusion, and related problems.” In: *Proceedings of the Royal Society of London A: Mathematical, Physical and Engineering Sciences*. Vol. 241. 1226. The Royal Society. 1957, pp. 376–396.

[182] William P Kuykendall, William D Cash, David M Barnett, and Wei Cai. “On the existence of Eshelby’s equivalent ellipsoidal inclusion solution.” In: *Mathematics and Mechanics of Solids* 17.8 (2012), pp. 840–847.

[183] Y1 Benveniste. “A new approach to the application of Mori-Tanaka’s theory in composite materials.” In: *Mechanics of materials* 6.2 (1987), pp. 147–157.

[184] Mauro Ferrari. “Composite homogenization via the equivalent poly-inclusion approach.” In: *Composites Engineering* 4.1 (1994), pp. 37–45.

[185] AV Hershey. “The elasticity of an isotropic aggregate of anisotropic cubic crystals.” In: *Journal of Applied mechanics-transactions of the ASME* 21.3 (1954), pp. 236–240.

[186] Ekkehart Kröner. “Berechnung der elastischen Konstanten des Vielkristalls aus den Konstanten des Einkristalls.” In: *Zeitschrift für Physik* 151.4 (1958), pp. 504–518.

[187] R1 Hill. “A self-consistent mechanics of composite materials.” In: *Journal of the Mechanics and Physics of Solids* 13.4 (1965), pp. 213–222.

[188] VoigtW. “UberdieBeziehungZwischendenBeiden ElastizitatskonstantenIsotroperKorper.” In: *Wied. Ann* 38.2 (1889), p. 573.

[189] A Reuss. “Berechnung der Fließgrenze von Mischkristallen auf Grund der Plastizitätsbedingung für Einkristalle.” In: *ZAMM-Journal of Applied Mathematics and Mechanics/Zeitschrift für Angewandte Mathematik und Mechanik* 9.1 (1929), pp. 49–58.

[190] Rm Hill. “The elastic behaviour of a crystalline aggregate.” In: *Proceedings of the Physical Society. Section A* 65.5 (1952), p. 349.

[191] Warren Carl Oliver and George Mathews Pharr. “An improved technique for determining hardness and elastic modulus using load and displacement sensing indentation experiments.” In: *Journal of materials research* 7.06 (1992), pp. 1564–1583.

[192] EG Herbert, GM Pharr, WC Oliver, BN Lucas, and JL Hay. “On the measurement of stress–strain curves by spherical indentation.” In: *Thin solid films* 398 (2001), pp. 331–335.

[193] JB Pethicai, R Hutchings, and WC Oliver. “Hardness measurement at penetration depths as small as 20 nm.” In: *Philosophical Magazine A* 48.4 (1983), pp. 593–606.

[194] GM Pharr, WC Oliver, and FR Brotzen. “On the generality of the relationship among contact stiffness, contact area, and elastic modulus during indentation.” In: *Journal of materials research* 7.03 (1992), pp. 613–617.

[195] David Tabor. *The hardness of metals*. Oxford university press, 2000.

[196] JR Cahoon, WH Broughton, and AR Kutzak. “The determination of yield strength from hardness measurements.” In: *Metallurgical Transactions* 2.7 (1971), pp. 1979–1983.

[197] EJ Pavlina and CJ Van Tyne. "Correlation of yield strength and tensile strength with hardness for steels." In: *Journal of Materials Engineering and Performance* 17.6 (2008), pp. 888–893.

[198] Osamu Takakuwa, Yusuke Kawaragi, Hitoshi Soyama, et al. "Estimation of the yield stress of stainless steel from the Vickers hardness taking account of the residual stress." In: *Journal of Surface Engineered Materials and Advanced Technology* 3.04 (2013), p. 262.

[199] N Azeggagh, L Joly-Pottuz, J Chevalier, M Omori, T Hashida, and D Nélias. "To appear in: Materials Science & Engineering A." In: (2015).

[200] MW Finnis and JE Sinclair. "A simple empirical N-body potential for transition metals." In: *Philosophical Magazine A* 50.1 (1984), pp. 45–55.

[201] Fabrice Richard. "Identification du comportement et évaluation de la fiabilité des composites stratifiés." PhD thesis. Université de Franche-Comté, Besançon, 1999.

[202] Nacer Azeggagh. "Damage mechanisms in silicon nitride materials under contact loading." PhD thesis. Lyon, INSA, 2015.

[203] Aranzazu Diaz and Stuart Hampshire. "Characterisation of porous silicon nitride materials produced with starch." In: *Journal of the European Ceramic Society* 24.2 (2004), pp. 413–419.

[204] Aranzazu Diaz, Stuart Hampshire, Jian-Feng Yang, Tatsuki Ohji, and Shuzo Kanzaki. "Comparison of mechanical properties of silicon nitrides with controlled porosities produced by different fabrication routes." In: *Journal of the American Ceramic Society* 88.3 (2005), pp. 698–706.

[205] Felix Fritzen, Samuel Forest, Thomas Böhlke, Djimedo Kondo, and Toufik Kanit. "Computational homogenization of elasto-plastic porous metals." In: *International Journal of Plasticity* 29 (2012), pp. 102–119.

[206] Guangxu Wang and Renbin Zhan. "A new species of middle Rhuddanian Halysites (Tabulata) from Meitan, northern Guizhou, Southwest China." In: *Estonian Journal of Earth Sciences* 64.1 (2015), p. 105.

[207] Yan Liu, Maoqiu Wang, Jie Shi, Weijun Hui, Gang Fan, and Han Dong. "Fatigue properties of two case hardening steels after carburization." In: *International Journal of Fatigue* 31.2 (2009), pp. 292–299.

[208] Guanghong Wang, Shengguan Qu, Lianmin Yin, Xiaoqiang Li, Wen Yue, and ZhiQiang Fu. "Rolling contact fatigue property and failure mechanism of carburized 30CrSiMoVM steel at elevated temperature." In: *Tribology International* 98 (2016), pp. 144–154.

[209] Masahiro Fujii, Jiabin Ma, Akira Yoshida, Sadato Shigemura, and Kazumi Tani. "Influence of coating thickness on rolling contact fatigue of alumina ceramics thermally sprayed on steel roller." In: *Tribology international* 39.11 (2006), pp. 1447–1453.

[210] Masahiro Fujii, Akira Yoshida, Jiabin Ma, Sadato Shigemura, and Kazumi Tani. "Rolling contact fatigue of alumina ceramics sprayed on steel roller under pure rolling contact condition." In: *Tribology international* 39.9 (2006), pp. 856–862.

[211] XC Zhang, BS Xu, FZ Xuan, ST Tu, HD Wang, and YX Wu. "Rolling contact fatigue behavior of plasma-sprayed CrC–NiCr cermet coatings." In: *Wear* 265.11 (2008), pp. 1875–1883.

[212] Jixi Zhang, Rajesh Prasannavenkatesan, Mahesh M Shenoy, and David L McDowell. "Modeling fatigue crack nucleation at primary inclusions in carburized and shot-peened martensitic steel." In: *Engineering Fracture Mechanics* 76.3 (2009), pp. 315–334.

[213] Hongbin Xiao, Qing Chen, Eryu Shao, Dengzhen Wu, Zhaohong Chen, and Zhengle Wang. "The effect of shot peening on rolling contact fatigue behaviour and its crack initiation and propagation in carburized steel." In: *Wear* 151.1 (1991), pp. 77–86.

[214] Steve Ooi and HKDH Bhadeshia. "Duplex hardening of steels for aeroengine bearings." In: *ISIJ international* 52.11 (2012), pp. 1927–1934.

[215] Bong-Seok Suh and Won-Jong Lee. "Surface hardening of AISI 316L stainless steel using plasma carburizing." In: *Thin Solid Films* 295.1 (1997), pp. 185–192.

[216] Sheng-guang Zhang, Wen-zhong Wang, Hai-bo Zhang, and Zi-qiang Zhao. "The effect of hardness distribution by carburizing on the elastic–plastic contact performance." In: *Tribology International* (2015).

[217] Kenan Genel and Mehmet Demirkol. "Effect of case depth on fatigue performance of AISI 8620 carburized steel." In: *International Journal of Fatigue* 21.2 (1999), pp. 207–212.

[218] Osman Asi, Ahmet Çetin Can, James Pineault, and Mohammed Belassel. "The relationship between case depth and bending fatigue strength of gas carburized SAE 8620 steel." In: *Surface and Coatings Technology* 201.12 (2007), pp. 5979–5987.

[219] S Preston. "Bending fatigue strength of carburising steel SS 2506." In: *Materials Science and Technology* 7.2 (1991), pp. 105–110.

[220] Sriram Pattabhiraman, George Levesque, Nam H Kim, and Nagaraj K Arakere. "Uncertainty analysis for rolling contact fatigue failure probability of silicon nitride ball bearings." In: *International Journal of Solids and Structures* 47.18 (2010), pp. 2543–2553.

[221] Bruce Boardman. "Fatigue resistance of steels." In: *ASM Handbook* Vol 1: Properties and Selection: Irons, Steels, and High-Performance Alloys ASM Handbook Committee (1990), pp. 673–688.

[222] Kazuhiro Yagita and Chikara OHKI. "Plasma nitriding treatment of high alloy steel for bearing components." In: *TECHNICAL REVIEW* (2010).

[223] M Tsujikawa, N Yamauchi, N Ueda, T Sone, and Y Hirose. "Behavior of carbon in low temperature plasma nitriding layer of austenitic stainless steel." In: *Surface and Coatings Technology* 193.1 (2005), pp. 309–313.

[224] Qin Xie, Geng Liu, Tian Xiang Liu, and Jane Q Wang. "Elastic-Plastic Contact Analysis of Materials with Gradient Yield Strength." In: *Materials Science Forum*. Vol. 532. Trans Tech Publ. 2006, pp. 881–884.

[225] Guanghong Wang, Shengguan Qu, Fuqiang Lai, Xiaoqiang Li, Zhiqiang Fu, and Wen Yue. "Rolling contact fatigue and wear properties of 0.1 C–3Cr–2W–V nitrided steel." In: *International Journal of Fatigue* 77 (2015), pp. 105–114.

[226] Z Sun, CS Zhang, and MF Yan. "Microstructure and mechanical properties of M50NiL steel plasma nitrocarburized with and without rare earths addition." In: *Materials & Design* 55 (2014), pp. 128–136.

[227] D Cleugh, C Blawert, J Steinbach, H Ferkel, BL Mordike, and T Bell. "Effects of rare earth additions on nitriding of EN40B by plasma immersion ion implantation." In: *Surface and Coatings Technology* 142 (2001), pp. 392–396.

[228] Shinichiro Adachi and Nobuhiro Ueda. "Surface hardness improvement of plasma-sprayed AISI 316L stainless steel coating by low-temperature plasma carburizing." In: *Advanced Powder Technology* 24.5 (2013), pp. 818–823.

[229] S Suresh. "Graded materials for resistance to contact deformation and damage." In: *Science* 292.5526 (2001), pp. 2447–2451.

[230] IS Choi, M Dao, and S Suresh. "Mechanics of indentation of plastically graded materials—I: Analysis." In: *Journal of the Mechanics and Physics of Solids* 56.1 (2008), pp. 157–171.

[231] S Ramanathan and VM Radhakrishnan. "Investigation of rolling contact fatigue damage of a case-carburized low alloy steel." In: *Wear* 45.3 (1977), pp. 323–333.

[232] L-M Berger, K Lipp, J Spatzier, and J Bretschneider. "Dependence of the rolling contact fatigue of HVOF-sprayed WC–17% Co hardmetal coatings on substrate hardness." In: *Wear* 271.9 (2011), pp. 2080–2088.

[233] Wen Yue, Zhiqiang Fu, Song Wang, Xiaocheng Gao, Haipeng Huang, and Jia-jun Liu. "Tribological synergistic effects between plasma nitrided 52100 steel and molybdenum dithiocarbamates additive in boundary lubrication regime." In: *Tribology International* 74 (2014), pp. 72–78.

[234] DI Fletcher, P Hyde, and A Kapoor. "Modelling and full-scale trials to investigate fluid pressurisation of rolling contact fatigue cracks." In: *Wear* 265.9 (2008), pp. 1317–1324.

[235] Yanqiu Xia, Feng Zhou, Shinya Sasaki, Takashi Murakami, and Meihuan Yao. "Remarkable friction stabilization of AISI 52100 steel by plasma nitriding under lubrication of alkyl naphthalene." In: *Wear* 268.7 (2010), pp. 917–923.

[236] Sina Mobasher Moghaddam, Farshid Sadeghi, Kristin Paulson, Nick Weinzapfel, Martin Correns, Vasilios Bakolas, and Markus Dinkel. "Effect of non-metallic inclusions on butterfly wing initiation, crack formation, and spall geometry in bearing steels." In: *International Journal of Fatigue* 80 (2015), pp. 203–215.

[237] Yi Shen, Sina Mobasher Moghadam, Farshid Sadeghi, Kristin Paulson, and Rodney W Trice. "Effect of retained austenite–compressive residual stresses on rolling contact fatigue life of carburized AISI 8620 steel." In: *International Journal of Fatigue* 75 (2015), pp. 135–144.

[238] CG He, YB Huang, L Ma, J Guo, WJ Wang, QY Liu, and MH Zhu. "Experimental investigation on the effect of tangential force on wear and rolling contact fatigue behaviors of wheel material." In: *Tribology International* 92 (2015), pp. 307–316.

[239] M-H Evans, L Wang, H Jones, and RJK Wood. "White etching crack (WEC) investigation by serial sectioning, focused ion beam and 3-D crack modelling." In: *Tribology International* 65 (2013), pp. 146–160.

[240] Guo-Fa Mi, Hong-Yan Nan, Yan-Lei Liu, Bin Zhang, Hong Zhang, and Guo-Xiang Song. "Influence of inclusion on crack initiation in wheel rim." In: *Journal of Iron and Steel Research, International* 18.1 (2011), pp. 49–54.

[241] Jia-jie Kang, Bin-shi Xu, Hai-dou Wang, and Cheng-biao Wang. "Influence of contact stress on rolling contact fatigue of composite ceramic coatings plasma sprayed on a steel roller." In: *Tribology International* 73 (2014), pp. 47–56.

[242] M-H Evans, JC Walker, Chao Ma, L Wang, and RJK Wood. "A FIB/TEM study of butterfly crack formation and white etching area (WEA) microstructural changes under rolling contact fatigue in 100Cr6 bearing steel." In: *Materials Science and Engineering: A* 570 (2013), pp. 127–134.

[243] Y Shen, J Garnier, L Allais, J Crepin, O Ancelet, and J-M Hiver. "Experimental and numerical characterization of anisotropic damage evolution of forged Al6061-T6 alloy." In: *Procedia Engineering* 10 (2011), pp. 3429–3434.

[244] Eric E Magel. *Rolling contact fatigue: a comprehensive review*. Tech. rep. 2011.

[245] Fausto Pedro García Márquez, Andrew Mark Tobias, Jesús María Pinar Pérez, and Mayorkinos Papaelias. "Condition monitoring of wind turbines: Techniques and methods." In: *Renewable Energy* 46 (2012), pp. 169–178.

[246] Leonard M Rogers. "Detection of incipient damage in large rolling element bearings." In: *Advanced Materials Research*. Vol. 13. Trans Tech Publ. 2006, pp. 37–44.

[247] YB Guo and Dale W Schwach. "An experimental investigation of white layer on rolling contact fatigue using acoustic emission technique." In: *International journal of fatigue* 27.9 (2005), pp. 1051–1061.

[248] Jianguo Yu, Paul Ziehl, Boris Zárate, and Juan Caicedo. "Prediction of fatigue crack growth in steel bridge components using acoustic emission." In: *Journal of Constructional Steel Research* 67.8 (2011), pp. 1254–1260.

[249] Zhang Zhi-qiang, Li Guo-lu, Wang Hai-dou, Xu Bin-shi, Piao Zhong-yu, and Zhu Li-na. "Investigation of rolling contact fatigue damage process of the coating by acoustics emission and vibration signals." In: *Tribology International* 47 (2012), pp. 25–31.

[250] Vincent Boucly. "Semi-analytical modeling of the transient thermal-elastic-plastic contact and its application to asperity collision, wear and running-in of surfaces." PhD thesis. 2008.

[251] W Wayne Chen and Q Jane Wang. "Thermomechanical analysis of elastoplastic bodies in a sliding spherical contact and the effects of sliding speed, heat partition, and thermal softening." In: *Journal of Tribology* 130.4 (2008), p. 041402.

[252] Yong Hoon Jang, Hanbum Cho, and JR Barber. "The thermoelastic Hertzian contact problem." In: *International Journal of Solids and Structures* 46.22 (2009), pp. 4073–4078.

[253] Pawel Rycerz Amir Kadiric. "Initiation and Propagation of Rolling Contact Fatigue Cracks." In: *Joint workshop on "Frontier in Tribology" between LICP and Imperial College London Lanzhou, 22-23 Sep.* 2014.

[254] Michael A Klecka, Ghatu Subhash, and Nagaraj K Arakere. "Microstructure–property relationships in M50-NiL and P675 case-hardened bearing steels." In: *Tribology Transactions* 56.6 (2013), pp. 1046–1059.

[255] M Tsujikawa, S Noguchi, N Yamauchi, N Ueda, and T Sone. "Effect of molybdenum on hardness of low-temperature plasma carburized austenitic stainless steel." In: *Surface and Coatings Technology* 201.9 (2007), pp. 5102–5107.

[256] Donald J Wulpi. *Understanding how components fail.* ASM international, 2013.

[257] Lee Tucker, Stephen Downing, and Louis Camillo. *Accuracy of simplified fatigue prediction methods.* Tech. rep. SAE Technical Paper, 1975.

[258] Cao Hong-de. "Mechanics of Plastic Deformation and Theory of Rollin." In: *Beijing: Mechanical Industry Press* (1981).

[259] W Wayne Chen, Kun Zhou, Leon M Keer, and Q Jane Wang. "Modeling elasto-plastic indentation on layered materials using the equivalent inclusion method." In: *International Journal of Solids and Structures* 47.20 (2010), pp. 2841–2854.

[260] YP Chiu. "On the internal stresses in a half plane and a layer containing localized inelastic strains or inclusions." In: *Journal of Applied Mechanics* 47.2 (1980), pp. 313–318.

[261] Joseph Boussinesq. *Application des potentiels a l'etude de l'equilibre et du mouvement des solides elastiques: principalement au calcul des deformations et des pressions que produisent, dans ces solides, des efforts quelconques exerces sur une petite partie de leur surface ou de leur interieur: memoire suivi de notes etendues sur divers points de physique, mathematique et d'analyse.* Vol. 4. Gauthier-Villars, 1885.

[262] V Cerruti. "Richerche intorno all equilibrio de corpi elastici isotropi." In: *Atti Accad. Naz. Lincei Mem. Cl. Sci. Fis. Mat. Nat. Sez* 13 (1888), p. 81.

[263] IA Polonsky and LM Keer. "A fast and accurate method for numerical analysis of elastic layered contacts." In: *Journal of tribology* 122.1 (2000), pp. 30–35.

[264] IA Polonsky and LM Keer. "A numerical method for solving rough contact problems based on the multi-level multi-summation and conjugate gradient techniques." In: *Wear* 231.2 (1999), pp. 206–219.

[265] Fan Wang and Leon M Keer. "Numerical simulation for three dimensional elastic-plastic contact with hardening behavior." In: *Journal of Tribology* 127.3 (2005), pp. 494–502.

[266] Daniel Nelias, Vincent Boucly, and Michel Brunet. "Elastic-plastic contact between rough surfaces: proposal for a wear or running-in model." In: *Journal of Tribology* 128.2 (2006), pp. 236–244.

[267] W Wayne Chen, Q Jane Wang, Yuchuan Liu, Wei Chen, Jiao Cao, Cedric Xia, Raj Talwar, and Rick Lederich. "Analysis and convenient formulas for elasto-plastic contacts of nominally flat surfaces: average gap, contact area ratio, and plastically deformed volume." In: *Tribology Letters* 28.1 (2007), pp. 27–38.

[268] Daniel NĂŠlias, Eduard Antaluca, and Vincent Boucly. "Rolling of an elastic ellipsoid upon an elastic-plastic flat." In: *Journal of Tribology* 129.4 (2007), pp. 791–800.

[269] J Nyqvist, A Kadiric, S Ioannides, and R Sayles. "Semi-analytical model for rough multilayered contacts." In: *Tribology International* 87 (2015), pp. 98–112.

[270] *M50 datasheet, M50 property, M50 standard specification, M50 standard download.* URL: http://www.steel-grades.com/Steel-Grades/Tool-Steel-Hard-Alloy/M50.html.

[271] Michael M Dezzani and Philip K Pearson. *Improved Hybrid Bearings.* Tech. rep. DTIC Document, 1994.

[272] Donald C Zipperian. “Metallographic Specimen Preparation Basics.” In: *Pace Technologies. Disponível em http://www. metallographic. com/Basics. htm. Acesso em Agosto* (2006).

[273] Udomchok Phromsuwan, Chitnarong Sirisathitkul, Yaowarat Sirisathitkul, Bunyarit Uyyanonvara, and Paisarn Muneesawang. “Application of image processing to determine size distribution of magnetic nanoparticles.” In: *Journal of Magnetics* 18.3 (2013), pp. 311–316.

[274] Pavla Vozková and Jana Salačová. “Elastic Properties of Woven Composite.” In: *CD Proceedings of the Conference 15th Annual International Conference on Composites/Nano Engineering*. 2007.

[275] Nathan A Branch, Ghatu Subhash, Nagaraj K Arakere, and Michael A Klecka. “A new reverse analysis to determine the constitutive response of plastically graded case hardened bearing steels.” In: *International Journal of Solids and Structures* 48.3 (2011), pp. 584–591.

[276] HKDH Bhadeshia and W Solano-Alvarez. “Critical assessment 13: elimination of white etching matter in bearing steels.” In: *Materials Science and Technology* 31.9 (2015), pp. 1011–1015.

[277] Ashby and Jones. “An Introduction to their Properties and Applications.” In: *Engineering Materials* (1980).

[278] Julien Réthoré, Jean-Philippe Tinnes, Stéphane Roux, Jean-Yves Buffière, and François Hild. “Extended three-dimensional digital image correlation (X3D-DIC).” In: *Comptes Rendus Mécanique* 336.8 (2008), pp. 643–649.

[279] D Spriestersbach, P Grad, and E Kerscher. “Influence of different non-metallic inclusion types on the crack initiation in high-strength steels in the VHCF regime.” In: *International Journal of Fatigue* 64 (2014), pp. 114–120.

[280] Sina Mobasher Moghaddam, Farshid Sadeghi, Nick Weinzapfel, and Alexander Liebel. “A damage mechanics approach to simulate butterfly wing formation around nonmetallic inclusions.” In: *Journal of Tribology* 137.1 (2015), p. 011404.

[281] Yu-gui LI, Qing-xue HUANG, Guang-xian SHEN, XIAO Hong, Si-qin PANG, and Jian-mei WANG. “Simulation of strip rolling using elastoplastic contact BEM with friction.” In: *Journal of Iron and Steel Research, International* 15.1 (2008), pp. 34–38.

[282] Piao Zhong-yu, Xu Bin-shi, Wang Hai-dou, and Wen Dong-hui. “Influence of surface nitriding treatment on rolling contact behavior of Fe-based plasma sprayed coating.” In: *Applied Surface Science* 266 (2013), pp. 420–425.

[283] Zhong-yu Piao, Bin-shi Xu, Hai-dou Wang, and Dong-hui Wen. “Influence of surface roughness on rolling contact fatigue behavior of Fe-Cr alloy coatings.” In: *Journal of materials engineering and performance* 22.3 (2013), pp. 767–773.

[284] George Levesque and Nagaraj K Arakere. “An investigation of partial cone cracks in silicon nitride balls.” In: *International Journal of Solids and Structures* 45.25 (2008), pp. 6301–6315.

[285] Annika M Diederichs, Soeren Barteldes, Alexander Schwedt, Joachim Mayer, and Walter Holweger. “Study of subsurface initiation mechanism for white etching crack formation.” In: *Materials Science and Technology* 32.11 (2016), pp. 1170–1178.

[286] HKDH Bhadeshia. “Steels for bearings.” In: *Progress in materials Science* 57.2 (2012), pp. 268–435.

[287] PC Becker. “Microstructural changes around non-metallic inclusions caused by rolling-contact fatigue of ball-bearing steels.” In: *Metals Technology* 8.1 (1981), pp. 234–243.

[288] Y-C Xiao, S Li, and Z Gao. “A continuum damage mechanics model for high cycle fatigue.” In: *International Journal of Fatigue* 20.7 (1998), pp. 503–508.

[289] J Lemaitre. “A Course on Damage Mechanics Springer-Verlag Berlin MATH.” In: (1992).

[290] HPCO Swahn, PC Becker, and O Vingsbo. “Martensite decay during rolling contact fatigue in ball bearings.” In: *Metallurgical Transactions A* 7.8 (1976), pp. 1099–1110.

[291] Abir Bhattacharyya, Ghatu Subhash, and Nagaraj Arakere. “Evolution of subsurface plastic zone due to rolling contact fatigue of M-50 NiL case hardened bearing steel.” In: *International Journal of Fatigue* 59 (2014), pp. 102–113.

[292] Daniel Zwillinger. *Table of integrals, series, and products*. Elsevier, 2014.

[293] Kenneth Langstreth Johnson. *Contact mechanics*. Cambridge university press, 1987.

FOLIO ADMINISTRATIF
THESE DE L'UNIVERSITE DE LYON OPEREE AU SEIN DE L'INSA LYON

NOM : AMUZUGA — DATE de SOUTENANCE : 16 Décembre 2016

Prénom : Kwassi

TITRE : Étude des mécanismes d'endommagement liés à la présence d'hétérogénéités dans un contact élasto-plastique hybride céramique/acier

NATURE : Doctorat — Numéro d'ordre : 2016LYSEI154

École doctorale : MEGA

Spécialité : Mécanique - Génie Mécanique - Génie Civil

RÉSUMÉ :
La durée de vie des pièces mécaniques en contact est fortement affectée par la présence d'hétérogénéités dans le matériau, comme des renforts (fibres, particules), des précipités, des porosités, ou encore des fissures. Des hétérogénéités dures et de formes complexes peuvent créer des surcontraintes locales, initiatrices de fissures par fatigue à proximité de la surface de contact. La présence d'hétérogénéités influence grandement les propriétés physiques et mécaniques du matériau à l'échelle locale et globale. Une analyse quantitative des surcontraintes créées par les hétérogénéités est nécessaire à la compréhension des mécanismes d'endommagement. Cette étude s'applique à des roulements de ligne d'arbre qui font partie des éléments critiques de moteurs en aéronautique. Les performances recherchées pour ces roulements ont conduit SKF Aerospace à mettre en œuvre une nouvelle technologie de roulement hybride avec des éléments roulants céramiques et des bagues en acier doublement traité en surface (cémentation suivi de nitruration). L'étude vise à déterminer précisément la distribution du champ de pression sur l'aire effective de contact et à prédire le profil et l'évolution des champs de contraintes/déformations à chaque passage de la charge sur un volume élémentaire représentatif prenant en compte le gradient de dureté, la présence de carbures et l'existence des contraintes initiales d'origine thermochimique.
Une partie de l'étude est consacrée au développement d'un solveur du problème de contact roulant élasto-plastique avec présence d'hétérogénéité par les méthodes semi analytiques assurant un excellent gain en temps et ressources de calculs. Ensuite, un algorithme homogénéisation a été conçu pour analyser le comportement effectif d'un massif élasto-plastique hétérogène sous indentation. Enfin une partie expérimentale est dédiée à la caractérisation microstructurale des aciers étudiés dans le but de déterminer leurs propriétés. Une description du comportement les carbures dans la matrice, a été réalisée lors d'essais de micro-traction sous observation MEB in-situ.
Les analyses des résultats de cette étude concourent à soutenir que bien que les inclusions de particules non métalliques soient responsables de la haute résistance de ces matériaux, certaines d'entre elles (celles de longueur dépassant les dizaines de micromètre ou celles qui forment des chaines dans une direction particulière) deviennent, au cours des cycles de fatigue, les principales sources d'endommagement depuis l'échelle locale jusqu'à la rupture globale de la structure.

MOTS CLÉS : Roulement, Semi-Analytique, Hétérogénéité, Plasticité, Fatigue

Laboratoire(s) de recherche : Laboratoire de Mécanique des Contacts et des Solides
UMR CNRS 5514 - INSA de Lyon
20, avenue Albert Einstein
69621 Villeurbanne Cedex FRANCE

Directeur de thèse : Monsieur le Professeur Daniel NÉLIAS

Président du jury : firstname LASTNAME

Composition du jury :

Sylvie POMMIER	Djimedo KONDO
Farshid SADEGHI	Daniel NÉLIAS
Guillermo MORALES	Sophie CAZOTTES
Alexandre MONDELIN	Thibaut CHAISE